Virtual Fields Method for the Dynamic Behaviour of Metallic Materials under Purely Inertial Loads

Pascal Bouda

▶ **To cite this version:**

Pascal Bouda. Virtual Fields Method for the Dynamic Behaviour of Metallic Materials under Purely Inertial Loads. Engineering Sciences [physics]. UNIVERSITE POLYTECHNIQUE HAUTS-DE-FRANCE, 2019. English. NNT : 2019VALE003 . tel-02132396

HAL Id: tel-02132396
https://hal.science/tel-02132396v1

Submitted on 17 May 2019

HAL is a multi-disciplinary open access archive for the deposit and dissemination of scientific research documents, whether they are published or not. The documents may come from teaching and research institutions in France or abroad, or from public or private research centers.

L'archive ouverte pluridisciplinaire **HAL**, est destinée au dépôt et à la diffusion de documents scientifiques de niveau recherche, publiés ou non, émanant des établissements d'enseignement et de recherche français ou étrangers, des laboratoires publics ou privés.

Distributed under a Creative Commons Attribution 4.0 International License

N° d'ordre: 19/03

Thèse de doctorat

Pour obtenir le grade de Docteur de

l'UNIVERSITÉ POLYTECHNIQUE HAUTS-DE-FRANCE

Discipline, spécialité selon la liste des spécialités pour lesquelles l'Ecole Doctorale est accréditée :

Mécanique

Présentée et soutenue publiquement par Pascal BOUDA

Le 11/03/2019, à Lille

École doctorale :
Sciences Pour l'Ingénieur (ED SPI 072)

Équipe de recherche, Laboratoire :
Laboratoire d'Automatique, de Mécanique et d'Informatique Industrielles et Humaines (LAMIH - UMR 8201)

Méthode des Champs Virtuels pour la caractérisation du comportement dynamique de matériaux métalliques sous chargement purement inertiel

JURY

M.	Julien RÉTHORÉ, Directeur de Recherche CNRS au Laboratoire GEM de Nantes	Président du Jury
M.	Michel GRÉDIAC, Professeur de l'Université Clermont Auvergne	Rapporteur
M.	Jean-Philippe PONTHOT, Professeur de l'Université de Liège (Belgique)	Rapporteur
M.	Eric MARKIEWICZ, Professeur de l'Université Polytechnique Hauts-de-France	Directeur de thèse
M.	Fabrice PIERRON, Professeur de l'Université de Southampton (UK)	Co-directeur de thèse
Mme	Patricia VERLEYSEN, Professeur de l'Université de Gand (Belgique)	Examinateur
M.	Bertrand LANGRAND, Directeur de Recherche à l'ONERA	Examinateur
Mme	Delphine NOTTA-CUVIER, Maître de Conférences de l'Université Polytechnique Hauts-de-France	Examinateur

"Il n'y a pas d'Hommes incapables, il n'y a que des paresseux."
Un proverbe africain

"No free meal !"
Ted Belytschko

A vous, Maman et Papa,

Contents

Acknowledgements

Avant de dérouler ce manuscrit, je souhaite remercier tous les acteurs qui ont permis à cette thèse d'aboutir car elle est le fruit de trois ans de travail et une collaboration tripartite entre l'Office National d'Études et de Recherches Aérospatiales (ONERA), l'Université Polytechnique Hauts-de-France et l'Université de Southampton. Je remercie également l'ONERA et la Région Hauts-de-France pour le co-financement de cette thèse.

Tout d'abord, je remercie les Professeurs Michel Grédiac de l'Université Clermont Auvergne et Jean-Philippe Ponthot de l'Université de Liège pour l'intérêt porté à ce travail en acceptant de le rapporter. Je remercie également les autres membres extérieurs du jury que sont le Professeur Patricia Verleysen de l'Université de Gand et Monsieur Julien Réthoré du laboratoire GEM de Nantes pour leur intérêt porté à ce travail et pour avoir accepté de l'examiner.

Cette thèse aboutit notamment grâce à un encadrement envers qui je suis grandement reconnaissant. Aussi, je souhaitais remercier mes deux directeurs de thèse, les Professeurs Eric Markiewicz de l'Université Polytechnique Hauts-de-France et Fabrice Pierron de l'Université de Southampton. Même si la distance géographique était importante, les nombreux échanges que nous avons eus ont été déterminants dans l'avancée et la conclusion de ces travaux de thèse.

Ayant passé la majorité de mon temps à l'ONERA, je souhaitais aussi exprimer ma grande gratitude envers Monsieur Bertrand Langrand qui a été bien plus qu'un encadrant "local". En effet, sa disponibilité et son regard critique mais toujours objectif ont largement contribué à ma formation par la recherche. Constament à l'écoute, ces travaux n'auraient pas pu aboutir sans lui ! Je remercie aussi mon encadrante Madame Delphine Notta-Cuvier de l'Université Polytechnique Hauts-de-France. Nos conversations nourries ont en effet permis la sortie de situations parfois délicates.

Ma période à l'ONERA a également été l'occasion de sympathiser avec de nombreuses personnes. Au sein de l'unité Conception et Résistance Dynamique (CRD) qui m'a chaleureusement accueilli, je souhaite donc remercier Bernard, David, Didier, Eric, Fabien, Gérald, Jacques, Jean-Luc, Julien, Laurent, Matthieu, Roland, Romain, Steve et Thomas, mais aussi les jeunes retraités que sont Alain et Jean-François. Je remercie également mes camarades de galère récemment thésés ou qui le seront bientôt: mon successeur Jean-David (!), Magali, Nicolas, Noelig et Tovignon. Que ce soit sur le plan scientifique ou humain, la relation entretenue avec chacun d'entre vous a été globalement agréable, et je suis persuadé que le contexte créée a largement contribué à l'aboutissement de ces travaux.

Je tenais enfin à remercier tous les acteurs la campagne d'essais mécaniques réalisée à l'Université de Southampton. Je remercie d'abord les membres du groupe de travail Photodyn pour leur accueil et leur bienvieillance: Alex, Frances, Jared, Lloyd (a thousand thanks for the perfect IBII tests…) et Xavier. Je n'oublie pas aussi de remercier l'unité Ateliers Maquettes pour Souffleries (AMS) de l'ONERA pour la qualité remarquable des éprouvettes usinées.

Enfin, je ne peux conclure ces remerciements sans attribuer une mention spéciale à ma famille qui me supporte depuis bientôt vingt-sept ans. Maman, Papa, Mathieu, Fleur et Richard, je vous dis tout simplement merci ...

Nomenclature

Mathematical quantities & operators:

$\underline{(.)}$	first-order tensor (vector) $(.)$
$\underline{\underline{(.)}}$	second-order tensor (matrix) $(.)$
$\underline{\underline{\underline{\underline{\mathscr{M}}}}}$	fourth-order tensor $\mathscr{M}$
$(.)^T$	Transpose of matrix $(.)$
$\underline{\underline{I}}$	Identity matrix
$\mathrm{Tr}\,[(.)]$	Trace of matrix $(.)$
$\nabla(.)$	Gradient of $(.)$
$\dot{(.)}$	Time derivative of $(.)$
$\vec{a} \times \vec{b}$	Cross product between 2D vectors $\vec{a}$ and $\vec{b}$

Mechanical quantities:

$\underline{\underline{F}}$	Transformation gradient tensor
$\underline{u}$	Displacement vector
$\underline{v}$	Velocity vector
$\underline{\gamma}$	Acceleration vector
$\underline{\underline{\sigma}}$	Cauchy stress tensor
$\underline{\underline{\varepsilon}}$	Strain tensor
$\underline{\underline{\varepsilon}}^e$	Elastic strain tensor
$\underline{\underline{\varepsilon}}^{in}$	Inelastic strain tensor
$\underline{\underline{\varepsilon}}^p$	Plastic strain tensor
$\underline{\underline{\varepsilon}}^{vp}$	Viscoplastic strain tensor
$\mathscr{C}$	Stiffness matrix
E	Young's modulus
ν	Poisson's ratio
λ	First Lamé's coefficient
μ	Second Lamé's coefficient (shear modulus)

Introduction

In air transport, improvement of passengers safety has always been a top priority and ratio between number of fatalities and number of passengers is one of the lowest in transport industries, as shown by Figure 1 for the United States. However, each accident draws public attention since in case of commercial airplanes, the number of casualties may be important, this enhances the ongoing research to be carried on. Among the tackled topics, crashworthiness deals with the behaviour of aircraft structures undergoing extreme loading conditions such as crash, impact or explosions.

An example of recent advances in this field is the successful ditching on the Hudson river. On January 15, 2009, an Airbus A320-214 of US Airways connecting New York and Charlotte cities (USA) underwent a complete loss of thrust in both engines, eight minutes after take-off. Yet, the aircaft was successfully ditched on the river without any casualties (Figure 2). This incident was due to engines encounter with a flock of birds, hence the large ingestion of foreign bodies. According to the National Transportation Safety Board (NTSB) report [1], several factors have contributed to this favourable outcome. In addition to the crew members decisions and actions, it was notably noticed that the airplane "was equipped for an extended overwater flight, [...] even though it was not required to be so equipped". By contrast, other accidents remind us the continuous necessity to enhance the ongoing research. On April 17, 2018, a Boeing 737-700 of Southwest Airlines was connecting New York and Dallas cities (USA) when one of the left engine fan blade made of lightweight alloy suddenly broke off, causing inlet fragments strike a window, which eventually led to a fatality among passengers. "The aerospace industry [...] has to be safe, of course, but it also has to be light, and those two things counteract each other", said a professor at an hearing following the engine failure[1]. After thorough investigations [2], the NTSB reported the presence of "fatigue fracture features" at the broken blade root, causing huge damages on the engine (Figure 3), whereas the blade should not have reached the inlet.

To better predict and understand these phenomena, one solution may be *in-situ* test experiments which are really expansive in such cases. By contrast, numerical simulations are getting a growing interest, but modelling/solving the problem is often challenging as shown in [3] to simulate ditching for example. Thus, the knowledge of materials behaviour - from early stages of the loading until fracture - is required. Indeed, aircraft structure materials mostly undergo dynamic loadings under a wide range of strain rates and temperatures.

Material dynamic behaviour characterization is often performed through standard tests. Their setup (possibly their processing) is often based on standards which have been initially defined for quasi-static tests. For instance, the standard ASTM E8-04 [4] reports a methodology for uniaxial tension testing of metallic materials. It relies on a statically determinate approach implying strong hypotheses on experimental test conditions. Thus, analysis assumes homogeneous small level of strain over the specimen gauge length. Then, considering that the longitudinal nominal stress is proportional to load measured from test machine load cell, materials parameters can be extracted from the uniaxial stress-strain curve. However, the extension of such standards to high strain-rate testing is not straightforward because of the difficulty to achieve homogeneous mechanical fields, in particular the strain-rate [5].

[1] http://www2.philly.com/philly/health/science/southwest-flight-1380-engine-blade-ntsb-20181120.html

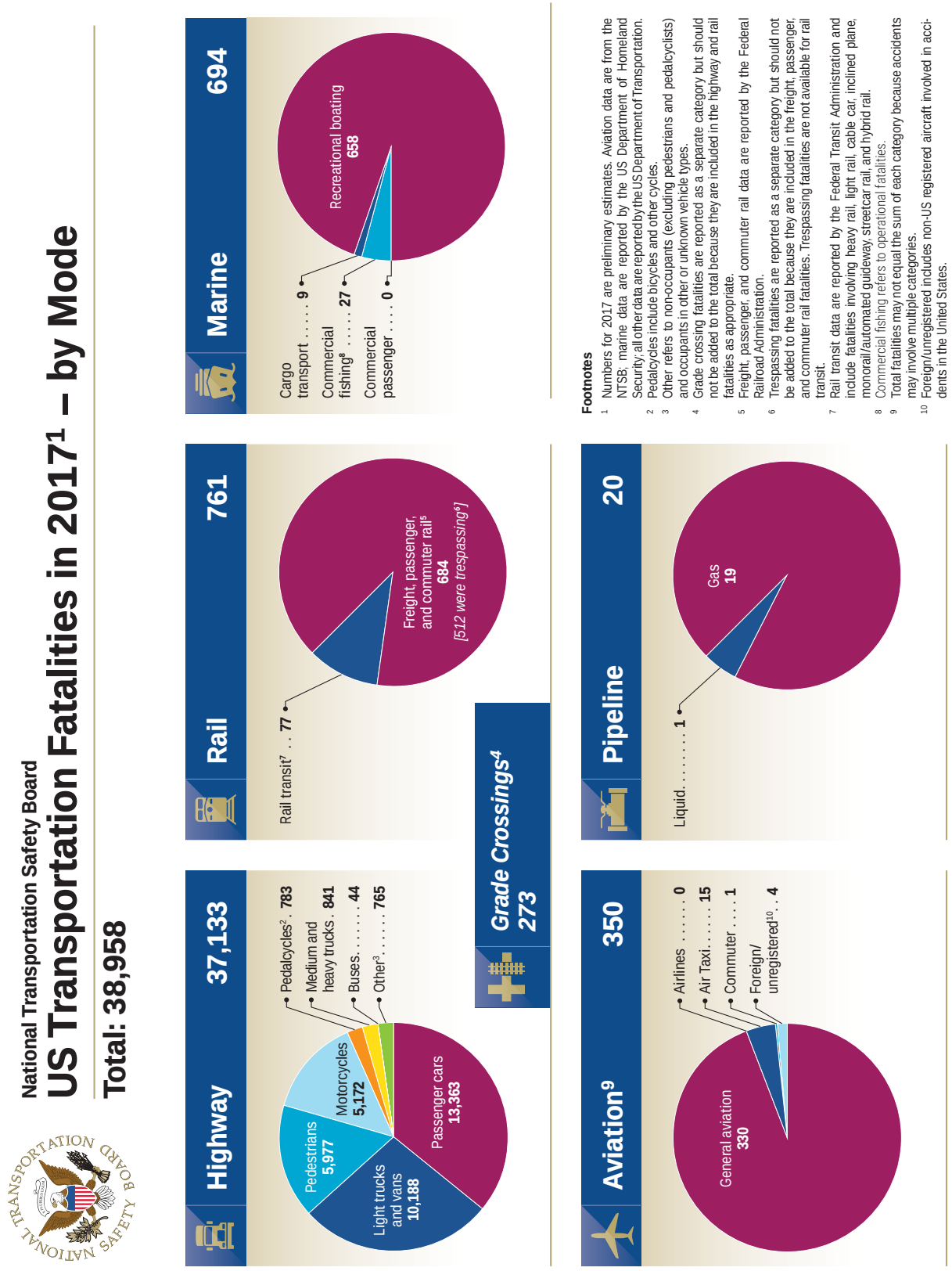

Figure 1: United States transportation fatalities in 2017 - Source: https://www.ntsb.gov

Figure 2: Picture after US Airways Flight 1549 ditching on Hudson river - Source: NTSB report [1]

Figure 3: Southwest Airlines Flight 1380 left engine CFM-56-7B after failure - Source: NTSB report [2]

For rate-dependent materials, the test campaign itself is more challenging because a high number of experiments is necessary with these approaches to characterize material behaviours over large spectra of strain and strain rate.

Owing to the dramatic improvements in imaging technology, it is now possible to measure kinematic fields at a large number of points over specimen surface (often referred to as "full-field measurements"). This is now also possible at high frame rates thanks to the growing technological developments in high speed cameras. Then, several inverse methods have been developed for identification of material parameters from full-field measurements. For dynamic testing and characterization of viscoplastic material behaviour, full-field measurement can be useful if strain rate is strongly heterogeneous. Among the available inverse methods, the Virtual Fields Method (VFM) was used to characterize viscoplastic Johnson-Cook (JC) model at intermediate high strain rates (up to about 500 s^{-1}) using a limited number of dynamic tests [6].

Image-Based Inertial Impact (IBII) tests have been recently proposed to take advantage of the VFM for material behaviour characterization at high strain rate [7] (up to about 1000 s^{-1}). It consists in a thin-plate specimen hit by a cylindrical projectile on its edge at several tens of meters per second, while

the opposite edge is free to move, this leading to a longitudinal wave propagation through the tested specimen. This methodology may be suitable to drastically reduce the test campaign. Indeed, heterogeneous strain and strain rate fields may be generated on a single specimen, hence a characterization over a wide range of strain and strain rate would be possible. Up to now, IBII tests have been used mostly to characterize elastic behaviour [7] or elastoplastic behaviour [8].

The available literature about VFM with inertia effects for viscoplasticity characterization [9, 10] extends a study based on a bending test [11]. However, the specimen underwent small deformations only (0.02 at best) because the test configuration was not especially designed to sweep a wide range of strain. Therefore, the material behaviour was characterized on a narrow viscoplastic spectra. To extend the IBII test methodology to rate-dependent material behaviour, one needs to understand the influence of several test parameters such as projectile velocity and geometry, or specimen geometry, or metrological features like camera specifications and full-field measurements regularization parameters. Indeed, these parameters all influence the resulting identification and it is essential to set them using a rational approach.

The following four chapters present the methodology followed in this work for this extension:

- Chapter 1 presents a brief overview about the existing literature for material mechanical behaviour modelling and testing, focused on behaviour characterization of isotropic metallic materials. First, some basic notions about material behaviour modelling are recalled. Then, standard techniques for material parameters extraction and suitable methodologies for processing are presented. Methodologies and tools for material parameters identification are then presented. The review focuses on the Virtual Fields Method (VFM) which will be extended in this manuscript to viscoplasticity characterization at high strain rate;

- Chapter 2 presents the numerical toolbox developed to design the test matrix based on IBII tests suitable for non-linear behaviour characterization with dynamic VFM, *i.e.*, the computation of stress fields from strain fields and a given set of material parameters, a methodology to extract strain and acceleration fields from full-field measurements, a FE-based toolchain to enable a thorough investigation of IBII test configurations numerically. This includes a synthetic images generator to deal with quantitative assessment in the VFM process;

- Chapter 3 is dedicated to the exploitation of the numerical toolbox to optimize IBII tests for Johnson-Cook model characterization with the VFM. Beforehand, FE-based design criteria are set to discriminate test configurations and select suitable tests for viscoplasticity characterization. Then, a parametric study is performed on both impact conditions and specimen shape, based on FE simulations and synthetic images generator. Finally, regularization parameters used to compute strains and accelerations from displacement fields are optimized through uncertainty quantification for the proposed test configurations;

- Chapter 4 presents the test campaign which have been carried out with the IBII methodology to characterize the strain-rate sensitivity of a titanium alloy (Ti6Al4V) used in aerospace industry. A series of IBII tests are performed at the University of Southampton (UK), considering different geometries defined with the numerical analysis. The dynamic VFM is used to identify the Johnson-Cook model viscoplastic parameter. Prior to the identification, metrological performance is also assessed. Finally, a critical comparison between numerical analysis and IBII tests results is performed. This includes the kinematic fields, the identified parameters, the reconstructed mechanical fields and the viscoplastic spectra.

Chapter 1

Material behaviour modelling and identification of constitutive parameters: An overview

Contents

Abstract

This chapter presents a brief overview about the existing literature for material mechanical behaviour modelling and testing, focused on behaviour characterization of isotropic metallic materials. First, some basic notions about material behaviour modelling are recalled. Then, standard techniques for material parameters extraction and suitable methodologies for processing are presented. Furthermore, measurement techniques such as the grid method and Digital Image Correlation (DIC) method are introduced. Methodologies for material parameters identification using such full-field measurement techniques are then presented. The review focuses on the Virtual Fields Method (VFM) which will be extended in this manuscript to viscoplasticity characterization at high strain rate. In particular, a comparative review of dynamic VFM applications is carried out (advantages, drawbacks and limitations).

1.1 Material behaviour modelling

The deformation of a material is characterized by its microstructure evolution. If initial configuration is recovered, the deformation is reversible and known as elastic (or viscoelastic for rate-dependent materials). Then, plasticity theory [12, 13] assumes an initial elasticity limit beyond which microstructure is permanently deformed. Then, the transformation is known as irreversible - *i.e.*, (visco)plastic - depending if the deformation is rate-dependent or not. Above a deformation threshold inherent to the material, germination, growth and coalescence of microcavites leads to discontinuities within microstructure (damage). Finally, the material fracture occurs beyond a critical threshold. The latter is qualified as brittle when no irreversible deformation has occurred previously, ductile otherwise.

N.B: This section is dedicated to metallic materials with an incompressible isotropic mechanical behaviour. The framework of small deformations is also considered.

Constitutive models have been developed to describe the mechanical behaviour of materials. Then, a strain tensor denoted $\underline{\underline{\varepsilon}}$, is defined from displacement field, $\underline{u}$ according to Equation 1.1.

$$\underline{\underline{\varepsilon}} = \frac{1}{2}\left[\nabla \underline{u} + (\nabla \underline{u})^T\right] \tag{1.1}$$

Hypothesis of additive decomposition considers $\underline{\underline{\varepsilon}}$ as the sum of an elastic strain, $\underline{\underline{\varepsilon}}^e$, and an inelastic one, $\underline{\underline{\varepsilon}}^{in}$, so that $\underline{\underline{\varepsilon}} = \underline{\underline{\varepsilon}}^e + \underline{\underline{\varepsilon}}^{in}$, where $\underline{\underline{\varepsilon}}^{in} = \underline{\underline{\varepsilon}}^p$ for plastic behaviour and $\underline{\underline{\varepsilon}}^{in} = \underline{\underline{\varepsilon}}^{vp}$ for viscoplastic behaviour. Moreover, Cauchy stress tensor $\underline{\underline{\sigma}}$ is also considered. The latter is linked to $\underline{\underline{\varepsilon}}$ by constitutive equations which describe the material behaviour.

Assuming linear elastic material behaviour under isotherm conditions, $\underline{\underline{\sigma}}$ is related to $\underline{\underline{\varepsilon}}$ by the so called Hooke's law such as $\underline{\underline{\sigma}} = \mathscr{C} : \underline{\underline{\varepsilon}}^e$ where $\mathscr{C}$ is the stiffness tensor. For isotropic behaviour, the contracted product can be developed to get a more suitable formula (Equation 1.2).

$$\underline{\underline{\sigma}} = 2\mu(\underline{\underline{\varepsilon}}^e) + \lambda \mathrm{Tr}(\underline{\underline{\varepsilon}}^e)\underline{\underline{I}} \tag{1.2}$$

As soon as yield stress is reached, this sole equation is not able to model the mechanical behaviour anymore. Plastic or viscoplastic models - possibly non-linear - are then set up to describe material hardening. The related constitutive relations are mainly based on thermodynamics equations [14] *i.e.*, internal and observable state variables are considered. For example, total strain is an observable variable. When plasticity is described, elastic and plastic strain are considered as internal variables, as well as other variables denoted V_k, like kinematic hardening variables for instance. Each internal variable, V_k, is related to an associate one, A_k. The existence of a dissipation potential $F(A_k)$ is then assumed. The latter governs the evolution of internal variables according to the state equations and normality assumption (Equation 1.3).

$$\dot{V}_k = -\dot{\gamma}\frac{\partial F}{\partial A_k}, \quad \gamma \in \mathbb{R} \tag{1.3}$$

For associated plasticity, F can be chosen as the yield surface, denoted f. Within stress space, f delimits the domain in which any stress variation leads to elastic strains only. This threshold is reached when an equivalent stress denoted σ_{eq}, equals the flow stress, σ_y whose evolution is defined according to the modeled behaviour. Within J_2-plasticity framework - which is often suitable for metallic materials - it comes $f = \sigma_{eq} - \sigma_y$, where σ_{eq} is the von-Mises equivalent stress. Then yield

surface equation can be detailed (Equation 1.4). While a $\underline{\underline{\beta}}$-variation leads to yield surface translation (*i.e.*, kinematic hardening), shape morphing (*i.e.*, isotropic hardening) - is driven by r (Figure 1.1).

$$f = \sigma_{eq} - \sigma_y(r), \text{ where } \left| \begin{array}{ll} \sigma_{eq} = \sqrt{\frac{3}{2}\left(\underline{\underline{S}} - \underline{\underline{\beta}}\right) : \left(\underline{\underline{S}} - \underline{\underline{\beta}}\right)} & \text{the equivalent stress} \\ \underline{\underline{S}} = \underline{\underline{\sigma}} - \frac{1}{3}\mathrm{Tr}(\underline{\underline{\sigma}}) & \text{the stress deviator} \\ \underline{\underline{\beta}},\ r & \text{the hardening variables} \end{array} \right. \tag{1.4}$$

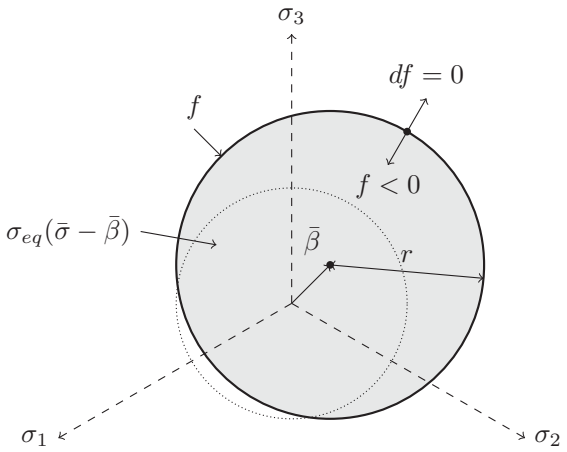

Figure 1.1: Yield surface representation within principal stress space - dotted line: initial yield surface - thick line: updated yield surface

For rate-independent plasticity, admissible stress states must be located within the yield surface *i.e.*, $f \leq 0$, knowing that $f = 0$ means a plastic flow. Another condition is that $\dot{f} = 0$ during the whole loading process. Thus, an increase of stress level implies a simultaneous increase of the flow stress (Figure 1.1). Furthermore, $f = 0$ or $\dot{f} < 0$ corresponds to elastic unloading states while plastic variables remain constant. The condition $\dot{f} = 0$ can be developed to become the consistency condition, such as:

$$df = \frac{\partial f}{\partial\left(\underline{\underline{\sigma}} - \underline{\underline{\beta}}\right)} : d\left(\underline{\underline{\sigma}} - \underline{\underline{\beta}}\right) + \frac{\partial f}{\partial r} : dr = 0 \tag{1.5}$$

Equation 1.5 is used to calculate plastic multiplier, γ, using the state equations (Equation 1.6) applied to associated plasticity. Then it comes:

$$\left| \begin{array}{l} \frac{\partial \underline{\underline{\varepsilon}}^{in}}{\partial t} = \dot{\gamma}\frac{\partial f}{\partial \underline{\underline{\sigma}}} \\ \frac{\partial r}{\partial t} = -\dot{\gamma}\frac{\partial f}{\partial \sigma_y} \end{array} \right. \tag{1.6}$$

Within J_2-viscoplasticity framework and in absence of kinematic hardening ($\underline{\underline{\beta}} = \underline{\underline{0}}$), Equation 1.6 can

be simplified. Indeed:

$$\begin{aligned}\frac{\partial \underline{\underline{\varepsilon}}^{in}}{\partial t} &\underset{(1.6)}{=} \dot{\gamma}\frac{\partial f}{\partial \underline{\underline{\sigma}}} = \sqrt{\frac{3}{2}}\dot{\gamma}\frac{\partial}{\partial \underline{\underline{\sigma}}}\left[\sqrt{\underline{\underline{S}} : \underline{\underline{S}}}\right] = \sqrt{\frac{3}{2}}\dot{\gamma}\frac{\frac{\partial}{\partial \underline{\underline{\sigma}}}\left[\underline{\underline{S}} : \underline{\underline{S}}\right]}{2\sqrt{\underline{\underline{S}} : \underline{\underline{S}}}} \\ &= \sqrt{\frac{3}{2}}\dot{\gamma}\frac{2\underline{\underline{S}}}{2\sqrt{\underline{\underline{S}} : \underline{\underline{S}}}} = \frac{3}{2}\dot{\gamma}\frac{\underline{\underline{S}}}{\sqrt{\frac{3}{2}\underline{\underline{S}} : \underline{\underline{S}}}} \\ &= \frac{3}{2}\dot{\gamma}\frac{\underline{\underline{S}}}{\sigma_{eq}(\underline{\underline{\sigma}})}\end{aligned} \tag{1.7}$$

The set of conditions for admissible stress states within rate-independent plasticity framework are known as Kuhn-Tucker conditions (Equation 1.8).

$$\left|\begin{array}{l}\dot{\gamma} \geq 0 \\ f \leq 0 \\ \dot{\gamma} f = 0\end{array}\right. \tag{1.8}$$

Finally, cumulated plastic strain p is defined by Equation 1.9. For a virgin (*i.e.*, not damaged) material, p is equal to isotropic hardening variable r and is therefore linked to γ as defined by Equation 1.6.

$$p = \int_0^t \sqrt{\frac{2}{3}\dot{\underline{\underline{\varepsilon}}}^{in} : \dot{\underline{\underline{\varepsilon}}}^{in}}\, dt \tag{1.9}$$

Within J_2-viscoplasticity framework and in absence of kinematic hardening, $\dot{p}$ is directly linked to $\dot{\gamma}$. Indeed:

$$\dot{p} = \sqrt{\frac{2}{3}\dot{\underline{\underline{\varepsilon}}}^{in} : \dot{\underline{\underline{\varepsilon}}}^{in}} \underset{(1.7)}{=} \sqrt{\frac{3}{2}}\dot{\gamma}\frac{\sqrt{\underline{\underline{S}} : \underline{\underline{S}}}}{\sigma_{eq}(\underline{\underline{\sigma}})} = \dot{\gamma} \tag{1.10}$$

Selection of suitable constitutive laws to describe material behaviour strongly depends on material itself and loading conditions. To describe isotropic hardening for rate-independent behaviour, several models has been proposed in the literature. Generally speaking, they are such as $\sigma_y(p) = \sigma_0 + R(p)$, with σ_0 the initial yield stress and R the hardening stress. For instance, the Prandtl-Reuss model [14] assumes a power hardening law $R(p) = Kp^n$, where K and n are material parameters (known as isotropic hardening modulus and exponent respectively). Voce model [15] combines a linear hardening and an exponential correction such as $R(p) = Kp + \sigma_\infty[1 - e^{-bp}]$, where K, σ_∞ and b are material parameters. Armstrong-Frederick model [16] is an example of a model for kinematic hardening, where $\frac{d}{dt}\left[\frac{\underline{\underline{\beta}}}{C}\right] = \frac{2}{3}\dot{\underline{\underline{\varepsilon}}}^{in} - \frac{2}{3}\frac{B}{C}\|\dot{\underline{\underline{\varepsilon}}}^{in}\|\underline{\underline{\beta}}$ (B and C are material parameters). Linear Prager model [14] for kinematic hardening is often encountered such as $\frac{\partial \underline{\underline{\beta}}}{\partial t} = \frac{2}{3}H\frac{\partial \underline{\underline{\varepsilon}}^{in}}{\partial t}$, where H denotes the kinematic hardening modulus.

Within viscoplasticity framework, the same variables can be naturally defined substituting a viscoplastic strain tensor, denoted $\underline{\underline{\varepsilon}}^{vp}$, to the plastic strain tensor $\underline{\underline{\varepsilon}}^{p}$. Yet, consistency conditions (Equation 1.5) are not mandatory anymore since $\dot{f}$ might be nonzero. Generally speaking, the whole set of Kuhn-Tucker conditions (Equation 1.8) might be unverified, depending on how viscous effects are modelled.

A first approach consists in describing the development of viscous flow stress and the evolution of plastic flow separately, as it is done for the Norton's model [14, 17]. Another approach consists in incorporating viscous effects in the expression of σ_y (with modelling of viscous overstress effects). Kuhn-Tucker conditions (Equation 1.8) may then be valid so that $f = \sigma_y - \sigma_{eq} \leq 0$. Some available

models are based on this methodology [18]. An example is the Johnson-Cook (JC) model [19] which integrates both viscoplasticity and thermal effects (Equation 1.11). In the flow rule, the contribution of each term is activated from a threshold value. Thus, thermal softening is activated when the temperature T reaches T_0 which is a material parameter. Parameters m and T_f (melting temperature under SCTP) then drive the thermal softening. Likewise, viscous effects are activated when cumulated plastic strain-rate (denoted $\dot{p}$) is higher than a threshold, $\dot{\varepsilon}_{eq,0}$, while Johnson-Cook viscoplastic parameter M drives the evolution of the stress correction caused by viscous hardening. Furthermore, it can be noted that below the viscoplastic threshold and in absence of thermal effects, JC model is equivalent to the Prandtl-Reuss hardening model, with σ_0 the initial yield stress, K and n the isotropic linear hardening modulus and exponent respectively.

$$\sigma_y = \left[\sigma_0 + Kp^n\right]\left[1 + M\ln\left(\frac{\dot{p}}{\dot{\varepsilon}_{eq,0}}\right)\right]\left[1 - \left(\frac{T - T_0}{T_f - T_0}\right)^m\right] \tag{1.11}$$

In practice, JC model has been widely used to describe the dynamic behaviour of isotropic metallic materials using statically determinate tests [20–25] and statically undeterminate tests [6] (see next sections for meaning of statically (un)determinate tests). Thanks to its limited number of material parameters, the latter is easily implemented in transient dynamics solvers, thus making it one of the most used models, with other ones like Cowper-Symonds [26] or Jones [27] models. By contrast, ones like Zerilli-Amstrong [28] and Rusinek-Klepazcko [29] models are also popular owing to their strong physical theoretical background (dislocation mechanics and thermodynamics), whereas JC model is semi-empirical. For an accurate description, the reader is referred to the aforementioned references, but their application is equivalent to the JC model within J_2-plasticity framework (*i.e.*, von-Mises-driven hardening).

In conclusion, material behaviour constitutive laws have to take into account the different steps of the microstructure evolution *i.e.*, elastic and (visco)plastic strain with(out) damage until fracture. This section has presented some examples and related models but the list is far from being exhaustive. Yet, it is very important to chose the constitutive laws in accordance to the physical phenomena to be described, the loading conditions. Thereafter, the set of material parameters of selected constitutive laws has to be extracted using experimental tests. Most of them are strongly standardized to enable statically determinate processes. However, the use of statically undeterminate tests may have important advantages. The following sections highlight their main features.

1.2 Identification with statically determined tests

During a mechanical test, some of physical variables can be quantified directly *e.g.*, loads (using dynamometers or load cells), displacements (extensometers), strains (strain gauges), temperatures (thermocouple probes) and time. In this case, single-channel sensors are often used. Then, one could only monitored 1D and non-local quantities, as mean strain over the gauge length versus time for instance. So those measurements are restricted and are not sufficient for behaviour characterization, unless strong assumptions are stated. The most important is to assume that mechanical fields are homogeneous over the gauge length: this is known as the staticity assumptions. The related approach is called statically determinate because stress fields are assumed to be known *a priori* since their evolution could be analytically computed from the loading path which is experimentally measured [5].

Theoretically speaking, any experimental test might be processed based on this approach. Nevertheless, these assumptions may be difficult to be respected in practice, notably when material behaviour is characterized under extreme conditions (*e.g.*, dynamic loading, very high/low ambient temperature). For instance, generation of homogeneous fields over gauge length is often challenging. Consequently, one has to think wisely about tested configurations features (*e.g.*, loading path, specimen geometry)

and constitutive equations validity domain. Based on these ideas, standard procedures have been established to "ensure" the respect of staticity hypotheses. In particular, those standards[1] set specimen geometry, sensors setup and boundary conditions. Furthermore, one of the most critical constraints for high strain-rate testing is the strain-rate which has to remain constant along the gauge length. Then, the material behaviour is characterized for a given strain-rate.

Tensile tests are often used for material behaviour characterization. When staticity hypotheses are assumed, material parameters can be extracted using gauge length elongation, here denoted ΔL, and load, denoted F. Nominal strain ε_n is defined as gauge length relative elongation, *i.e.*, $\varepsilon_{n(t)} = \frac{\Delta L(t)}{L_0}$, where t is the time and L_0 the initial gauge length. Nominal stress, σ_n, is the ratio between the load F and the initial cross-section S_0. However, staticity hypothesis become meaningless when material undergo physical localisation. For tensile tests, assumptions are then valid until necking. In practice, transition is set when $\frac{d\sigma_n}{d\varepsilon_n} = 0$ (Figure 1.2).

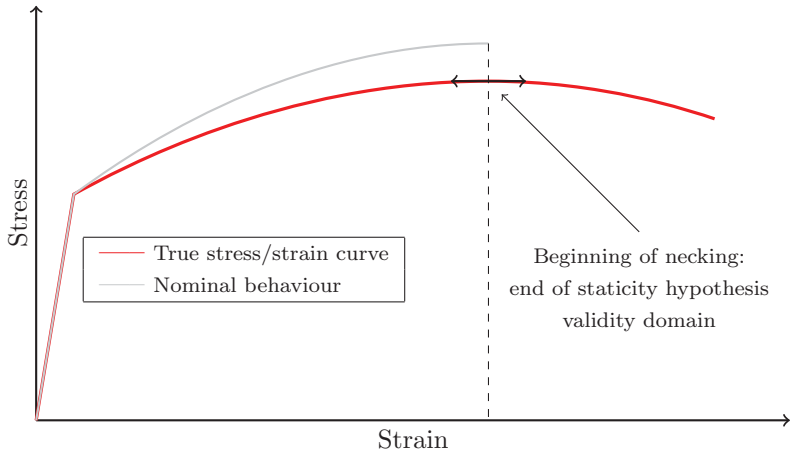

Figure 1.2: Nominal/True tensile behaviour

Nonetheless, the nominal behaviour does not match with material "true" behaviour. In fact, true strain ε, is defined as accumulation of relative elongation (Equation 1.12). In the case of metallic materials assumed in N.B. p. 19, true stress σ may be calculated using Equation 1.13.

$$\varepsilon_{\,t_1 \to t_2} = \int_{L(t_1)}^{L(t_2)} \frac{dL}{L} = \ln\left[\frac{L(t_2)}{L(t_1)}\right] = \ln(1 + \varepsilon_{n\,t_1 \to t_2}) \tag{1.12}$$

$$\sigma(t) = \frac{F(t)}{S(t)} = \frac{F(t)}{S_0}\,(1 + \varepsilon_{n\,0 \to t}) \tag{1.13}$$

Figure 1.2 shows a schematic true stress/strain curve for an elastoplastic isotropic material. Assuming unidimensional stress state, the Young's modulus, E, and initial yield stress, σ_0, are calculated using curve linear part and Hooke's law $\sigma = E\varepsilon$. Plastic strain is then deduced thanks to additive decomposition assumption, such as $\varepsilon^p = \varepsilon - \frac{\sigma}{E}$. Hardening modulus and exponent (K and n respectively) can be determined using a logarithmic diagram as in Figure 1.3(a). When the material behaviour is rate-dependent, several tests needs to be performed at different strain-rate $\dot{\varepsilon}$ [5]. For each test, strain rate must be homogeneous over the ROI, this being more are more challenging as $\dot{\varepsilon}$ is increasing [18]. True stress/strain curves are then analysed for each test. For instance, viscoplastic parameters M et $\dot{\varepsilon}_0$ of Equation 1.11 can then be extracted as shown in Figure 1.3(b). Previously, static part may have been identified using the method illustrated in Figure 1.3(a).

[1]The main standards are AFNOR NF EN 10002-1 to 10002-5 (France), ASTM E8M-96 (US) or ISO 6892 (International). They are detailed depending on the tested material and the test conditions. For instance, standard ISO 6892-1 set a test at "ambient temperature", standard ISO 6982-2 à at "high temperature" for metallic materials.

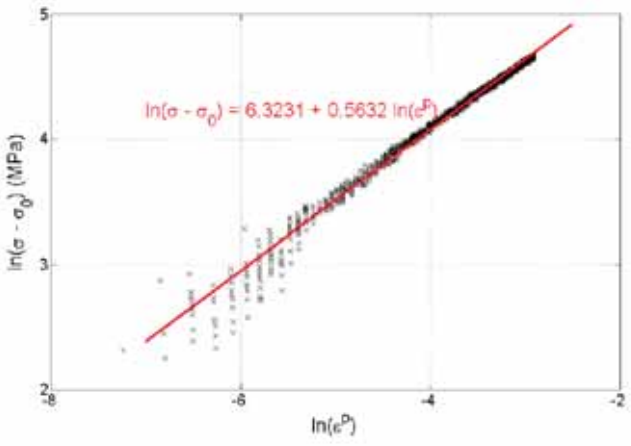

(a)

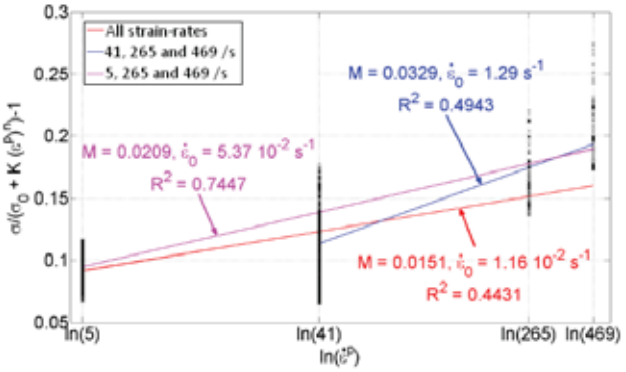

(b)

Figure 1.3: Determination of JC model parameters for a titanium alloy [6]: (a) - static parameters (b) - dynamic parameters

Generally speaking, material parameters can also be extracted by minimizing a global cost function φ, which may be defined as a sum of normalized square errors between the stress curve calculated with the model σ^{MOD} and experimental true stress curve σ^{EXP} (Equation 1.14), where $\underline{X}$ denotes the set of material parameters - *e.g.*, $\underline{X} = [\sigma_0, K, n, M, \dot{\varepsilon}_0]$ for JC model - and N the number of sampling points. For non-linear behaviour, one way to calculate the stress might be based on algorithms used to perform the numerical time-integration of constitutive equations [13, 30].

$$\varphi(\underline{X}) = \sum_{i}^{N} \left[\frac{\sigma^{EXP}(i) - \sigma^{MOD}(i)(\underline{X})}{\sigma^{EXP}(i)} \right]^2 \tag{1.14}$$

Nelder-Mead heuristic algorithm [31] is often suitable to minimize function φ insofar as direction of research computation does not require cost-function derivatives w.r.t material parameters. Despite the drawbacks (unconstrained research, less robust for ill-conditioned functions), the main advantage is the limited number of iterations compared to genetic algorithms [32–34] which are more robust (ensured convergence towards global minima) but less cost efficient and less accurate for multidimensional problems.

In conclusion, extracting material parameters with standard techniques "only" requires to measure load and displacement (or strain). Nonetheless, the use of related procedures is challenging because of the strong assumptions. As mechanical test settings are then constrained, several tests are generally needed for identification of complex behaviour as shown here for the case of viscoplasticity but also to identify damage models as done by Bennani *et al.* [35] for instance. The number of required tests

increases both with constitutive equations complexity and problem dimension. Moreover, the identified model is only valid within the domain framed by the staticity assumptions, *i.e.*, a large portion of experimental curves cannot be exploited.

In a nutshell, the collected data potential is clearly underexploited when using those approaches. Improvement could come from the use of heterogeneous fields, *i.e.*, statically undeterminate approaches. Indeed, thanks to the continuous improvement of sensors, full-field measurement techniques are more and more suitable for kinematic fields extraction in material testing. Consequently, one may take advantage of the considerably enriched experimental data at best. For instance, wider spectra of strain and specially strain-rate might be encountered while processing a single specimen. Thus, this may strongly reduce the number of tests needed for material characterization.

The next section presents some of such measurement techniques and recent advances in their practice in material characterisation. Methods suitable to their process - *i.e.*, statically undeterminate - will also be presented.

1.3 Full field measurements techniques

Recent advances in optical sensors (*e.g.*, CCD cameras) and continuous improvements in image processing makes full-field measurement techniques more and more suitable for quantitative analysis in experimental mechanics. Thanks to them, fields of different nature can be measured such as displacements or temperatures, and all the related quantities which may be deduced (*e.g.*, strains or accelerations). To measure temperature for instance, infrared cameras may be used for various issues. Thus, Jones *et al.* [36] perform a non-destructive control of damage within a composite. More recently, infrared thermography was also used for crack density analysis within the matrix of a composite [37] or dissipative phenomena monitoring on a composite joint [38] at intermediate strain-rate. Strain fields can be extracted using shearography [39,40], shear speckle photography [41], Moiré fringe displacement [42], or the grid method [43,44]. Nevertheless, strain fields are often calculated from the numerical differentiation of displacements, which are the most frequently measured mechanical fields. The following part describes suitable techniques for this.

1.3.1 Displacement fields measurement techniques

1.3.1.1 Interferometric methods

Interferometric methods consists in comparing two monochromatic beams coming from the same source, but with different optical paths. While the first one encounters no obstacles (reference) the second one lights the tracked specimen surface, so that the displacement fields can be linked to the differences between optical paths. As the variation could be very small (*e.g.*, a few nanometres), interferometric methods are suitable to extract very small displacements. Nonetheless, they are very sensitive to external perturbations, as vibrations for instance. Among them, Moiré and speckle interferometry are the most frequently used by the community.

For the first technique, a reference grid pattern is compared to a current configuration, *i.e.*, deformed during the mechanical test [45,46]. The grid pitch could be very small (1000+ lines/mm [47]). Moiré fringes are then obtained overlapping the two grid patterns, hence the displacements on the surface can be known [46]. The same method can also be used to calculate out of plane displacements [48]. In that case, the grid is bounded perpendicularly to the specimen surface. However, Moiré interferometry can be difficult to use in practice. Indeed, the results are very sensible to optical noises. In addition to be strongly sensitive to external perturbations, Moiré fringes highly depends on the material surface, so that specimen surface needs to be polished. Speckle interferometry [49] might be less delicate to use insofar no grid has to be transferred onto the specimen, so no polishing is required. However, the material has to disperse light. Indeed, the combination of light beams - resulting

from the reflection of coherent source on specimen surface - with a laser beam gives a description of the surface (speckle pattern) owing to phase shifting. Then, displacements can be extracted correlating the speckle pattern before and during loading.

To conclude, interferometric techniques may be very efficient. However, their use in practice may be challenging for testing under extreme conditions (*e.g.*, dynamic loading). Thus, white-light-based techniques whose setting is easier have been developed. The next section describes two of them.

1.3.1.2 White light methods

➥ *The Digital Image Correlation method*

The Digital Image Correlation method consists in tracking motions and deformations of a random speckle pattern [50–54]. In practice, the latter may be obtained spraying black drops onto a white-painted specimen (Figure 1.4). Recorded images are then analysed numerically as grey level maps. Another solution is also to use material microstructure itself as a speckle, if grey level gradients are strong enough for the post-processing [55]. Finally, the set of images is analysed with a correlation algorithm.

Figure 1.4: Example of a speckle pattern

Displacements are extracted finding the best matching patterns for a given set of subsets between an image witnessing a specimen deformed state and an image witnessing the reference state. Mathematically, one shows that it is equivalent to minimize a cost function using cross-correlation coefficients and interpolation. The available criteria are mostly based on SSD (Sum of Square Differences). Table 1.1 collects some examples for a given subset S, where F and G denote grey level function of reference and deformed image respectively, $\bar{F}$ and $\bar{G}$ average values over S and i is pixel summation index within a subset. In practice, choice of criterion is a trade off between computational efficiency and algorithm robustness w.r.t. testing conditions (*e.g.*, lighting or speckle pattern contrast). SSD criterion is known to be fast but does not compensate illumination variations between two images. Normalized Sum of Square Differences (NSSD) and Zero Normalized Sum of Square Differences (ZNSSD) are able to do so, but are much more slower. One way to deduce displacement fields is to view the problem at a local scale, so that within the criterion collection, each subset (*i.e.*, measurement point) is considered independently [56,57]. Otherwise, global techniques - a.k.a Integrated Digital Image Correlation (IDIC) - have also been proposed recently. Therefore, the same problem is considered globally in a variational formulation as FEA [58–62].

➥ *The grid method*

The grid method [63–65] is a full-field measurement method suitable for extracting 1D or 2D kinematic fields. As a white light technique, it is based on intensity analysis of a grid bonded onto the tested specimen. Grid pitch - which could be 1 to 1000+ lines per millimetre - is chosen in accordance with optical setup features. The grid can be engraved, printed or glued (Figure 1.5) on the surface [66–68]. The procedure to extract displacements from grid images is described and analysed by Grédiac *et al.* [65].

Table 1.1: SSD-based DIC criteria

Name	Cost function
SSD	$\sum_{i\in S}\Big\{F_i - G_i\Big\}^2$
NSSD	$\sum_{i\in S}\left\{\frac{F_i}{\sqrt{\sum_{j\in S}F_j^2}} - \frac{G_i}{\sqrt{\sum_{j\in S}G_j^2}}\right\}^2$
ZNSSD	$\sum_{i\in S}\left\{\frac{\bar{F}_i}{\sqrt{\sum_{j\in S}\bar{F}_j^2}} - \frac{\bar{G}_i}{\sqrt{\sum_{j\in S}\bar{G}_j^2}}\right\}^2$

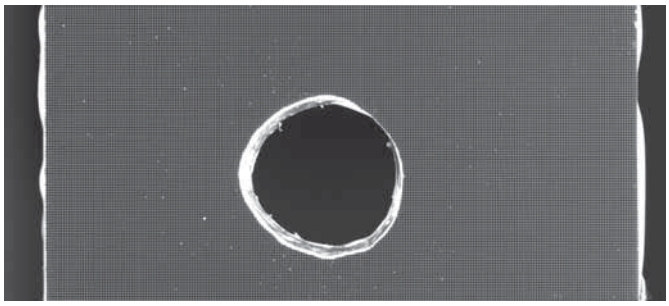

Figure 1.5: Example of a glued grid pattern - Source: http://www.thegridmethod.net

A quasi-periodic function (Equation 1.15) is assumed to describe the fringes pattern, where A and γ governs grid contrast, "frng" is a periodic function, ω is the grid pulsation and $\underline{\phi}$ the vector carrying grid modulations. Within an Eulerian framework, as grid movements are responsible for variations of phase modulations, one can demonstrate that displacement and phase fields are related according to an implicit relation (Equation 1.16), where exponents ^{REF} and ^{DEF} denote reference and deformed state, respectively. For small perturbations, Equation 1.16 may be linearised. Therefore, it comes $\underline{u}(\underline{x}) = -\frac{1}{\omega}[\underline{\phi}^{DEF}(\underline{x}) - \underline{\phi}^{REF}(\underline{x})]$. In case of large displacements (*e.g.*, when large rigid body motions occurs), displacements can be calculated with an iterative approach [65].

$$I(x,y) \;=\; A\Big\{1 \;+\; \gamma\Big[\mathrm{frng}\Big(\omega x \;+\; \phi_x(x,y)\Big) + \mathrm{frng}\Big(\omega y \;+\; \phi_y(x,y)\Big)\Big]\Big\} \tag{1.15}$$

$$\underline{u}(\underline{x}) \;=\; -\frac{1}{\omega}\Big\{\underline{\phi}^{DEF}\big[\underline{x} + \underline{u}(\underline{x})\big] - \underline{\phi}^{REF}\big[\underline{x}\big]\Big\} \tag{1.16}$$

Furthermore, phase modulations can be retrieved through a Local Spectrum Analysis (LSA) [65, 69]. Assuming that phase (the grid deformations carrier) information is concentrated within spikes in the Fourier spectrum of the monitored grid, LSA consists in convolving the grid signal s with a local analysis window g (Equation 1.17) to extract this information. Thus, it comes $\underline{\phi} = \mathrm{Arg}[\underline{\hat{s}}] + 2n\pi,\ n \in \mathbb{Z}$. In practice, this is often done using Windowed Discrete Fourier Transform (WDFT) [65]. However, phase maps are at this moment defined modulo 2π. As phase extraction is performed locally in space (analysis window) and in time (deformed images are processed separately), phase jumps often occur. Then, phase maps needs to be unwrapped both spatially and temporally. To do so, bidimen-

sionnal [70] or tridimensional [71] unwrapping algorithms are used to cancel phase jumps.

$$\begin{array}{l|rcl} \text{along } x & \hat{s}_x(x,y,\omega) & = & \displaystyle\int_{\mathbb{R}^2} s(u,v)g(x-u,y-v)\exp[-\omega x]dudv \\ \text{along } y & \hat{s}_y(x,y,\omega) & = & \displaystyle\int_{\mathbb{R}^2} s(u,v)g(x-u,y-v)\exp[-\omega y]dudv \end{array} \tag{1.17}$$

In practice, the grid method is less simple to use than the DIC method because of several constraints (*e.g.*, regular pattern, grid transfer) [72]. However, its metrological performance (*i.e.*, measurement resolutions) makes it very interesting for applications in critical conditions (*e.g.*, high speed tests). Indeed, it has been recently addressed as better than the DIC if a compromise between spatial resolution (number of measurement points) and displacement resolution (smallest trackable displacement) is looked for [69].

To conclude, full-field measurement techniques are suitable to track displacement fields. Indeed, previous examples have showed they can enable their extraction under various conditions. However, the result will strongly depend on the available equipment to image mechanical tests, notably under dynamic loading conditions owing to high rate cameras drawbacks (*e.g.*, low spatial resolution). Yet, optical devices are continuously being improved. The next section presents recent advances in High-Speed imaging with a focus on Ultra-High-Speed cameras.

1.3.2 Ultra-High-Speed imaging

High Speed imaging is getting more and more attention in experimental mechanics, notably since the spectacular development of Charged Couple Devices (CCD) and Complementary Metal Oxide Semiconductor (CMOS) sensors and their integration in commercial cameras. Actually, High-speed (HS) imaging - framerate > 10^5 fps, see Figure 1.6 - are used since several decades. However, image storage is often performed outside the chip during imaging, so that data offload rate is the limiting factor to increase frame rate. By contrast, Ultra-High-Speed (UHS) imaging has recently enabled to increase the frame rate thanks to new technical improvements, therefore allowing their use for high speed tests monitoring. Those solutions are presented hereafter.

➥ *Rotating mirrors cameras*

In this case, several sensors are embedded in the camera (Figure 1.7). During the recording process, light is split towards multiple sensors owing to a rotating mirror (Figure 1.7(c)). This increases drastically the frame rate while keeping a satisfying spatial resolution. Finally, frame rate is only limited by the rotating mirror system. However, several drawbacks arise such as sensors synchronization, lenses distortion, optical path variations and low light exposure.

➥ *Beam splitting cameras*

Beam splitting cameras are based on a very closed principle but light intensifiers (Figure 1.8) are incorporated to increase light exposure, this leading to higher temporal resolution but increasing optical path complexity.

➥ *On chip storage cameras*

Another way to increase temporal resolution is to use on-chip-storage cameras (Figure 1.9(a)). As encoded images are stored within the imaging system, readout rate does not limit temporal resolution. However, active part (photodiode) of the sensor is reduced because of memory chip (Figure 1.9(b)). As a consequence, spatial resolution and maximum number of recorded images are limited by the chips size and storage capacity respectively. The Shimadzu HPV-X camera is based on this technology (Figure 1.6).

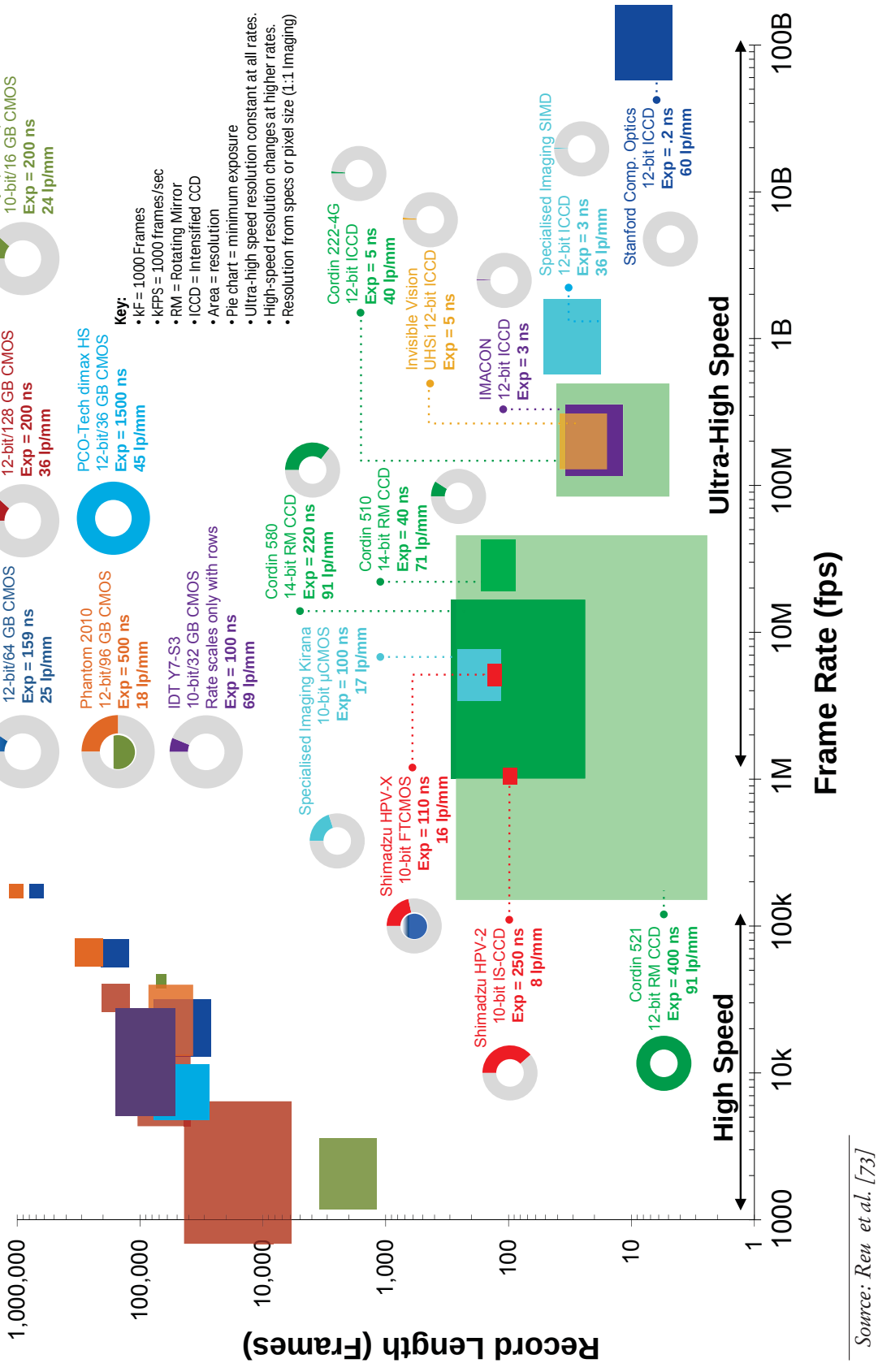

Source: Reu et al. [73]

Figure 1.6: Chart of available (U)HS cameras on the market

(a) (b)

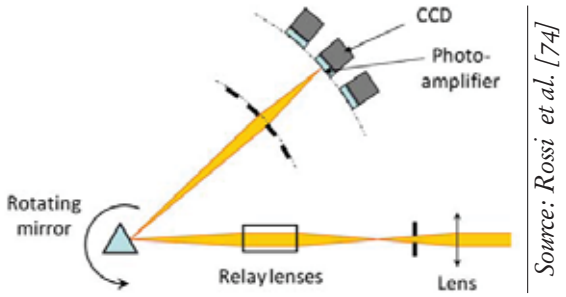

(c)

Figure 1.7: Cordin 550 available at ONERA: (a) - Overview (b) - Inside view - (c) Schematic representation

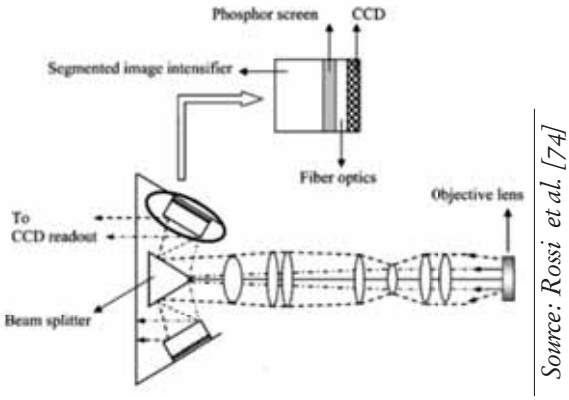

Figure 1.8: Beam splitting technology

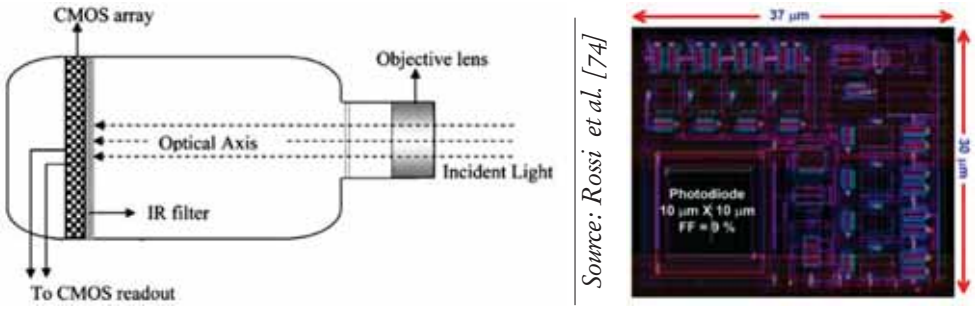

(a) (b)

Figure 1.9: On chip storage CMOS technology: (a) - General principle (b) - CMOS sensor

1.4 Identification with statically undetermined approaches

Section 1.2 has shown that statically determinate tests could be performed to extract constitutive parameters. However, tests remain underexploited with these approaches, so that for dynamic behaviour characterization for instance, large test campaigns are necessary. By contrast, statically undeterminate approaches deal with heterogeneous fields. In particular, material parameters may then be identified on a wider range of strain and strain rates from a single test, as long as suitable metrological toolchain is available (*e.g.*, UHS camera + full field measurement technique in case of dynamic tests).

The following section briefly presents five techniques to process non standard tests based on literature reviews [54,75], namely the Constitutive Equation Gap Method (CEGM), the Reciprocity Gap Method (RGM), the Equilibrium Gap Method (EGM), Finite Element Model Updating (FEMU) approaches and the Virtual Fields Method (VFM). Afterwards, a deeper review of the VFM is presented.

1.4.1 Overview

1.4.1.1 Constitutive Equation Gap Method (CEGM)

CEGM have been initially introduced to validate FEA simulations [76]. Within small perturbation framework and for elastic behaviour, the set of unknown parameters is extracted minimizing Equation 1.18, where $\underline{v}$ the displacement field, $\underline{\underline{\varepsilon}}$ the strain tensor, $\underline{\underline{\tau}}$ a physically admissible stress tensor and $\mathscr{C}$ the stiffness matrix. Cost function $\mathscr{C}$-norm is derivated from FEA modal analysis (Rayleigh's quotients) where modes normalization is performed through weighted cross product, using stiffness or mass matrix [77]. Thus, as ($\underline{v}$, $\underline{\underline{\tau}}$) minimizes PVW in FEA, the solution minimizes Equation 1.18 in CEGM.

$$E(\underline{v}, \underline{\underline{\tau}}, \mathscr{C}) = \|\underline{\underline{\tau}} - \mathscr{C} : \underline{\underline{\varepsilon}}(\underline{v})\|_{\mathscr{C}} \tag{1.18}$$

In addition to elastic behaviour, elastoplastic constitutive models has also been characterized [78]. For this non-linear identification (J_2-plasticity and kinematic hardening) a return-mapping algorithm has been developed to enable stress reconstruction.

1.4.1.2 Reciprocity Gap Method (RGM)

Its theoretical background is based on two equations of continuum mechanics: Principle of Virtual Work (PVW) and Maxwell-Betti theorem. Considering PVW for a material current state and another one for a virtual (adjoint) state, it comes:

$$\forall \underline{u}^*, \quad \int_V \underline{\underline{\varepsilon}}(\underline{u}) : [\mathscr{C} - \mathscr{C}^*] : \underline{\underline{\varepsilon}}(\underline{u}^*)\, dV \;=\; \int_{\partial\Omega} (\hat{\underline{t}}.\underline{u}^* - \underline{t}^*.\hat{\underline{u}})\, dS \tag{1.19}$$

where V the monitored volume of material, $\underline{u}$ the displacement field, $\hat{\underline{t}}$ the traction forces, $\hat{\underline{u}}$ the displacement field at boundaries, $\underline{t}^*$ the adjoint state displacement field of $\underline{u}^*$ the adjoint displacement field. As the related stress state satisfies the reciprocity theorem, the set of material parameters can be extracted directly combining Equation 1.19 for several adjoint states. Though it has first been applied for elastic parameters, it has been notably extended to fracture mechanics to monitor crack propagations [79].

1.4.1.3 Equilibrium Gap Method (EGM)

EGM is a identification method which is not suitable for all inverse problems. Indeed, it consists in comparing a reference (known) state to an unknown one. Assuming the knowledge of an elastic behaviour for instance, damage affects stiffness components values. Thus, modified stiffness matrix $\mathscr{C}(x) = D(x)\mathscr{C}_0$ may be identified, where $\mathscr{C}_0$ corresponds to the purely elastic behaviour. To compute

both states, the idea could be incorporated within a Finite Element Model Updating (FEMU) approach, in order to compare two FE models. More interesting, the method can be used directly for damage parameters identification if the purely elastic material behaviour is already characterized. More details about various methodologies could be found in the paper of Avril *et al.* [75]. Naturally, damage maps have been extracted from a biaxial test on composites for example [80].

1.4.1.4 Finite Element Model Updating (FEMU)

The FEMU approach is the most intuitive method for processing heterogeneous fields if one has access to a FE solver. Assuming a FE model of the mechanical test, one finds the set of material parameters which maximize cross-correlation between FE results and experimental data (load or kinematic fields).

There is a broad literature about constitutive parameters extraction with FEMU methods. For instance, Meuwissen *et al.* [81] identified elastic-plastic parameters for isotropic (von-Mises) and anisotropic (Hill) yield criteria on an Aluminum alloy. More recently, elastic-viscoplastic behaviour have been characterized [82, 83] using Perzyna [84] and Johnson-Cook [19] model at high strain rates (10^4-10^5 s^{-1}) with tensile tests and speckle photography. Furthermore, the method has also been used to identify Gurson damage model [85, 86] for aluminium alloys in aeronautic [87] or steels for automotive sectors [88].

The main drawback of FEMU approaches is their strong dependency on the FE model. In particular, boundary conditions are critical to build a consistent model. Thus, their knowledge during the test is mandatory, in addition to their control not to violate FE model assumptions. Moreover, the cost function is very sensitive to FEA intrinsic parameters (*e.g.*, elements type and size, time integration steps for transient dynamic problems, constitutive equation implementation) so that it might be difficult to retrieve standard results. One way to overcome those limits could be to use a refined model for a better robustness, but computational costs may become prohibitive, notably for complex constitutive equations.

1.4.1.5 The Virtual Fields Method (VFM)

The VFM has been introduced in the late 80's as an interesting alternative for simultaneous identification of material parameters without using a FE solver [89]. Its theoretical background [90] is based on the Principle of Virtual Work (PVW),*i.e.*, the weak form of equilibrium equations:

$$\begin{array}{ccccccc} -\displaystyle\int_V \underline{\underline{\sigma}}(\underline{X}) : \underline{\underline{\varepsilon}}^* \, dV & + & \displaystyle\int_{\partial V} \underline{t}.\underline{u}^* \, dS & + & \displaystyle\int_V \underline{f}.\underline{u}^* \, dV & = & \displaystyle\int_V \rho \underline{\gamma}.\underline{u}^* \, dV \\ -\quad W^*_{int}(\underline{X}) & + & W^*_{ext} & & & = & W^*_{acc} \end{array} \tag{1.20}$$

where V denotes the monitored volume of material, $\underline{\underline{\sigma}}$ the Cauchy stress tensor computed from full-field strain measurements and constitutive law using the set of parameters $\underline{X}$. $\underline{u}^*$ is the virtual displacement field, $\underline{\underline{\varepsilon}}^*$ the related virtual strain tensor, $\underline{t}$ the traction vector, $\underline{f}$ the body load, ρ the density and $\underline{\gamma}$ the acceleration vector. Internal virtual work W^*_{int} is the only term that depends on material parameters $\underline{X}$. W^*_{ext} is the external virtual work which stands for the contribution of load during material testing. W^*_{acc} is the contribution of acceleration and inertia effects. Whereas the term may be negligible for quasi-static monotonic tests, it becomes significant for dynamic testing. Finally, the aim of the method is to find out - for a given test - the set of material parameters which fits the PVW (Equation 1.20) at best. This is notably done feeding this equation with collected full-field measurements.

In case of linear constitutive laws (*e.g.*, linear elastic behaviour). VFM-based identification relies on a simple linear resolution. Otherwise, constitutive equations have to be solved numerically to compute stress fields from strains measurement. Consequently, the identification consists in minimizing square gaps to PVW, hence the definition of a scalar cost function of unknown material parameters.

This principle will be detailed in next sections.

Furthermore, VFM identifications could also be categorized in two families:

- VFM with external load measurement which is based on a balance between internal virtual work $W^*_{int}(\underline{X})$ and external load contribution W^*_{ext}. This is suitable for quasi-static tests (or dynamic) if virtual fields are well chosen. W^*_{acc} has to be negligible w.r.t. W^*_{int} and W^*_{ext}. Finally, the PVW is reduced to Equation 1.21. This will be detailed in Section 1.4.2.

$$\int_V \underline{\underline{\sigma}}(\underline{X}) : \underline{\underline{\varepsilon}}^* dV = \int_{\partial V} \underline{t}.\underline{u}^* dS \tag{1.21}$$

- dynamic VFM which is based on the balance between internal virtual work $W^*_{int}(\underline{X})$ and acceleration contribution W^*_{acc}. This is suitable for dynamic tests, in particular when inertia effects are significant. Virtual fields are then selected to cancel W^*_{ext}, so that external force measurement is not needed. Finally, the PVW is reduced to Equation 1.22. This will be detailed in Section 1.4.3.

$$\int_V \underline{\underline{\sigma}}(\underline{X}) : \underline{\underline{\varepsilon}}^* dV + \int_V \rho\underline{\gamma}.\underline{u}^* dV = 0 \tag{1.22}$$

1.4.2 The Virtual Fields Method with external load measurement

1.4.2.1 Linear behaviour

In the case of linear constitutive equations, there is a direct relation between stress tensors $\underline{\underline{\sigma}}$ and $\underline{\underline{\varepsilon}}$ (Equation 1.2). As $\underline{\underline{\varepsilon}}$ is measured, VFM may rely on a linear system. The latter is build by expressing the PVW defined by Equation 1.21 for a number of virtual fields equal to the number of unknown material parameters [89, 90].

For a linear isotropic behaviour and a plane stress state, Hooke's law could be expressed by Equation 1.23.

$$\begin{bmatrix} \sigma_{xx} \\ \sigma_{yy} \\ \sigma_{xy} \end{bmatrix} = \begin{bmatrix} Q_{xx} & Q_{xy} & 0 \\ Q_{xy} & Q_{xx} & 0 \\ 0 & 0 & \frac{Q_{xx}-Q_{xy}}{2} \end{bmatrix} \begin{bmatrix} \varepsilon_{xx} \\ \varepsilon_{yy} \\ \varepsilon_{xy} \end{bmatrix} \quad \text{where} \quad \left| \begin{array}{l} Q_{xx} = \dfrac{E}{1-\nu^2} \\ \\ Q_{xy} = \dfrac{\nu E}{1-\nu^2} \end{array} \right. \tag{1.23}$$

Then, Equation 1.21 can be expanded using Equation 1.23. As plane stress state is assumed, the domain on which the integral is expressed is the surface S on which full-field measurements are performed. For a given virtual field ($\underline{u}^*$ and consequently $\underline{\underline{\varepsilon}}^*$), Equation 1.21 becomes:

$$\begin{aligned} Q_{xx}\left[\int_S \varepsilon_{xx}\varepsilon^*_{xx} + \varepsilon_{yy}\varepsilon^*_{yy} + \frac{1}{2}\varepsilon_{xy}\varepsilon^*_{xy}\, dV\right] + Q_{xy}\left[\int_S \varepsilon_{yy}\varepsilon^*_{xx} + \varepsilon_{xx}\varepsilon^*_{yy} - \frac{1}{2}\varepsilon_{xy}\varepsilon^*_{xy} dV\right] \\ = \int_{\partial S} t_x u^*_x + t_y u^*_y \, dS \end{aligned} \tag{1.24}$$

Therefore, considering Equation 1.24 for two virtual fields is equivalent to Equation 1.25, where the unknowns are always the stiffness components.

$$\begin{bmatrix} A_{11} & A_{12} \\ A_{21} & A_{22} \end{bmatrix} \begin{bmatrix} Q_{xx} \\ Q_{xy} \end{bmatrix} = \begin{bmatrix} B_1 \\ B_2 \end{bmatrix}$$
$$A \qquad Q \quad = \quad B \tag{1.25}$$

where, for $i \in \{1,\ 2\}$ (i the virtual field number):

$$\left|\begin{array}{l} A_{i1} = \displaystyle\int_S \varepsilon_{xx}\varepsilon_{xx}^{*\,(i)} + \varepsilon_{yy}\varepsilon_{yy}^{*\,(i)} + \frac{1}{2}\varepsilon_{xy}\varepsilon_{xy}^{*\,(i)}\, dS \\ A_{i2} = \displaystyle\int_S \varepsilon_{xx}\varepsilon_{yy}^{*\,(i)} + \varepsilon_{yy}\varepsilon_{xx}^{*\,(i)} - \frac{1}{2}\varepsilon_{xy}\varepsilon_{xy}^{*\,(i)}\, dS \\ B_i = \displaystyle\int_S \left[t_x u_x^{*\,(i)} + t_y u_y^{*\,(i)}\right] dS \end{array}\right.$$

Then, the set of virtual fields ($\underline{u}^{*\,(1)}$, $\underline{\underline{\varepsilon}}^{*\,(1)}$) and ($\underline{u}^{*\,(2)}$, $\underline{\underline{\varepsilon}}^{*\,(2)}$) has to be defined. In practice, any kinematically admissible virtual field can be used but one has to ensure their orthogonality (*i.e.*, linearly independent). However, it is relevant to choose virtual fields that enable to express the matrix A and vector B as quantities that only depends on measurable quantities such as load resultant F and strain fields over ROI zones that will contribute to material parameters extraction [89, 90]. Finally, the calculation of Q_{xx} and Q_{xy} is easily performed by inverting the system of Equation 1.25. Later, it was also proposed to build virtual fields automatically, using polynomial expansions (Equation 1.26). They are referred as Special Virtual Fields (SVF) [91, 92]. Monomial coefficients may be constrained to calculate the stiffness directly - *i.e.*, enforcing $[A_{ij}]$ to be the identity matrix in Equation 1.25 - or to make explicit measurable quantities.

$$\left|\begin{array}{l} u_x^* = \displaystyle\sum_{i,j} a_{ij} x^i y^j \\ u_y^* = \displaystyle\sum_{i,j} b_{ij} x^i y^j \end{array}\right. \tag{1.26}$$

VFM with external load measurement has been widely used for the identification of isotropic but also anisotropic elastic parameters [93–95]. Moreover, it was also used to analyse damage evolution in composite materials [96, 97] by modelling it as a linear correction of stress, so that $\sigma_{xy} = Q_{xy}\varepsilon_{xy} - dQ_{xy}\varepsilon_{xy}^3$, where d is the damage parameter.

1.4.2.2 Non-linear behaviour

In case of non-linear constitutive laws, there is no explicit relation between stress and strain tensor to be input in Equation 1.21 *a priori*. To calculate $W_{int}^*(\underline{X})$, numerical methods like return mapping algorithms [13, 30] have therefore been proposed to compute $\underline{\underline{\sigma}}(\underline{X})$ from full-field measurements and a given set of material parameters $\underline{X}$. Finally, non-linear VFM with external load measurement relies on the minimization of a cost function φ which expresses the normalized square errors to PVW, according to given constitutive laws, at each monitored load step i (Equation 1.27).

$$\varphi\left(\underline{X}\right) = \sum_i \left[\frac{W_{int}^{*\,(i)}(\underline{X}) - W_{ext}^{*\,(i)}}{W_{ext}^{*\,(i)}}\right]^2 \tag{1.27}$$

Most of the applications deal with elastoplastic behaviour characterization using "manual" virtual fields [98–100],*i.e.*, virtual fields chosen "by hand". For instance, a linear hardening model ($\sigma_y = \sigma_0 + Kp$) has been characterized. Later, a Voce model ($\sigma_y = \sigma_0 + Kp + \sigma_\infty[1 - e^{-bp}]$) has also been studied [101]. Furthermore, some studies have extended the concept of automatic virtual fields for non-linear behaviour [102, 103]. They are referred as Optimized Virtual Fields (OVF) since cost function bias due to noise is reduced.

The characterization of coupled models including both elastoplasticity and damage [104] was also investigated. The latter has been performed on simulated data on notched and holed specimens. Even

if experimental biases are not taken into account (PVW is input with FEA data), this work is seminal for those models. Finally, hardening parameters are well retrieved but there is a discrepancy for damage fields. The authors mentioned the difficulty to identify damage when time steps and time gradients of damage between load steps are high.

Nonetheless, only a few studies are dedicated to characterize non-linear constitutive equations for rate-dependent behaviour. A Perzyna model has been identified in [99]. Johnson-Cook (JC) model has been characterized at room temperature but at medium strain-rates [6] (until 500 s^{-1}). In this case, inertia effects contribution in Equation 1.20 were negligible so that is was possible to use VFM with external load measurement. JC model has also been identified including thermal effects but at much lower strain-rates [105]. In both cases, static part of the model - *i.e.*, σ_0, K et n in Equation 1.11 - is identified separately. In [6], dynamic part is identified with a single test using an high-speed hydraulic machine. In [105], both viscous effects and thermal softening - *i.e.*, M and m respectively in Equation 1.11 - are identified with a set of tensile tests at various temperatures (until 900°).

The two last examples exhibit the first drawbacks of VFM with external load measurement for material parameters extraction for dynamic tests. If high rate deformations occur, the assumption of negligible contribution of inertia effects may jeopardize the identification. To overcome this issue, it was proposed to use Equation 1.20 in a way to take advantage of inertia effects. This is presented in the next section.

1.4.3 The Virtual Fields Method with acceleration as a load cell

Dynamic behaviour characterization is still challenging for the experimental community mainly because of test settings, which are often more critical than in quasi-static conditions. For high strain rate characterization ($\dot{\varepsilon} \gg 100$ s^{-1}), only a few apparatus like Split Hopkinson Bar (SHB) apparatus [106, 107] are available. As mentioned in Section 1.2, the related tests could be processed with statically determinate approaches. However, it is known to be difficult to maintain homogeneous strain-rate over the ROI during the test. For rate-dependent models, those approaches also implies very large test campaigns to characterize the behaviour under a wide range of strain rate. It is therefore more judicious to use statically undeterminate approaches such as the VFM. As seen in the previous section, its "quasi-static" configuration has been successfully applied to medium rate testing as inertia effects were negligible [6]. However, this assumption may not be valid for characterization at higher strain rate. Therefore, one could process VFM "dynamic" configuration. The latter has been introduced in [108] as a way to extract material parameters without external load measurement. Indeed, if virtual field is well selected, the PVW can be rewritten as Equation 1.21.

In this case, virtual field $\underline{u}^*$ is chosen to cancel external forces contribution *i.e.*, $\forall \underline{x} \in \partial V,\ \underline{u}^*(\underline{x}) = 0$. Thus, constitutive parameters could be extracted with the sole knowledge of kinematic fields. Imaging and full-field measurement techniques introduced in Section 1.3 are then the only necessary tools to perform the dynamic VFM. Indeed, strains and accelerations may be obtained from displacement fields owing to a single differentiation in space and a double differentiation in time respectively.

The following parts give an overview about recent literature dealing with dynamic VFM. To the author knowledge, nine papers can be found about:

- Fiber Reinforced Plastics (FRP) elastic behaviour characterization [108],
- three-point-bending-test analysis under dynamic loading [11],
- spalling tests for concrete elastic behaviour characterization [109],
- a new apparatus for FRP elastic behaviour characterization [7],

- Friction Stir Welding (FSW) welds elastoplastic behaviour identification [110],
- rubber hyperelastic behaviour characterization [111],
- copper viscoplastic parameters identification with a three point bending test [9, 10],
- polymer composite interlaminar tensile properties characterization [112],
- tungsten carbide cermets characterization [113].

To compare the advantages, drawbacks and limitations of each study, a comparative review is carried out in next paragraph on experimental setups, full-field measurement techniques, data processing methodologies and material parameters identifications.

1.4.3.1 Experimental setup

Dynamic VFM has been first performed on SHB tests [106, 107]. Then, most of the studies used the same apparatus [9–11, 108–110]. By contrast, a drop test was performed for rubber characterization [111] because this setup was more suitable for materials undergoing large strains.

Later, it was proposed a new apparatus more suitable for dynamic VFM [7]. It consists in a gas gun throwing a projectile on a thin specimen slice (Figure 1.10). The setup was designed in order to increase acceleration levels. Indeed, inertia effects are magnified owing to the free edge. This is crucial for the dynamic VFM methodology insofar as its robustness may be improved with more trackable accelerations. Several papers applied this methodology [112, 113].

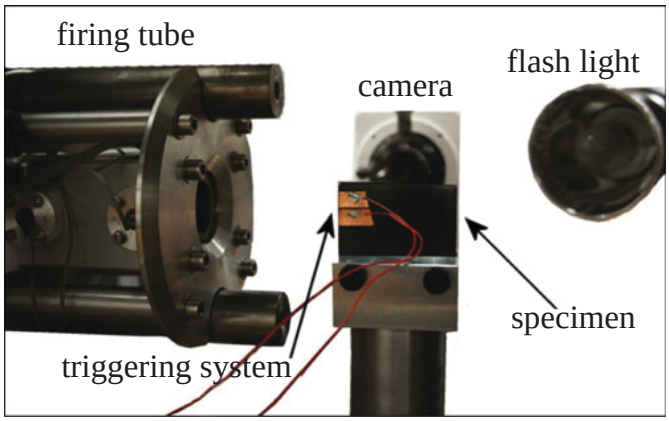

Figure 1.10: Image-Based Inertial Impact (IBII) test apparatus [7]

N.B: Apparatus on Figure 1.10 will later be referred to as “Image-Based Inertial Impact” (IBII).

1.4.3.2 Full-field measurements

Metrological performance is a key point in VFM process. This is all the more critical for dynamic configuration as acceleration fields (computed from displacement double time differentiation) are needed. Thus, the choice among available full-field measurement technique and camera (Table 1.2) is often constrained by the needed measurement resolutions (spatial and temporal).

For instance, the grid method has been used in [109] to reach a strain resolution which may have been difficult to get using DIC. In [110], both grid and DIC methods have been used with different cameras. The best displacement resolution has been obtained with the first technique whereas it is the opposite for acceleration resolution. However, the latter strongly depends on the methods used to regularize displacements before differentiation and reconstruction of missing/corrupted data (*e.g.*, on

Table 1.2: DVFM cinematography

	Full-field measurement technique	UHS camera
Moulart *et al.* [108]	grid method	Cordin 550-62 (1000×1000)
Pierron *et al.* [11]	DIC	IMACON 200 (1280×1024)
Pierron *et al.* [109]	grid method	Shimadzu HPV-1 (312×260)
Pierron *et al.* [7]	grid method	SIMX16 (1280×960), Shimadzu HPV-X (400×250)
Le Louedec *et al.* [110]	grid method + DIC	SIM16 (1360×1024), IMACON 200 (1280×1024)
Yoon *et al.* [111]	DIC	Grasshopper3 USB 3.0 (215×684)
Koohbor *et al.* [9]	DIC	Shimadzu HPV-X (400×250)
Van Blitterswyk *et al.* [112]	grid method	Shimadzu HPV-X (400×250)
Fletcher and Pierron [113]	grid method	Shimadzu HPV-X (400×250)

specimen edges). Indeed, when displacements are extracted, strains and accelerations may be calculated from differentiation. Because of experimental noise, regularization operation(s) is (are) necessary to extract robust derivatives. Thus, various techniques are used in the literature (Table 1.3), this leading to different acceleration resolutions (Table 1.4).

Table 1.3: Overview of regularization techniques

	Spatial smoothing	Temporal smoothing
Moulart *et al.* [108]	diffuse approximation	piecewise fourth-order fitting
Pierron *et al.* [11]	diffuse approximation	No
Pierron *et al.* [109]	No	piecewise second-order fitting
Pierron *et al.* [7]	gaussian	piecewise third-order fitting
Le Louedec *et al.* [110]	least-square convolution	No
Yoon *et al.* [111]	N/A	nine-order fitting
Koohbor *et al.* [9,10]	gaussian	piecewise fitting
Van Blitterswyk *et al.* [112]	gaussian smoothing	piecewise fitting
Fletcher and Pierron [113]	gaussian smoothing	piecewise fitting

Table 1.4: Overview of acceleration fields extraction

	Acceleration computation	Resolution(*) ($\times 10^5$ m.s^{-2})
Moulart *et al.* [108]	analytic	2 (Cordin 550-62)
Pierron *et al.* [11]	finite-difference	N/A
Pierron *et al.* [109]	analytic	0.4 (HPV-1)
Pierron *et al.* [7]	analytic	5 (SIMX16), 0.2 (HPV-X)
Le Louedec *et al.* [110]	finite-difference + analytic	0.66 (SIM16), 0.45 (IMACON200)
Yoon *et al.* [111]	No	N/A
Koohbor *et al.* [9,10]	finite-difference	N/A
Van Blitterswyk *et al.* [112]	finite-difference	up to 5.1
Fletcher and Pierron [113]	finite-difference	N/A

(*) smallest trackable acceleration

Various full-field measurement toolchains have been used for strain and acceleration extraction. Grid method has been used mainly because, as mentioned in Section 1.3, it often offers a better compromise between acceleration resolution and spatial resolution measurement for UHS cameras with a low number of pixels (Table 1.4). However, the identification robustness also relies on the methodology used for material parameters extraction. This is discussed in the next section.

1.4.3.3 Material parameter identification

Almost all studies deal with linear dynamic behaviour of materials by characterizing Hooke's law for small strains [7, 11, 108, 109] and Odgen model for large strains (hyperelasticity) [111]. Later, nonlinear behaviour identification have been considered for Prandtl-Reuss model [110]. More recently, JC model was characterized [9, 10]. The next parts describe the proposed methodologies.

➥ *Linear behaviour*

As in [108], linear dynamic VFM has been mainly applied using "simple" virtual fields (*i.e.*, manually defined) to build a linear system of equations (Equation 1.28). For isotropic behaviour, this system is equivalent to that of Equation 1.25 except right vector that embeds in present case the acceleration contribution in place of external loads. Figure 1.11 illustrates some kinematic fields which have been obtained.

$$\begin{bmatrix} A_{11} & A_{12} \\ A_{21} & A_{22} \end{bmatrix} \begin{bmatrix} Q_{xx} \\ Q_{xy} \end{bmatrix} = \begin{bmatrix} B_1 \\ B_2 \end{bmatrix} \qquad A \quad Q = B \tag{1.28}$$

where

$$\left| \begin{array}{l} A_{i1} = -\int_S \varepsilon_{xx}\varepsilon_{xx}^{*\,(i)} + \varepsilon_{yy}\varepsilon_{yy}^{*\,(i)} + \frac{1}{2}\varepsilon_{xy}\varepsilon_{xy}^{*\,(i)}\, dS \\ A_{i2} = -\int_S \varepsilon_{xx}\varepsilon_{yy}^{*\,(i)} + \varepsilon_{yy}\varepsilon_{xx}^{*\,(i)} - \frac{1}{2}\varepsilon_{xy}\varepsilon_{xy}^{*\,(i)}\, dS \\ B_i = \int_S \left[a_x u_x^{*\,(i)} + a_y u_y^{*\,(i)}\right] dS \end{array} \right.$$

In [108] elastic parameters are extracted at several timesteps. The corresponding longitudinal strain maps and average accelerations are shown in Figure 1.11. Tough identified values are irregular (standard deviation $\approx$ 10%), the best results are obtained when accelerations levels are high, this also corresponding to strain maps which seems to be less noisy (Figure 1.11).

➥ *Non-linear behaviour*

Le Louëdec *et al.* [110] applied non-linear dynamic VFM for linear isotropic hardening characterization. A cost function similar to Equation 1.27 was optimized, considering W_{acc}^* in place of W_{ext}^*. However, cost function gradient w.r.t hardening modulus was very low (Figure 1.12(a)) so that is was not possible to extract both plastic parameters (*i.e.*, initial yield stress and hardening modulus) simultaneously. Thus, initial yield stress σ_0 was assumed to be known and a monovariate optimization lead to the identification of hardening modulus.

Koohbor *et al.* [9, 10] applied the method to Johnson-Cook model. As in [105], static parameters (*i.e.*, elastic part and static term of the flow rule) have been characterized with standard quasi-static tests. Then, the dynamic constitutive parameters have been extracted in a second time. It is worth noticing that this problem was reduced to a monovariate optimization assuming constant activation of viscous effects (see Figure 1.12(b), where C is the JC viscoplastic parameter denoted M in Equation 1.11). Finally, the identified parameters were in good accordance with the literature data.

To conclude, the dynamic VFM have been first applied to the identification of elastic parameters. Afterwards, it has been naturally extended to cases of non-linear constitutive laws (*e.g.*, linear hardening model in [110]). However, a few problems are arising, such as the cost function sensitivity when parameters are identified simultaneously. This has to be taken into account for future achievements, notably when aiming at characterizing rate-dependent models.

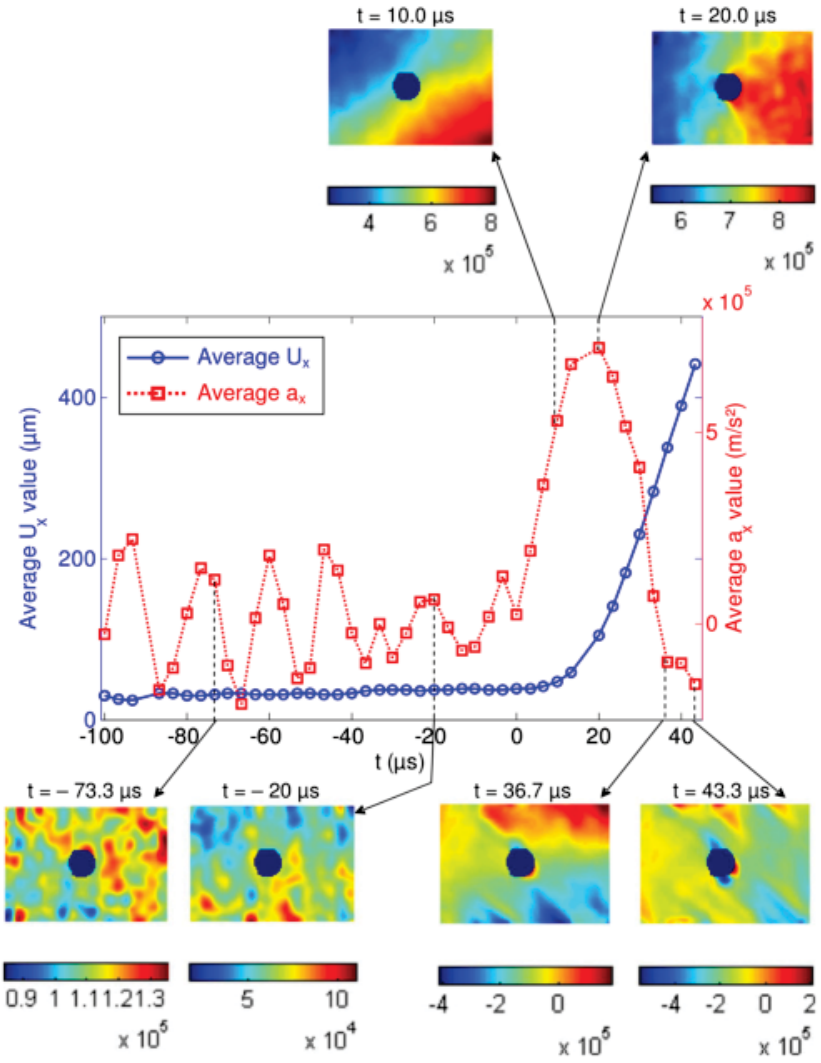

Figure 1.11: Strain maps and mean acceleration [108]

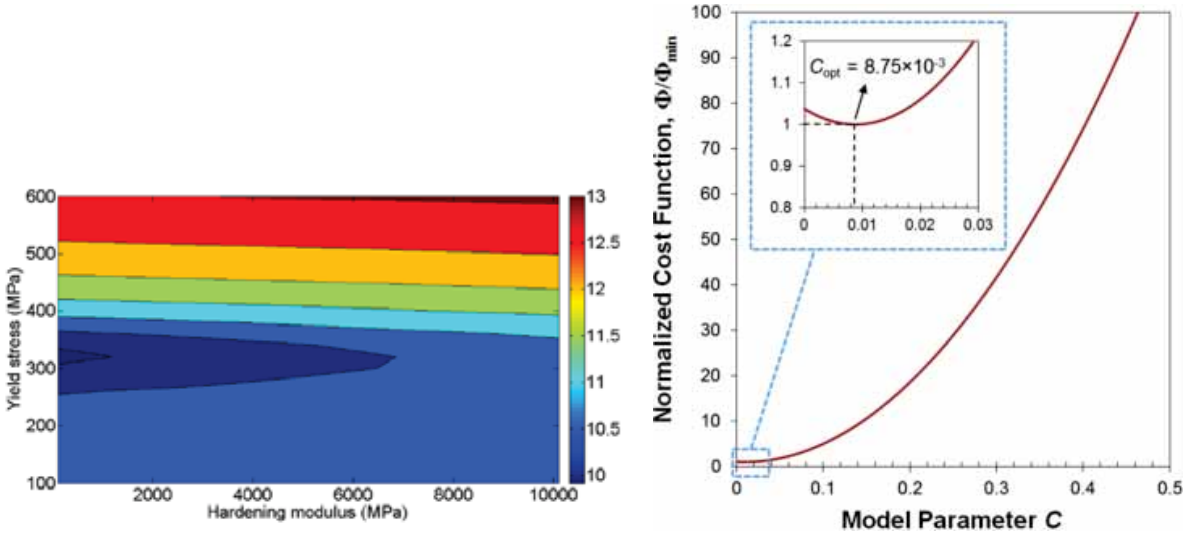

(a) (b)

Figure 1.12: Cost functions for non-linear dynamic VFM : (a) Le Louëdec *et al.* [110] - (b) Koohbor *et al.* [9,10]

1.5 Summary

This chapter gives a brief overview about current available methodologies to describe and to model dynamic behaviour of metallic materials. Statically determinate approaches have been widely used for a long time. However, experimental data is often underexploited because of strong hypothesis made to process tests. In particular, those assumptions are very difficult to respect when localized phenomenons occurs (*e.g.*, necking), hence an identification procedure which is easily jeopardized. Thus, high rate testing becomes challenging inasmuch as in addition to experimental constraints (*e.g.*, homogeneous strain-rate), a lot of tests are necessary to characterize the dynamic behaviour, notably for rate-dependent ones. By contrast, statically undetermined approaches can be used to overcome those obstacles. Indeed, no assumptions are made *a priori* on mechanical fields so that any test could be potentially processed up to failure. Theoretically, a test which generates heterogeneous mechanical fields may then be analysed, which can be a real advantage for dynamic testing. For rate-dependent models for instance, the test campaign may be then drastically reduced. Nevertheless, suitable full-field measurement techniques and UHS camera are necessary to extract kinematic fields.

Several advanced methods of identification can be input with those kinematic fields. FEMU-based approaches are popular because of their simplicity when one owns a FE solver. Nonetheless, Virtual Fields Method (VFM) has been getting more and more attention because a detailed knowledge of boundary conditions is not necessary. This is clearly an advantage for transient dynamics insofar as for those applications, loading conditions monitoring and driving still remains challenging. In this case, tests may then be easier to set up and more importantly, the test design space itself is less constrained.

Recent literature shows that VFM may be applied to a large variety of tests and material behaviour. Its configuration with external load measurement has been intensively used for both linear and non-linear behaviour characterization. More recently, its dynamic configuration has been proposed notably for high rate testing ($\dot{\varepsilon} > 10^3\ s^{-1}$) with SHB. The use of dynamic VFM for extraction of constitutive parameters relies on the sole knowledge of strain and acceleration fields, hence no load measurement is necessary. To take advantage of dynamic VFM, a non-standard test methodology has been introduced [7]. It consists in a projectile fired by a gas gun towards a thin-plate specimen. This has been successfully applied to elastic parameters extraction on composite materials. More recently, it has also been extended to linear hardening characterization [110].

Then, one can think about extending the method to material parameters extraction on much more complex constitutive laws as rate-dependent models. However, several questions are still pending considering the available literature review. Based on this, two improvements paths may be opened:

- even if a new apparatus was proposed, most of the related test parameters were chosen intuitively. Thus, one has to better understand the influence of each test intrinsic parameter (*e.g.*, specimen geometry) to develop a robust method for the non-linear dynamic VFM,
- dynamic VFM toolchain (full-field measurements technique, data processing, identification toolchain) has to be studied in more depth. This includes notably the choice of virtual fields, the cost function building, but above the optimization of full-field measurement processing.

Generally speaking, obstacles arising from extension of dynamic VFM are mainly related to a better understanding of test parameters (both intrinsic and extrinsic) to ensure an accurate and robust identification. To do so, FEA could be used as a basis to assess test configuration features. This has already been addressed for quasi-static applications [114,115]. The next chapter presents the numerical toolbox which have been developed for this task and dynamic VFM.

Chapter 2

Development of a numerical toolbox for Image-Based Inertial Impact tests analysis

Contents

Abstract

This chapter presents the numerical toolbox developed to design the test matrix based on IBII tests suitable for non-linear behaviour characterization with dynamic VFM. To enable the full computation of PVW, a Return Mapping Algorithm (RMA) for J_2-viscoplasticity and Johnson-Cook model is first developed to compute stress fields from strain fields and a given set of material parameters. This is coupled with a methodology implemented to extract strain and acceleration fields from full-field measurements in realistic conditions. Furthermore, a FE-based toolchain is developed to enable a thorough investigation of IBII test configurations numerically. Indeed, further analysis (perhaps optimization) of tests parameters involves design parameters (e.g., specimen and projectile geometry, projectile velocity) but also the features of the VFM toolchain such as the imaging features (e.g., camera and grid method features). Thus, a methodology is implemented to generate reliable FE simulations using the research codes Cast3M® and Europlexus®. Moreover, a synthetic images generator is also developed to deal with quantitative assessment of measurement bias (camera spatial and temporal resolution, camera noise and digitization features) in the VFM process.

2.1 Return Mapping Algorithm for Johnson-Cook model and J_2-(visco)plasticity

The non-linear dynamic VFM relies on the computation of stress fields to express the PVW (Equation 1.20) for a given constitutive model and a set of material parameters. Therefore, it is crucial to have at disposal an efficient and robust tool to perform this task.

Aside from some very particular cases, the resolution of constitutive laws for (visco)plastic behaviour of materials cannot be done analytically. Indeed, the related models are driven by non-linear time differential equations contrary to Hooke's law (Equation 1.2) - for elastic deformations - which links $\underline{\underline{\varepsilon}}$ and $\underline{\underline{\sigma}}$ explicitly. Consequently, numerous numerical strategies have been set up to solve those constitutive equations using strain-driven process, *i.e.*, $\underline{\underline{\varepsilon}}$ inputs incremental integration of constitutive laws [13, 30]. They were developed with a view to compute stress fields in Finite Element Analysis (FEA).

The same methodology can be used to process strain fields to input the VFM. At ONERA, an in-house algorithm has been developed for J_2-(visco)plasticity and Johnson-Cook (JC) model to input VFM [116]. However, some issues were still pending after validation tests, such as computation of cumulated plastic strain rate $\dot{p}$ in Equation 1.11 and computational efficiency which may jeopardize the identification process when the number of monitored time steps is high. This section aims at updating the proposed algorithm by increasing its robustness (including calculation of $\dot{p}$) and decreasing computational cost, starting with constitutive equations discretization.

2.1.1 Theoretical background

In the literature, most of algorithms are based on elastic predictor/plastic correction strategy [13, 30]. In other words, a trial state ^{trial} is computed from strain increment (purely elastic) between steps $k+1$ and k assuming a fully known mechanical state at step k and Hooke's law (Equation 1.2). If $f_{k+1}^{trial} = \sigma_{eq}(\underline{\underline{\sigma}}_{k+1}^{trial}) - \sigma_y^k \leq 0$, the evolution is truly elastic and $\underline{\underline{\sigma}}_{k+1} = \underline{\underline{\sigma}}_{k+1}^{trial}$ and $\sigma_y^{k+1} = \sigma_y^k$. Otherwise, a (visco)plastic correction is needed (Figure 2.1).

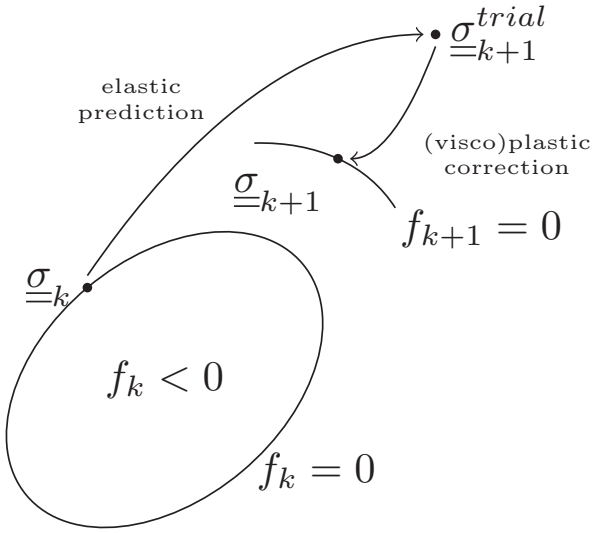

Figure 2.1: Illustration of plastic correction strategy

Within stress space, correction is computed using data from time step $k+\theta$, $\theta \in [0, 1]$. Finally, a family of Return Mapping Algorithms (RMA) is build considering different values for θ. Consequently, time integration can be fully explicit ($\theta = 0$) or implicit ($\theta = 1$). The latter is often used because

numerical scheme stability is unconditional. The next paragraphs present a strategy to compute this correction for JC viscoplastic model.

The yield stress σ_y is assumed to follow JC flow rule (Equation 2.1) at room temperature. Thus, its expression can be simplified in Equation 2.2.

$$\sigma_y = \left[\sigma_0 + Kp^n\right]\left[1 + M\ln\left(\frac{\dot{p}}{\dot{\varepsilon}^p_{eq,0}}\right)\right]\left[1 - \left(\frac{T - T_0}{T_f - T_0}\right)^m\right] \tag{2.1}$$

$$\sigma_y = \begin{cases} \sigma_0 + Kp^n & \text{if} \quad \dot{p} \leq \dot{\varepsilon}^{vp}_{eq,0} \\ \left[\sigma_0 + Kp^n\right]\left[1 + M\ln\left(\dfrac{\dot{p}}{\dot{\varepsilon}^{vp}_{eq,0}}\right)\right] & \text{if} \quad \dot{p} > \dot{\varepsilon}^{vp}_{eq,0} \end{cases} \tag{2.2}$$

Mechanical quantities at increment $k+1$ are calculated using strains at steps k and $k+1$ and updated quantities at step k. Like previous works [6, 116], first order time derivatives are discretized using implicit backward Euler scheme ($\theta = 1$) as in Equation 2.3 for any variable x.

$$\left.\frac{\partial x}{\partial t}\right|_{k+1} = \frac{x_{k+1} - x_k}{t_{k+1} - t_k} = \frac{\Delta x_{k+1}}{\Delta t_{k+1}} \tag{2.3}$$

Writing Hooke's law for trial and final state $k+1$ leads to the expression of $\underline{\underline{\sigma}}^{trial}_{k+1}$ correction to compute $\underline{\underline{\sigma}}_{k+1}$:

$$\left|\begin{array}{l} \underline{\underline{\sigma}}^{trial}_{k+1} = 2\mu(\underline{\underline{\varepsilon}}_{k+1} - \underline{\underline{\varepsilon}}^{vp}_{k}) + \lambda[\mathrm{Tr}(\underline{\underline{\varepsilon}}_{k+1}) - \underbrace{\mathrm{Tr}(\underline{\underline{\varepsilon}}^{vp}_{k})}_{=0}]\underline{\underline{I}} \\ \\ \underline{\underline{\sigma}}_{k+1} = 2\mu(\underline{\underline{\varepsilon}}_{k+1} - \underline{\underline{\varepsilon}}^{vp}_{k+1}) + \lambda[\mathrm{Tr}(\underline{\underline{\varepsilon}}_{k+1}) - \underbrace{\mathrm{Tr}(\underline{\underline{\varepsilon}}^{vp}_{k+1})}_{=0}]\underline{\underline{I}} \end{array}\right. \Rightarrow \boxed{\underline{\underline{\sigma}}_{k+1} = \underline{\underline{\sigma}}^{trial}_{k+1} - 2\mu\Delta\underline{\underline{\varepsilon}}^{vp}_{k+1}} \tag{2.4}$$

This correction can be calculated integrating Equation 1.7 incrementally:

$$\Delta\underline{\underline{\varepsilon}}^{vp}_{k+1} = \frac{3}{2}\Delta\gamma_{k+1}\frac{\underline{\underline{S}}_{k+1}}{\sigma_{eq}(\underline{\underline{\sigma}}_{k+1})} \underset{(1.10)}{=} \frac{3}{2}\Delta p_{k+1}\frac{\underline{\underline{S}}_{k+1}}{\sigma_{eq}(\underline{\underline{\sigma}}_{k+1})} \tag{2.5}$$

Yield stress σ_y is a function of p and $\dot{p}$ (Equation 2.2). Thus, σ_y^{k+1} is a scalar function varying with plastic strain increment only Δp_{k+1} (Equation 2.6):

$$\sigma_y^{k+1}(\Delta p_{k+1}) = \begin{cases} \sigma_0 + K(p_k + \Delta p_{k+1})^n & \text{if} \quad \dfrac{\Delta p_{k+1}}{\Delta t_{k+1}} \leq \dot{\varepsilon}^{vp}_{eq,0} \\ \left[\sigma_0 + K(p_k + \Delta p_{k+1})^n\right]\left[1 + M\ln\left(\dfrac{\frac{\Delta p_{k+1}}{\Delta t_{k+1}}}{\dot{\varepsilon}^{vp}_{eq,0}}\right)\right] & \text{if} \quad \dfrac{\Delta p_{k+1}}{\Delta t_{k+1}} > \dot{\varepsilon}^{vp}_{eq,0} \end{cases} \tag{2.6}$$

The increment Δp_{k+1} and $\underline{\underline{\sigma}}_{k+1}$ are the two unknowns of the non-linear problem. In order to solve it, the condition of leaning on the yield surface is expressed for mechanical state at step $k+1$ (Equation 2.7).

$$f_{k+1} = \sigma_{eq}(\underline{\underline{\sigma}}_{k+1}) - \sigma_y^{k+1}(\Delta p_{k+1}) = 0 \tag{2.7}$$

Equation 2.4 may be transposed to deviatoric stresses as $\mathrm{Tr}\left[\Delta\underline{\underline{\varepsilon}}^{vp}_{k+1}\right]$ is null (cf. Equation 2.5):

$$\underline{\underline{S}}_{k+1} = \underline{\underline{S}}^{trial}_{k+1} - 2\mu\Delta\underline{\underline{\varepsilon}}^{vp}_{k+1} \underset{(2.5)}{=} \underline{\underline{S}}^{trial}_{k+1} - 3\mu\Delta p_{k+1}\frac{\underline{\underline{S}}_{k+1}}{\sigma_{eq}(\underline{\underline{\sigma}}_{k+1})}$$

$$\Rightarrow \boxed{\underline{\underline{S}}^{trial}_{k+1} = \left[1 + 3\mu\frac{\Delta p_{k+1}}{\sigma_{eq}(\underline{\underline{\sigma}}_{k+1})}\right]\underline{\underline{S}}_{k+1}} \tag{2.8}$$

Likewise, the same relation could be obtained for equivalent stress:

$$\begin{aligned}
\sigma_{eq}(\underline{\underline{\sigma}}^{trial}_{k+1}) &= \sqrt{\frac{3}{2}}\sqrt{\underline{\underline{S}}^{trial}_{k+1} : \underline{\underline{S}}^{trial}_{k+1}} \\
&\underset{(2.8)}{=} \left[1 + 3\mu\frac{\Delta p_{k+1}}{\sigma_{eq}(\underline{\underline{\sigma}}_{k+1})}\right]\sqrt{\frac{3}{2}}\sqrt{\underline{\underline{S}}_{k+1} : \underline{\underline{S}}_{k+1}} \\
&= \left[1 + 3\mu\frac{\Delta p_{k+1}}{\sigma_{eq}(\underline{\underline{\sigma}}_{k+1})}\right]\sigma_{eq}(\underline{\underline{\sigma}}_{k+1}) \\
\Rightarrow &\boxed{\sigma_{eq}(\underline{\underline{\sigma}}_{k+1}) = \sigma_{eq}(\underline{\underline{\sigma}}^{trial}_{k+1}) - 3\mu\Delta p_{k+1}}
\end{aligned} \tag{2.9}$$

Equation 2.7 could then be written as a function of Δp_{k+1}:

$$\boxed{-f_{k+1} = 3\mu\Delta p_{k+1} + \sigma_y^{k+1}(\Delta p_{k+1}) - \sigma_{eq}(\underline{\underline{\sigma}}^{trial}_{k+1}) = 0} \tag{2.10}$$

N.B.: Another useful relation:

$$\begin{aligned}
\underline{\underline{S}}^{trial}_{k+1} &\underset{(2.8)}{=} \left[1 + 3\mu\frac{\Delta p_{k+1}}{\sigma_{eq}(\underline{\underline{\sigma}}_{k+1})}\right]\underline{\underline{S}}_{k+1} \\
&\underset{(2.10)}{=} \left[1 + \frac{\sigma_{eq}(\underline{\underline{\sigma}}^{trial}_{k+1}) - \sigma_{eq}(\underline{\underline{\sigma}}_{k+1})}{\sigma_{eq}(\underline{\underline{\sigma}}_{k+1})}\right]\underline{\underline{S}}_{k+1} \\
&= \frac{\sigma_{eq}(\underline{\underline{\sigma}}^{trial}_{k+1})}{\sigma_{eq}(\underline{\underline{\sigma}}_{k+1})}\underline{\underline{S}}_{k+1} \\
\Rightarrow &\boxed{\frac{\underline{\underline{S}}^{trial}_{k+1}}{\sigma_{eq}(\underline{\underline{\sigma}}^{trial}_{k+1})} = \frac{\underline{\underline{S}}_{k+1}}{\sigma_{eq}(\underline{\underline{\sigma}}_{k+1})}}
\end{aligned} \tag{2.11}$$

In practice, Notta *et al.* [6, 116] have introduced an iterative resolution over Δp_{k+1} and $\sigma_{eq}(\underline{\underline{\sigma}}_{k+1})$. Here, we propose to follow the literature approaches [13,30] where a single scalar equation with Δp_{k+1} as the sole unknown is considered. This makes the resolution more efficient and robust because any numerical method for real-valued functions roots research may then be used, as the Newton-Raphson (NR) algorithm.

2.1.2 A Newton-Raphson-based strategy for Johnson-Cook model integration

Previous section enabled to transform trial stress correction problem into a scalar root research of a non-linear function (Equation 2.10). However, its direct resolution with a NR based approach is

clearly unstable for JC constitutive model. Indeed, as the direction of research is proportional to the derivative $\frac{\partial \sigma_y}{\partial \Delta p}$, the latter has to be defined for admissible values of Δp, *i.e.*, on $\mathbb{R}^+$. Yet, one can demonstrate that for JC flow rule at room temperature, $\frac{\partial \sigma_y}{\partial \Delta p} = \alpha + \frac{\beta}{\Delta p}$, $(\alpha, \beta) \in \mathbb{R}^2$, so that the function is not finite if $\Delta p \to 0$. Therefore, the resolution may be strongly unstable, notably when plastic strain increment Δp is small.

Finally, gradient-based methods like NR algorithm cannot be applied for the initial JC flow rule. One solution may be to use a finite difference to approximate the derivative (secant method) as done in [117], but this drastically harms rate of convergence (which is linear and quadratic for secant and NR methods respectively). Here, we introduce a bijective change of variable (Equation 2.12), so that $\Delta p_{k+1} = e^z$. For convenience, the new function $\tilde{f}$ which is analysed is such as $\tilde{f}(z) = -f(\Delta p_{k+1})$.

$$\begin{array}{rccc} \phi : & \mathbb{R}_+^* & \longrightarrow & \mathbb{R}_+^* \\ & \Delta p_{k+1} & \longrightarrow & z = \ln(\Delta p_{k+1}) \end{array} \tag{2.12}$$

Then, one has to solve:

$$\boxed{\tilde{f}(z) = 3\mu e^z + \tilde{\sigma}_y^{k+1}(z) - \sigma_{eq}(\underline{\underline{\sigma}}_{k+1}^{trial}) = 0} \tag{2.13}$$

Like Simo et Hughes [30], a NR-based strategy can hence be applied, *i.e.*, the unknown z is iteratively updated until convergence (Equation 2.14). As the problem is well-posed (one can demonstrate that $\forall z \in \mathbb{R}, \frac{d\tilde{f}}{dz}(z) > 0$), number of iterations is finite and small thanks to quadratic rate of convergence.

$$z^{(n+1)} = z^{(n)} - \frac{\tilde{f}(z^{(n)})}{\frac{d\tilde{f}}{dz}(z^{(n)})} \quad \text{where} \quad \left| \begin{array}{l} \tilde{f}(z) = 3\mu e^z + \tilde{\sigma}_y^{k+1}(z) - \sigma_{eq}(\underline{\underline{\sigma}}_{k+1}^{trial}) \\ \\ \dfrac{d\tilde{f}}{dz}(z) = 3\mu e^z + \dfrac{d\tilde{\sigma}_y^{k+1}}{dz}(z) \end{array} \right. \tag{2.14}$$

In practice, JC flow rule expression is only used when computing $\tilde{\sigma}_y^{k+1}(z)$ and $\frac{d\tilde{\sigma}_y^{k+1}}{dz}(z)$:

If $z \leq \ln(\dot{\varepsilon}_{eq,0}^{vp} \Delta t_{k+1})$:

$$\left| \begin{array}{l} \tilde{\sigma}_y^{k+1}(z) = \sigma_0 + K(p_k + e^z)^n \\ \\ \dfrac{d\tilde{\sigma}_y^{k+1}}{dz}(z) = ne^z K(p_k + e^z)^{n-1} \end{array} \right. \tag{2.15}$$

If $z > \ln(\dot{\varepsilon}_{eq,0}^{vp} \Delta t_{k+1})$:

$$\left| \begin{array}{l} \tilde{\sigma}_y^{k+1}(z) = \left[\sigma_0 + K(p_k + e^z)^n\right] \left\{1 + M\left[z - \ln\left(\dot{\varepsilon}_{eq,0}^{vp} \Delta t_{k+1}\right)\right]\right\} \\ \\ \dfrac{d\tilde{\sigma}_y^{k+1}}{dz}(z) = \left[ne^z K(p_k + e^z)^{n-1}\right] \left\{1 + M\left[z - \ln\left(\dot{\varepsilon}_{eq,0}^{vp} \Delta t_{k+1}\right)\right]\right\} + M\left[\sigma_0 + K(p_k + e^z)^n\right] \end{array} \right. \tag{2.16}$$

Finally, the NR-based Return Mapping Algorithm (RMA) is implemented in Python® (Table 2.1). Note that as the RMA is used for the VFM on thin-plate specimens, the user can choose to use plane-stress hypothesis to retrieve through-thickness strain component ε_{zz}. Indeed, its elastic part is

calculated enforcing plane stress state in Hooke's law (Equation 2.17). Then, its (visco)plastic part is directly updated owing the return mapping correction. Indeed, the condition of incompressible isotropic mechanical behaviour - *i.e.*, $\mathrm{Tr}[\underline{\underline{\varepsilon}}^{vp}] = 0$ - provides an explicit relation (Equation 2.18).

$$\varepsilon^{e}_{zz} = \frac{\nu}{\nu - 1}\left[\varepsilon^{e}_{xx} + \varepsilon^{e}_{yy}\right] \tag{2.17}$$

$$\varepsilon^{vp}_{zz} = -\left[\varepsilon^{vp}_{xx} + \varepsilon^{vp}_{yy}\right] \tag{2.18}$$

2.1.3 Validation on virtual tests

To validate the RMA implementation, a 4-element square patch test has been loaded with various load paths with Europlexus® [118], which is an FE explicit solver developed by the "Commissariat à l'Énergie Atomique et aux énergies alternatives" (CEA), the Joint Research Centre (JRC) and ONERA. A JC model drives the material behaviour. The reference values of material constants (Table 2.2) have been obtained with a statically determinate approach [6]. As JC model implementation in Europlexus have been thoroughly validated [117], FE data will be considered as reference values. The square-shaped patch test is of 10 mm length. Several load paths are modelled: uniaxial tension, uniaxial tension-compression, shear, and biaxial tension. Elements are loaded at strain-rate $\dot{\varepsilon} \in \{ 1, 100, 1000 \}$ s^{-1} to span a wide range of strain-rate and so that slowest tests will only activate JC model "static" part.

2.1.3.1 FEA model

Each patch test is build with bilinear bidimensional continuum elements, fully integrated (4 Gauss points). Displacement-based loading conditions are imposed during the time t_0. Their amplitudes are obtained by integrating a normalized velocity signal $\phi(\tilde{t})$ (Figure 2.2), with $\tilde{t} \in [0, 1]$. Then, displacement is so that $u_i(t/t_0) = \int v_i(t/t_0)dt = v_0 \int \phi_i(t/t_0)dt$ where i depends on the loading, v_0 drives the strain-rate and t_0 drives strain levels maxima. Table 2.3 collects the different test cases with parameters values to obtain boundary conditions plotted in Figure 2.2.

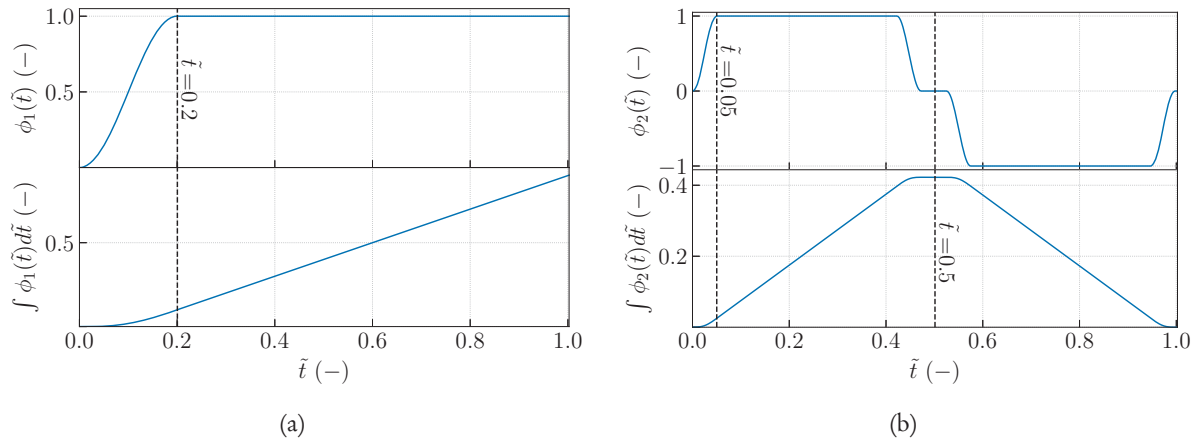

Figure 2.2: Normalized signals for displacement-based boundary conditions: (a) monotonous load (ϕ_1) - (b) cyclic load (ϕ_2)

For post-processing, output mechanical quantities are recorded for all time steps, excepting for "quasi-static" tests. Indeed, FE simulation of low velocity loading with an explicit code requires tiny time increments, whereas in our test cases, a high level of strain (30%) is targeted. Therefore, the chosen sampling of output quantities if $\dot{\varepsilon} = 1$ s^{-1} (1/100) is likely to introduce an additional bias, contrary to one when $\dot{\varepsilon} \in \{ 100, 1000 \}$ s^{-1} (1/1) because in the first case, strain increments input in the RMA are different from FEA ones.

Table 2.1: Return Mapping Algorithm (RMA) for J_2-(visco)plasticity framework

Inputs:
$\underline{\underline{\varepsilon}}_{k+1}$, variables at increment k, material parameters, problem dimension DIM
Maximum number of iterations n_{MAX}, convergence tolerance ϵ.
Outputs:
Variables at increment $k+1$.

Computation of elastic trial step: $\underline{\underline{\sigma}}^{trial}_{k+1} = 2\mu(\underline{\underline{\varepsilon}}_{k+1} - \underline{\underline{\varepsilon}}^{vp}_{k}) + \lambda \mathrm{Tr}(\underline{\underline{\varepsilon}}_{k+1})\underline{\underline{I}}, \qquad f^{trial}_{k+1} = \sigma_{eq}(\underline{\underline{\sigma}}^{trial}_{k+1}) - \underline{\underline{\sigma}}^{k}_{y}$
If $f^{trial}_{k+1} \leq 0$ **Then:**
  Elastic evolution: updated quantities at increment $k+1$ are equal to trial test quantities.
  If DIM = 2 Then:
    $\varepsilon_{zz,k+1} = \frac{\nu}{\nu-1}\left[\varepsilon^{e,k+1}_{xx} + \varepsilon^{e,k+1}_{yy}\right] - \left[\varepsilon^{vp,k}_{xx} + \varepsilon^{vp,k}_{yy}\right]$
  End If.
Else:
  # Plastic increment computation: trial stress state relaxation
  $z^{(0)} = 0$
  Do:
    $$z^{(n)} \leftarrow z^{(n-1)} - \frac{3\mu e^{z^{(n-1)}} + \tilde{\sigma}^{k+1}_{y}(z^{(n-1)}) - \sigma_{eq}(\underline{\underline{\sigma}}^{trial}_{k+1})}{3\mu e^{z^{(n-1)}} + \frac{d\tilde{\sigma}^{k+1}_{y}}{dz}(z^{(n-1)})}$$
    If $n = n_{MAX}$ **Or** $|z^{(n)} - z^{(n-1)}| \leq \epsilon$ **Then:**
      $\Delta p_{k+1} = \exp[z^{(n)}]$
      $\sigma^{k+1}_{y} = \tilde{\sigma}^{k+1}_{y}(z^{(n)})$
      Stop.
    End If.
  End Do.
  $$\Delta\underline{\underline{\varepsilon}}^{vp}_{k+1} = \frac{3}{2}\Delta p_{k+1}\frac{\underline{\underline{S}}^{trial}_{k+1}}{\sigma_{eq}(\underline{\underline{\sigma}}^{trial}_{k+1})}$$
  $p_{k+1} = p_k + \Delta p_{k+1}$
  $$\dot{\varepsilon}^{vp}_{eq,k+1} = \frac{\Delta p_{k+1}}{\Delta t_{k+1}}$$
  # New stress state computation
  $\underline{\underline{\sigma}}_{k+1} = \underline{\underline{\sigma}}^{trial}_{k+1} - 2\mu\Delta\underline{\underline{\varepsilon}}^{vp}_{k+1}$
  If $\sigma_{eq}(\underline{\underline{\sigma}}_{k+1}) - \sigma^{k+1}_{y} \neq 0$ **Then:**
    $$\underline{\underline{\sigma}}_{k+1} \leftarrow \frac{\sigma^{k+1}_{y}}{\sigma_{eq}(\underline{\underline{\sigma}}^{k+1})}\underline{\underline{\sigma}}_{k+1}$$
  End If.
  $\underline{\underline{\varepsilon}}^{vp}_{k+1} = \underline{\underline{\varepsilon}}^{vp}_{k} + \Delta\underline{\underline{\varepsilon}}^{vp}_{k+1}$
  $\underline{\underline{\varepsilon}}^{e}_{k+1} = \underline{\underline{\varepsilon}}_{k+1} - \underline{\underline{\varepsilon}}^{vp}_{k+1}$
  If DIM = 2 Then:
    $\varepsilon_{zz,k+1} = \frac{\nu}{\nu-1}\left[\varepsilon^{e,k+1}_{xx} + \varepsilon^{e,k+1}_{yy}\right] - \left[\varepsilon^{vp,k+1}_{xx} + \varepsilon^{vp,k+1}_{yy}\right]$
  End If.
End If.

2.1.3.2 Analysis and validation

To assess RMA robustness, relevant mechanical quantities are plotted for tension (Figure 2.4), tension/compression (Figure A.1), shear (Figure A.2) and biaxial loading (Figure A.3): a strain/stress

Table 2.2: Ti6Al4V material constants for the Johnson-Cook's model [6]

Material constant	**Value**
Young modulus, E (MPa)	114 000
Poisson ratio, ν (-)	0.34
Initial yield stress, σ_0 (MPa)	973
Isotropic hardening modulus, K (MPa)	557
Isotropic hardening exponent, n (-)	0.563
Viscoplastic parameter, M (-)	0.033
Equivalent strain-rate threshold, $\dot{\varepsilon}^p_{eq,0}$ (s^{-1})	1.29

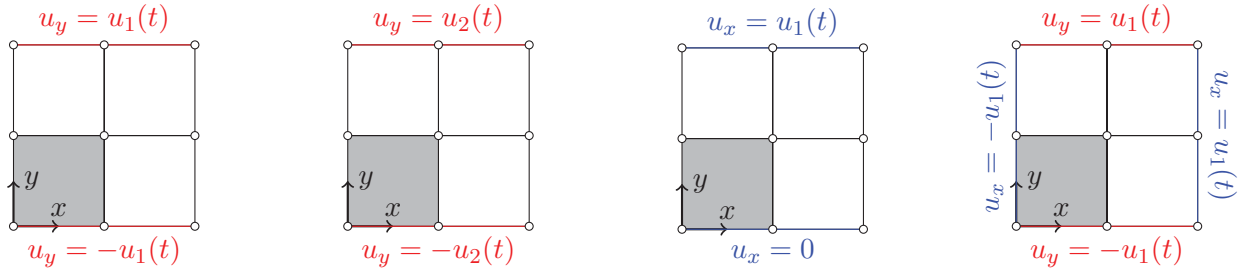

In grey: Post-processed element

Figure 2.3: Displacement-based boundary conditions: (a) - tension (b) - tension-compression (c) - shear (d) - biaxial

Table 2.3: Virtual tests loading conditions

Test n^o	Loading(*)				v_0 (m.s^{-1})			t_0 (ms)			$\dot{\varepsilon}$ (s^{-1})		
	T	TC	Sh	B	0.01	1	10	0.2	2	200	1	100	1000
1	✓				✓					✓	✓		
2		✓			✓					✓	✓		
3			✓		✓					✓	✓		
4				✓	✓					✓	✓		
5	✓					✓			✓			✓	
6		✓				✓			✓			✓	
7			✓			✓			✓			✓	
8				✓		✓			✓			✓	
9	✓						✓	✓					✓
10		✓					✓	✓					✓
11			✓				✓	✓					✓
12				✓			✓	✓					✓

(*) T: tension - TC: tension-compression - Sh: shear - B: biaxial

curve of the most relevant strain/stress component, flow stress σ_y vs cumulated plastic strain p, and cumulated plastic strain rate $\dot{p}$ vs cumulated plastic strain p. Note that curve data are obtained from a Gauss point of highlighted element in Figure 2.3.

Globally, the RMA computes mechanical quantities with a very good accuracy, whichever the boundary conditions and the load velocity. The only observable gaps "with the naked eye" concern quasi-static loading. However, this was expected because strain fields are already sub-sampled (every 100th FE time step) owing to the huge number of small strain increments, contrary to tests at higher velocities for which RMA strain increments equal FEA strain increments. Finally, discrepancies already exist because of high sensitivity of "quasi-static" explicit simulations w.r.t. time increments. To validate those observations, mean relative gaps have also been plotted (Figure 2.5). Those charts show that

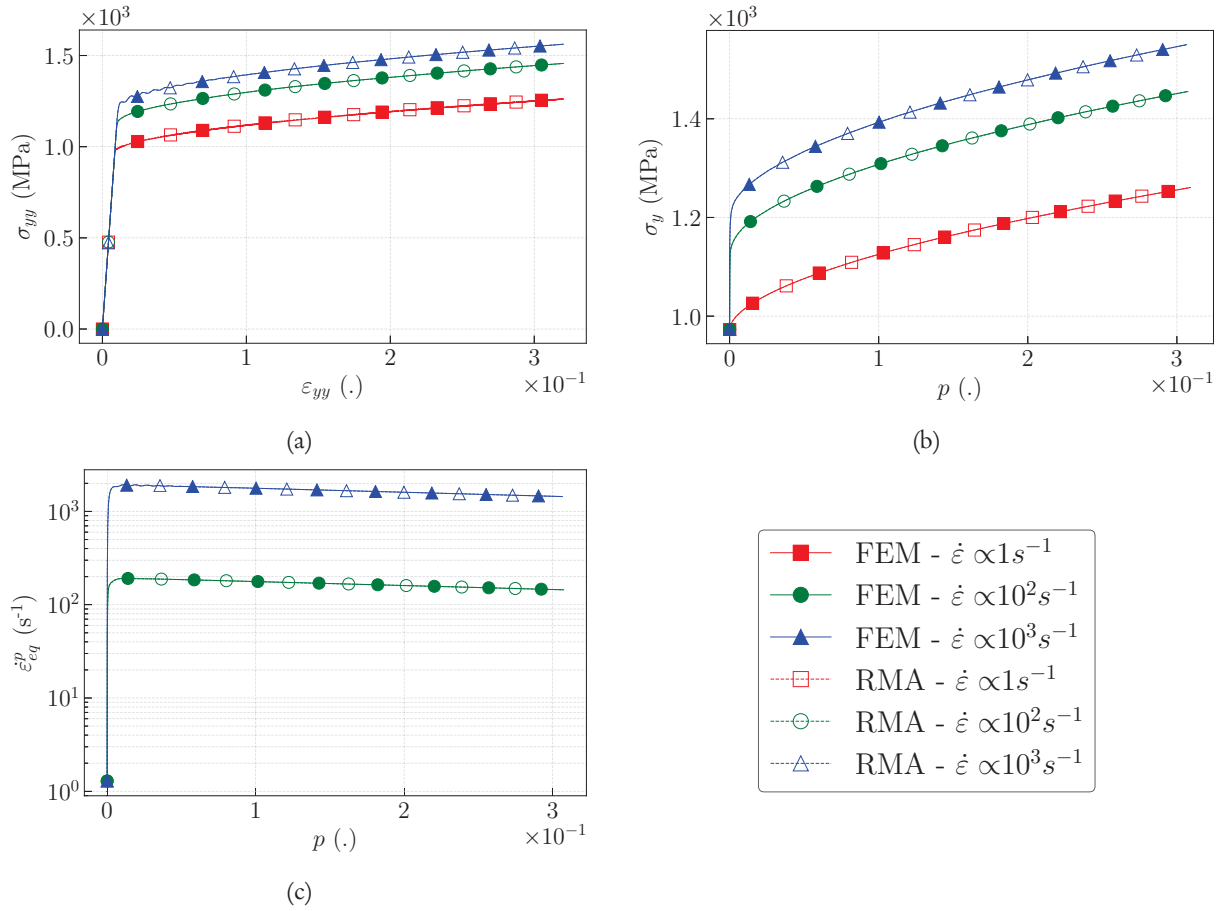

Figure 2.4: Virtual tensile tests results - (a) σ_{yy} / ε_{yy} - (b) σ_y vs p - (c) $\dot{p}$ vs p

in all cases, gaps are lower than 1%. As seen previously, slightly higher gaps can be computed for quasi-static tests.

In order to assess the algorithm robustness, the RMA has also be input with strain fields which were highly sub-sampled (one point over five of FEA strain data). Then, offsets are observed between yield stress curves, in particular for tension/compression virtual tests during transient phases of the loading (Figure 2.6). Therefore, longitudinal stress fields are constantly overestimated in this case (Figure 2.6), especially when $\dot{\varepsilon} = 1000\ s^{-1}$. Those remarks are confirmed by the evolution of mean relative gaps (Figure A.4) which have increased compared to the initial sampling. Even if gaps are amplified at high strain rate, the results remains consistent with initial data.

2.1.4 Conclusion

This section presents a NR-based RMA to compute stress fields using JC model constitutive equations and strain fields. The available work [6, 116] has been successfully updated. Indeed, the new algorithm incorporates a NR loop to compute plastic strain p, so that for the (visco)plastic problem, rate of convergence drastically increases (quadratic vs linear without harming the robustness owing to a change of variable).

To validate RMA implementation, a virtual test campaign has been performed. Inputting the algorithm with strain fields leads to very accurate results if time increments match with ones of FE simulations. Otherwise, discrepancies between FEA and RMA fields increase with strain sub-sampling but results remain consistent. However, this has to be carefully taken into account when stress field will be reconstructed with experimental data which is often "sub-sampled" due to experimental constraints (*i.e.*, camera frame rate).

From now on, the numerical toolbox for the dynamic VFM incorporates a routine to compute

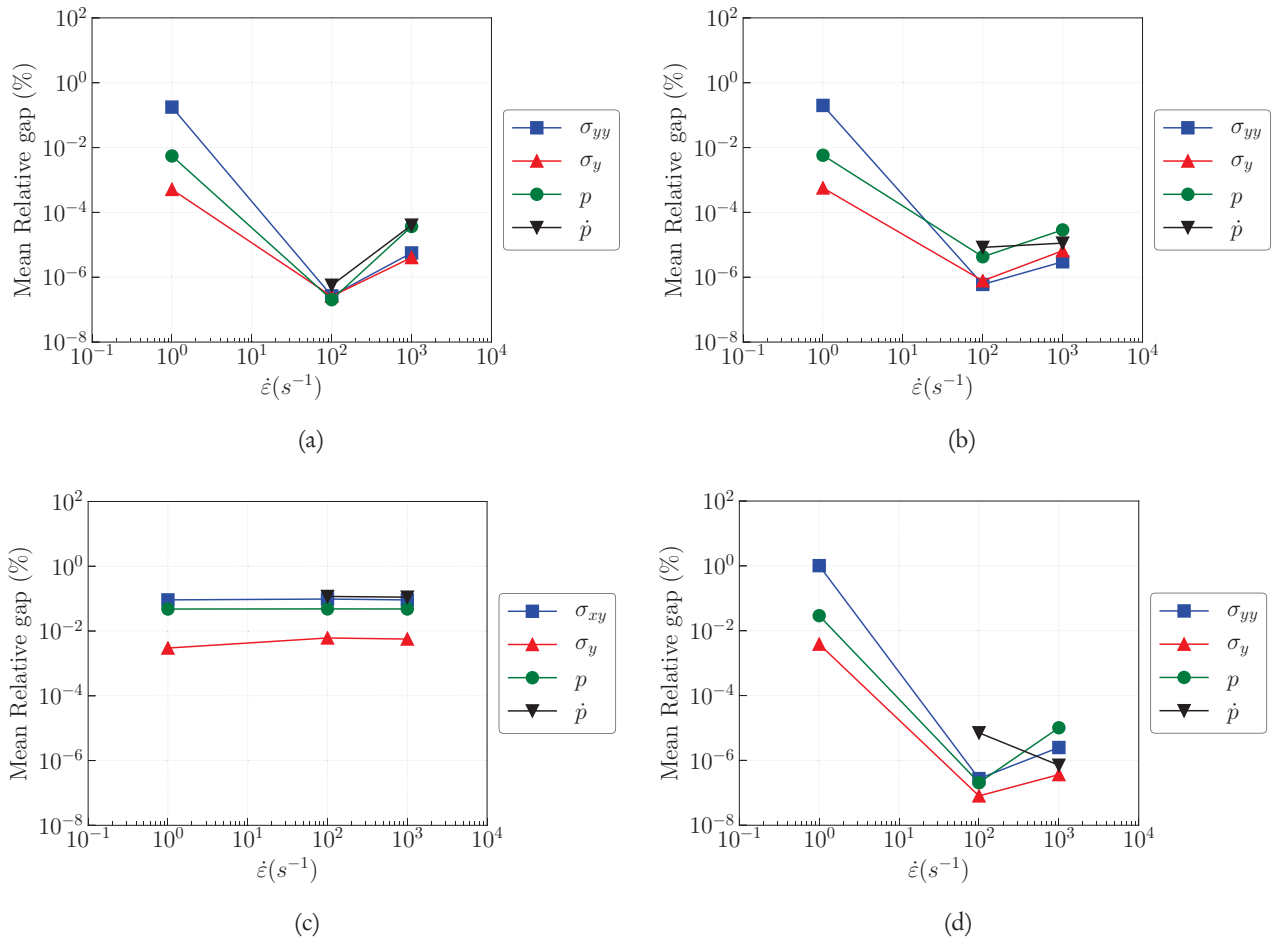

Figure 2.5: RMA/FEA comparison: Mean relative gap - (a) uniaxial tension - (b) uniaxial tension/compression - (c) shear - (d) biaxial tension

stress fields to calculate W_{int}^* in the PVW. This will enable the extraction of material constitutive parameters from IBII tests if one has access to strains and accelerations (cf. Chapter 1). In practice, the latter are extracted owing to full-field measurement technique. The next section presents the methodology implemented to extract strain and acceleration fields with the grid method.

2.2 The grid method: from greyscale images to strain and acceleration fields

In Section 1.3, the main principles of the grid method have been recalled. Among available techniques for full-field measurements, the latter allows to reach a good compromise between spatial resolution and displacement resolution, that favours a better tracking of strongly heterogeneous kinematic fields when using low resolution cameras [69].

Therefore, up to the computation of displacements, the classical methodologies described in [65, 69] have been implemented in our toolbox. As introduced in Section 1.3.1.2, Local Spectrum Analysis (LSA) is performed through a Windowed Discrete Fourier Transform (WDFT) (Equation 1.17) to extract grid modulations. Then, an iterative approach (Equation 1.16) enables the extraction of displacement fields. Note that for the WDFT, a bi-triangular window has been implemented instead of a Gaussian one. The latter is more suitable for Ultra High-Spped (UHS) imaging since the Gaussian window has to span more grid pitches to be efficient, *i.e.*, "isolate" as much as possible phase modulation in the Fourier spectrum of a greyscale image [119]. Then, its use may jeopardize the VFM

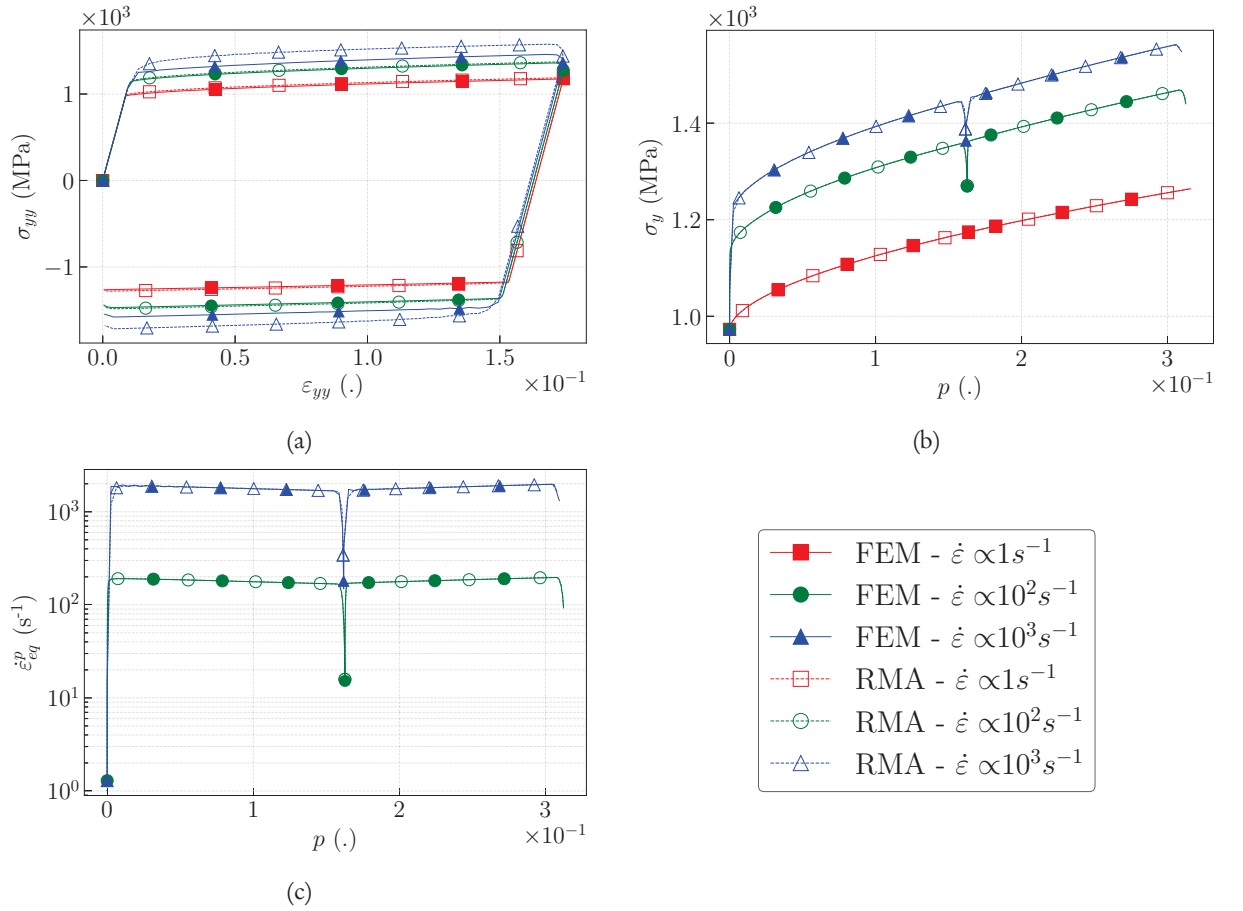

Figure 2.6: Virtual tension/compression tests results (with subsampling) - (a) σ_{yy} / ε_{yy} - (b) σ_y vs p - (c) $\dot{p}$ vs p

because owing to the low number of pixels of UHS cameras (*e.g.*, 400×250 pixels for the Shimadzu HPV-X), the WDFT performed at the edges of the ROI provides a larger amount of corrupted data which is therefore lost. However, the bi-triangular window is less efficient at noise cancelling [119]. This is highly critical because displacements maps have to be differentiated to compute strains and accelerations, which can amplify impact of noise. Finally, it is then crucial to implement a methodology suitable to extract strain and acceleration fields in a noisy environment.

Among the available literature, Savitzky-Golay (SG) filters [120] might be one of the most used to smooth signals or compute derivatives of noisy signals. Indeed, they enable low pass filtering of displacement fields and derivative calculations simultaneously. SG filters belong to a class of filters which may be applied through data convolution if points are equally spaced. Then, n-order differential of a quantity ψ along a variable s is based on a centered stencil of neighbouring points (*i.e.*, a weighted sum of discrete values of ψ). Finally $\frac{\partial^n \psi}{\partial s^n}$ is such as Equation 2.19, where N_p is a user-defined parameter driving the stencil size, Δs the spacing and a_i ($i \in \mathbb{Z}$) the weighting coefficients. For SG filters, coefficients a_i are the analytic solution of a least-square problem, where the smoothed signal is locally fitted with a low-order polynomial [120]. Then, the filter is designed in the temporal domain, this might be a disadvantage when one wants to give a "physical sense" to the regularization.

$$\left.\frac{\partial^n \psi}{\partial s^n}\right|_m = \frac{1}{\Delta s^n}\left[a_m \psi_m + \sum_{i=1}^{N_p} a_{m-i}\psi_{m-i} + (-1)^n a_{m+i}\psi_{m+i}\right] \tag{2.19}$$

By contrast, Smooth Noise-Robust (SNR) differentiators [121] belong to the same class but they are designed in the frequency domain. Indeed, coefficients a_i are computed zeroing tangent values of the magnitude response of the filter at high frequencies [121]. Therefore, their magnitude response

$|H(\omega)|$ (Figure 2.7) is null for high angles (*i.e.*, high frequencies in the Fourier domain) contrary to SG filters for which magnitude response has some undulations at high frequencies (Figure 2.7), this may lead to oscillations in the filtered signal.

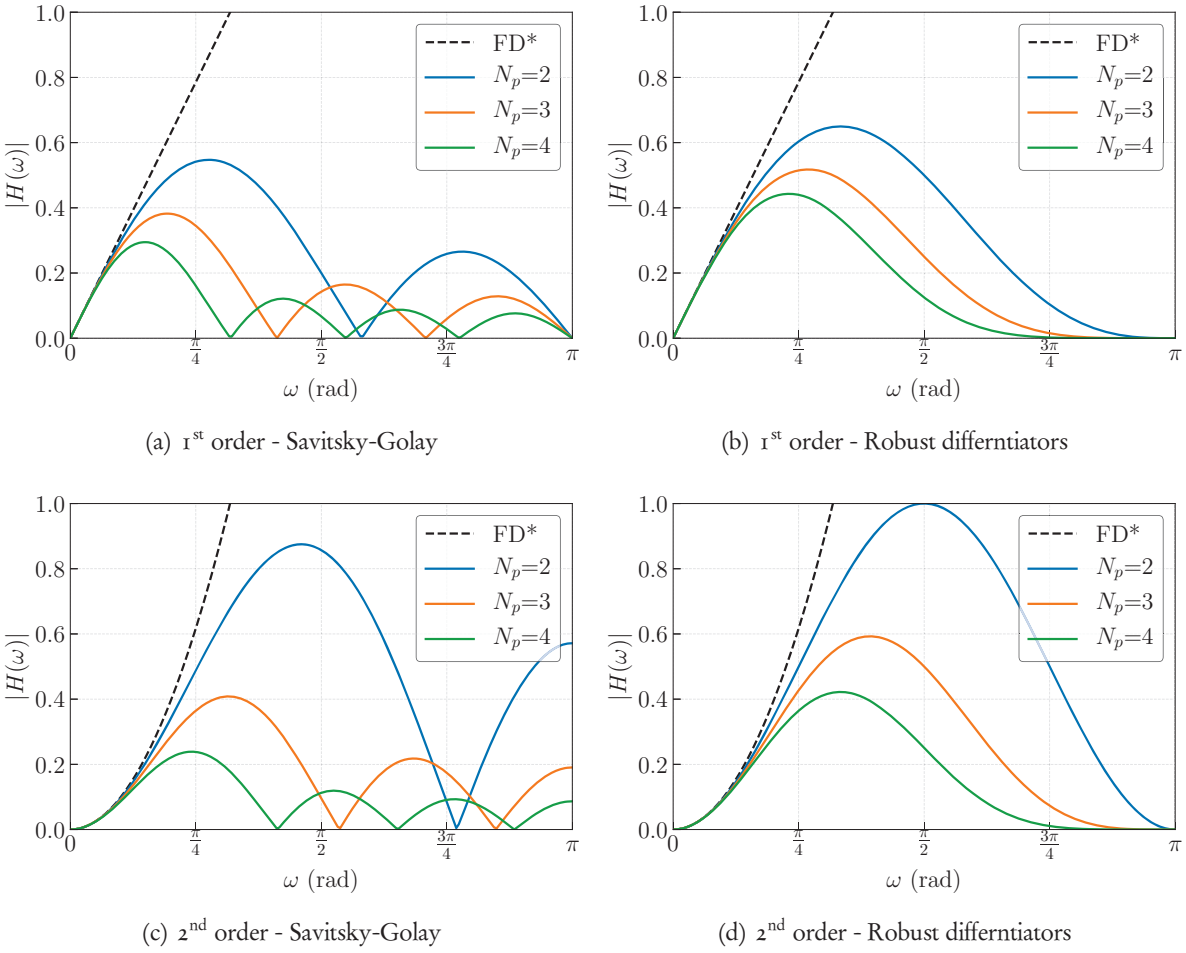

(a) 1st order - Savitsky-Golay

(b) 1st order - Robust differntiators

(c) 2nd order - Savitsky-Golay

(d) 2nd order - Robust differntiators

(*) FD: central Finite Difference ($N_p = 1$)

Figure 2.7: SG differentiators and SNR differentiators in the Fourier domain for different values of N_p

In practice, a 2nd-order time SNR differentiator is implemented to compute acceleration fields from displacement maps $\underline{u}(t)$, and strain maps are extracted owing to a 1st-order one applied to same displacement maps $\underline{u}(t)$ (Table 2.4), so that the kinematic fields are known for each measurement point for all stages of the recorded time during testing. More details about the coefficients definition can be found in the literature [121]. Finally, stencil sizes N_{p1} and N_{p2} (for strain and acceleration fields respectively) will be referred as the regularization parameters, as the "smoothness" is driven by their value (Figure 2.7). Thus, their tuning has to be taken into account in the VFM process. The whole procedure is reported in Figure 2.8.

To conclude, this section presents the methodology implemented to deduce strain and acceleration maps from greyscale images using the grid method. Whereas the LSA leads to the extraction of displacement fields, SNR differentiators are implemented to compute $\underline{\underline{\varepsilon}}$ and $\underline{\gamma}$. Finally, their combination with the Return Mapping Algorithm presented in Section 2.1 provide a toolchain to compute all terms of the PVW in the VFM process for given constitutive parameters and a set of images.

Yet, the influence of the aforementioned toolchain parameters has to be assessed thoroughly during the design process. For instance, strain and acceleration maps can be very sensitive to the set of SNR parameters (N_{p1},N_{p2}). An in-depth analysis on that will be performed here thanks to FE-based virtual

Table 2.4: SNR formulæ for strain and acceleration extraction - (a): strain $\underline{\underline{\varepsilon}}$ (b): acceleration $\underline{\gamma}$

Formulæ	$\forall s \in \{x, y\}, \quad \left.\frac{\partial \underline{u}}{\partial s}\right\|_m = \frac{1}{\Delta s}\left[a_m \underline{u}_m + \sum_{i=1}^{N_{p1}} a_{m-i}\underline{u}_{m-i} - a_{m+i}\underline{u}_{m+i}\right]$
Coefficients $(a_i)_{i\in\mathbb{Z}}$	$\frac{1}{2^{2N_{p1}-1}}\left[\binom{2(N_{p1}-1)}{N_{p1}-i} - \binom{2(N_{p1}-1)}{N_{p1}-i-2}\right]$

(a)

Formula	$\left.\frac{\partial^2 \underline{u}}{\partial t^2}\right\|_m = \frac{1}{\Delta t^2}\left[a_m \underline{u}_m + \sum_{i=1}^{N_{p2}} a_{m-i}\underline{u}_{m-i} + a_{m+i}\underline{u}_{m+i}\right]$
Coefficients $(a_i)_{i\in\mathbb{Z}}$	$\begin{cases} 0 & \text{if } i > 2N_{p2}+1 \\ 1 & \text{if } i = 2N_{p2}+1 \\ \frac{1}{2^{2N_{p2}-1}(N_{p2}-i)}\left[2(N_{p2}-2)a_{i+1} - (N_{p2}-i-2)a_{i+2}\right] & \text{otherwise} \end{cases}$

(b)

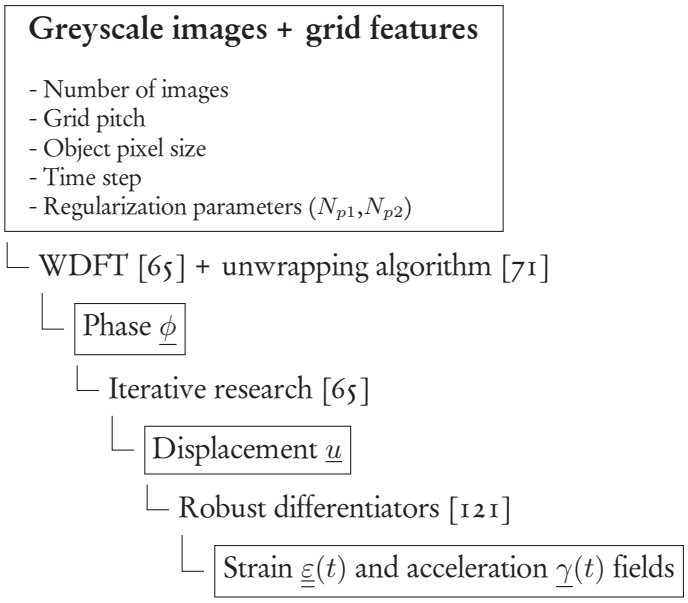

Figure 2.8: Toolchain procedure for strain and acceleration fields extraction from greyscale images

tests. Other parameters which are directly linked to the IBII test configurations itself also will be analysed thoroughly (*e.g.*, specimen and projectile geometry, projectile velocity) in Chapter 3. However, this use of IBII tests virtual data for design optimization requires reliable FE simulations. In other words, one needs to generate and process reliable FE data in quick succession. The toolchain which has been implemented to handle this task is presented in the next section.

2.3 A FE-based procedure to generate and process reliable simulated test configurations

The numerical assessment of IBII test configurations involves a simulation through FEA. To guarantee the generation of realistic virtual tests in quick succession, one needs to develop a numerical toolchain taking into account as much test conditions as possible, as the analysis of in-plane full-field measurements on the specimen skin for instance. This section presents the implemented methodology and the tools to evaluate the "reliability" of each simulation.

2.3.1 On the use of Cast3M® and Europlexus® for FEA of IBII tests

In this work, FEA is performed owing to two research codes: Cast3M [122], which is an object-oriented FE software developed by the CEA and Europlexus, a computer program for FE simulation of fluid/structure systems under transient dynamic loading [118]. For both codes, a dataset is produced through command lines, that favour scripting. Therefore, a Python® toolchain has been developed to handle the whole FEA toolchain, from the FE model inputs (specimen and projectile features, material parameters,...) to the results.

A Cast3M script (Appendix A) has been implemented to generate 8-node brick elements meshes for simulated IBII tests. Firstly, a projectile (radius R_p and length L_p) is generated. Then, the specimen is built from a thin solid plate (external length L_s, width D_s and thickness H_s) which may be perforated to generate several geometric singularities. The implemented script enables the incorporation of circular holes and/or notches at any position. Figure 2.9 illustrates the different steps needed for specimen generation.

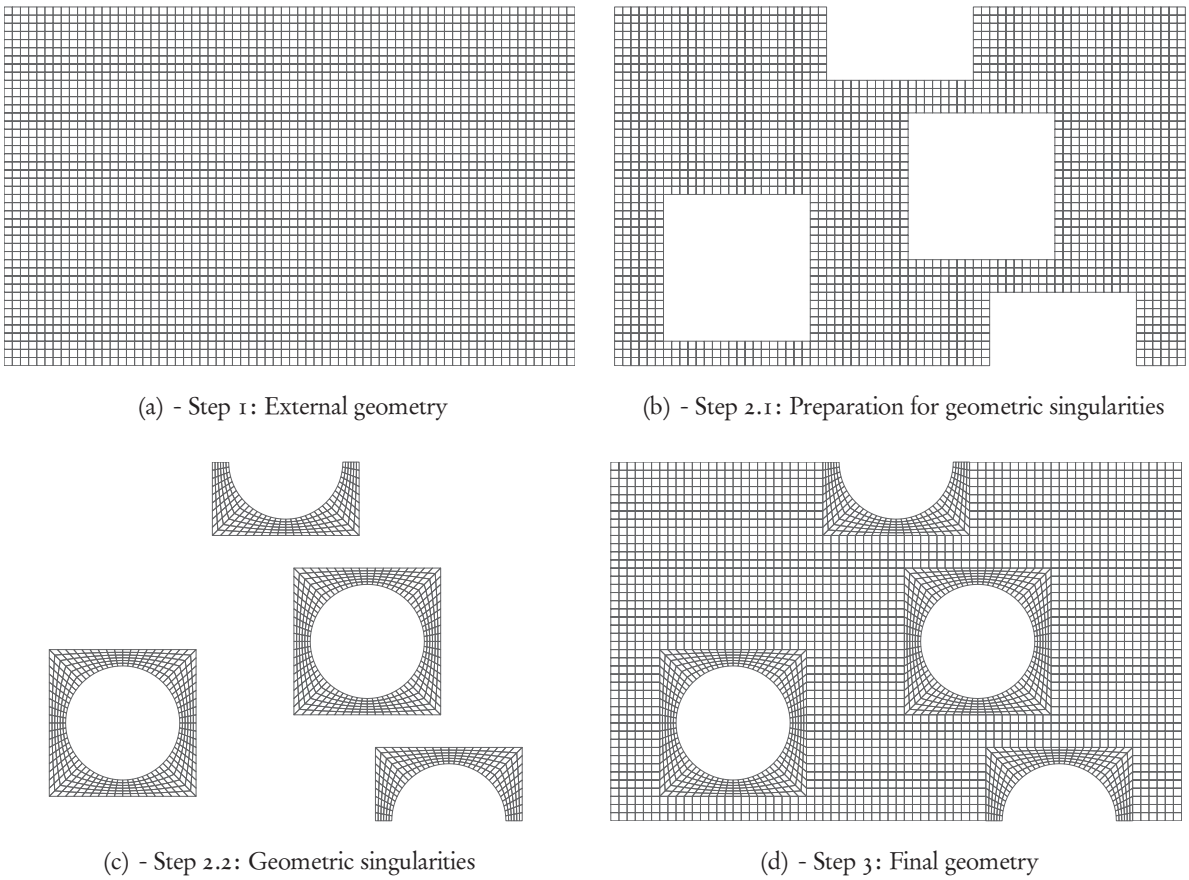

(a) - Step 1: External geometry

(b) - Step 2.1: Preparation for geometric singularities

(c) - Step 2.2: Geometric singularities

(d) - Step 3: Final geometry

Figure 2.9: Incorporation of geometric singularities in the specimen FE model- Nominal mesh size: 1.5mm

Finally, a FE mesh as in Figure 2.10 is obtained. The distance between the projectile and the specimen is tuned according to impact velocity. It is worth noticing that in addition to geometrical features, the script involves other parameters related to mesh properties such as its refinement near singularities or the projectile section meshing.

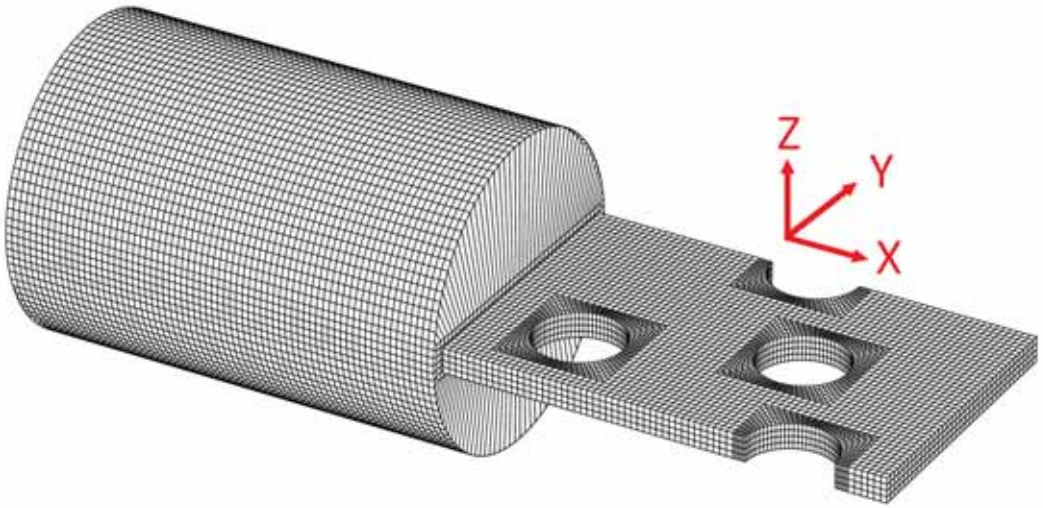

Figure 2.10: Example of a 3D mesh (projectile and specimen)

Once the mesh is generated, FEA is carried out with Europlexus® with JC viscoplastic model. Elements are fully integrated, time step is constant and no artificial damping is incorporated. As for boundary conditions, an initial velocity is imposed to the projectile. Its contact with the specimen is managed by a Pinball algorithm, which enables the robust simulation of contacts [118, 123–125].

In experimental VFM process, in-plane full-field measurements techniques provide displacement fields on the specimen surface only. Then, to perform consistent simulations, kinematic and mechanical fields from FEA are also extracted from specimen surface. More precisely, the specimen upper elements (grey elements in Figure 2.11) and upper skin (grey edges in Figure 2.11) are extracted to reconstruct a 4-node 2D mesh (denoted later on as skin mesh).

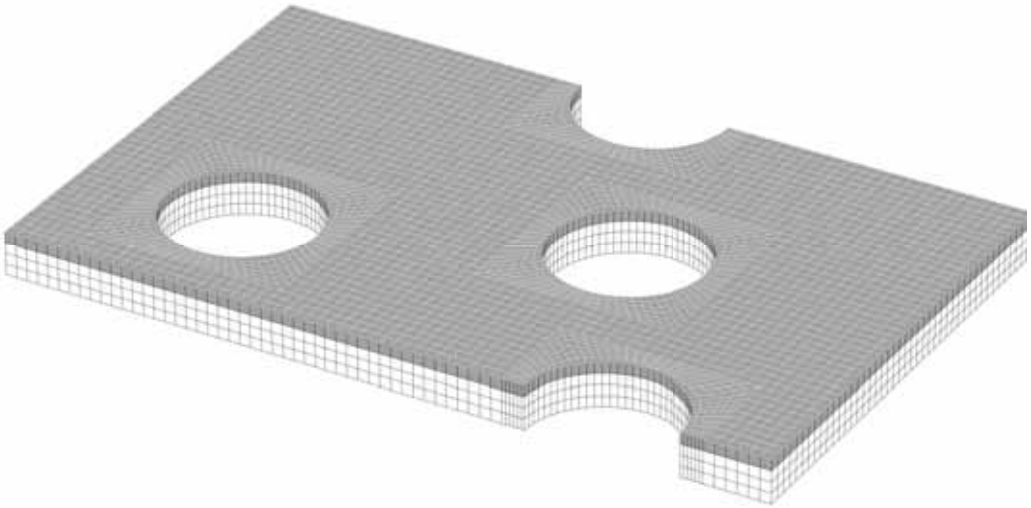

Figure 2.11: Mesh processed during IBII tests analysis

2.3.2 FEA post-processing

FEA lead to the prediction of kinematic fields on the skin mesh (coordinates, velocities and accelerations) and mechanical fields (*e.g.*, strains, stresses) on Gauss points of elements in upper layer. To mimic a metrological toolchain which provides experimental data on a specimen upper layer, the aforementioned fields are projected onto the 4-node elements of the skin mesh. Then, any projected data will be considered as constant over each element, by analogy with DIC facets for instance. The choice of the projection method have been notably driven by the computational accuracy. Indeed, one has to limit additional errors as much as possible, aside from FEA discretization.

2.3.2.1 Projection of node-related kinematic fields on elements

For a given node-related field, the mean value on a M-node element can be computed accurately. Indeed, shape functions enable the averaging owing to an integration (Equation 2.20) on the deformed element (Figure 2.12(b)).

$$\overline{\theta} = \frac{1}{S}\int_S \sum_i^M \theta_i N_i(x,y)dxdy \tag{2.20}$$

where N_i is the i-th shape function of node P_i in the element, S the element area, and $\overline{\theta}$ the mean value over the element.

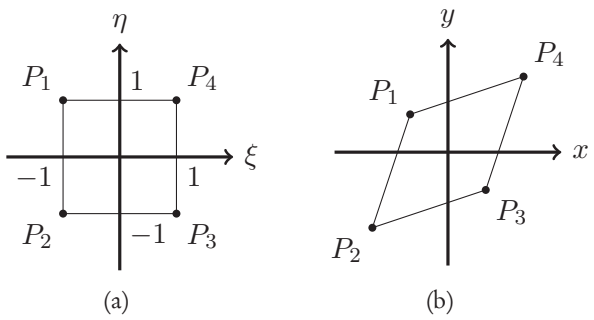

Figure 2.12: Notation conventions for isoparametric/deformed element - (a) Isoparameteric element - (b) Deformed element

Using Gaussian quadrature, Equation 2.20 can be computed very rapidly for any element type. Here, an exact expression is proposed for the 4-node element which is used in skin meshes of IBII tests, thus avoiding any additional bias.

Assuming the deformed element of Figure 2.12(b), the mean value $\overline{\theta}$ is such as Equation 2.21. To compute the integrals, the so-called isoparameteric coordinates are used. Then, shape functions are given by Equation 2.22.

$$\overline{\theta} = \frac{\int_S \sum_i \theta_i N_i(x,y)dxdy}{\int_S dxdy} \tag{2.21}$$

$$\left|\begin{array}{lcl} N_1(\xi,\eta) & = & \frac{1}{4}(1-\xi)(1+\eta) \\ N_2(\xi,\eta) & = & \frac{1}{4}(1-\xi)(1-\eta) \\ N_3(\xi,\eta) & = & \frac{1}{4}(1+\xi)(1-\eta) \\ N_4(\xi,\eta) & = & \frac{1}{4}(1+\xi)(1+\eta) \end{array}\right. \tag{2.22}$$

Integrals of Equation 2.21 are calculated thanks to the change of variable from the deformed element

(Figure 2.12(b)) to the reference element (Figure 2.12(a)):

$$\overline{\theta} = \frac{\displaystyle\int_S \sum_i \theta_i N_i(\xi,\eta)|J(\xi,\eta)|d\xi d\eta}{\displaystyle\int_S |J(\xi,\eta)|d\xi d\eta} \tag{2.23}$$

$|J(\xi,\eta)|$ can be determined analytically:

$$J(\xi,\eta) = \begin{vmatrix} \displaystyle\sum_i \frac{\partial N_i}{\partial \xi} x_i & \displaystyle\sum_i \frac{\partial N_i}{\partial \xi} y_i \\ \displaystyle\sum_i \frac{\partial N_i}{\partial \eta} x_i & \displaystyle\sum_i \frac{\partial N_i}{\partial \eta} y_i \end{vmatrix} = \boxed{\frac{1}{4}\sum_i \alpha_i N_i(\xi,\eta)} \quad \text{where} \quad \left| \begin{array}{rcl} \alpha_1 &=& \overrightarrow{P_1P_2} \times \overrightarrow{P_1P_4} \\ \alpha_2 &=& \overrightarrow{P_1P_2} \times \overrightarrow{P_2P_3} \\ \alpha_3 &=& \overrightarrow{P_2P_3} \times \overrightarrow{P_3P_4} \\ \alpha_4 &=& \overrightarrow{P_1P_4} \times \overrightarrow{P_3P_4} \end{array} \right. \tag{2.24}$$

Finally, Equation 2.24 can input Equation 2.21 to calculate the integrals:

$$\begin{aligned} \overline{\theta} &= \frac{\displaystyle\int_S \sum_i^M \theta_i N_i(\xi,\eta)|J(\xi,\eta)|d\xi d\eta}{\displaystyle\int_S |J(\xi,\eta)|d\xi d\eta} \\ \Leftrightarrow \quad \overline{\theta} &= \frac{\displaystyle\int_S \sum_i \theta_i N_i(\xi,\eta)\frac{1}{4}\sum_j \alpha_j N_j(\xi,\eta)d\xi d\eta}{\displaystyle\int_S \frac{1}{4}\sum_j \alpha_j N_j(\xi,\eta)d\xi d\eta} \\ \Leftrightarrow \quad \overline{\theta} &= \frac{\displaystyle\sum_{i,j} \theta_i\alpha_j \int_S N_i(\xi,\eta)N_j(\xi,\eta)d\xi d\eta}{\displaystyle\sum_i \alpha_i \underbrace{\int_S N_i(\xi,\eta)d\xi d\eta}_{=1}} \\ \Leftrightarrow \quad \overline{\theta} &= \frac{\displaystyle\sum_{i,j} \alpha_i\theta_j\Phi_{ij}}{\displaystyle\sum_i \alpha_i} \end{aligned} \tag{2.25}$$

where $\Phi_{ij} = \int_S N_i(\xi,\eta)N_j(\xi,\eta)d\xi d\eta$, whose calculation is direct on the isoparametric element. Finally it comes:

$$\boxed{\overline{\theta} = \frac{\sum_{i,j}\alpha_i\theta_j\Phi_{ij}}{\sum_i \alpha_i} = \frac{\underline{A}^T\,\underline{\underline{\Phi}}\,\underline{\Theta}}{\|\underline{A}\|_1}} \tag{2.26}$$

where:

$$\underline{\underline{\Phi}} = \frac{1}{9}\begin{bmatrix} 4 & 2 & 1 & 2 \\ 2 & 4 & 2 & 1 \\ 1 & 2 & 4 & 2 \\ 2 & 1 & 2 & 4 \end{bmatrix} \quad \underline{A} = \begin{bmatrix} \overrightarrow{P_1P_2} \times \overrightarrow{P_1P_4} \\ \overrightarrow{P_1P_2} \times \overrightarrow{P_2P_3} \\ \overrightarrow{P_2P_3} \times \overrightarrow{P_3P_4} \\ \overrightarrow{P_1P_4} \times \overrightarrow{P_3P_4} \end{bmatrix} \quad \underline{\Theta} = \begin{bmatrix} \theta_1 \\ \theta_2 \\ \theta_3 \\ \theta_4 \end{bmatrix}$$

N.B.: Equation 2.26 is equivalent to an arithmetic average if and only if $\forall i \in [\![1,4]\!]$, $\alpha_i = 1$, this corresponding to the case when the deformed element is rectangular (see Equation 2.24).

2.3.2.2 Projection of Gauss-point-related mechanical fields on elements

Any element-related field is projected onto each element by an arithmetical average of N Gauss points values in the element:

$$\overline{\theta} = \frac{1}{N}\sum_{i}^{N}\theta_i \tag{2.27}$$

This is an approximation of the exact mean value insofar as in practice, the integration is based on Gaussian quadrature. However, this may require the tracking of a huge amount of data (*e.g.*, 8 Gauss points for a fully integrated brick element) contrary to a "basic" average which is directly provided by the FE code.

2.3.2.3 Conclusion

This section introduces a methodology (collected in Table 2.5) to obtain FEA kinematic and mechanical quantities on the skin mesh of the impacted specimen. Aside from mesh coordinates, all other quantities are projected onto the 4-node elements of the skin mesh. However, those fields are realistic only if the FE model is reliable, notably from the mesh size point of view. To define the latter, the PVW of VFM process can be used as an objective criteria. This is presented in the following section.

Table 2.5: Formulæ for data projection onto skin mesh

Element-related data	Node-related data
$\overline{\theta} = \frac{1}{N}\sum_{i}\theta_i$	$\overline{\theta} = \frac{\sum_{i,j}\alpha_i\theta_j\Phi_{ij}}{\sum_{i}\alpha_i}$

2.3.3 IBII virtual tests reliability assessment

2.3.3.1 Theoretical aspects

FEA results can notably be driven by the mesh size. To set the latter, the optimal mesh size can be defined in our case as the largest one that enables to respect the PVW when inputing with FE data in VFM process. IBII virtual tests are assessed on the specimen skin mesh (Figure 2.13) and the VFM with plane stress hypothesis.
Using notations of Figure 2.13, the PVW expressed in Equation 1.20 is reduced if the virtual field is such as $\underline{u}^* = (1, 0)$:

$$-\underbrace{\int_S \underline{\underline{\sigma}}(\underline{X}) : \underline{\underline{\varepsilon}}^*\, dS}_{=0} + \underbrace{\int_{\partial S} \underline{t}.\underline{u}^*\, dS}_{\int_{D(x)} \underline{t}_x dl} = \underbrace{\int_S \rho\underline{\gamma}.\underline{u}^*\, dS}_{\int_{S(x)} \rho\underline{\gamma_x}\, dS} \tag{2.28}$$

Assuming a loading wave which is mainly unidirectional, the second integral can be simplified. Then is comes:

$$\left|\begin{array}{lcl} \underbrace{\frac{1}{D(x)}\int_{D(x)} \underline{t}_x dl}_{\overline{\sigma_{xx}(x)}} & = & \frac{1}{D(x)}\int_{S(x)} \rho\gamma_x dS \\ \sigma_{EPX}(x) & = & \sigma_{REC}(x) \end{array}\right. \tag{2.29}$$

This configuration of the dynamic VFM is referred as the non-parametric approach [7] because stress field can be expressed as a function of the acceleration field only. In practice, this equation leads

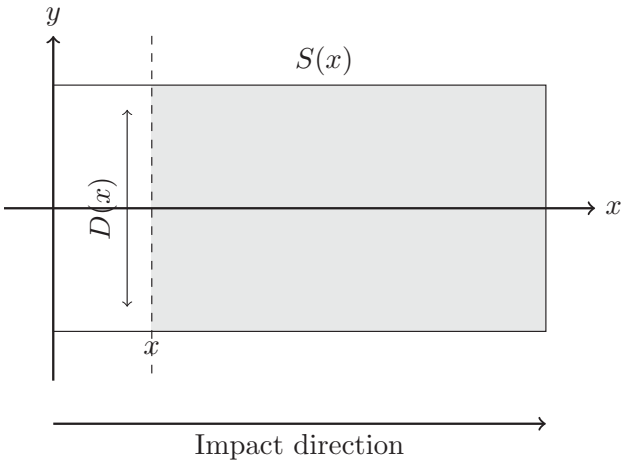

Figure 2.13: Conventions for IBII virtual tests assessment

to the reconstruction of stress fields without any assumption on the constitutive equations which drive the computation of stresses from strains, even if loading conditions are constrained.

For a given IBII virtual test, Equation 2.29 is used on the skin mesh to evaluate - for a specimen cross section at $x = k,\ k \in \mathbb{R}$ - the reconstruction of $\sigma_{EPX}(x)$. The latter can be expressed as follows:

$$\sigma_{EPX}(x) \ = \ \frac{1}{D(x)} \int_{D(x)} \sigma_{xx}(x,y)\ dy \ = \ \frac{1}{D(x)} \sum_i \sigma_{xx}(i) \underbrace{\int_{d(x,i)} dy}_{=d(x,i)} \tag{2.30}$$

where i is the summation index over the elements intersecting $D(x)$ and $d(x,i)$ the intersection length between i-th element and the material line. Note that $D(x)$ may be discontinuous in a case of internal geometric singularities such as holes. Finally it comes:

$$\boxed{\sigma_{EPX}(x) \ = \ \sum \omega(x,i)\sigma_{xx}(i)} \quad \text{where} \quad \omega(x,i) = \frac{d(x,i)}{D(x)} \tag{2.31}$$

$\sigma_{REC}(x)$ can also be expressed with the same methodology:

$$\sigma_{REC}(x) = \frac{1}{D(x)} \int_{S(x)} \rho\gamma_x\ dS = \frac{\rho}{D(x)} \sum \gamma_x(x,j) \underbrace{\int_{S(x,j)} dS}_{=S(x,j)} \tag{2.32}$$

where $S(x,j)$ the intersection between j-th element area and $S(x)$ (grey rectangle in Figure 2.13). Finally it comes:

$$\boxed{\sigma_{REC}(x) = \frac{\rho}{D(x)} \sum_j \gamma_x(x,j) S(x,j)} \tag{2.33}$$

2.3.3.2 Application to a validation case

To validate the methodology, a rectangular (45 ×70 mm) specimen have been loaded with an analytical pulse on its edge. Varying the mesh size, longitudinal stress fields have been reconstructed for several values of $S(x)$ in Figure 2.13 for the N_t monitored time steps. Finally, mean time relative error defined by Equation 2.34 is analysed.

$$\frac{1}{N_t} \sum_{t=1}^{N_t} \left| \frac{\overline{\sigma_{EPX}(x,t)} - \overline{\sigma_{REC}(x,t)}}{\overline{\sigma_{EPX}(x,t)}} \right| \tag{2.34}$$

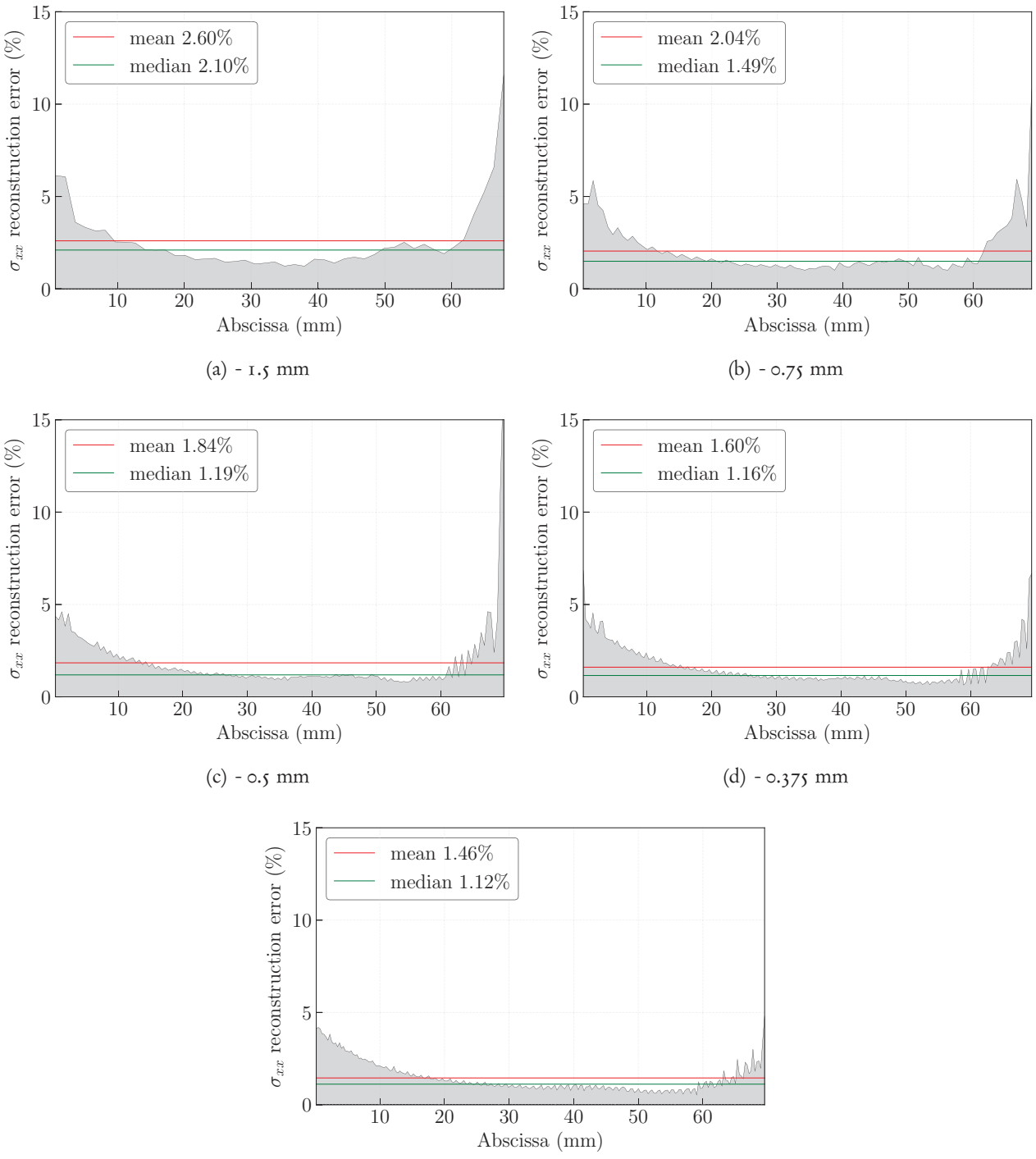

Figure 2.14: Stress reconstruction mean time error (Equation 2.34) for different mesh size

Figure 2.14 shows that mean and median error are different. This was expected because for stress reconstruction involving low stress levels and/or small surfaces, the reconstruction is easily affected by the hypotheses such as the 1D wave propagation or the averaging of stress and acceleration field. Moreover, though mean error is continuously decreasing, median error decreases before reaching a plateau (Figure 2.15). Finally, optimal mesh size may be set after three refinements, this corresponding in this work to a mesh size of 0.5mm.

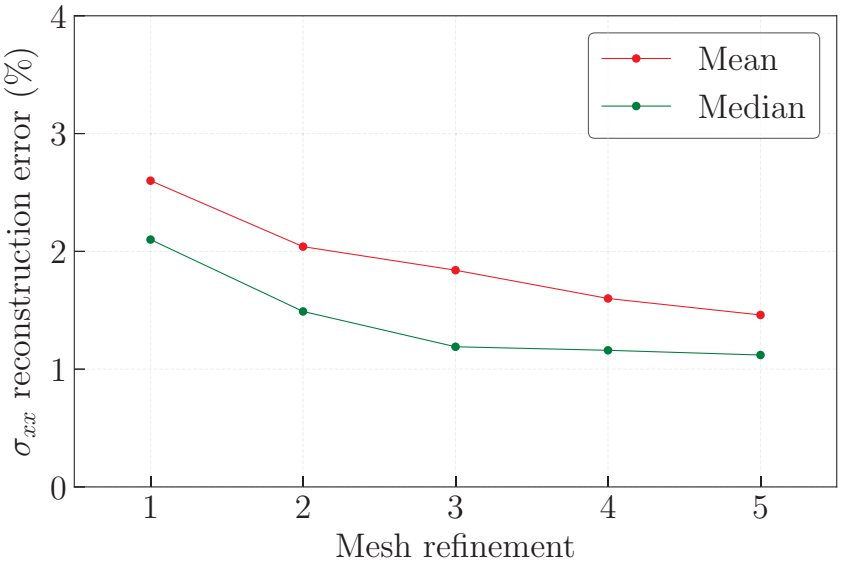

Figure 2.15: Stress reconstruction - Convergence analysis

2.4 A FE-based simulation of full-field measurements: Development of a synthetic images generator

2.4.1 A mapping-based algorithm to generate synthetic images

In order to include the measurement toolchain in the design process, synthetic images were generated to simulate full-field measurements. This has already been addressed to quantify uncertainties in 2D-DIC [126] or to analyse the identification of elastic parameters with the VFM using quasi-static [114, 115] and high strain-rate [113, 127] tests. In these algorithms, an undeformed image of the specimen's region of interest (ROI) covered by a speckle pattern (in case of DIC measurements) or a grid (grid method) is generated. Then sets of deformed images are built based on nodal displacements extracted from FEA. However, grey levels calculation does not include a fill factor, which is the fraction of the area of camera sensor which captures light intensity [128]. This is particularly critical for on-chip-storage UHS cameras insofar as their fill factor is low [129]. More recently, a mapping-based algorithm was proposed [130] but the fill factor is still not considered. In this work, an updated algorithm is implemented (Figure 2.16). This is explained thereafter.

The methodology presented in [130] relies on isoparametric coordinates uniqueness (Figure 2.17). To compute grey levels of a given integration point (x_d, y_d) of a deformed image (cf. Figure 2.16), its isoparametric coordinates (ξ_i, η_i) are first computed. Then, regular mapping is used to compute its initial coordinates (x_u, y_u). Contrary to regular mapping which is based on an explicit formula, the equation to compute isoparametric coordinates from point coordinates for any finite element is implicit. Thus, it was proposed a Newton-Raphson iterative procedure compatible with all element types [130]. For a cost-efficient inverse mapping during the deformation process, we proposed an explicit expression for the isoparametric coordinates for the 4-node elements, as it was done earlier for node data extrapolation onto elements (Section 2.3.2.1). Assuming the notations on the Figure 2.17, the shape functions are like Equation 2.22. Thus, any point $M(x_M, y_M)$ - belonging to the deformed element of Figure 2.17 - verifies:

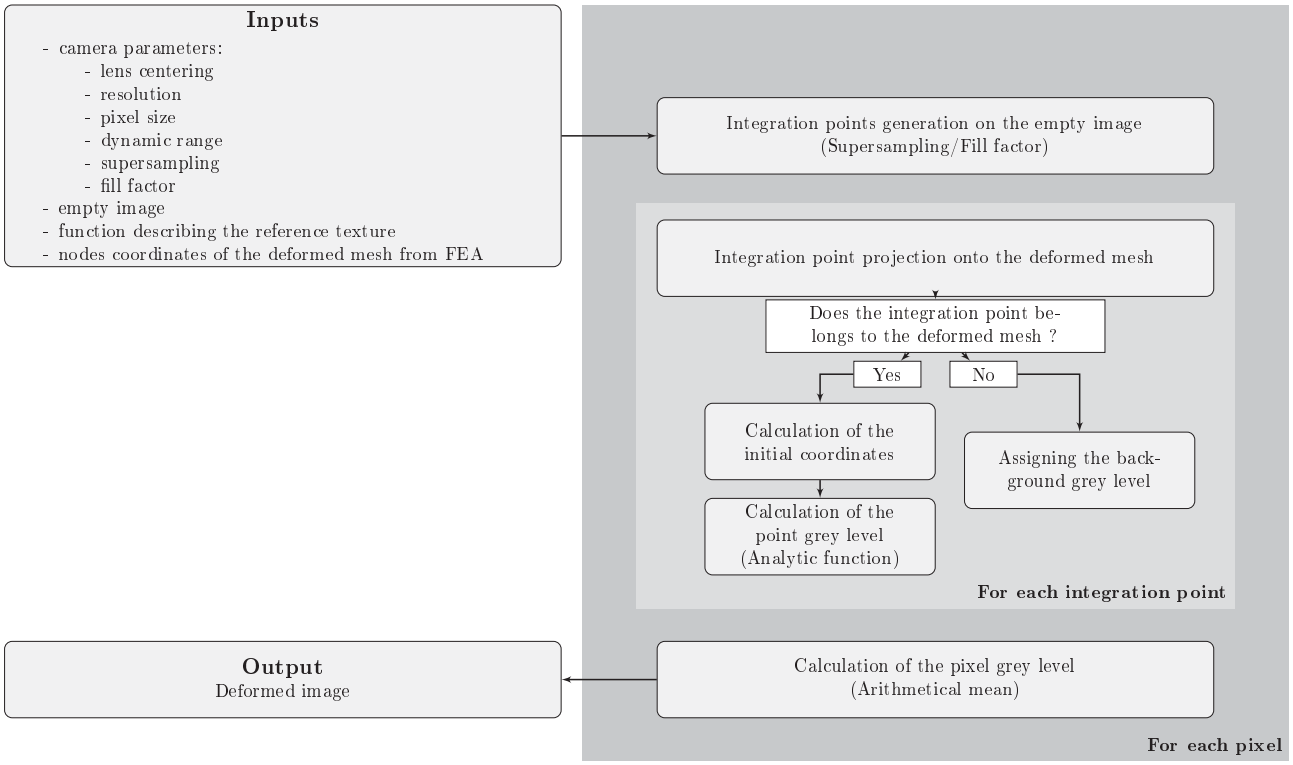

Figure 2.16: Algorithm to generate synthetic images from IBII virtual tests

$$\begin{aligned} 4x_M &= \underbrace{(x_1+x_2+x_3+x_4)}_{4x_G} + (x_{24}+x_{13})\ \xi_M + \\ &\qquad (x_{24}-x_{13})\ \eta_M + (x_{24}+x_{13})\ \xi_M\eta_M \end{aligned} \tag{2.35}$$

$$\begin{aligned} 4y_M &= \underbrace{(y_1+y_2+y_3+y_4)}_{4y_G} + (y_{24}+y_{13})\ \xi_M + \\ &\qquad (y_{24}-y_{13})\ \eta_M + (y_{24}+y_{13})\ \xi_M\eta_M \end{aligned} \tag{2.36}$$

Factorizing the Equation 2.36 by η_M and substituting it into the Equation 2.35 cancels its η_M-dependency:

$$\begin{aligned} & (y_{24}-y_{13})(4x_M-4x_G) + [(y_{24}-y_{13})(4x_M-4x_G) - (x_{24}+x_{13})(y_{24}-y_{13})]\xi_M \\ = \quad & (x_{24}-x_{13})(4y_M-4y_G) + [(x_{24}-x_{13})(4y_M-4y_G) - (x_{24}-x_{13})(y_{24}+y_{13})]\xi_M \end{aligned}$$

Finally:

$$\xi_M = \frac{2\overrightarrow{MG}\times(\overrightarrow{P_1P_3}-\overrightarrow{P_2P_4})}{\overrightarrow{P_1P_3}\times\overrightarrow{P_2P_4}+2\overrightarrow{MG}\times(\overrightarrow{P_1P_2}+\overrightarrow{P_3P_4})} \tag{2.37}$$

where $\forall(i,j),\ \overrightarrow{P_iP_j} = (x_{ij}, y_{ij}) = (x_j - x_i, y_j - y_i)$ and $G(x_G, y_G)$ is the element barycenter. The expression for η_M is obtained by substituting Equation 2.35 into the Equation 2.36. Then:

$$\eta_M = \frac{2\overrightarrow{MG}\times(\overrightarrow{P_1P_3}+\overrightarrow{P_2P_4})}{\overrightarrow{P_1P_3}\times\overrightarrow{P_2P_4}-2\overrightarrow{MG}\times(\overrightarrow{P_1P_2}+\overrightarrow{P_3P_4})} \tag{2.38}$$

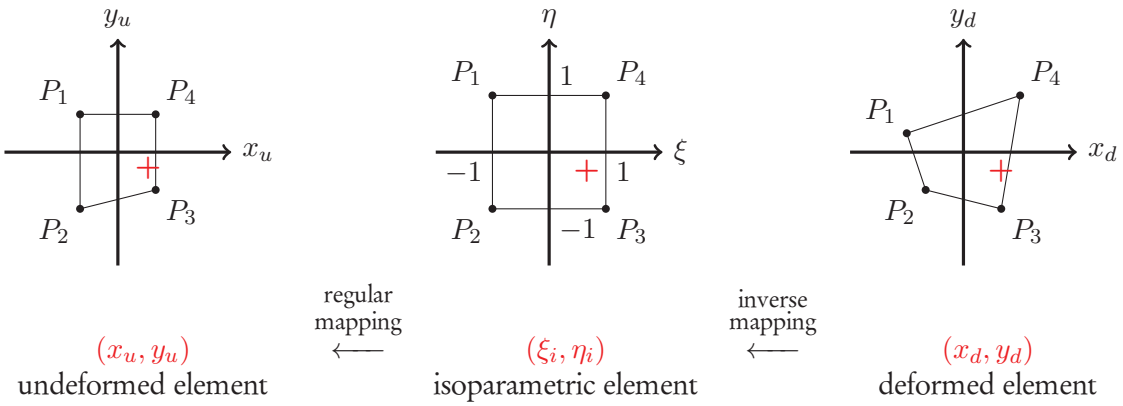

Figure 2.17: Back-and-forth mapping for a 4-node element

As the grid method is used here to track displacement fields, the texture of the initial image can be defined analytically [114,115,127]. Indeed, light intensity, I, at coordinates (x, y) may be described by Equation 2.39, where (I_0, γ) are the mean intensity and the contrast respectively, and ω is the spatial pulsation of the grid ($\frac{2\pi}{\Delta}$, where Δ is the grid pitch). Note that if noise is taken into account, distributed random integers are added to pollute the encoded light intensity. Their definition domain is a fraction of the simulated camera dynamic range (a few percents).

$$I(x,y) = I_0\Big\{1 + \gamma\Big[\cos(\omega x) + \cos(\omega y) - \big|\cos(\omega x) - \cos(\omega y)\big|\Big]\Big\} \tag{2.39}$$

2.4.2 Validation on analytic cases

To validate the implementation of the synthetic images generator, a 4-node element of 2mm-long (Figure 2.18) has been deformed according to analytic transformation gradients $\underline{\underline{F}}(\underline{x}, t)$. Two elementary loadings have been considered: a simple shear (Loading 1) and an uniaxial deformation (Loading 2). The related analytical kinematic tensors $\underline{\underline{F}}$, $\underline{u}$ and $\underline{\underline{\varepsilon}}$ are collected in Table 2.6. Constant parameters α_1 and α_2 of Table 2.6 are such that $\alpha_1(t) = t^3$ and $\alpha_2(t) = \sin(\pi t)$, $t \in [0, 1]$ ms.

Then, the produced fields of coordinates have input the virtual images simulator for the creation of synthetic grid images, so that a set of 50 images was generated for each loading case. Therefore, the grid method was applied according to the methodology presented in Section 2.2 to extract displacement, strain, velocity and acceleration fields. Note that the SNR parameters are such as (N_{p1},N_{p2}) = (1,1), this corresponding to central difference formulæ (Table 2.4). A high resolution camera have been used (1200×750 pixels) and the supersampling assumes 9 (3×3) integration points.

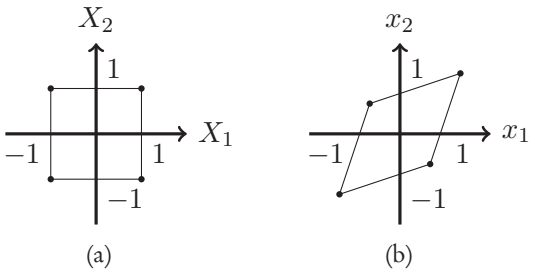

Figure 2.18: Notations for analytic cases - (a) Initial element - (b) Deformed element

Figure 2.19 maps the relevant displacement field at different times for each loading. Qualitatively speaking, displacement maps are consistent with analytical expressions α_i. For the shear test, displacement evolution is cubic, *i.e.*, slowly increasing before increasing drastically. For the uniaxial deformation, a linear elongation towards the tension direction occurs, and then a compression. Figure 2.20

Table 2.6: Kinemetic of analytical transformations

Transformation		$\underline{\underline{F}}$	$\underline{u}$	$\underline{\underline{\varepsilon}}$
Simple shear	$\begin{cases} x_1 = X_1 + \alpha_1(t)X_2 \\ x_2 = X_2 \end{cases}$	$\begin{bmatrix} 1 & \alpha_1(t) \\ 0 & 1 \end{bmatrix}$	$\begin{bmatrix} \alpha_1(t)X_2 \\ 0 \end{bmatrix}$	$\frac{1}{2}\begin{bmatrix} 0 & \alpha_1(t) \\ \alpha_1(t) & 0 \end{bmatrix}$
Uniaxial	$\begin{cases} x_1 = [1 + \alpha_2(t)]X_1 \\ x_2 = X_2 \end{cases}$	$\begin{bmatrix} 1 + \alpha_2(t) & 0 \\ 0 & 1 \end{bmatrix}$	$\begin{bmatrix} \alpha_2(t)X_2 \\ 0 \end{bmatrix}$	$\begin{bmatrix} 0 & \alpha_2(t) \\ 0 & 0 \end{bmatrix}$

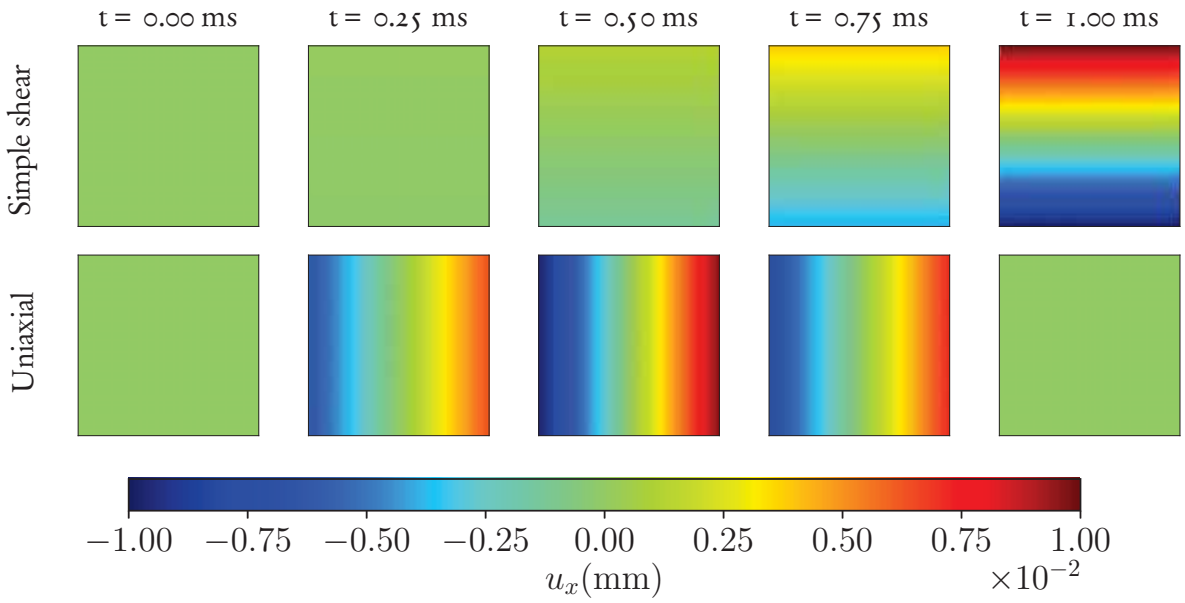

Figure 2.19: Displacement maps extracted with the grid method

shows a quantitative comparison of mechanical fields extracted from analytic solution or computed using the grid method toolchain presented in Section 2.2. One can observe that time-independent fields are overlapping, this validating both the image generator and the grid method to extract displacements and strains. However, errors are noticed for velocity and acceleration. This was expected because derivatives of analytical functions α_i, $i \in \{1, 2\}$ are approximated by central finite difference formulæ (Table 2.4). Thus, small time increments might be necessary to approximate the derivative, notably if α_i is not polynomial. However, it is worth noticing that in practice, UHS cameras also limit temporal resolution, although the recent advances in high-speed imaging (cf. Section 1.3.2). Moreover, displacements maps are determined separately, so that for each measurement point, displacement evolution upon time may not be smooth enough for time-differentiation. Finally, computed velocity fields are more accurate than acceleration fields because 1st-order derivatives are less sensitive than 2nd-order derivatives to the aforementioned factors.

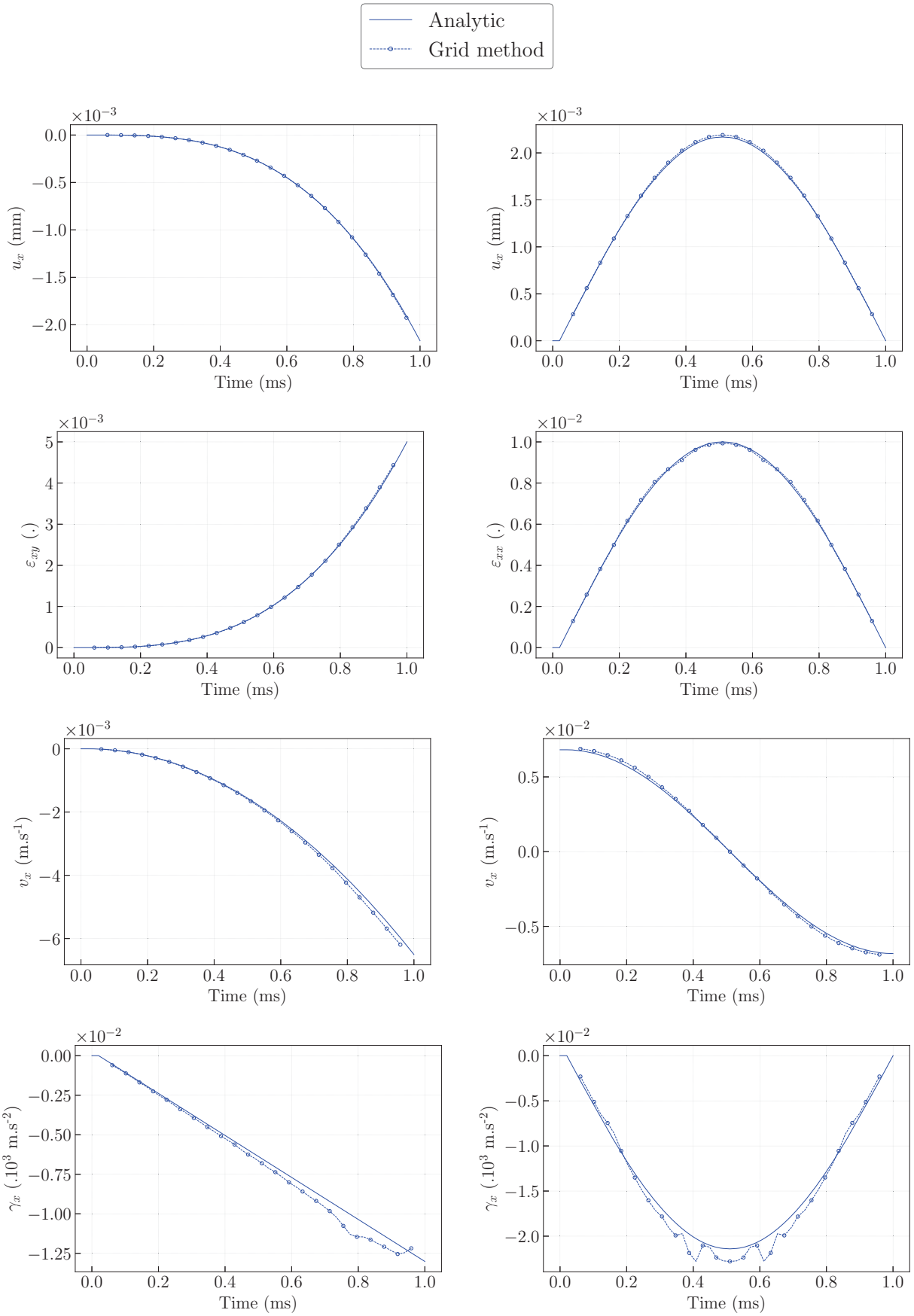

(a) - Simple shear

(b) - Uniaxial deformation

Figure 2.20: Analytical mechanical fields vs data from the grid method - $(X_1, X_2) = (0.22, -0.22)$ mm

2.5 Summary

This chapter presents the tools which have been developed for numerical IBII tests assessment and processing. It includes first the implementation of a Return Mapping Algorithm (RMA) suitable to compute stress fields $\underline{\underline{\sigma}}$ from strain $\underline{\underline{\varepsilon}}$. This is crucial for further material parameter extraction as $\underline{\underline{\sigma}}$ is required to express the PVW. Furthermore, a methodology to compute strain and acceleration fields in practice (*i.e.*, in a noisy environment due to experimental biases) is also implemented. It notably relies on the use of SNR differentiators which enable the computation of $\underline{\underline{\varepsilon}}$ and $\underline{\gamma}$ fields from displacement maps $\underline{u}$ owing to convolutions.

Then, a numerical toolchain has been developed for IBII virtual testing. Starting with a mesh built from an automated script, FEA processing is performed with the view to mimic in-plane full-field measurement techniques which provide displacements on a surface. Therefore, specimen skin mesh is extracted from the tridimensional simulation and FE mechanical and kinematic fields are projected onto this reconstructed 2D mesh. To enable the assessment of metrological performance, one needs to simulate full-field measurements. To do so, a generator of sets of synthetic images is finally developed.

Thus, this numerical toolbox incorporates basic tools for numerical assessment and processing of IBII test configurations. This is crucial because a through analysis - perhaps an optimization - of several test parameters (*e.g.*, specimen geometry, projectile velocity and geometry) and VFM toolchain parameters (*e.g.*, SNR differentiators parameters) is targeted. However, this requires a careful analysis, notably for the full-field measurement toolchain.

The next Chapter is dedicated to this task.

Chapter 3

Numerical optimization of Image-Based Inertial Impact tests for Johnson-Cook model characterization

Contents

Abstract

This chapter is dedicated to the exploitation of presented numerical toolbox to optimize IBII tests for Johnson-Cook model characterization with the VFM. Beforehand, FE-based design criteria are set to discriminate test configurations and select suitable tests for viscoplasticity characterization. Then, a parametric study is performed on both impact conditions and specimen shape, based on FE simulations and synthetic images generator. Finally, regularization parameters used to compute strains and accelerations from displacement fields are optimized through uncertainty quantification for the proposed test configurations.

3.1 Motivations

The IBII test methodology is based on a non-standard approach. Therefore, all tests parameters (*e.g.*, specimen geometry or projectile velocity) may be set according to user-defined design criteria. To do so, the available literature (*e.g.*, the work from [7]) advices to better understand influence of each test parameter (Chapter 1). This is all the more critical that this work on IBII tests for rate-dependent behaviour characterization is seminal.

Thus, a numerical toolbox has been developed (Chapter 2). For a given IBII test configuration, its use is based on FE simulation of mechanical fields on the specimen top surface (skin mesh), similarly to their extraction using surface full-field measurement techniques. Moreover, a synthetic images generator can provide a set of virtual images based on skin mesh coordinates. Any camera encoding process can be mimicked according to given features (*e.g.*, spatial and temporal resolution), so that virtual images are processed in more realistic conditions. Finally, the numerical toolbox can compute the whole PVW for the VFM, *i.e.*, strain and acceleration fields from greyscale images and stress fields from strain fields and a given set of material parameters.

In this chapter, the toolbox is applied to design IBII tests to characterize the behaviour of titanium alloy Ti6Al4V over a wide range of plastic strain and strain rate. This alloy is widely used in the aerospace industry owing to its high specific strength. In addition to Hooke's law for elastic linear behaviour, the JC flow rule defined by Equation 3.1 was considered to describe the viscoplastic flow. The temperature softening was neglected but could be introduced in the future if appropriate temperature measurements are available. Kinematic hardening and damage were not considered. Therefore, flow stress σ_y varies with cumulated plastic strain p and plastic strain-rate $\dot{p}$ only (Equation 3.1). The reference material parameters (Table 2.2, p. 51) have been obtained with a standard technique [6].

$$\sigma_y = \begin{cases} \sigma_0 + Kp^n & \text{if} \quad \dot{p} \leq \dot{\varepsilon}^{vp}_{eq,0} \\ \left[\sigma_0 + Kp^n\right]\left[1 + M \ln\left(\frac{\dot{p}}{\dot{\varepsilon}^{vp}_{eq,0}}\right)\right] & \text{if} \quad \dot{p} > \dot{\varepsilon}^{vp}_{eq,0} \end{cases} \tag{3.1}$$

In this work, an FEA-based procedure is developed to optimize the characterization of viscoplasticity (JC model) using IBII tests and the VFM. It relies on the analysis of viscoplastic spectra driving the identification of the strain rate dependence and on the influence of experimental biases on material parameters identification. Contrary to an approach with real tests, the importance of all tests parameters can therefore be studied thoroughly in quick succession. More precisely, the influence of impact velocity, specimen geometry and filtering parameters features will be analysed.
Assuming the knowledge of material behaviour, two design criteria have been selected to evaluate each test configuration:

- maximization of the range of validity of the identified viscoplastic model from single impact test: the configuration has therefore to span a viscoplastic spectrum (p, $\dot{p}$) as wide as possible;
- accuracy of material parameters identification with the VFM in realistic conditions: indeed, several parameters linked to the test itself (*i.e.*, projectile and specimen geometries, impact velocity) or to the test processing (*e.g.*, camera settings, full-field measurement technique, VFM toolchain features) influence the identification process, hence they must be taken into account in the design procedure of an optimized test.

In practice, each IBII test simulation was performed owing to the toolbox of Chapter 2. Mesh size was deduced from the convergence analysis presented in Section 2.3.3. The overall procedure based on FEA results and consisting in viscoplasticity analysis and identification of material parameters with the VFM is reported in Figure 3.1.

Inverse problems dealing with constitutive parameters identification often lead to the minimization of ill-conditioned cost-functions because of the imbalance in the sensitivities to the different material parameters, as in [110] for elastoplastic parameters. To avoid this problem, as a first step of development, monovariable cost-functions were considered. Thus, this study concentrates on the identification of JC viscoplastic parameter M only. The static part σ^{stat} of the model has been supposed known; in practice, it can be characterized using a standard tensile test performed under quasi-static loading conditions (Table 2.2, p. 51).

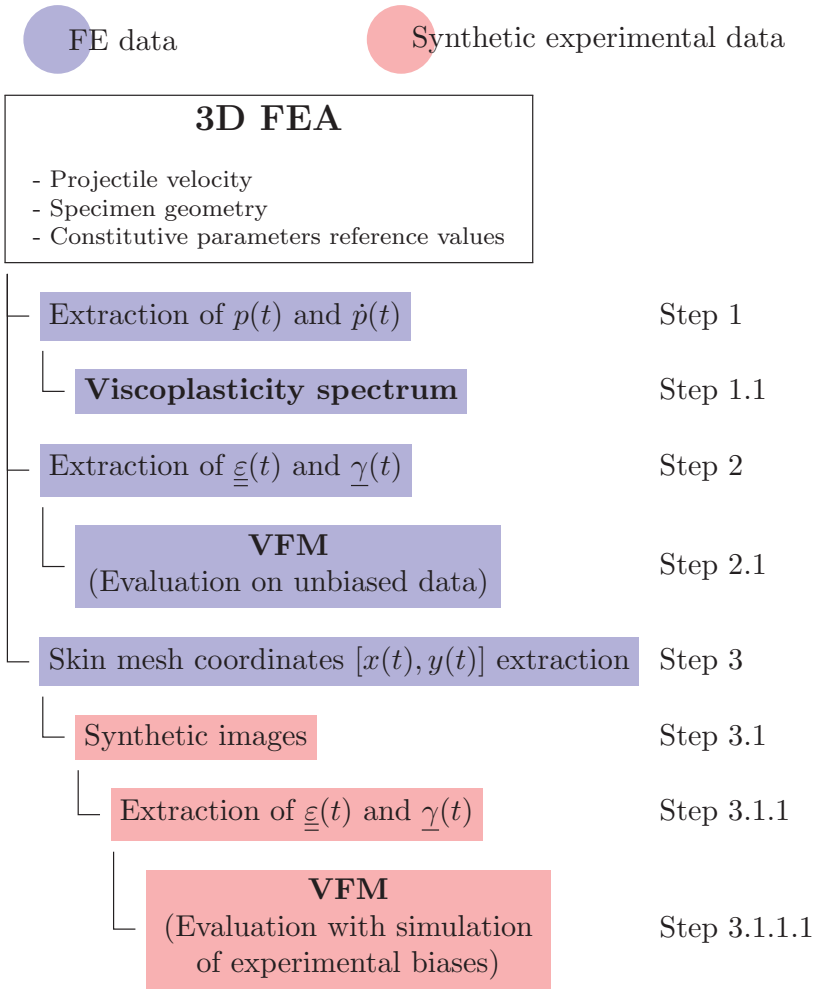

Figure 3.1: FEA-based IBII tests toolchain analysis

The following sections report the different steps of the optimization process based on the selected design criteria to set the future IBII test matrix:

1. setting IBII test parameters which are more or less constrained by experimental conditions (Section 3.2);
2. analysis of viscoplastic spectra for different impact velocities and specimen geometries (Section 3.3);
3. setting both projectile velocity and specimen geometry based on the VFM robustness/accuracy and viscoplastic spectra (Section 3.4);
4. setting/analysis of regularization parameters to improve strain/acceleration fields extraction from full-field measurements (Section 3.5);

Within the design space, there are two types of tests parameters: those which are directly linked to the test itself such as the geometries or the impact conditions (*e.g.*, projectile velocity and material), and those related to the test processing and tracking, *i.e.*, the grid pitch or the UHS camera features for instance. Figure 3.2 provides main tests parameters that are investigated in this work. Among them, some are constrained mainly for experimental reasons: they are described thereafter.

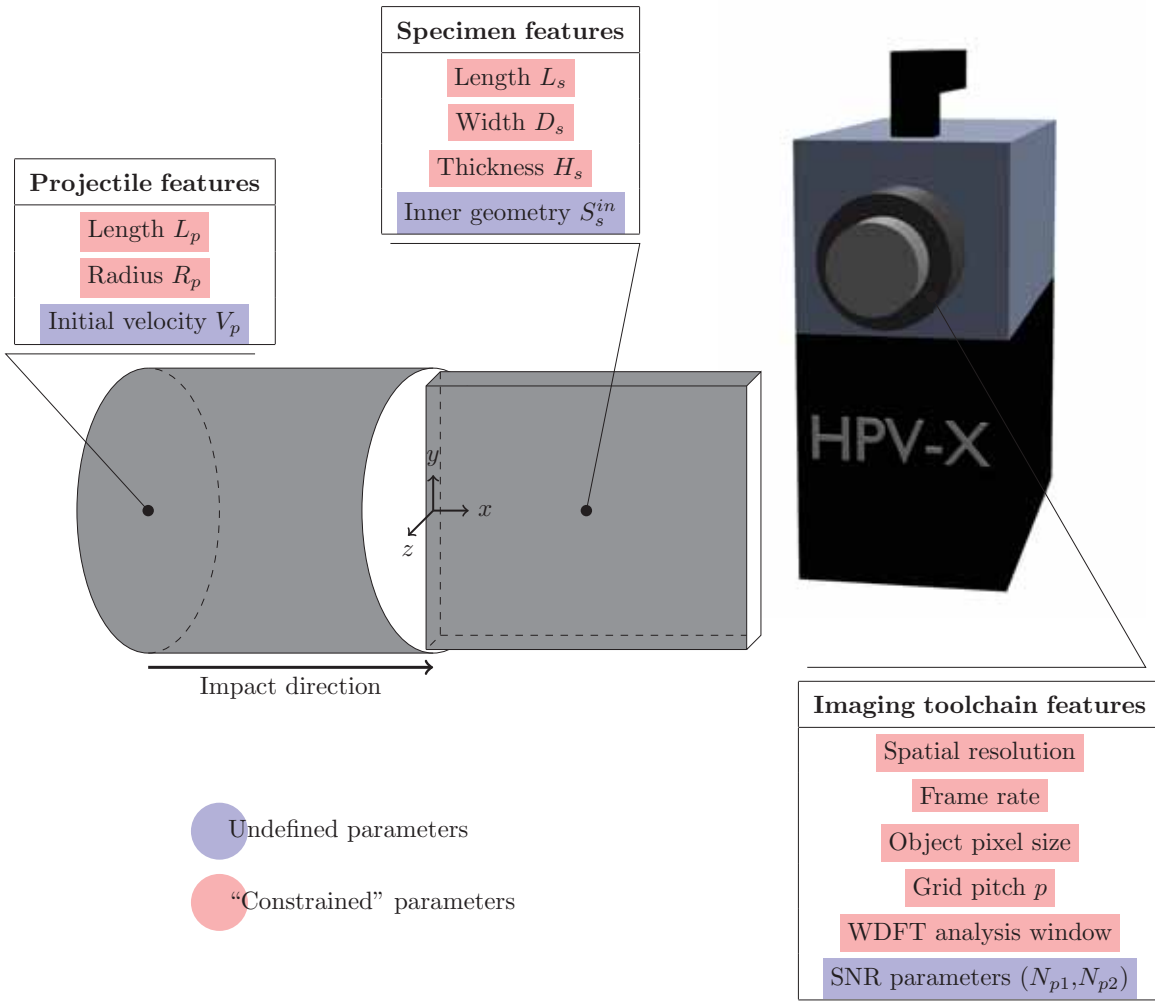

Figure 3.2: Inventory of IBII tests parameters for a given configuration

3.2 Setting the constrained test parameters

Most of the test parameters can be set because of the imaging toolchain. For instance, the Shimadzu HPV-X camera (Table 4.1) available at the University of Southampton constrains:

- spatial and temporal resolutions;
- grid pitch p: 5 pixels/period to optimize spatial resolution;
- WDFT analysis window: bi-triangular to efficiently isolate phase modulation with a limited window size.

The gas gun at the University of Southampton have been designed according to these imaging specifications [131], notably the bore size (50 mm) and the projectile maximum velocity ($\approx 100\,\mathrm{m.s^{-1}}$).

Table 3.1: Initial camera settings (based on Shimadzu HPV-X specifications)

Resolution	400×250 pixels
Interframe time	up to 0.2 μs (5 Mfps)
Dynamic range	10 bits (1024 grey levels)

Table 3.2: Test configurations constant parameters

Projectile features	
Length L_p (mm)	70
Base radius R_p (mm)	24.5
Specimen features	
Length L_s (mm)	70
Width (mm) D_s	45
Thickness H_s (mm)	4

Therefore, projectile and specimen external geometries were deduced intuitively. Table 3.2 collects impact test configuration, assuming notations in Figure 3.2.

To conclude, there are test parameters which are "constrained" by the testing conditions. This exhibits the parameters of Figure 3.2 which the study has to focus on. Indeed, projectile velocity V_p, specimen inner geometry S_s^{in} and SNR parameters remain undefined. The next sections are dedicated to this task.

3.3 Influence of impact velocity and specimen geometry on generated viscoplastic spectra

The goal of the optimization process is to enhance the characterization of the JC viscoplastic model on a wide range of strain and strain-rate. From the energetic point of view, different viscoplastic spectra can be obtained on specimens playing on either projectile kinetic energy or plastic strain energy. Among the considered test parameters which can be tuned (Figure 3.2), two of them are related to these energies: the impact velocity V_p and the specimen inner geometry S_s^{in}. Their influence is discussed thereafter.

As the studied material has a high initial yield stress (973 MPa, Table 2.2), it may be necessary to "machine" holes or notches in the initially designed rectangular specimen to ensure high levels of plastic strain and plastic strain rate and identify the JC model over a large range of strain and strain rate. Three specimen geometries have been analysed for IBII tests impact conditions (Figure 3.3): a rectangular one (Specimen 0) as already used for elastic(-plastic) behaviour characterization in the literature [7,8,112,113], a single-holed one (Specimen 1) and a double-notched one (Specimen 2) with the notch location at the same x-coordinate. The latter has been chosen among hand-picked positions to favour (visco)plastic wave propagation. Note that the same amount of material has been "machined" so that Specimens 1 and 2 have the same mass. As all specimens have the same length, impact duration - that corresponds to the back-and-forth travelling time of a longitudinal elastic wave through the specimens - is always of about 25μs. Furthermore, three velocities were also considered: V_p = 57, 70 and 80 m.s^{-1}. All of them ensure (visco)plastic strain within all chosen specimens. Their dimensions are collected in Figure 3.4.

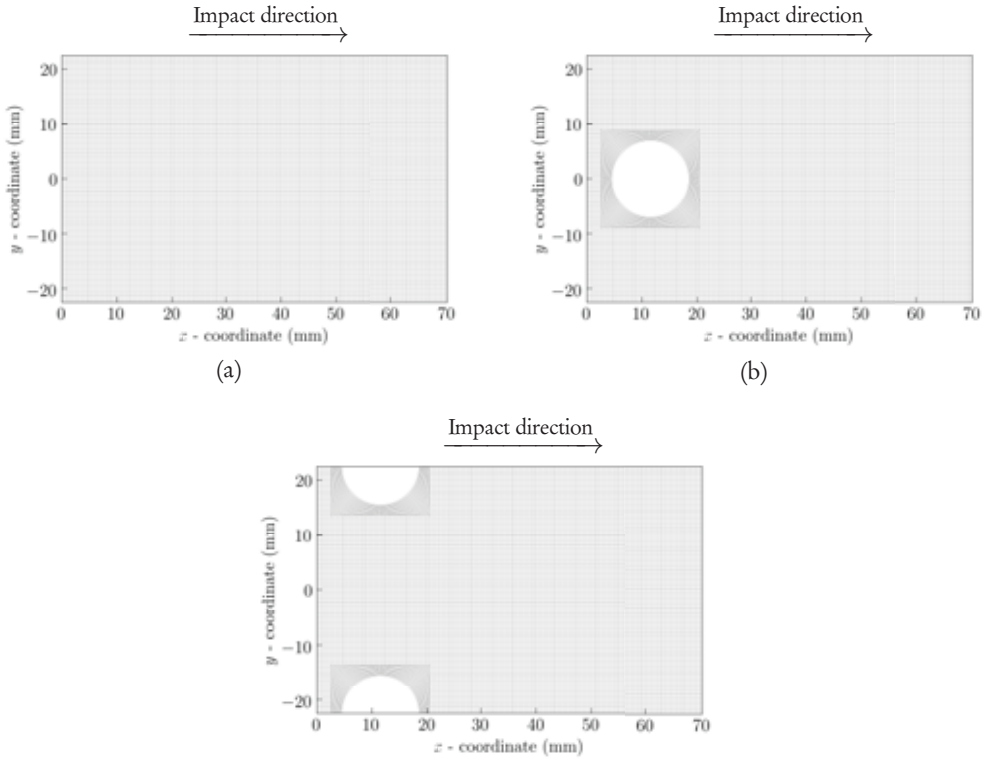

Figure 3.3: Specimen geometries - (a) Specimen 0 - (b) Specimen 1 - (c) Specimen 2

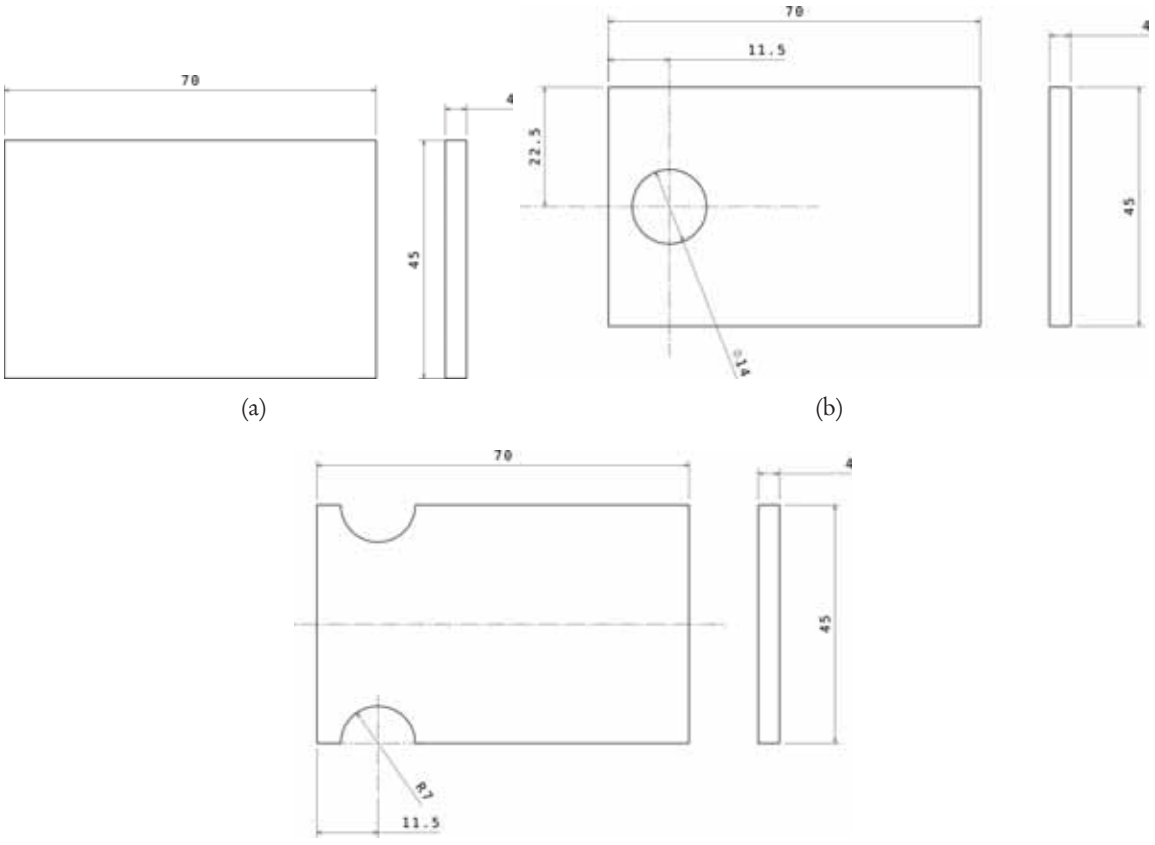

Figure 3.4: Tested specimen drafting - (a) Rectangular specimen - (b) Holed specimen - (b) Notched specimen

The numerical toolchain was run for the nine presented configurations. Their viscoplastic spectra are analysed thanks to histograms which account for viscoplastic flow development during impact tests (see Figure 3.1 - Step 1.1). All (visco)plastic states (p, $\dot{p}$) computed by FEA in the elements of the specimen skin mesh are collected. As the mesh was refined around the stress concentrators, the contribution of each element to the counting is proportional to its surface. Thus, viscoplastic states from a nominal element account for one whereas states from a refined element account for the ratio between its area and that of a nominal element. Figure 3.5, Figure 3.6 and Figure 3.7 report the evolution of viscoplastic spectra during one back-and-forth travel of impact wave. It can be observed that:

- all tests produced band-shaped viscoplastic spectra, *i.e.*, higher (resp. lower) plastic strain occurred at higher (resp. lower) plastic strain rate, whichever the specimen geometry. This is due to the loading which is mainly unidirectional, though load path could be locally heterogeneous;
- the intermediate (t $\approx 12\mu$s) and last (t $\approx 25\mu$s) viscoplastic spectra are similar, *i.e.*, viscoplastic flows has mostly expanded during early stages of wave propagation;
- the highest number of occurrences is observed for plastic strain rate about $\dot{p} \propto 10^3$ s^{-1}. This is in good agreement with an approximation of the mean strain-rate as $\dot{\varepsilon} \propto V_p/L_s = 10^{-3}$ s^{-1};
- owing to hole/notches, viscoplastic spectra (p, $\dot{p}$) of Specimen 1 and 2 are more heterogeneous than that of Specimen 0.

Figure 3.5 : Viscoplasticity histograms contour - Full specimen

Figure 3.6: Viscoplasticity histograms contour - Holed specimen

Figure 3.7: Viscoplasticity histograms contour - Notched specimen

One can also observe that geometrical singularities enrich the viscoplastic spectrum with a better coverage of the viscoplastic range (Figure 3.8). Yet, presence of singularities do not strongly enhance large viscoplastic strains at low rate ($p > 10^{-3}$ and $\dot{p} < 10^{2}$ s^{-1}), so that less than a half of the global zone is covered. Furthermore, these large spectra are a sign of larger strain gradients. Their presence may jeopardize the identification if Ultra-High-Speed (UHS) camera temporal and spatial resolution are not sufficient to deal with them.

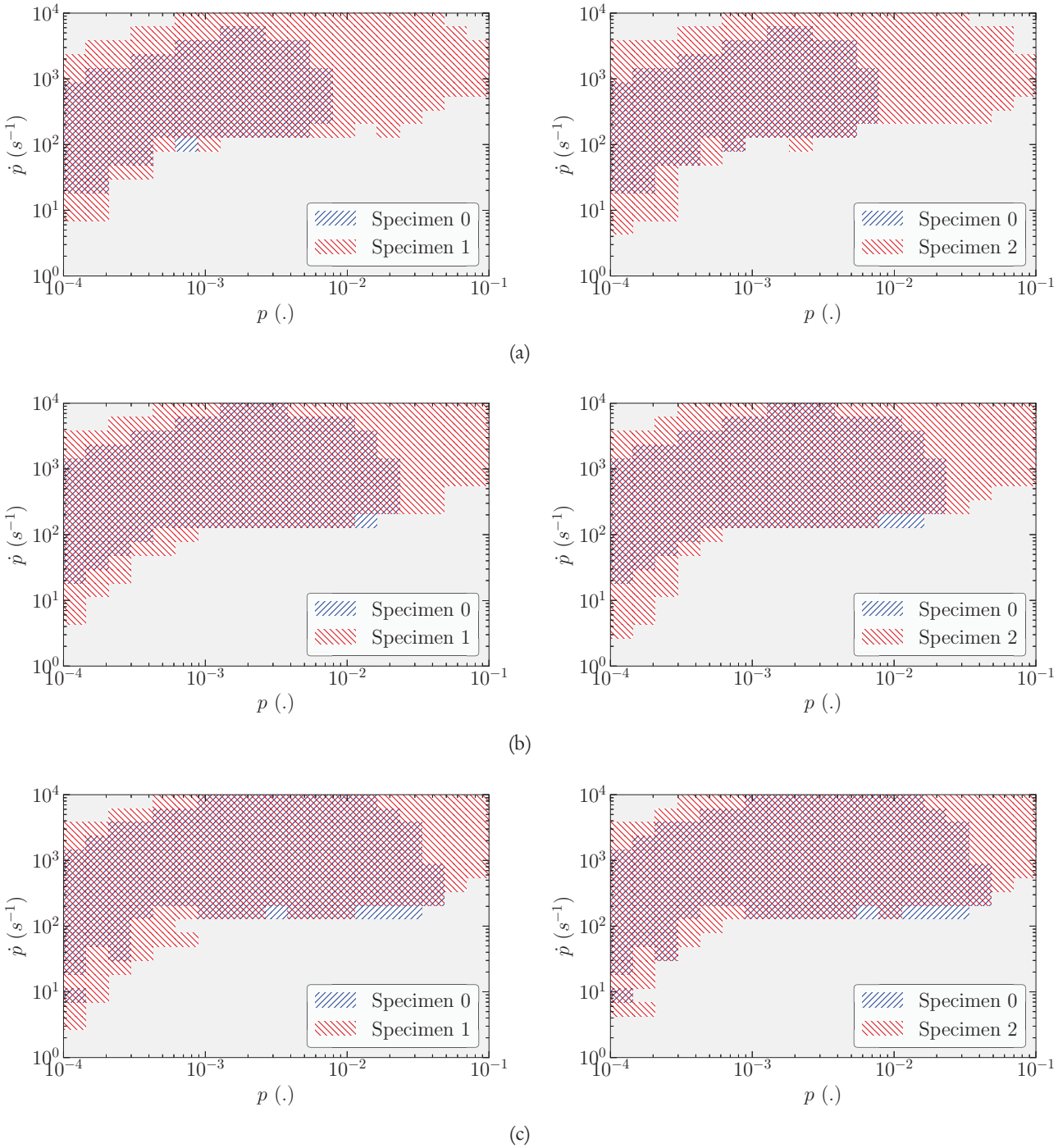

Figure 3.8: Specimen-based histograms overlap - (a) $V_p = 57$ m.s^{-1} - (a) $V_p = 70$ m.s^{-1} - (a) $V_p = 80$ m.s^{-1}

Aside the specimen geometry, the other test parameter which may influence viscoplastic spectra is the projectile velocity. Owing to a faster projectile, viscoplastic spectra are developing faster for each specimen geometry (Figures 3.5 to 3.7). However, the influence of V_p on viscoplastic spectra band shape is limited (Figure 3.8). Furthermore, this has to be balanced with the temporal resolution which

is limited by UHS camera interframe time in realistic conditions, so that computation of high temporal variation of p (*i.e.*, high values of $\dot{p}$) may be jeopardized.

As it was somewhat expected, the peak value of p increases (Figure 3.9) when V_p increases. This effect is more pronounced in Specimen ○ as it does not have the strain concentrators which mitigate the influence of increasing speed. Furthermore, plastic wave penetration seems to depend more on the specimen geometry than on projectile velocity, insofar as the penetration length decreases if there are singularities, whichever the value of V_p (Figure 3.9). More precisely, plastic waves do not penetrate behind holes/notches owing to the upstream wave reflections. By contrast, upper and lower boundary effects favour the penetration of plastic waves, hence the shape of its front end.

In a nutshell, those analyses highlight some advantages of holes/notches for viscoplastic flow expansion. For given impact conditions, their presence enhance the development of viscoplastic spectra which are suitable to characterize viscoplasticity over a wider range of strain and strain-rates. Moreover, projectile velocity is not as critical as one would have expected for the proposed configurations. However, this strengthens the idea that specimen design is a key point for IBII tests aiming at the extraction of constitutive parameters for a wide viscoplastic spectrum with a reduced number of tests. Finally, the present criterion (strain and strain-rate fields heterogeneity) does not tell anything about practical identifiability in real tests, this is investigated in the next section, based on FE data.

Figure 3.9: Cumulated plastic strain p at t = 12μs (thresholded at 10^{-4})

3.4 VFM-based selection of projectile velocity and specimen geometry

3.4.1 Through-thickness stress analysis

Before applying the VFM on IBII numerical tests, one has to confirm whether FE simulations are eligible for plane stress hypothesis. Then, through-thickness elements pile for which the upper element maximizes $\int_0^t \dot{p} dt$ has been monitored (Figure 3.10). For Specimen 1 and 2, piles were in the vicinity of geometrical singularity. The results are reported for the velocity $V_p = 70$ m.s^{-1} only.

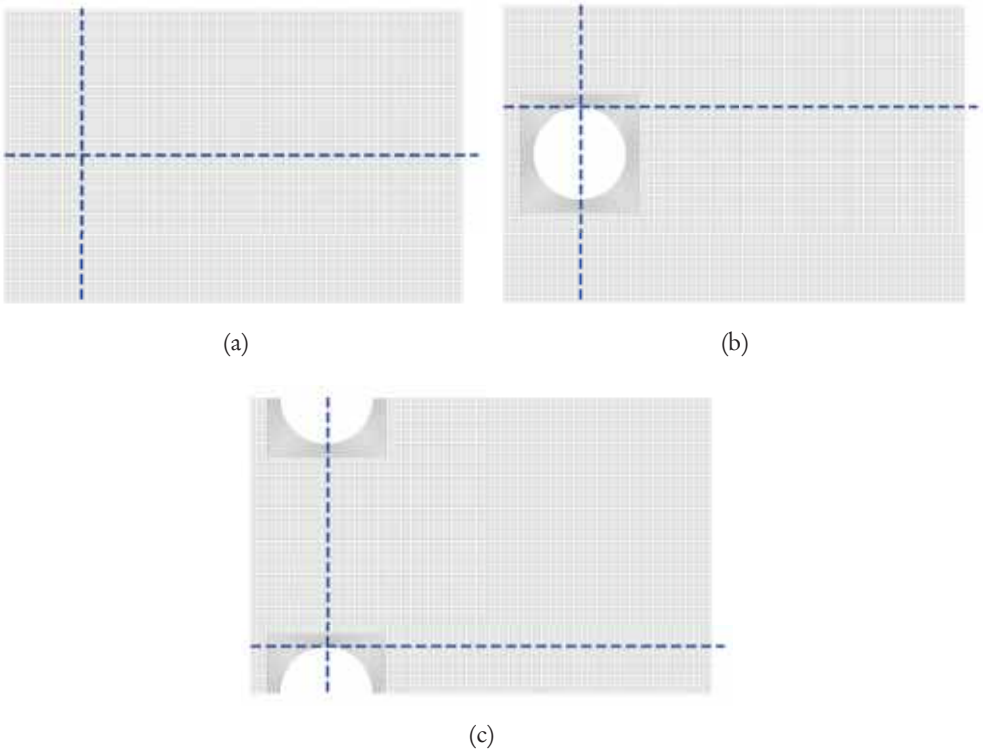

Figure 3.10: Monitored pile localization - (a) Specimen 0 - (b) Specimen 1 - (c) Specimen 2

3.4.1.1 Analysis of through-thickness effects on stress fields

To analyse through-thickness effects, stress component σ_{zz} (Figure 3.11), principal stresses (Figure 3.12) and their ratios (Figures C.1 and C.2) were computed for each pile. One can observe that:

- according to Figure 3.11, σ_{zz} levels are low w.r.t. equivalent pressure loading ($\propto 10^3$ MPa). Lowest values are closed to edges, *i.e.*, the farthest from the core, the more plane stress state is likely to be valid;
- according to Figure 3.12, Figures C.1 and C.2, the lowest principal stress (in magnitude) is not negligible compared to the others, notably for Specimens 1 and 2. For Specimen 0, ratios are lower than 2% (Figure C.1(a) and Figure C.2(a)) at the edges, hence plane stress hypothesis which may be assumed there. However, geometrical singularities neighbourhoods are confirmed to be critical as ratios are higher than 10% in those areas.

Finally, through-thickness effects seems more important for Specimens 1 and 2 than for Specimen 0. However, this does not tell anything about the consequences on stress fields computation. This is studied in the next paragraph.

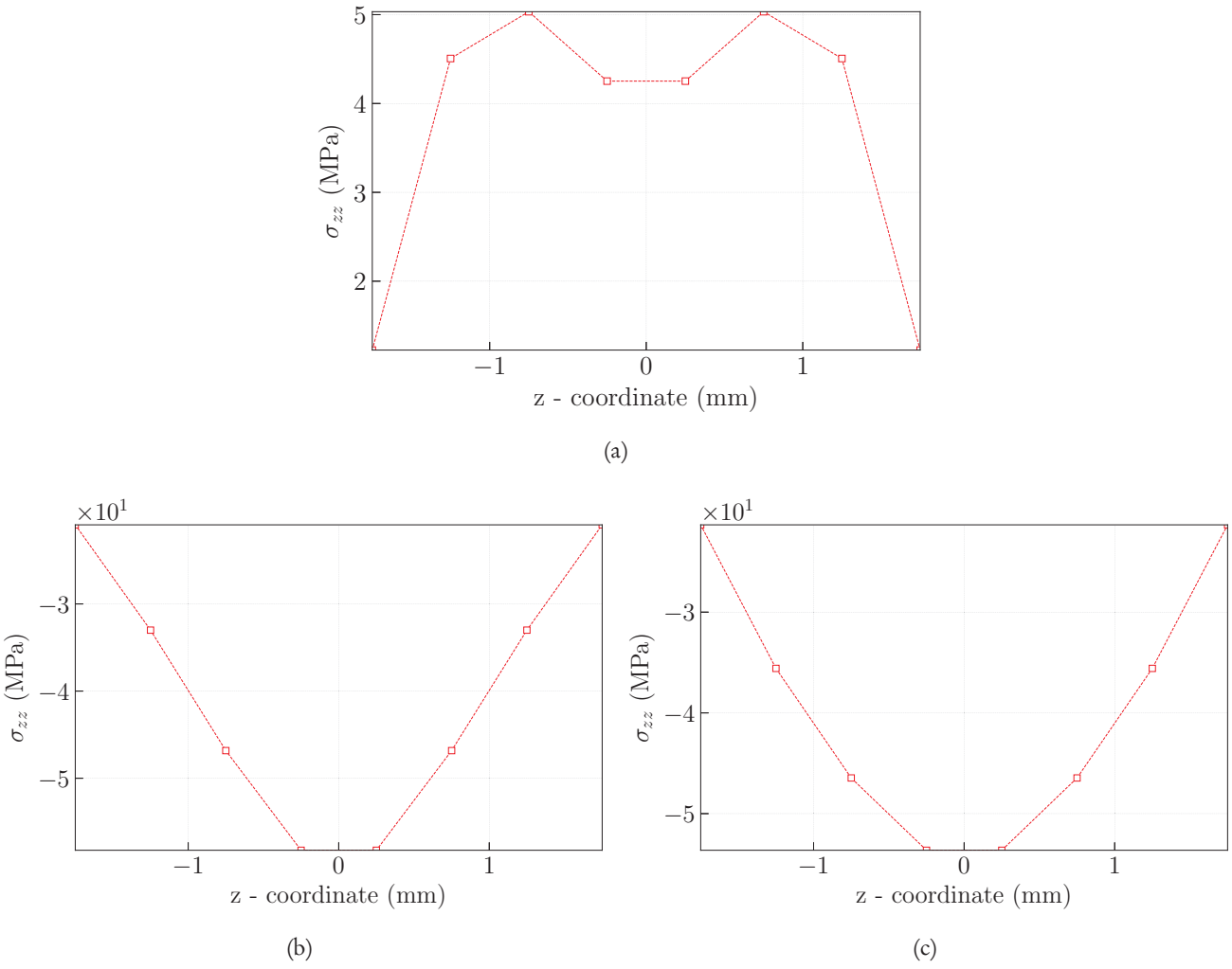

Figure 3.11: σ_{zz} mean time value, V_p= 70 m.s^{-1} - (a) Specimen 0 - (b) Specimen 1 - (c) Specimen 2

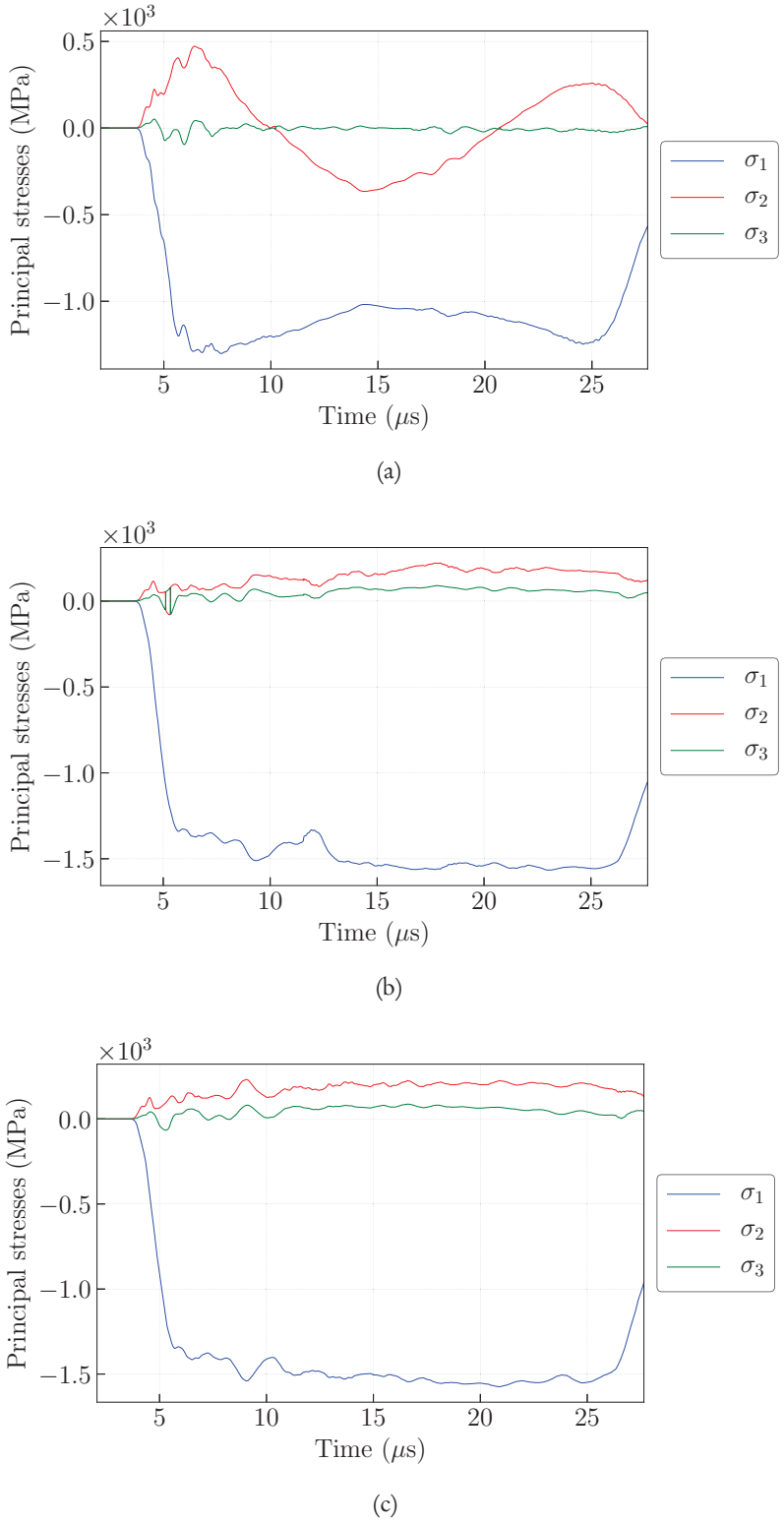

Figure 3.12: Principal stresses mean time value, V_p=70 m.s^{-1} - (a) Specimen 0 - (b) Specimen 1 - (c) Specimen 2

3.4.1.2 Influence of plane stress hypothesis on stress reconstruction

During the identification process, one part of systematic error is due to stress reconstruction. As only in-plane information is measured, plane stress hypothesis is assumed. However, the introduction of geometric singularities may hinder an accurate reconstruction as highlighted in previous paragraph. To quantify this influence, 2D and 3D reconstructions (Table 3.3) were performed using strain fields from the skin mesh using the Return Mapping Algorithm (RMA) of our numerical toolbox (see Section 2.1).

Table 3.3: RMA features

	Inputs	Outputs
Bidimensional (plane stress)	$\varepsilon_{xx}, \varepsilon_{yy}, \varepsilon_{xy}$	$\varepsilon_{zz}, \sigma_{xx}, \sigma_{yy}, \sigma_{xy}, \sigma_{zz} = 0$
Tridimensional	$\varepsilon_{xx}, \varepsilon_{yy}, \varepsilon_{zz}, \varepsilon_{xy}, \varepsilon_{yz}, \varepsilon_{xz}$	$\sigma_{xx}, \sigma_{yy}, \sigma_{zz}, \sigma_{xy}, \sigma_{yz}, \sigma_{xz}$

Figure 3.13, Figure 3.14, Figure 3.15 (complementary results are provided in Appendix C) report a comparison between 2D and 3D RMA outputs of each upper element of the pile as localized in Figure 3.10. It can be observed that:

- for both cases (2D and 3D) and for all specimens, stress fields (Figure 3.13) are well reconstructed;
- viscoplastic mechanical fields such as p (Figure 3.14), $\dot{p}$ (Figure 3.15) or σ_y (Figure C.3) does not seem to be affected by plane stress hypothesis;
- each configuration seems to be eligible for plane-stress hypothesis.

For all reported mechanical fields, no difference are observed "with the naked eye" except for the stress component σ_{xx} for Specimens 1 and 2. Even through-thickness strain ε_{zz} was well retrieved, though only surface information was used. Globally, stress fields reconstruction is not notably hindered by plane stress hypothesis, insofar as the gap between 3D and 2D reconstructions is lower than 5% (Figure C.7), this corresponding to about 50 MPa (Figure C.6). This effect is more pronounced near geometrical singularities, as expected.

3.4.1.3 Conclusion

This study quantifies effect of plane stress hypothesis on stress fields computation for the proposed IBII test configurations. Generally speaking, even if only in-plane components of strain fields were used, the computed mechanical fields were consistent. As expected, the results were more accurate in absence of holes and notches. However, gaps were observed locally (near the singularities), but the identification may not be jeopardized, since the stress reconstruction error remains low. To evaluate this influence, one needs to perform the identification with surface information only: this is discussed in the next section.

3.4.2 Influence of temporal resolution and impact velocity on viscoplastic parameter extraction

The cost function to be minimized through the VFM process (Equation 1.14) is built with the virtual field defined by Equation 3.2 (where L_s is the specimen length) which remains constant at each time step i because the PVW is always computed using initial coordinates of points of measurement. Finally, Equation 3.3 is obtained, where $\underline{X}$ is the set of material parameters (here reduced to JC viscoplastic parameter M), M_i the number of "generated" synthetic images and M_p the number of measurement points.

$$\left| \begin{array}{lcl} u_x^* & = & x(x - L_s) \\ u_y^* & = & 0 \end{array} \right| \quad \left| \begin{array}{lcl} \varepsilon_{xx}^* & = & 2x - L_s \\ \varepsilon_{yy}^* & = & 0 \\ \varepsilon_{xy}^* & = & 0 \end{array} \right| \tag{3.2}$$

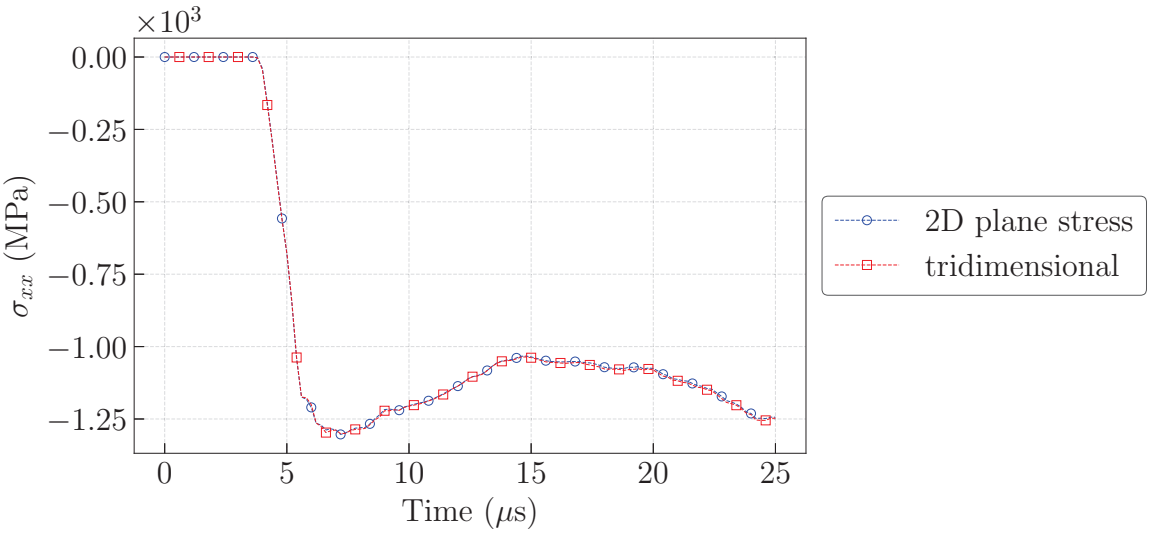

(a)

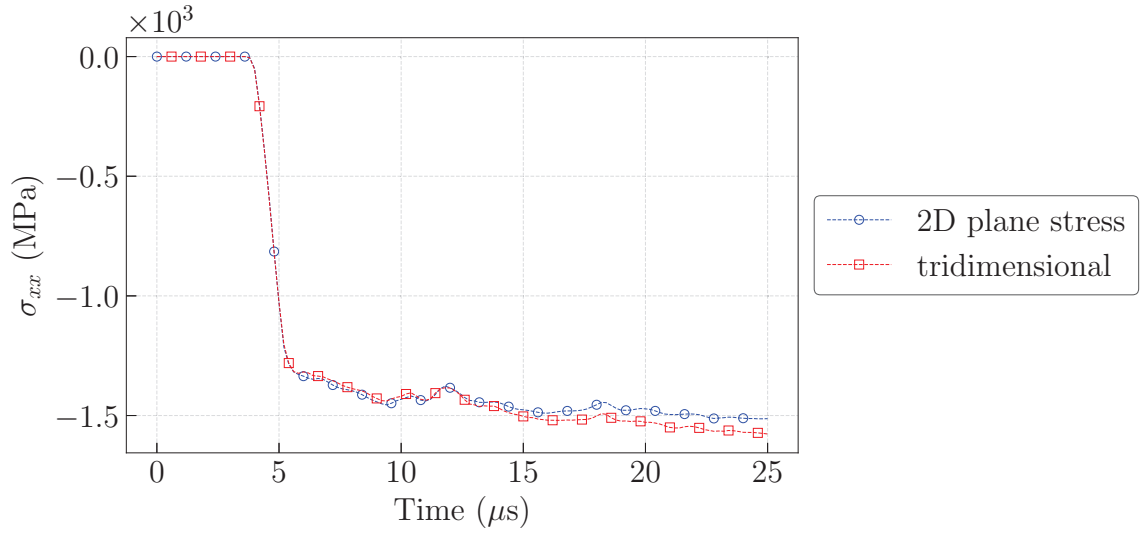

(b)

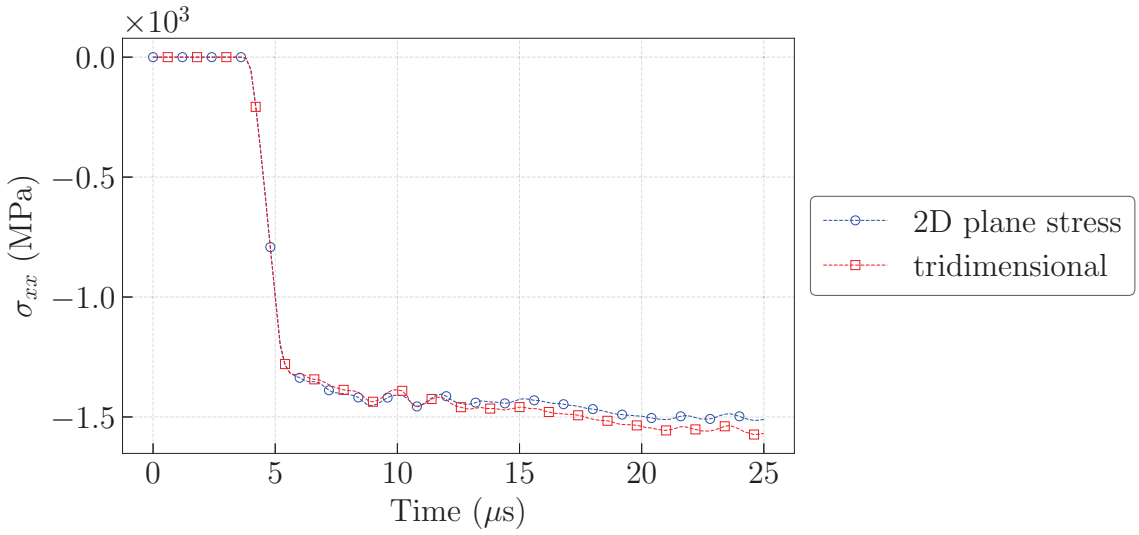

(c)

Figure 3.13: σ_{xx} reconstruction, V_p=70 m.s^{-1} at 5 Mfps - (a) Specimen 0 - (b) Specimen 1 - (c) Specimen 2

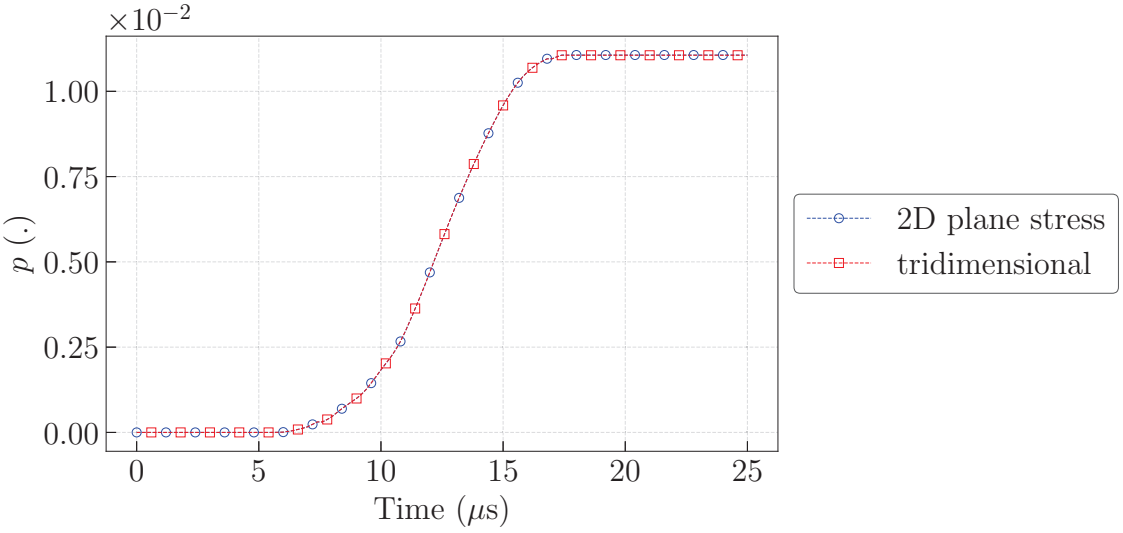

(a)

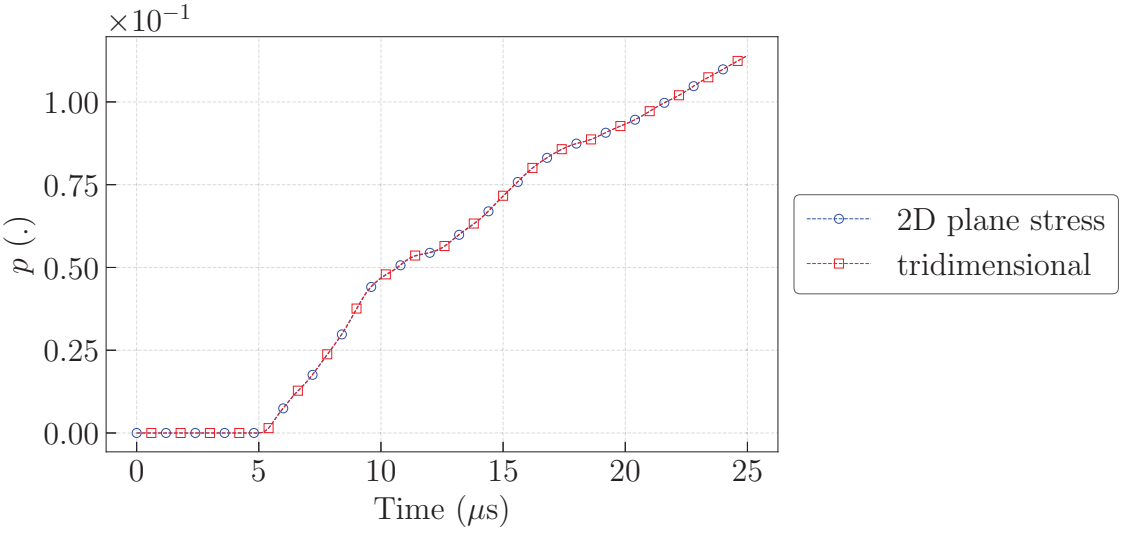

(b)

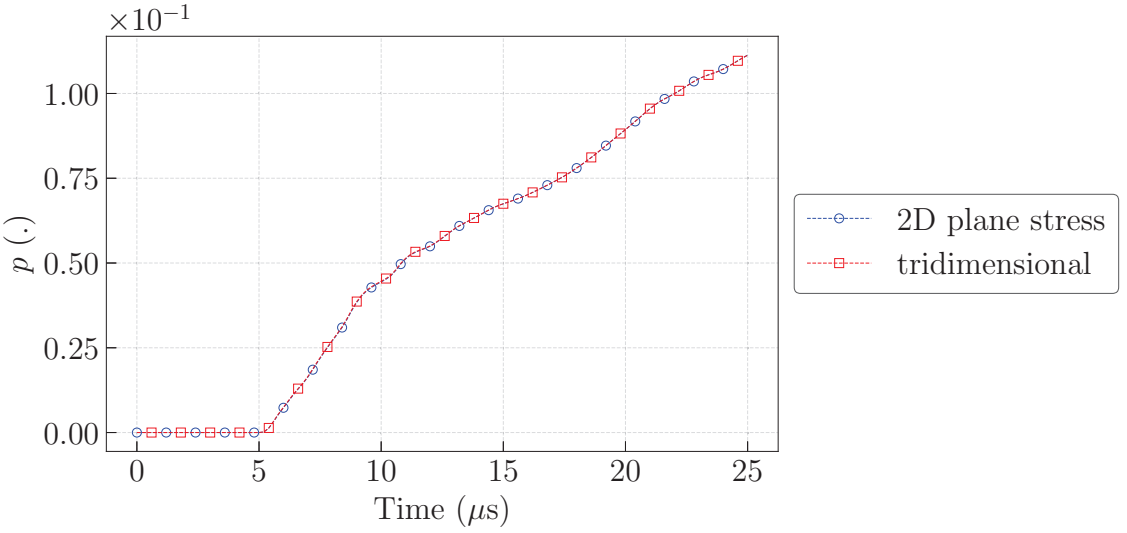

(c)

Figure 3.14: p reconstruction, V_p= 70 m.s^{-1} at 5 Mfps - (a) Specimen 0 - (b) Specimen 1 - (c) Specimen 2

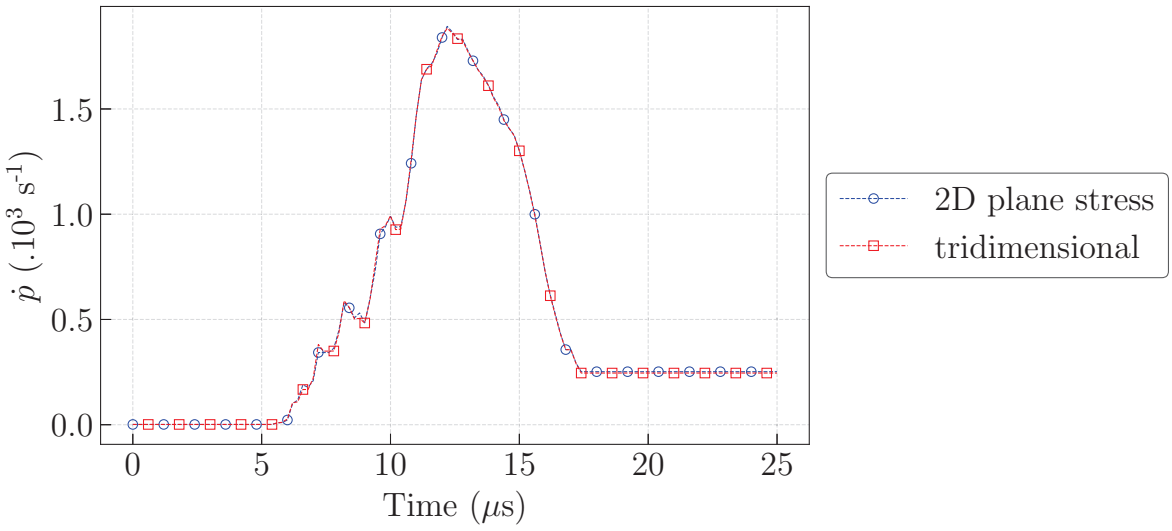

(a)

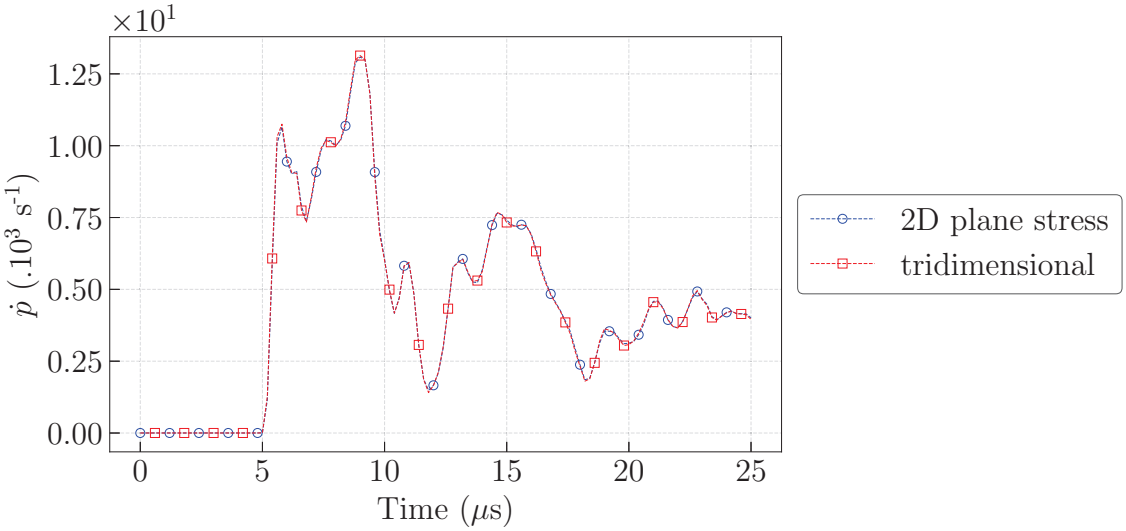

(b)

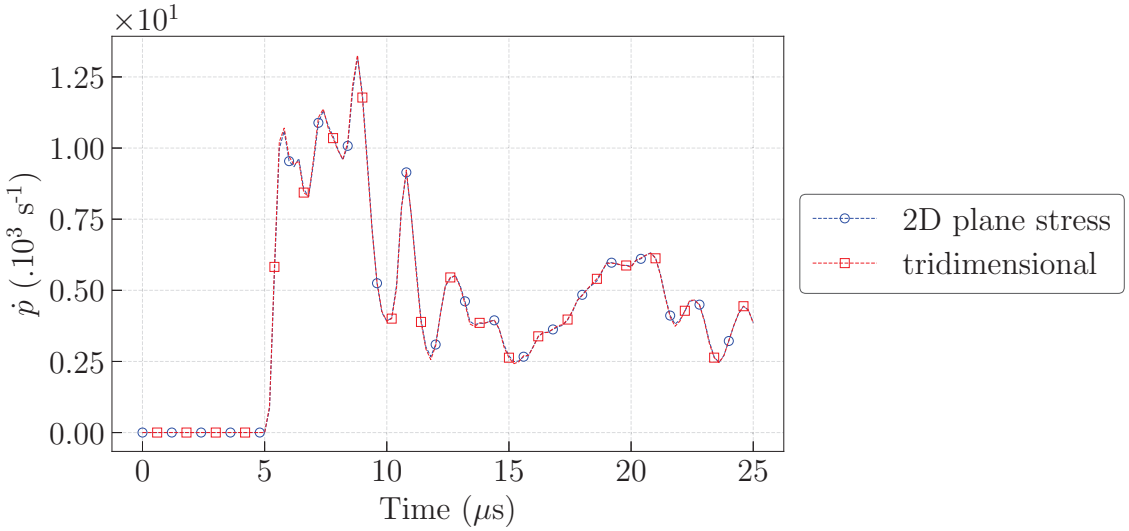

(c)

Figure 3.15 : $\dot{p}$ reconstruction, V_p= 70 m.s^{-1} at 5 Mfps - (a) Specimen 0 - (b) Specimen 1 - (c) Specimen 2

$$\Phi(\underline{X}) = \sum_{i}^{M_i} \left[1 + \frac{\sum_{k=1}^{M_p} \left[\sigma_{xx}(i,k,\underline{X}) \overline{2x - L_s}^{S(k)} \right]}{\rho \sum_{k=1}^{M_p} \left[\gamma_x(i,k) \overline{x(x-L_s)}^{S(k)} \right]} \right]^2 \tag{3.3}$$

Extraction of viscoplastic parameters with the VFM requires the knowledge of several mechanical quantities computed from temporal and spatial differentiations of displacements to express the cost-function $\Phi(\underline{X})$ (Equation 3.3) built from the reduced expression of the PVW (Equation 1.20). As presented in Section 2.1, a Return Mapping Algorithm was implemented and validated to compute stress fields from strains with the JC model rate-dependent constitutive equations. It uses a backward Euler method for time integration owing to its unconditional stability. However, this is a one step numerical scheme, hence integration highly depends on the size of the time increment, *i.e.*, experimentally on the camera frame rate.

The aforementioned VFM toolchain (enabling the identification of JC viscoplastic parameter M) was input with FEA strain and acceleration fields of the skin mesh for various temporal resolution in order to simulate different camera frame rates (see Figure 3.1 - Step 2.1). In practice, temporal resolution was varied by undersampling FEA ouputs. This enables the quantification of systematic identification errors due to temporal resolution and plane stress assumption. Indeed, results of 3D FE simulation (carried out with the suitable conditional time step) can be undersampled to match a given frame rate, and only data on the specimen surface are processed according to the procedure described in Section 2.4. Finally, the identified value of M is compared to the reference value (input in the FE simulation) for the three considered specimen geometries and the three impact conditions, *i.e.*, V_p = 57 m.s^{-1} (Figure 3.16(a)), V_p = 70 m.s^{-1} (Figure 3.16(b)) and V_p = 80 m.s^{-1} (Figure 3.16(c)).

For all IBII tests configurations, the identification converges towards the reference value (Figure 3.16), when the simulated frame rate matches the FE simulation time step (20 Mfps for Specimen 0 and 40 Mfps for Specimens 1 and 2). This demonstrates the relevancy of the plane stress assumption because JC viscoplastic parameter M reference value is retrieved based on surface strains and acceleration only. However, the identification is not robust before a minimum temporal resolution of 4 Mfps for all projectile velocities. Part of the systematic error is due to constitutive equation integration, whichever the specimen geometry. Furthermore, the identification of JC viscoplastic parameter M is sensitive to the impact speed, as expected. Indeed, the slowest velocity (Figure 3.16(a)) depicts a faster convergence towards reference value. If the velocity is higher, (Figure 3.16(b) and Figure 3.16(c)), p and $\dot{p}$ temporal gradients are logically higher, and identification is more sensitive to frame rate.

Now that systematic errors due to plane stress assumption and temporal resolution have been investigated based on FE data (*e.g.*, underestimation of value of M by 2%, 3.4% and 2.5% for Specimens 0, 1 and 2 respectively at 4 Mfps and V_p = 70 m.s^{-1}), the use of the synthetic grid deformation procedure is explored to study in more depth the effects of camera specifications (spatial and temporal resolution) and noise/regularization on the identification performance.

3.5 Optimization of kinematic fields extraction process through uncertainties quantification

3.5.1 Methodology

Because of limited interframe time and spatial resolution, UHS cameras may provide data which are not accurate enough for material parameters identification under high strain rate loadings, in the presence of high spatial and temporal gradients of displacement and strain. Even if recent cameras offer

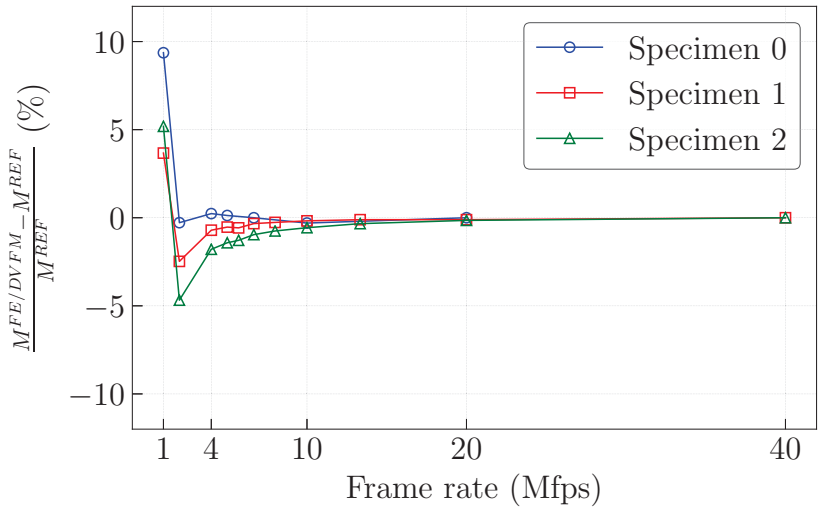

(a)

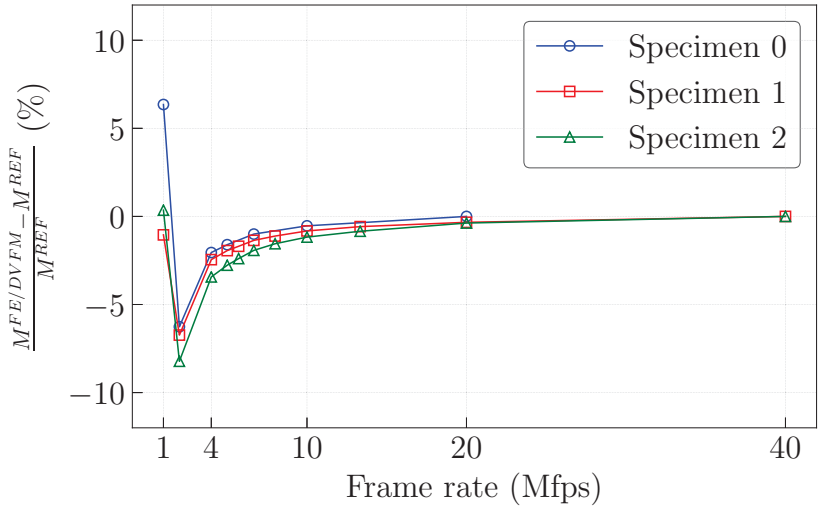

(b)

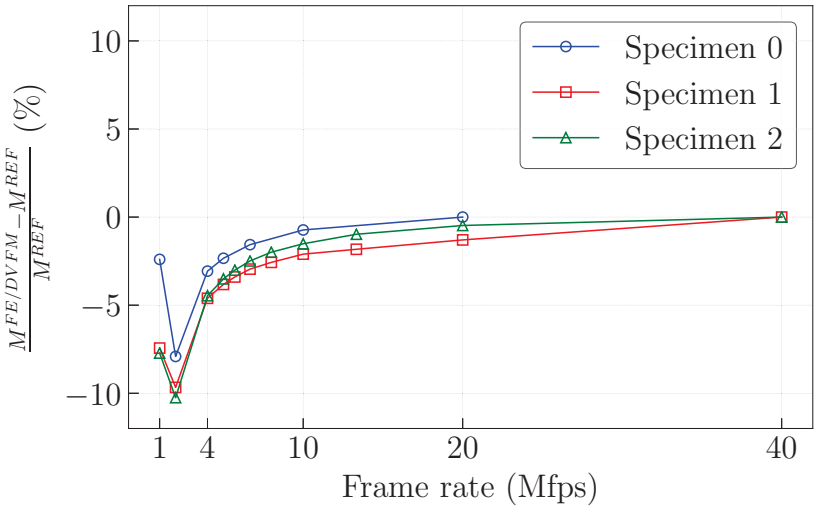

(c)

Figure 3.16: Identification results of viscoplastic parameter - (a) $V_p = 57$ m.s^{-1} - (b) $V_p = 70$ m.s^{-1} - (c) $V_p = 80$ m.s^{-1}

better temporal resolution suitable for dynamic testings (at least 1 Mfps), spatial resolution often remains low (see the Shimadzu HPV-X® properties in Table 4.1). In previous section, the minimum temporal resolution which is necessary for robust JC viscoplastic parameter for the proposed VFM toolchain was established at 4 Mfps. Yet, full-field measurements bias were not taken into account.

The aim of this section is to analyse for each proposed specimen the influence of camera temporal and spatial resolutions for the identification of viscoplastic parameter M (see Figure 3.1 - Step 3.1.1.1). Therefore, synthetic images have been generated from simulated IBII tests with V_p = 70 m.s^{-1} for the three specimens up to 10 Mfps. While the spatial resolution is directly taken into account by the digitization, temporal resolution is tuned by undersampling the results time history. Finally, the images are processed to identify parameter M using the complete chain summarized in Figure 3.17.

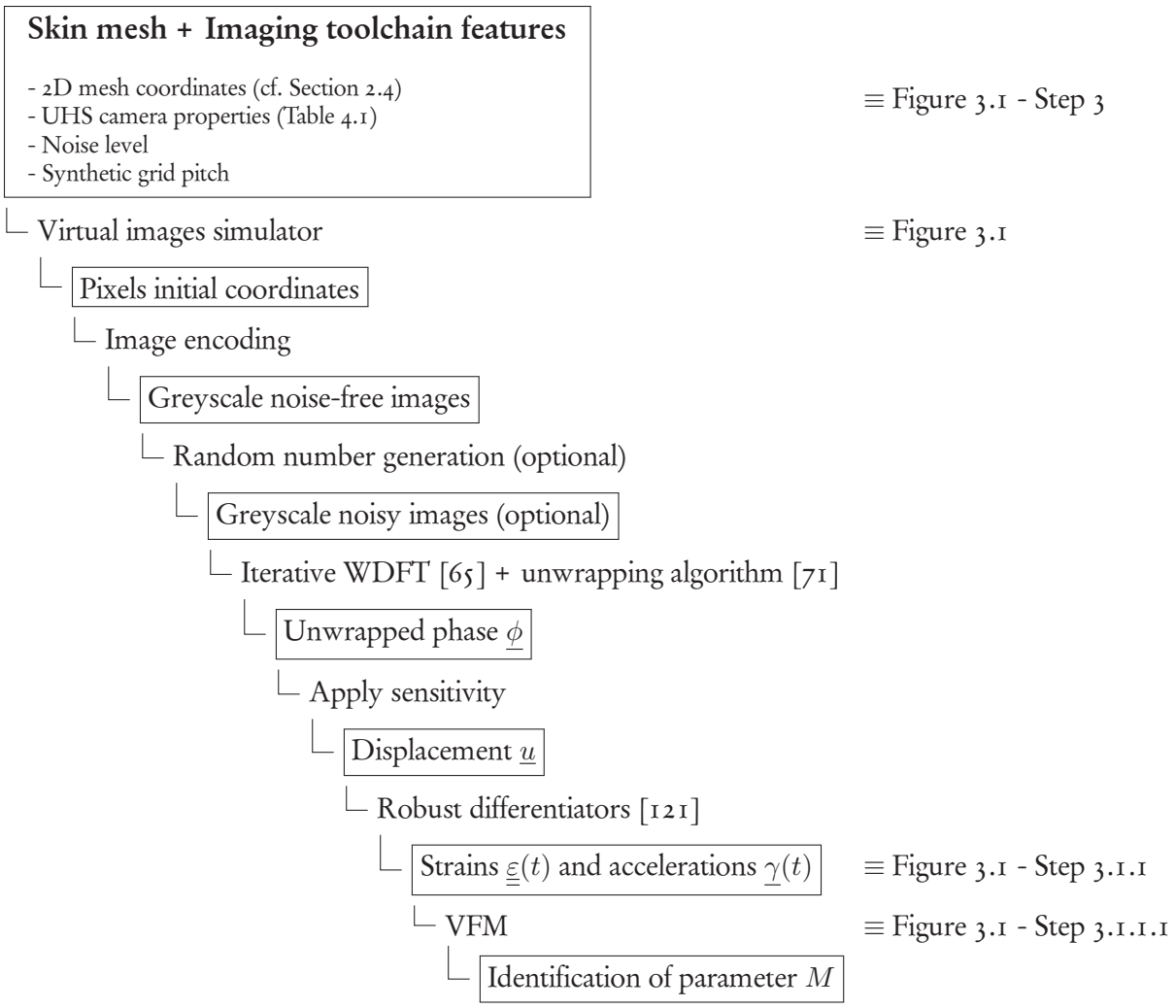

Figure 3.17: Flowchart for VFM on synthetic images

The procedure can be apply to perfect or noisy images (Figure 3.18). The latter are generated by adding random normally-distributed (over 1.5% of the camera dynamic range) integers to the noise-free greyscale images. The robust differentiators introduced in Section 2.2 are used on noisy images to provide some regularization. The stencil sizes, (N_{p1} and N_{p2}) (see Equation 2.19 and Table 2.4) are the regularization parameters.

For given camera properties, the regularization parameters will be selected as those minimizing the expanded uncertainty on the identified JC viscoplastic parameter M. The expanded uncertainty is defined here as $\epsilon^{expanded} = \epsilon^{noise-free} + \epsilon^{random}$, where $\epsilon^{noise-free}$ is the systematic error calculated based on noise-free images and $\epsilon^{random} = 2\sigma[\epsilon^{noise}]$ is the random error, computed here as the standard deviation of the distribution of identified M for six sets of noisy images for each specimen geometry.

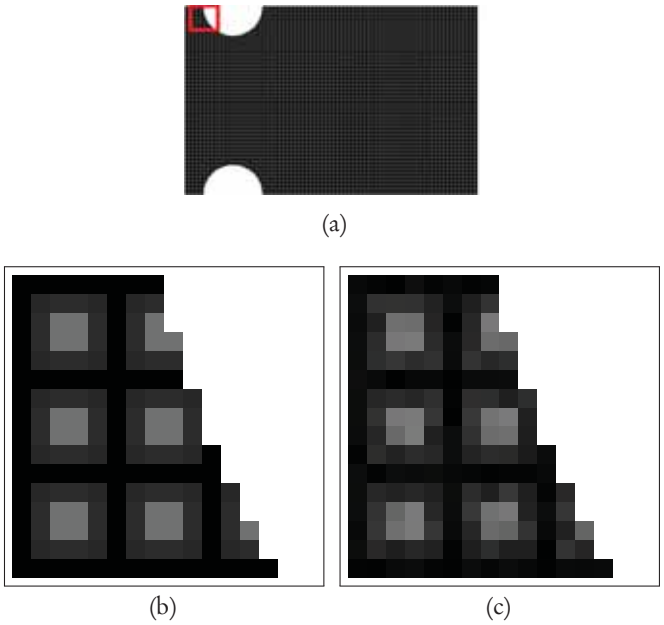

(a) (b) (c)

Figure 3.18: Example of synthetic images processed by the grid method - (a) Full initial synthetic image (Specimen 2) - (b) Zoomed in view without noise - (b) Zoomed in view with noise

3.5.2 Optimization of regularization parameters

Figure 3.19 maps the systematic error $\epsilon^{noise-free}$ on parameter M for the three specimen geometries imaged at 4 Mfps. For noise-free images, regularization reduces strain and acceleration peaks, so that the identification error increases with stencil size. The lowest error is obtained without regularization, corresponding to the use of central finite difference scheme to calculate strains and accelerations. As expected, notched and holed configurations (Specimens 1 and 2) are more sensitive to spatial regularization than Specimen 0, because of the presence of higher spatial gradients. They seem slightly more sensitive to temporal regularization though this may not be significant.

Figure 3.20 maps the expanded uncertainty $\epsilon^{expanded}$ in presence of noise, for the same identifications. It was impossible to identify a value for the JC viscoplastic parameter M without temporal regularization. This was somewhat expected as acceleration fields require a double time-differentiation. Consequently, the set of optimal parameters is "shifted" from no regularization (in case of noise-free data) to both/either temporal and/or spatial regularization to a bit of temporal regularization (5 data points stencil). The mapping of standard deviation ϵ^{random} (Figure 3.21) shows that its magnitude is hardly sensitive to regularization parameters, so that for a given set of temporal and spatial stencils, expanded uncertainty is mostly dominated by the systematic error rather than the random one.

Applying this methodology for different IBII test configurations and achievable frame rates enables uncertainty quantification with respect to regularization parameters. Table 3.4 reports some examples of optimized SNR parameters values for affordable spatial and temporal resolutions. The overall results are reported in Figure 3.22 with optimal regularization parameters. At 4 Mfps, the identification error (systematic and random) is stabilized for all specimens as with FEA data (Figure 3.16(b)).

Table 3.4: Optimized values for SNR parameters (based on Shimadzu HPV-X specifications)

	N_{p1} (Spatial)		N_{p2} (Temporal)	
	400 × 250, 4 Mfps	400 × 250, 5 Mfps	400 × 250, 4 Mfps	400 × 250, 5 Mfps
Specimen 0	1	4	2	4
Specimen 1	4	4	2	4
Specimen 2	1	4	2	4

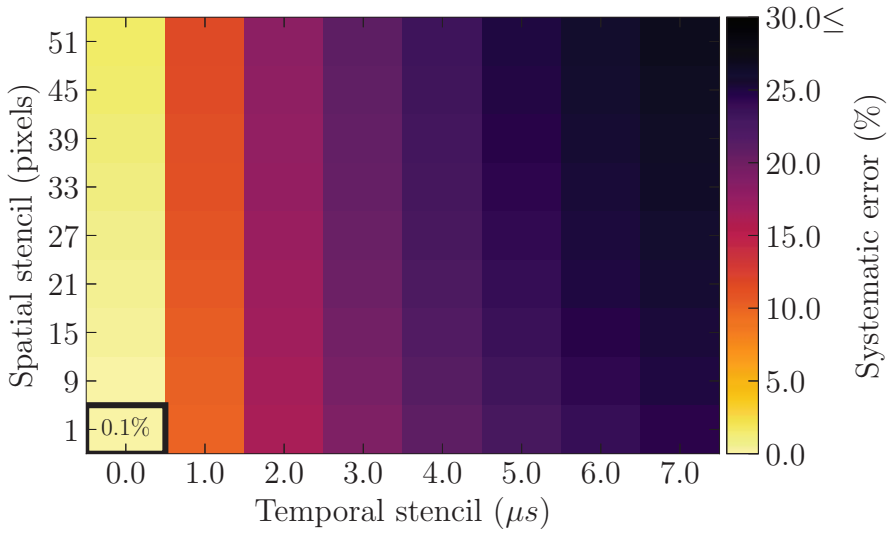

(a)

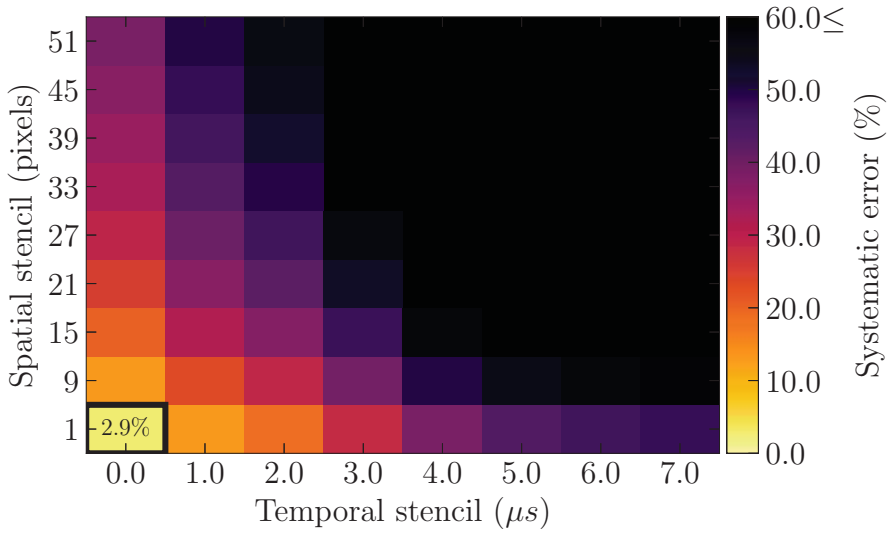

(b)

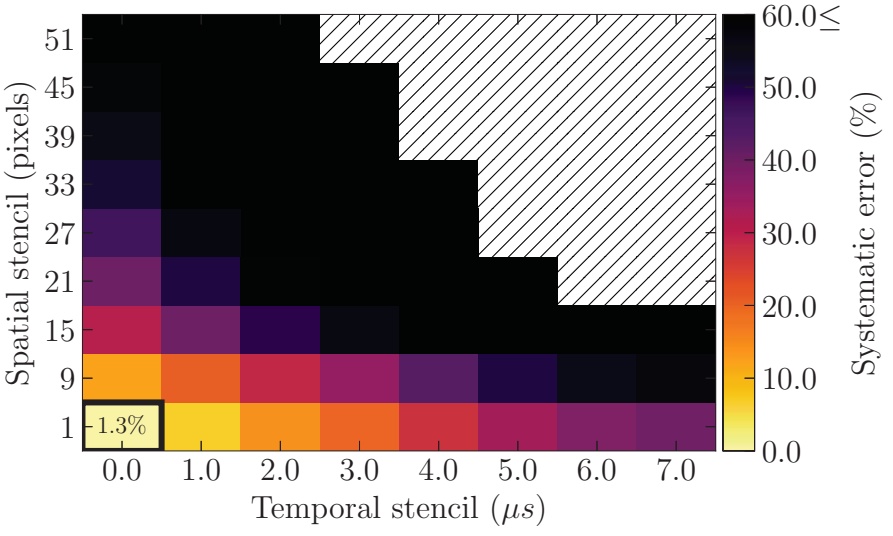

(c)

Figure 3.19: Systematic error $\epsilon^{noise-free}$ on parameter M at 4 Mfps and for V_p=70 m.s^{-1} (unsuccessful identifications in hatched lines) - (a) Specimen 0 - (b) Specimen 1 - (b) Specimen 2

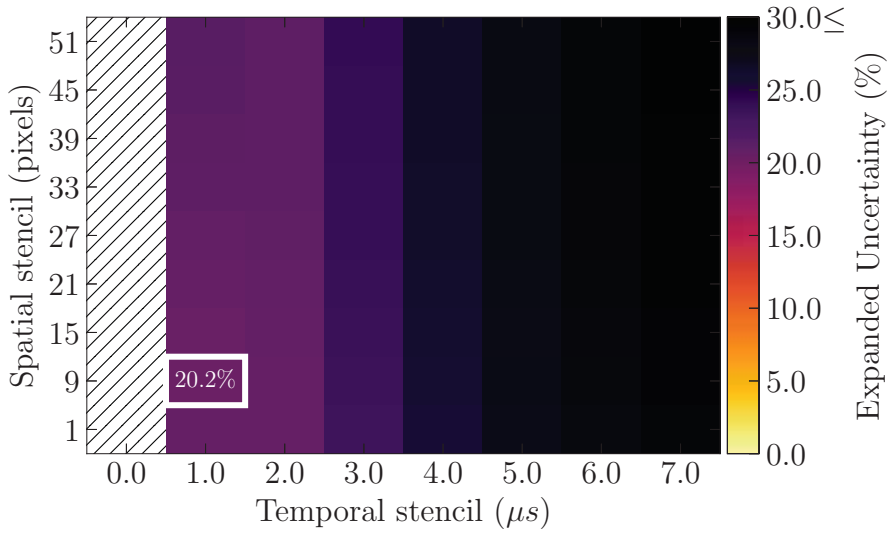

(a)

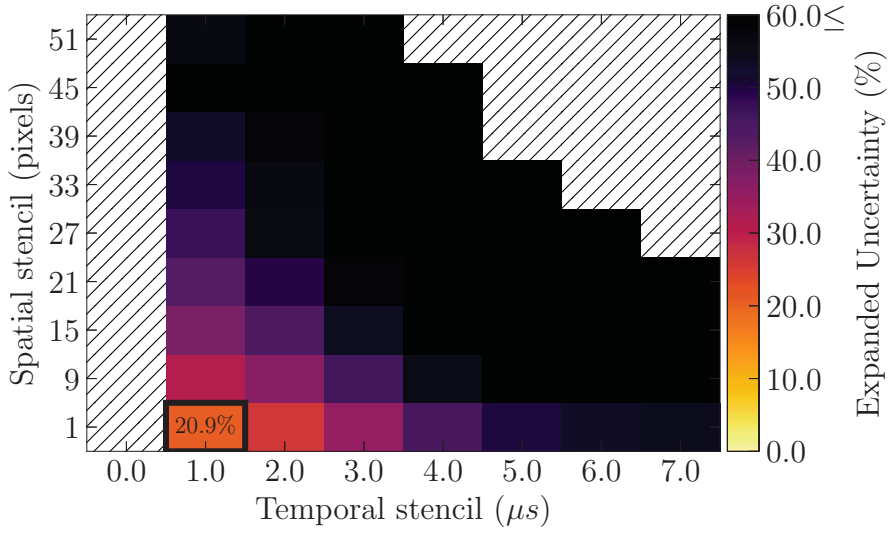

(b)

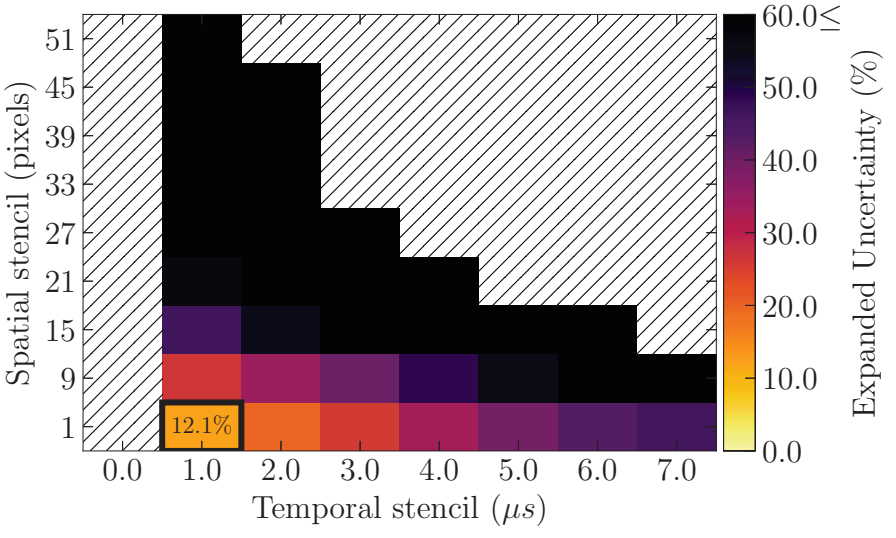

(c)

Figure 3.20: Expanded uncertainty $\epsilon^{expanded}$ on parameter M at 4 Mfps and for V_p=70 m.s^{-1} (unsuccessful identifications in hatched lines) - (a) Specimen 0 - (b) Specimen 1 - (b) Specimen 2

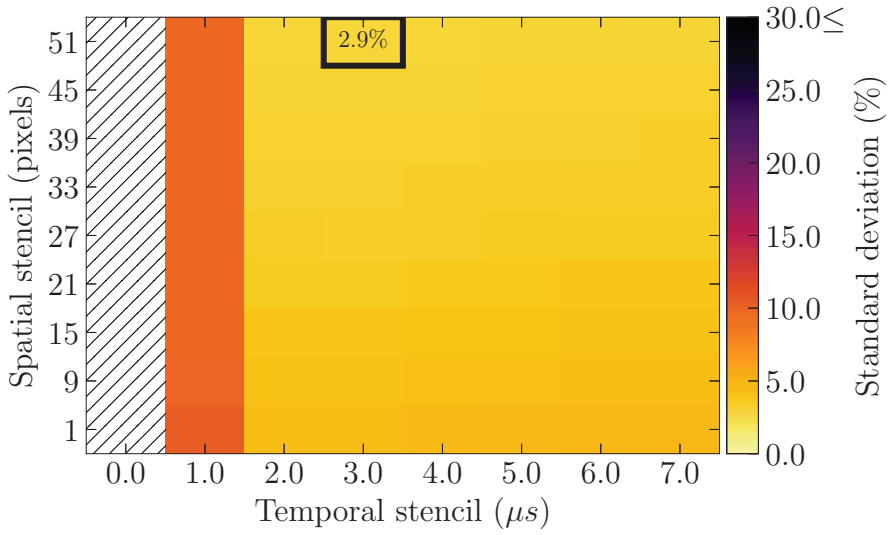

(a)

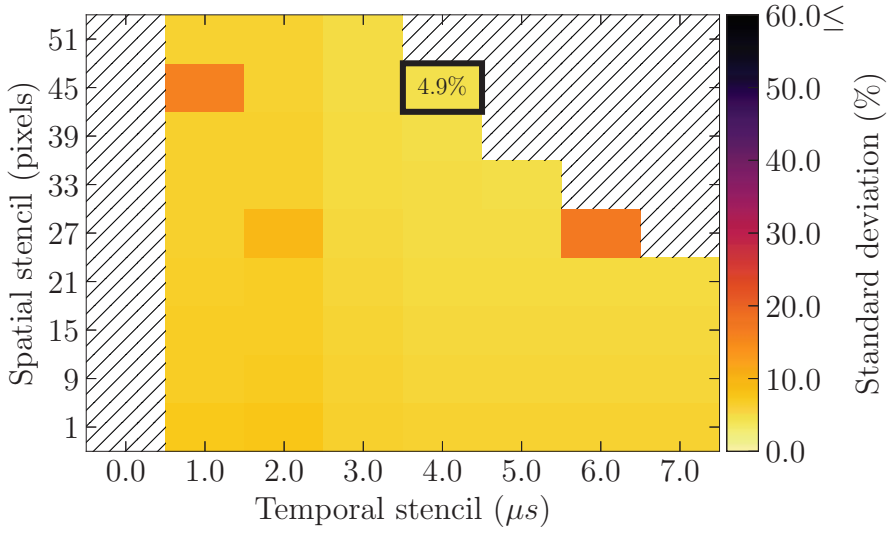

(b)

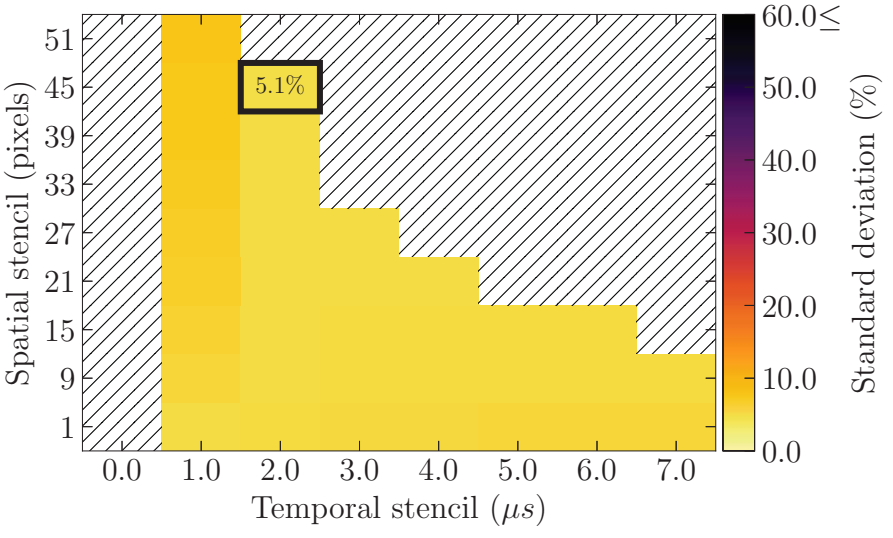

(c)

Figure 3.21: Random error ϵ^{random} on parameter M at 4 Mfps and for V_p=70 m.s^{-1} (unsuccessful identifications in hatched lines) - (a) Specimen 0 - (b) Specimen 1 - (b) Specimen 2

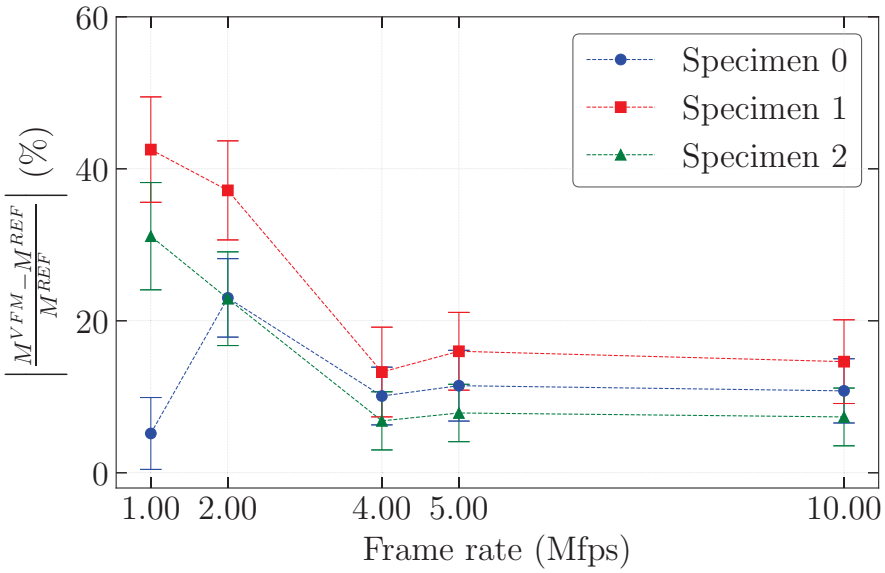

Figure 3.22: Identification gap w.r.t reference value on noisy images

To analyse the impact on material behaviour of the predicted expanded uncertainty on identified value of parameter M , the return mapping algorithm has been input with FEA strains for each specimen and values of M identified at 4 Mfps for the same specimen. Figure 3.23 shows the elements (pointed out by the dotted lines) that are monitored in each case. They have been chosen as critical zones over which viscoplastic parameter strongly influences the stress field (and therefore corresponds to areas where the impact of error on M value is maximized). For those elements, the reconstructed curves (with the identified parameter) of σ_y and $\dot{p}$ as a function of p have been compared to the ones extracted from FEA (Figure 3.24). It is worth noticing that identified parameters lead to consistent results, with a better accuracy for the notched specimen (Specimen 2) as expected according to the prediction of uncertainty. For this specimen, the yield stress computed by FEA almost lies within the uncertainty domain, whichever the cumulated plastic strain-rate (up to about 10^4 s^{-1}). However, the results are less satisfying for the two other specimens (Specimen 0 and 1). This was expected according to the higher expanded uncertainty.

This work on synthetic images reveals the advantages and drawbacks of the proposed IBII test configurations and VFM toolchain in more realistic conditions. The low systematic error on noise-free synthetic images validates full-field measurement processing, notably the plane stress assumption and data extrapolation due to information lost on specimen edges. This is particularly important as for the holed and notched specimens, large strains and strain rates occur at the edge root of the concentrator. Moreover, the analysis of the expanded uncertainty on the identification of M enables the selection of notched specimen with respect to rectangular and holed specimens.

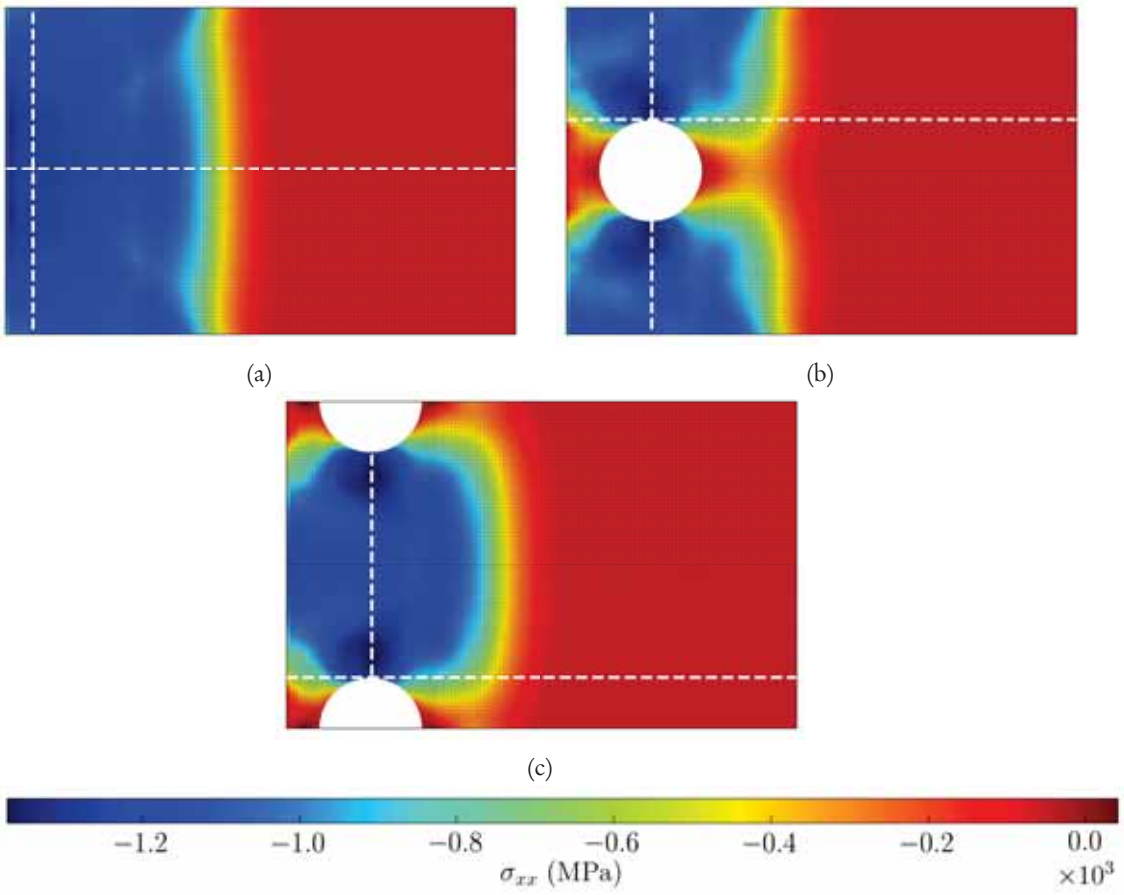

Figure 3.23: σ_{xx} at t = 6μs - (a) Specimen 0 - (b) Specimen 1 - (b) Specimen 2

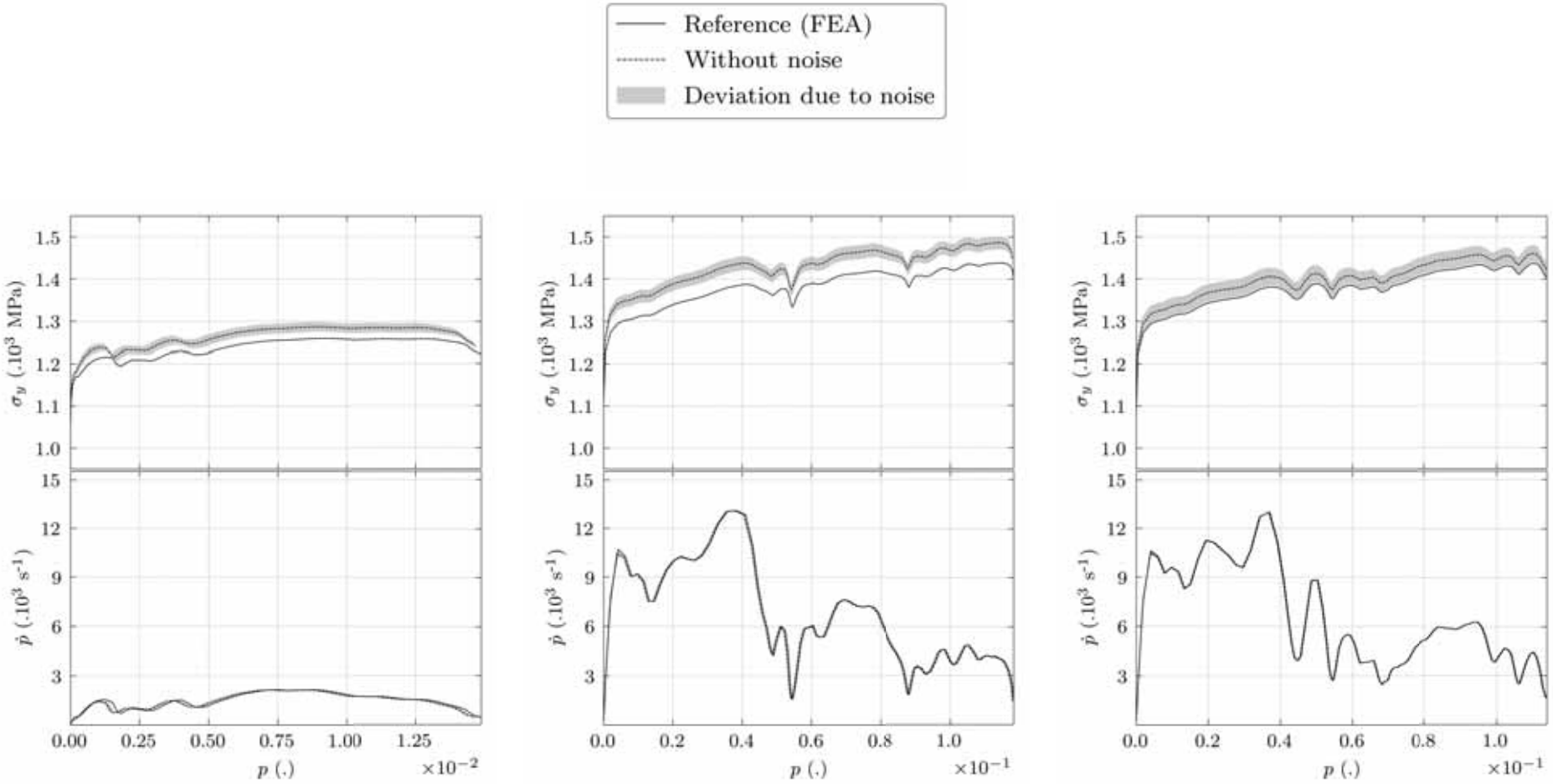

Figure 3.24: σ_{xx} reconstructed with identified values - (a) Specimen 0 - (b) Specimen 1 - (c) Specimen 2

3.6 Conclusion and further prospects

This chapter reports the methodology to design Image-Based Inertial Impact (IBII) tests for the characterization of viscoplasticity at high strain rate. This test has been recently introduced to take advantage of the VFM which enables the identification of material parameters with the sole knowledge of strain and acceleration fields. As this work is seminal for IBII tests and rate-dependent material behaviour characterization, it was attempted to understand IBII test parameters influence on the identification performance.

Finally, the current study has led to the following conclusions:

- to increase the strain rate heterogeneity, it is necessary to "machine" holes/notches. However, this has to be done carefully because it may jeopardize material parameter identification if spatial resolution is low;
- the VFM enables the identification of JC viscoplastic parameter M with IBII tests. However, the identification toolchain (including regularization parameters), has to be tuned carefully notably to extract strain and acceleration fields from noisy displacement maps;
- the notched specimen is less sensitive to noise while guaranteeing identification over a wider viscoplastic spectra than the rectangular and the holed specimen. However, this conclusion is only valid for the impact conditions and the VFM procedure considered in this work.

In conclusion, Shimadzu HPV-X® camera features with the proposed IBII tests are suitable for JC model characterization. This opens up the way to experimental implementations, which are reported in the next chapter.

Chapter 4

Image-Based Inertial Impact test campaign for Ti6Al4V strain-rate sensitivity characterization

Contents

Abstract

This chapter presents the test campaign which have been carried out with the IBII methodology to characterize the strain-rate sensitivity of a titanium alloy (Ti6Al4V). A series of eleven IBII tests is performed at the University of Southampton (UK), considering different geometries defined with the numerical analysis. The dynamic VFM is used to identify the Johnson-Cook model viscoplastic parameter. Prior to the identification, metrological performance is also assessed. Finally, a critical comparison between numerical predictions and IBII tests results is performed. This includes the kinematic fields, the identified parameters, the reconstructed mechanical fields and the viscoplastic spectra.

4.1 Description of the test campaign

Chapter 3 has opened up the way for titanium alloy Ti6Al4V viscoplastic behaviour characterization using IBII test methodology. For a projectile fired at $V_p = 70$ m.s^{-1}, the different configurations were suitable for JC model identification over wide ranges of strain and strain rate, depending on the specimen geometry. The further experimental implementation aims at undertaking the IBII test configurations which have been optimized owing to the numerical toolbox. This was done through a processing toolchain that includes the extraction of strain and acceleration fields using SNR differentiators (cf. Table 3.4, p. 95), and the computation of stress fields with the RMA which was implemented and a virtual field suitable for dynamic VFM.

4.1.1 Impact test protocol

The test campaign was performed with the Photodyn group[1] facilities at the University of Southampton (UK). A gas gun apparatus (Figure 4.1) has been designed to apply the IBII test methodology for material testing at high rate [131].

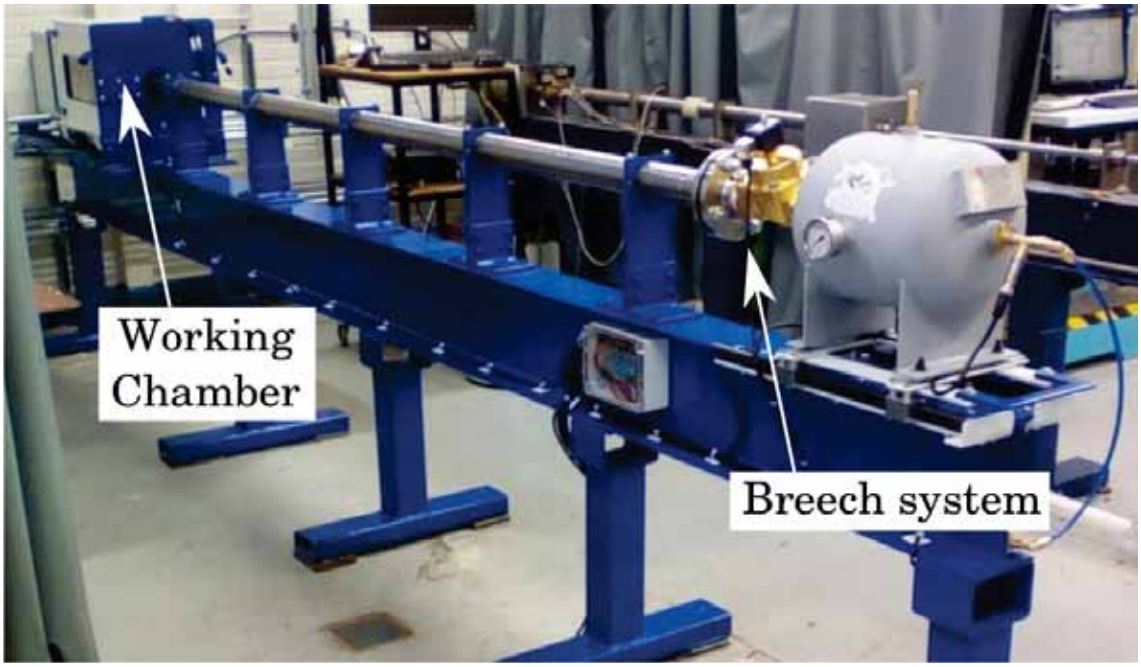

Figure 4.1: Gas gun overview

Some aspects of the testing protocol have been described in a recent paper by Fletcher and Pierron [131]. A breech system (Figure 4.1) enables to load cylindrical projectiles. The latter is set in a polymer sabot to be fired (Figure 4.2(a)). In the working section, specimens are glued to a waveguide with the same shape as the projectile (Figure 4.2(a)). The waveguide lies on a foam stand before impact (Figure 4.2(b)).

The imaging system (Figure 4.3) consists in a Bowens Gemini GM100 Pro® flash and a Shimadzu HPV-X® camera. When the projectile hits the waveguide, an electrical circuit is closed, this triggering the UHS camera recording process. Prior to the impact, projectile velocity is measured owing to light gates at the exit of the barrel and an Arduino Nano® in-house system that calculates the projectile speed in real-time. The calculated projectile speed allows for deriving a specific delay to trigger the flash to account for its 100 microsecond rise time. This is crucial when using the HPV-X camera since 128 frames "only" can be recorded on the FTCMOS sensors.

[1] http://photodyn.org/

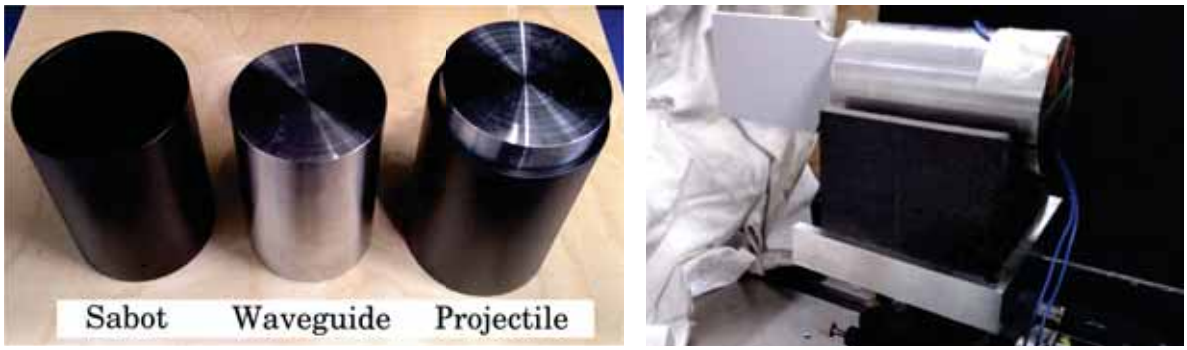

(a) (b)

Figure 4.2: Impact test setup main features - (a) sabot/projectile/waveguide - (b) waveguide on foam stand

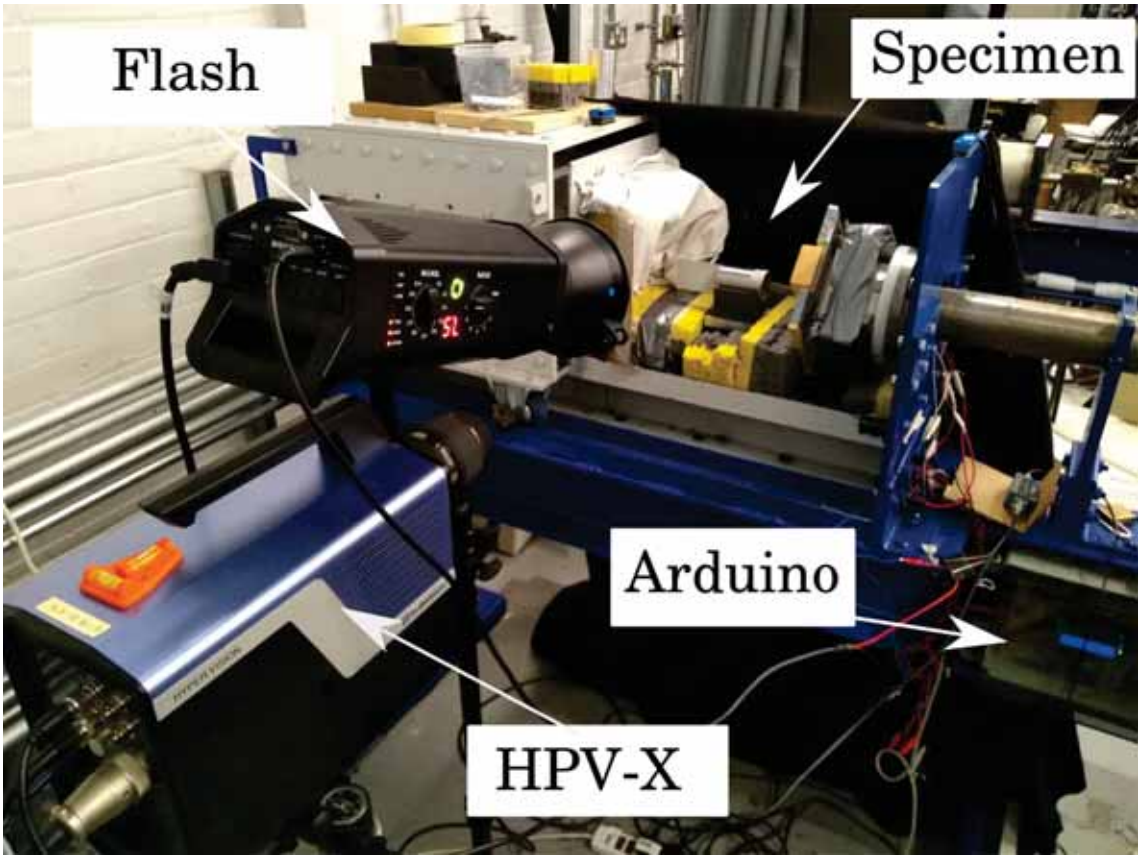

Figure 4.3: Imaging system

To measure displacement fields, grids have been deposited onto the tested specimens. Prior to printing, a thin coat of white paints was deposited onto the specimen to ensure optical contrast with a Canon Océ Arizona 1260 XT® printer. More details can be found online [132, 133]. Figure 4.4 shows an example of these grids. Table 4.1 reports the main features of the metrological toolchain.

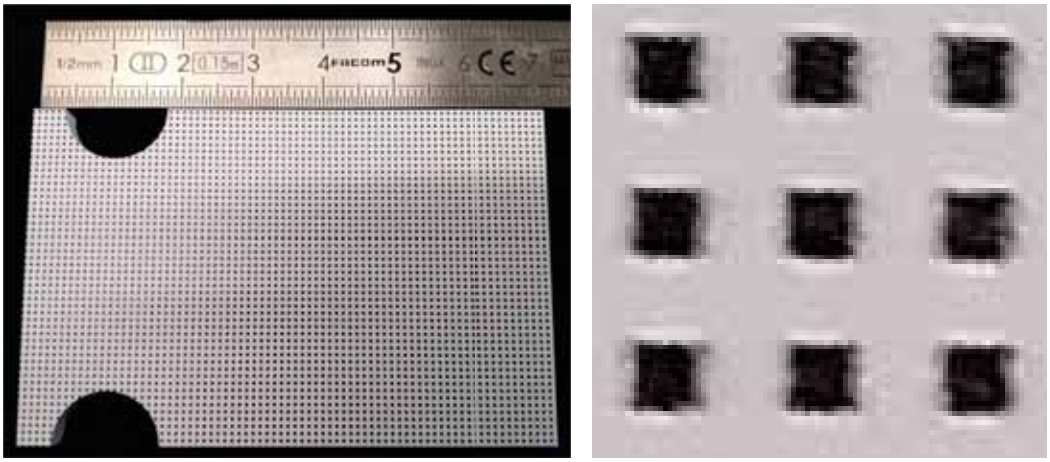

(a) (b)

Figure 4.4: Picture of a grid printed onto a notched specimen - (a) Overall view - (b) Zoomed-in view

Table 4.1: Grid method + features

Resolution	400×250 pixels
Frame rate	5 Mfps
Sensor	FTCMOS (on-chip storage)
Dynamic range	10 bits
Object pixel size	0.182 mm
Grid pitch	5 pixels (0.91 mm)

Projectiles were made of maranging steel. The velocity was constrained by the pressure level supplied in the shared lab (6 bars), corresponding to a projectile velocity of about $V_p = 57$ m.s^{-1}. Overall, eleven specimens (Figure 4.5) with three different geometries (cf. Figure 3.4, p. 77) were tested (Table 4.2).

It is worth noticing that among the reported IBII tests, the rectangular specimens (*i.e.*, ones denoted QUAL-FULL-##) were initially considered as "warm-up" tests. However, some preliminary analyses have shown that they were good enough quality, so they were included in the test matrix.

4.1.2 Metrological performance assessment

Prior to each impact test, a set of 128 images was recorded for each configuration without loading the specimen (referred as the "static reference"). Due to camera noise, their processing with the grid method led to noise maps. Then, measurement resolution of each computed field was calculated as the standard deviation of each data set. Table 4.3 reports the resolutions obtained for strain and acceleration fields. They are computed with and without regularization, the latter corresponding to the optimized SNR parameters determined in Chapter 3 (cf. Table 3.4, p. 95). For each mechanical field, the complete histograms can be found in Appendix D for the optimized SNR parameters.

As observed in Section 3.5 when it was tried to extract material parameters on noisy synthetic images without temporal regularization, acceleration data were incoherent, hence no resolution was reported here. By contrast, it was possible to extract strain maps but the resolution was poor. When optimized SNR parameters are used, the results are more consistent. In particular, the acceleration

Table 4.2: IBII test matrix

Test name	Geometry specifications			Projectile velocity ($m.s^{-1}$)
	Rectangular	Notched	Holed	
QUAL-FULL-01	✓			55.0
QUAL-FULL-02	✓			57.3
CHAR-NOTC-01		✓		57.3
CHAR-NOTC-02		✓		57.3
CHAR-NOTC-03		✓		57.6
CHAR-NOTC-04		✓		57.3
CHAR-NOTC-05		✓		57.7
CHAR-HOLE-01			✓	57.3
CHAR-HOLE-02			✓	57.3
CHAR-HOLE-03			✓	57.7
CHAR-HOLE-04			✓	58.0

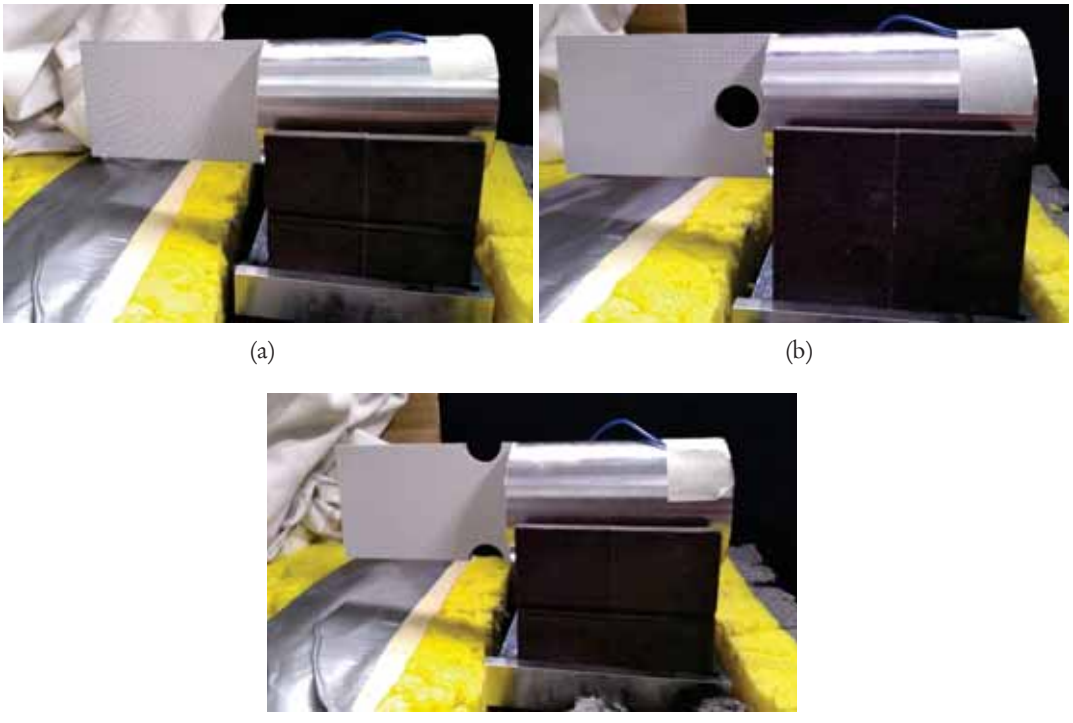

(a) (b)

(c)

Figure 4.5: Waveguide + tested specimens set up in the working chamber - (a) Rectangular specimen - (b) Holed specimen - (b) Notched specimen

resolutions are in good accordance with the literature review (cf. Table 1.4, p. 37). Finally, it is worth noticing that the different specimens lead approximatively to the same resolutions.

Table 4.3: IBII tests measurement resolutions

Test name	Strain resolution ($\times 10^{-5}$)		Acceleration resolution ($\times 10^{5}$ m.s^{-2})	
	Raw	Regularized	Raw	Regularized
QUAL-FULL-01	95	65	-	3.59
QUAL-FULL-02	100	64	-	3.40
CHAR-NOTC-01	136	53	-	3.12
CHAR-NOTC-02	95	63	-	3.49
CHAR-NOTC-03	141	78	-	4.28
CHAR-NOTC-04	123	90	-	3.59
CHAR-NOTC-05	200	68	-	3.33
CHAR-HOLE-01	131	72	-	3.71
CHAR-HOLE-02	206	90	-	3.64
CHAR-HOLE-03	112	75	-	3.82
CHAR-HOLE-04	121	68	-	3.5

4.2 Application of the dynamic VFM to viscoplasticity characterization

The aim of this section is to apply the dynamic VFM to JC model characterization (recalled in Equation 4.1). As in the previous chapter, the identification process is focused on the identification of the JC model viscoplastic parameter M. Dynamic VFM process is applied using:

- the toolchain optimized numerically (Figure 3.17, p. 94);
- the coordinates systems given by Figure 4.6;
- the virtual field given by Equation 4.2, where L_s is the specimen length and $\Phi(\underline{X})$ the cost function to be minimized (Equation 4.3), where $\underline{X}$ is actually reduced to M, and M_i and M_p denote the number of recorded images and the number of measurement points respectively.

It is worth noticing that SNR parameters have been obtained for the three specimen geometries tested at $V_p = 70$ m.s^{-1} (Table 3.4), whereas the IBII test campaign was conducted at $V_p = 57$ m.s^{-1}. However, the numerical analysis has demonstrated the similar identification performance of M if $V_p = 57$ or 70 m.s^{-1} and the frame rate was at least 4 Mfps (cf. Figure 3.16, p. 93). Therefore, the SNR parameters that were optimized for $V_p = 70$ m.s^{-1} were considered.

$$\sigma_y = \left| \begin{array}{ll} \sigma_0 + Kp^n & \text{if } \dot{p} \leq \dot{\varepsilon}^{vp}_{eq,0} \\ \left[\sigma_0 + Kp^n\right]\left[1 + M \ln\left(\frac{\dot{p}}{\dot{\varepsilon}^{vp}_{eq,0}}\right)\right] & \text{if } \dot{p} > \dot{\varepsilon}^{vp}_{eq,0} \end{array} \right. \tag{4.1}$$

$$\left| \begin{array}{lcl} u^*_x &=& x(x - L_s) \\ u^*_y &=& 0 \end{array} \right. \quad \left| \begin{array}{lcl} \varepsilon^*_{xx} &=& 2x - L_s \\ \varepsilon^*_{yy} &=& 0 \\ \varepsilon^*_{xy} &=& 0 \end{array} \right. \tag{4.2}$$

$$\Phi(\underline{X}) = \sum_{i}^{M_i} \left[1 + \frac{\sum_{k=1}^{M_p} \left[\sigma_{xx}(i,k,\underline{X}) \overline{(2x - L_s)}^{S(k)} \right]}{\rho \sum_{k=1}^{M_p} \left[\gamma_x(i,k) \overline{x(x - L_s)}^{S(k)} \right]} \right]^2 \tag{4.3}$$

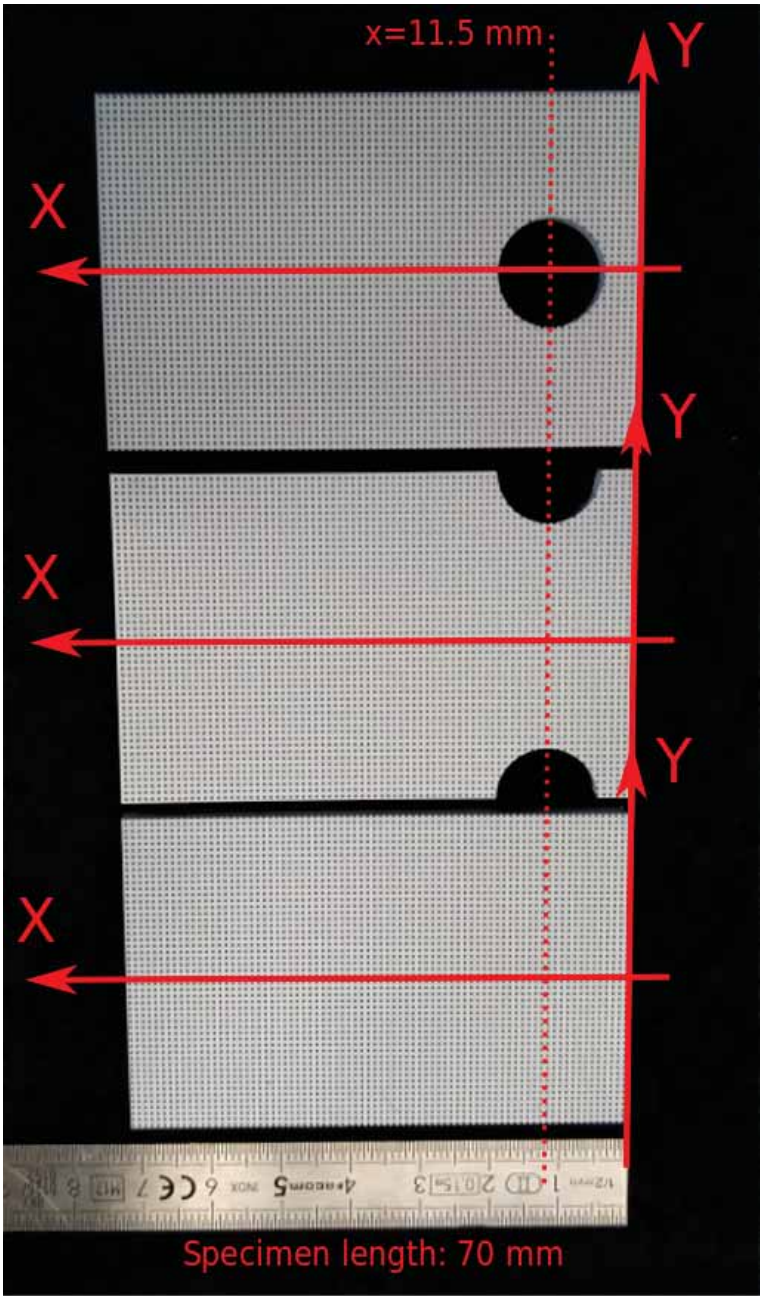

Figure 4.6: Axes systems for the VFM in experimental conditions

4.2.1 Strain and acceleration extraction

4.2.1.1 Full-field maps

Figure 4.7 and Figure 4.8 show maps of the longitudinal strain and acceleration for a sample of IBII tests. Globally, one can observe that:

- for all IBII tests, the wave propagation is not purely longitudinal because there was slight misalignment between the waveguide and the projectile. However, this did not impact the test processing because there is no a priori assumption on the symmetry of the mechanical fields;
- strain and acceleration fields reconstruction in corrupted zones (*i.e.*, at the specimen boundaries), seem consistent with non-corrupted zones since no spatial discontinuities are observed "with the naked eye", whichever the field map heterogeneity level;
- unfortunately, all the reported tests were triggered a little bit too late (cf. acceleration fields analysis thereafter). Indeed, about 20% of the loading pulse has not been recorded at all, hence a shorter set of images for viscoplasticity characterization. For the rectangular specimen, the losses were different because they were "warm-up" tests as already mentioned.

For the rectangular specimen, longitudinal strain levels reach about -0.01 at best whereas they reach more than -0.05 for the holed and notched specimens (Figure 4.7). Moreover, geometrical singularities enhanced the generation of strongly heterogeneous strain fields in their neighbourhood. However, these high levels of strain are very localised because about less than one-third of the specimens is concerned. Therefore, one can guess that the other part of the specimen will undergo elastic strains only.

Acceleration field maximum amplitude (Figure 4.8) is not really influenced by specimen geometries (about 10^7 m.s^{-2}). However, acceleration wave propagation is influenced by misalignments or geometrical singularities (see the whiplash near impact zone for the test CHAR-HOLE-04 at 4 μs). Nonetheless, it can be used to analyse the loading since for the notched and holed specimens for instance, acceleration wave front took approximatively 13 μs to reach the free edge (see acceleration maps at 4 and 16 μs), which is in good accordance with the analytical estimation $\Delta t = \frac{L_s}{\sqrt{E/\rho}} \approx 13$ μs.

4.2.1.2 Validation through dynamic VFM

A way to assess the coherence of strain and acceleration fields measurement is to use the dynamic VFM to calculate the Young's modulus. As already used in Section 2.3.3 (p. 61) to determine the nominal mesh size of IBII test simulations, it consists in the reconstruction of the mean longitudinal stress in a vertical slice of the specimen owing to acceleration fields (Equation 4.4).

$$\forall x,\ \overline{\sigma_{xx}}(x) = \frac{\rho}{D(x)} \sum_j \gamma_x(x,j) S(x,j) \tag{4.4}$$

Assuming an elastic material behaviour within material slice, the Young's modulus E is such as Equation 4.5. Finally, if Poisson's ratio ν is supposed to be known, stress/strain curves may be plotted for any slice to determine E. Figure 4.9 reports some examples of stress/strain curves obtained at various positions for the three different specimens.

$$\frac{E}{1-\nu^2} = \frac{\overline{\sigma_{xx}}}{\overline{\varepsilon_{xx} + \nu\varepsilon_{yy}}} \tag{4.5}$$

As expected, stress/strain curves are linear. For the rectangular specimen, the unloading path was not recorded at all, hence a straight line is observed. By contrast, several slices of notched and holed specimens saw a reversal of the loading path. To validate the approach, linear fitting has been performed in each case. The obtained values are very close to the reference (value of the Young's modulus: 114 GPa), with gaps up to only 6%. The "highest" one is observed for the notched specimen. However, this underestimation may be due to yielding. They will be quantified in the next paragraph owing to the identified flow rule and the Return Mapping Algorithm.

Figure 4.7: ε_{xx} maps for different geometries

Figure 4.8: a_x maps for different geometries

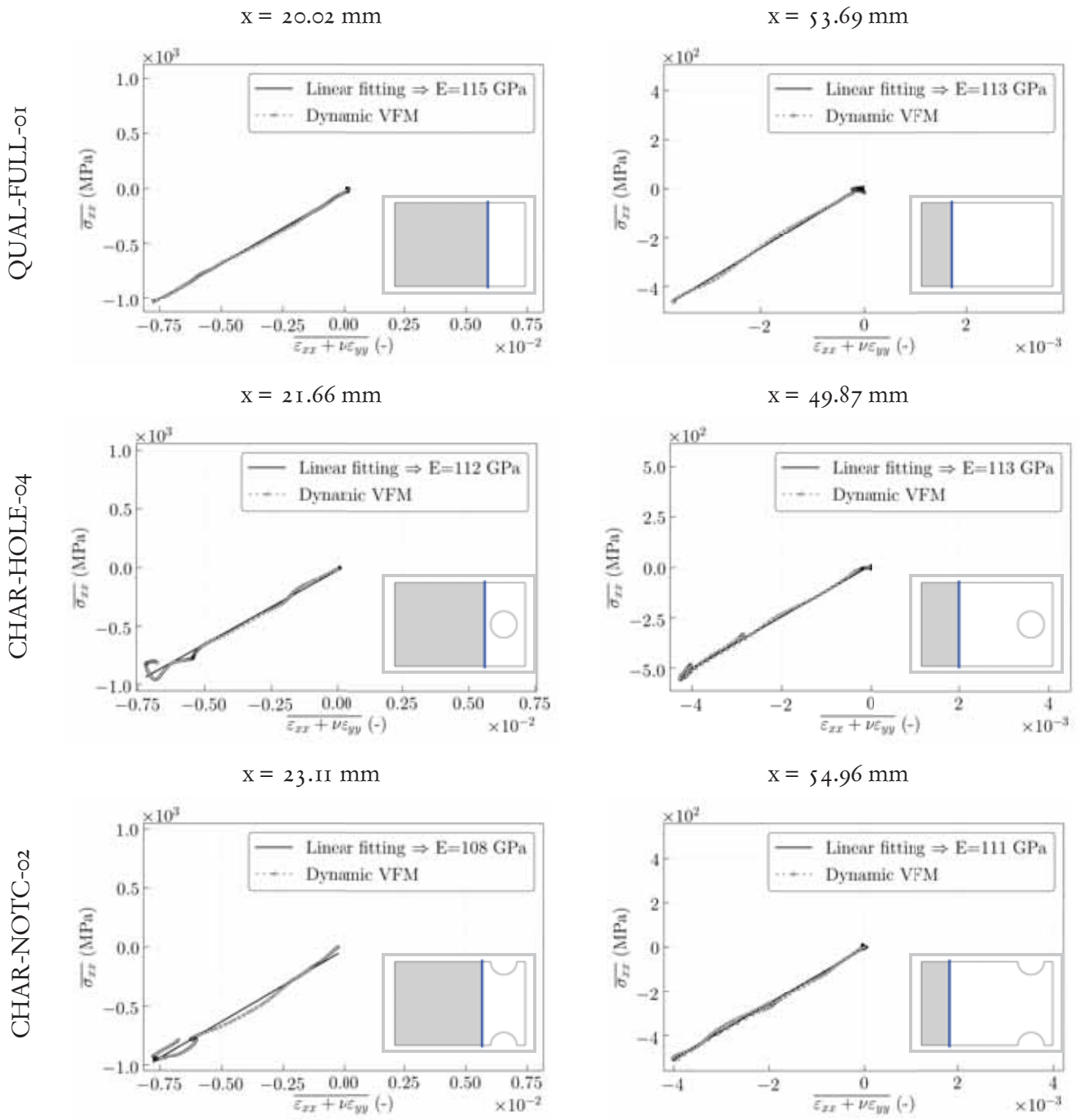

Figure 4.9: Stress/strain curves from non-parametric VFM

Finally, those results demonstrate the consistency of strain and acceleration fields computation. Now that strain and acceleration fields maps have been thoroughly assessed for the conducted IBII tests, they are used in the next section to identify JC viscoplastic parameter M with the dynamic VFM.

4.2.2 Viscoplastic parameter identification

Nelder-Mead algorithm was used to identify the value of parameter M using the eleven conducted IBII tests. To ensure the solution uniqueness, two identifications were carried out for each test with two different starting values (respectively 100 and 200 % over the reference value). The final results are collected in Figure 4.10. The JC viscoplastic parameter reference value (0.033) obtained with standard tests [6] is also reported. The identified values seem to be very consistent with literature results. Indeed, all identified values of parameter M are in the range [0.029, 0.043]. As there were enough

tests, standard deviation and mean value were computed for the notched and holed configurations. One can observe that in all cases, the identified values are consistent with the reference, since the latter is well within the bounds of $\pm\sigma$ (σ the standard deviation).

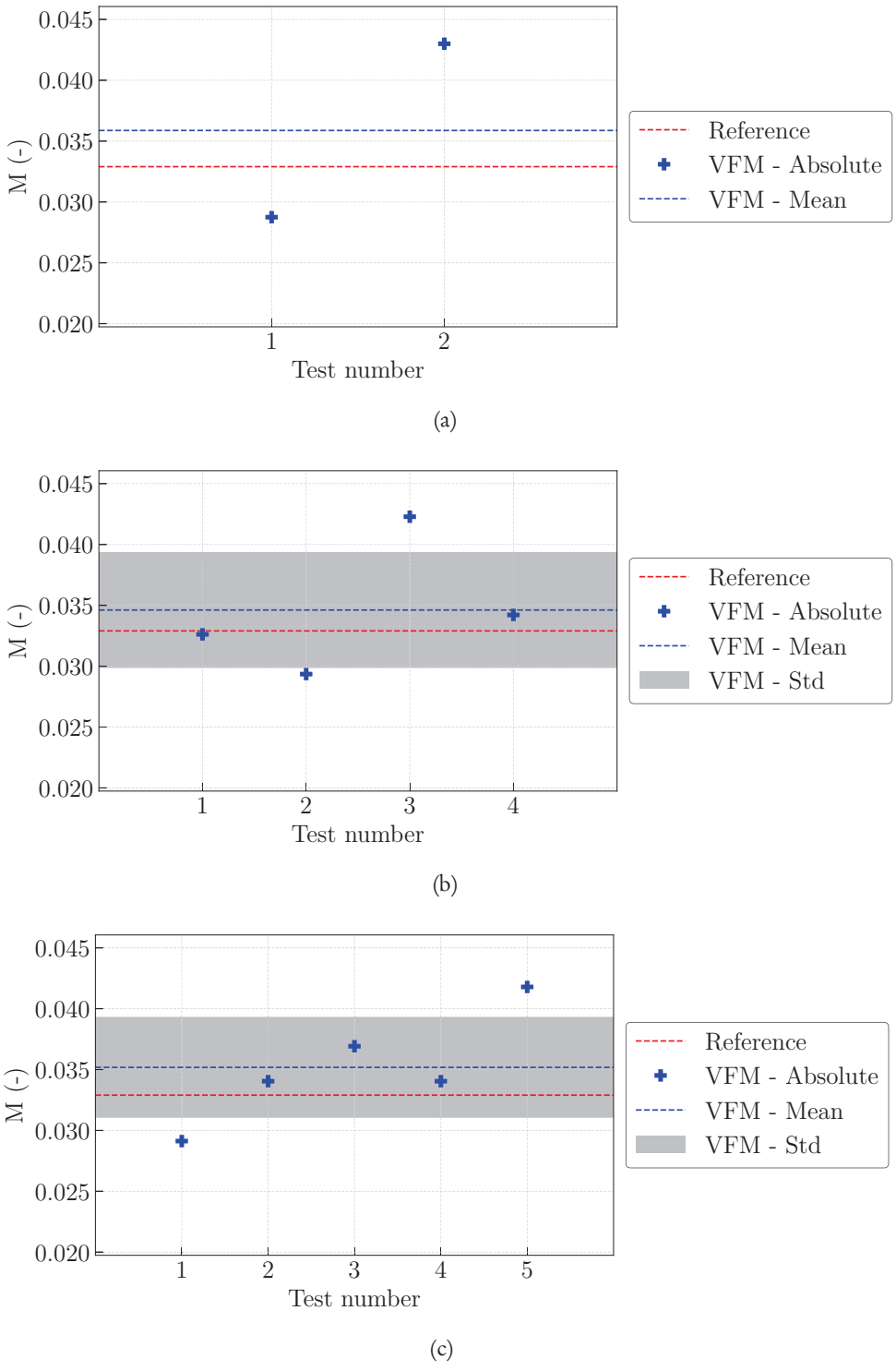

Figure 4.10: JC viscoplastic parameter identified values - (a) QUAL-FULL-## - (b) CHAR-HOLE-## - (c) CHAR-NOTC-##

A way to analyse the influence of standard deviation on stress evaluation is to quantify the viscoplastic correction in the JC model for the identified values. Figure 4.11 reports the evolution of the yield stress for these identified values on a wide range of plastic strain-rates. Note that as for the identification results, the IBII tests with rectangular specimens are not enough to estimate a standard

deviation. One can observe that if $\dot{p} < 100$ s^{-1} (intermediate rates), yield stress correction uncertainty lower than 5%. For higher values of $\dot{p}$, the uncertainty is higher. For Specimen 2, if $\dot{p} = 10000$ s^{-1} for instance, the uncertainty reaches 8% while the yield stress correction is about 35%.

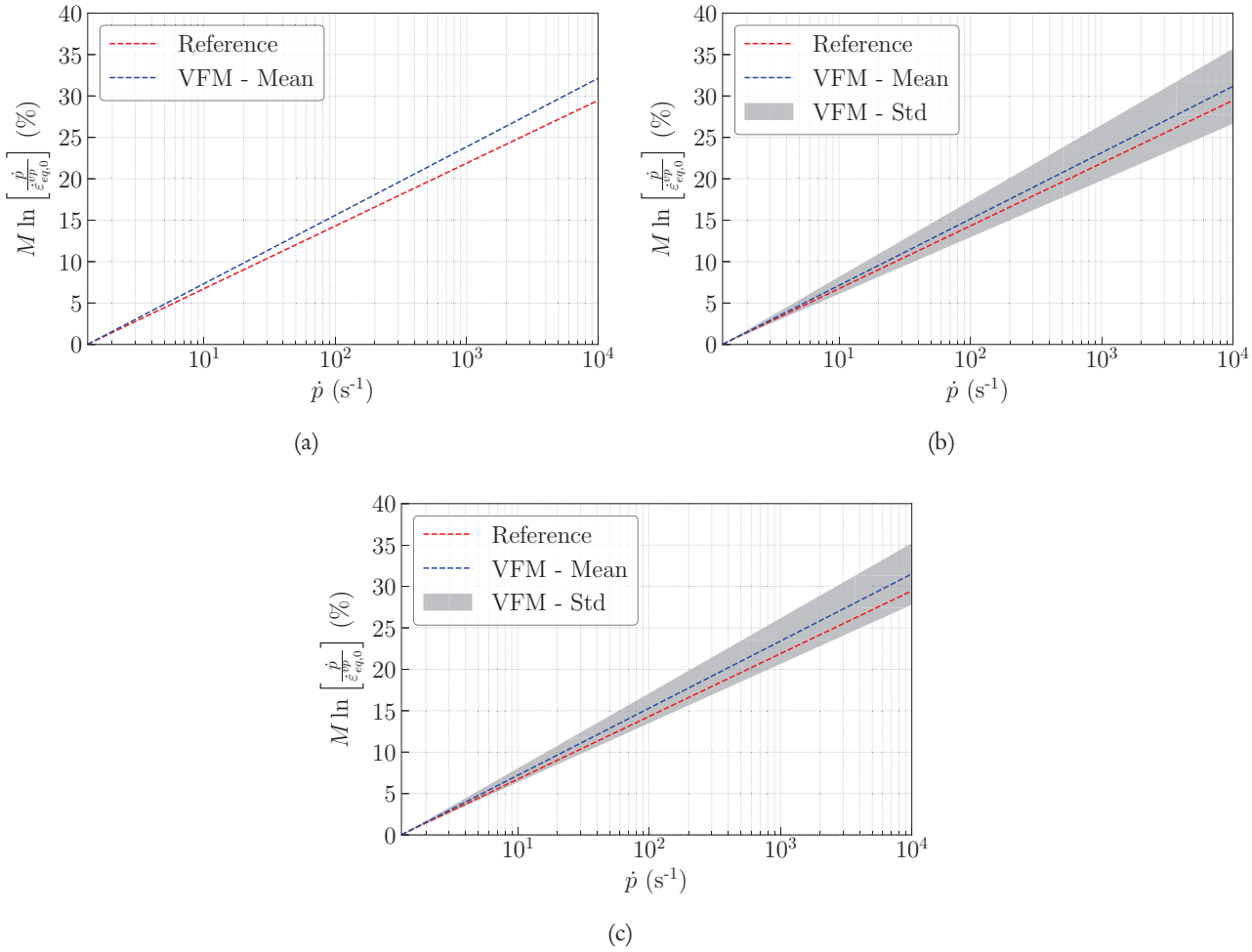

Figure 4.11: Influence of M on yield stress multiplicative viscoplastic correction - (a) QUAL-FULL-## - (b) CHAR-HOLE-## - (c) CHAR-NOTC-##

Assuming the knowledge of JC model static part (see Table 2.2, p. 51) and the equivalent strain-rate threshold, $\dot{\varepsilon}^{vp}_{eq,0}$, stress fields and other mechanical fields can be computed owing to the Return Mapping Algorithm. Figure 4.12 and Figure 4.13 map σ_{xx} and p respectively. Note that for each configuration, the results are obtained with the identified value of M.

Figure 4.13 shows the plastic strain distribution. As expected, the configuration without geometrical singularities provide a smaller range of plastic strains compared to ones with notches and holes. Indeed, plastic strain levels less than 0.01 are obtained at best. However, notched and holed specimens enable to reach much higher levels of p (about 0.08), whereas the projectile velocity remains unchanged. This advantage and the consistent identifications validate the use of notched/holed specimen for viscoplasticity characterization, in particular if the projectile velocity is limited as in current test campaign. Figure 4.14 shows the cumulated plastic strain rate distribution. One can observe that in all cases, the highest values of $\dot{p}$ are observed in the early stages of the loading, with a maximum amplitude value of about 3000 s^{-1} for Specimen 0 and 10000 s^{-1} for Specimen 1 and 2. However, the range of strain rate still has not be analysed; a quantitative study is performed in the next section.

Figure 4.12: σ_{xx} maps for different geometries

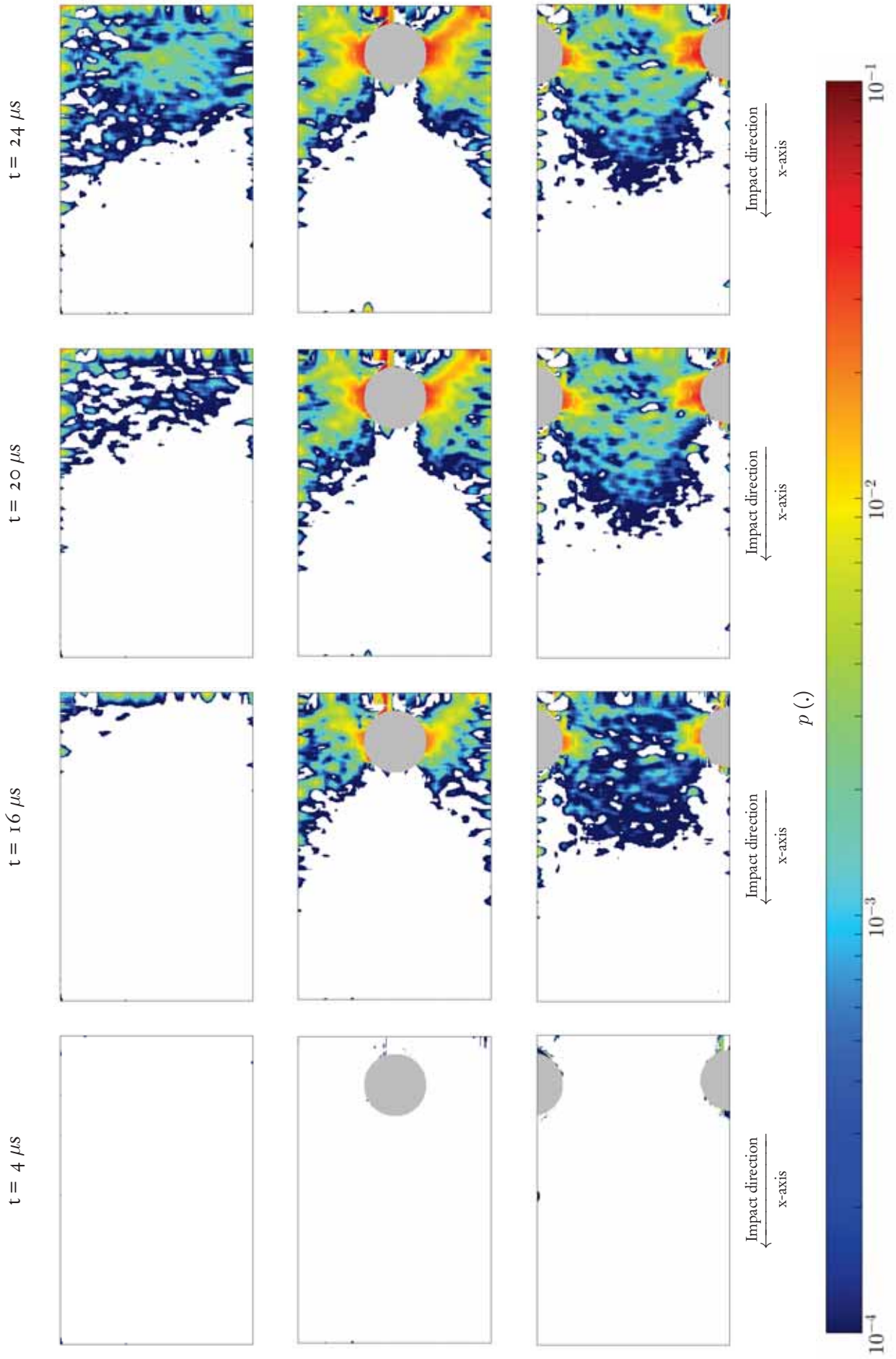

Figure 4.13 : p maps for different geometries

Figure 4.14: $\dot{p}$ maps for different geometries

4.2.3 Viscoplastic spectra analysis

With the same methodology presented in Section 3.3, p. 76, viscoplastic histograms $(p, \dot{p})$ have been plotted for the conducted IBII tests. Some results are reported in Figure 4.15. One can observe that viscoplastic spectra are "band-shaped", *i.e.*, high (visco)plastic strains occur at high strain rate and *vice-versa*. Moreover, as seen with the map of cumulated plastic strain, the rectangular specimen led to the smallest levels of plastic strain (approximatively one percent). For all specimens, collected viscoplastic states sweep approximatively two decades of for the plastic strain-rate (from 100 s^{-1} to 10^4 s^{-1}). This has to be compared to the range of strain-rate of the test campaign performed to identify the reference material constants (up to about 500 s^{-1}).

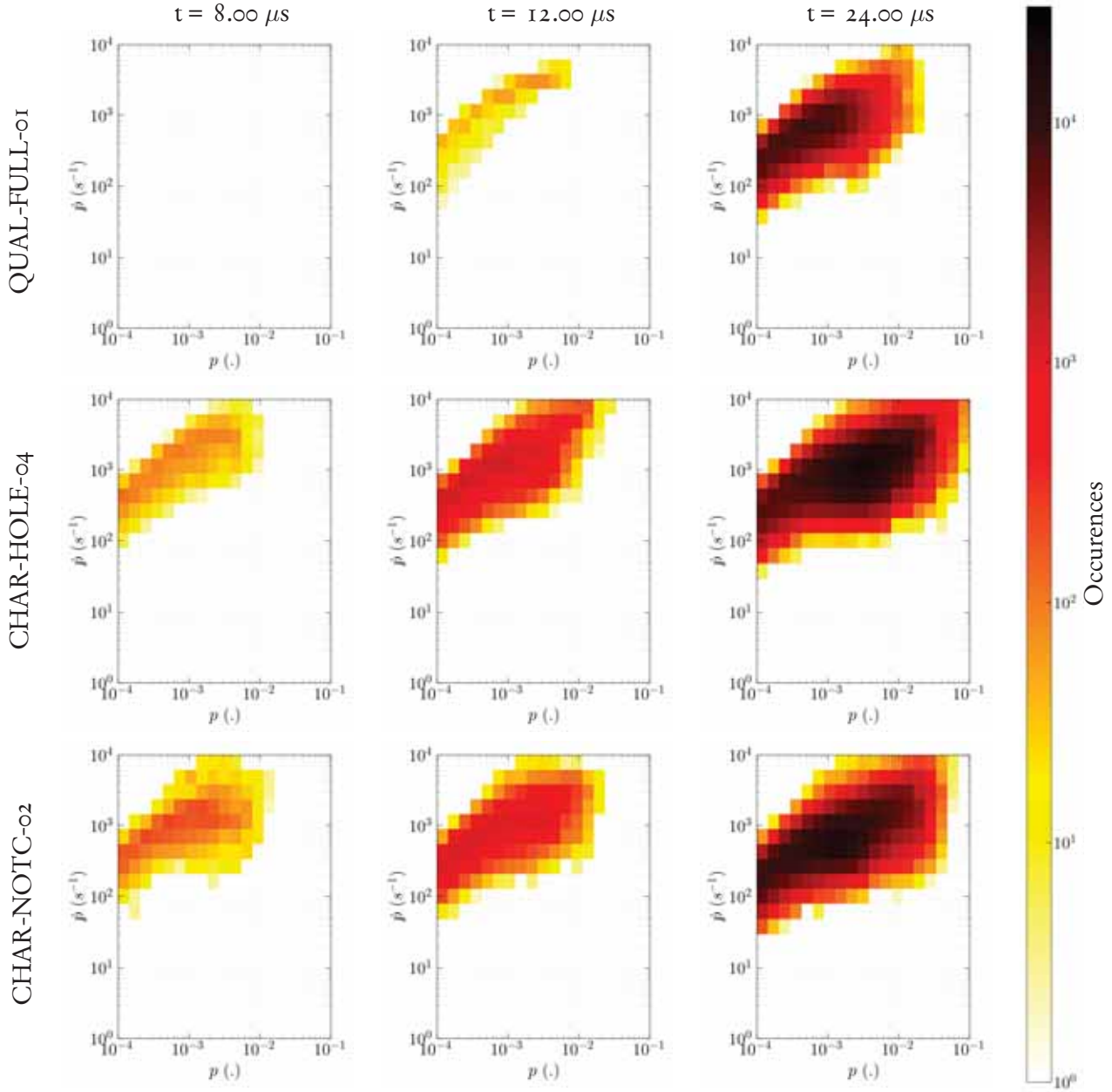

Figure 4.15: Viscoplasticity histograms contour - Test campaign

These results in the identification values and the characterized viscoplastic spectra are very satisfying. However, the sensitivity of the identification to the virtual field has not be assessed. This is done in the next section.

4.2.4 Sensitivity of the identification to the choice of virtual field

The dynamic VFM toolchain has been optimized for a set of choices in the methodology. This includes the virtual field defined at Equation 4.2 (referred as the quadratic virtual field) used in the computation of the PVW. This virtual field has been manually defined to be eligible for dynamic VFM, *i.e.*, cancelling the contribution of external forces in the PVW. One way to assess the toolchain robustness is to analyse the influence of the virtual field on the identification of M. To do so, the previous identifications have been carried out with the virtual field defined by Equation 4.6 (referred to as the linear virtual field). The results are reported in Figure 4.16.

Each identification result is different that obtained with the quadratic virtual field (Figure 4.10). However, the results are in good accordance since mean identified value and standard deviation are similar (Table 4.4). Therefore, though the use of different virtual field led to the identification of different values, using the linear virtual field does not worsen the results in tendency, and the scattering is eventually reduced for Specimens 1 and 2.

$$\left| \begin{array}{lcl} u_x^* & = & x/Ls \\ u_y^* & = & 0 \end{array} \right| \quad \left| \begin{array}{lcl} \varepsilon_{xx}^* & = & 1/Ls \\ \varepsilon_{yy}^* & = & 0 \\ \varepsilon_{xy}^* & = & 0 \end{array} \right| \tag{4.6}$$

Table 4.4: Influence of virtual field on identified values

	Linear	Quadratic
Rectangular specimen	0.037±##	0.036±##
Holed specimen	0.035±0.0002	0.035±0.0005
Notched specimen	0.035±0.0004	0.035±0.0004

The different analyses carried out in the previous section have demonstrated the consistence of the strain-rate sensitivity characterization. These analyses were all based on purely experimental data. A way to strengthen the demonstration is to enrich the discussion using synthetic data used to define the whole dynamic VFM toolchain. This is reported in the next section.

4.3 A critical comparison between experimental results and numerical predictions

The identification of JC viscoplastic parameter M was performed using the dynamic VFM toolchain optimized for given IBII test configurations. The aim of this section is to assess the robustness of the numerical toolchain used in Chapter 3, including the synthetic images generator for metrological performance analysis. As the study was performed for a different velocity than the experiments, six new sets of noisy synthetic images have been generated for $V_p = 57$ m.s^{-1} and the three specimen geometries. Finally, they have been processed as real images with optimized SNR parameters as done with the test campaign. The following section reports some comparisons of mechanical fields which have been measured or simulated.

4.3.1 Full-field maps comparison

N.B.: In this section, results are shown for the notched specimen only. The results for all specimens are available in Appendix E.

Figure 4.17 maps longitudinal strains about 14 μs after impact, this corresponding to a single travel of the loading wave. Experimental and synthetic maps seem globally in good accordance. For experimental maps, strains at the notch root do not match exactly because of the impact misalignment. Near

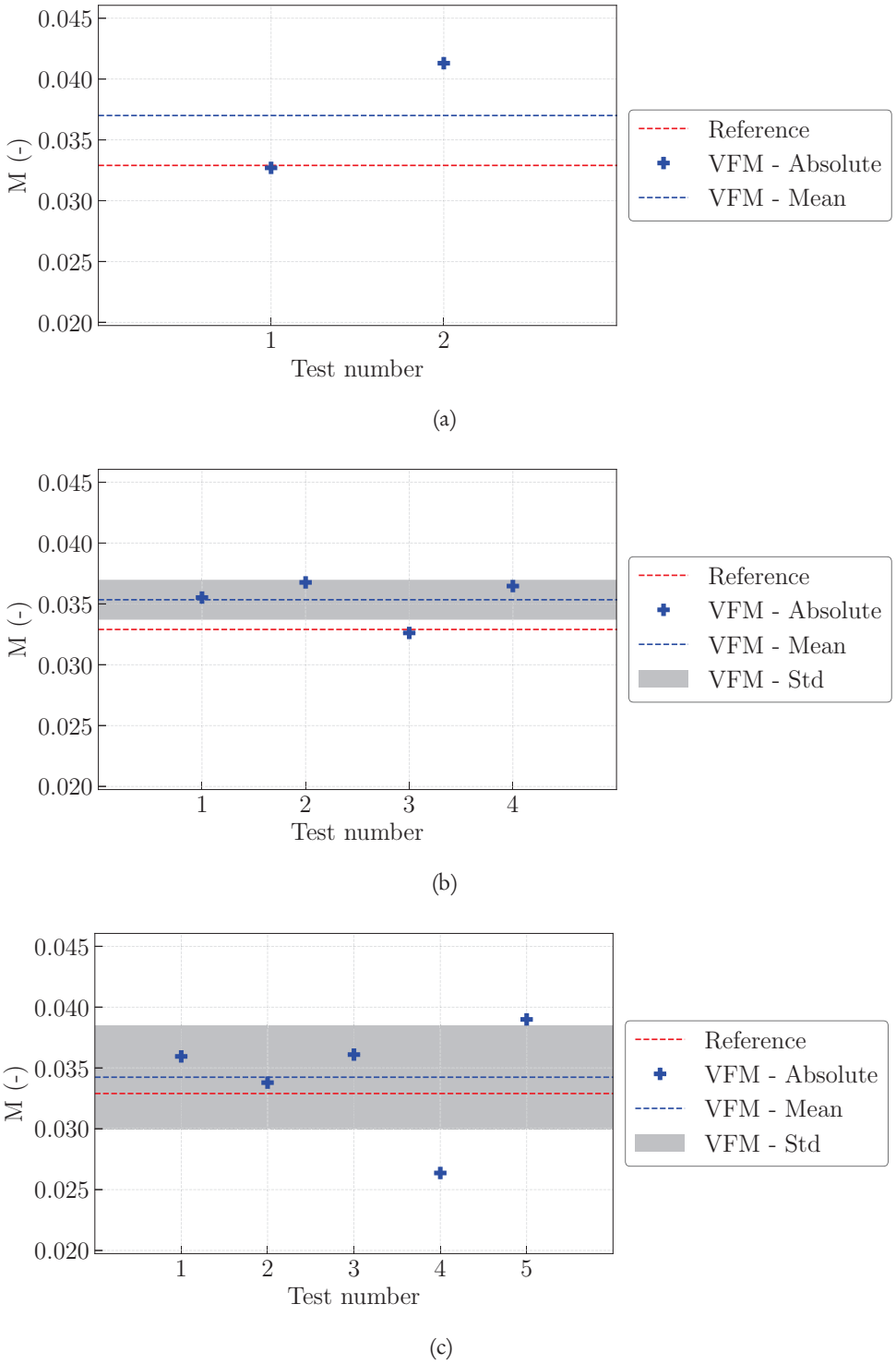

Figure 4.16: JC viscoplastic parameter identified values with the linear virtual field - (a) QUAL-FULL-## - (b) CHAR-HOLE-## - (c) CHAR-NOTC-##

the impact zone, the strain concentration of synthetic images cannot be analysed insofar as during experiments, the specimen edge is not fully imaged (loss of a grid pitch + flash light reflections on the waveguide). However, if information loss is limited (cf. test CHAR-NOTCH-04), strain concentration is visible in the vicinity of the impacted zone. Otherwise, strain peaks are similar, notably at the notch root. This is particularly critical because most of the plastic strains occurs there, and this is the most sensitive zone to JC viscoplastic parameter.

The same comparison can be done with the cumulated plastic strain p computed with the Return Mapping Algorithm (Figure 4.18). Previous remarks on longitudinal strains are still valid. Furthermore, plastic waves penetration lengths and front end shapes are in good accordance for notched and holed specimens (Figure 4.17 and Figure E.5), including plastic strains due to boundary effects. This is particularly true for the holed specimens in Figure E.5. However, plastic wave penetration on rectangular specimens seems more affected by misalignments since their front end is oblique. Notched and holed specimens might be less affected because of the geometrical singularities which have mitigated this effect.

Another way to compare strain and acceleration fields maps is to analyse some stress/strain curves as done in Section 4.2.1.2 to validate their coherence. To do so, synthetic and experimental curves at the same position (or the closest) are reported in Figure 4.19. In the case of synthetic images, input and reflected waves were recorded almost until total unloading. The calculated Young's modulus values demonstrate the coherence between synthetic and experimental images.

Now that full-field maps have been analysed, a comparison between identification results is performed in the next section.

4.3.2 Viscoplasticity characterization comparison

To assess the numerical predictor performance, one may also compare the identification results. Therefore, identifications have been carried out with the same toolchain, *i.e.*, for the two proposed virtual fields, the three geometries and the six sets of synthetic images. Results are reported in Figure 4.20 for the quadratic virtual field and in Figure 4.21 for the linear virtual field. They exhibit trends very similar to the experimental results, thus providing confidence in the identification. Indeed, for each specimen, mean value of M and standard deviation seem not sensitive to the virtual field. Another way to evaluate the prediction is to compare mean value and standard deviation computed with experimental and synthetic images. Values for notched and holed specimens only are reported in Table 4.5.

Table 4.5: Comparison of identified values of parameter M: Experimental vs numerical predictions

	Synthetic		Experimental	
	Linear	Quadratic	Linear	Quadratic
Holed specimen	0.035±0.0002	0.036±0.0002	0.035±0.0002	0.035±0.0005
Notched specimen	0.032±0.0004	0.035±0.0004	0.035±0.0004	0.035±0.0004

Experimental results are very consistent with numerical predictions. This is particularly true for the standard deviation, which validates the synthetic grid image deformation methodology. Furthermore, mean value seems also consistent; this demonstrates the consistence of critical camera features modelling (*e.g.*, noise level or fill factor). However, one can notice that contrary to Chapter 3 (where the notched configuration was the best if $V_p = 70$ m.s^{-1}), it was not possible here to discriminate notched and holed configurations as there is no significant differences between identification results. This may be due to the projectile velocity which makes the identification less sensitive to the geometry.

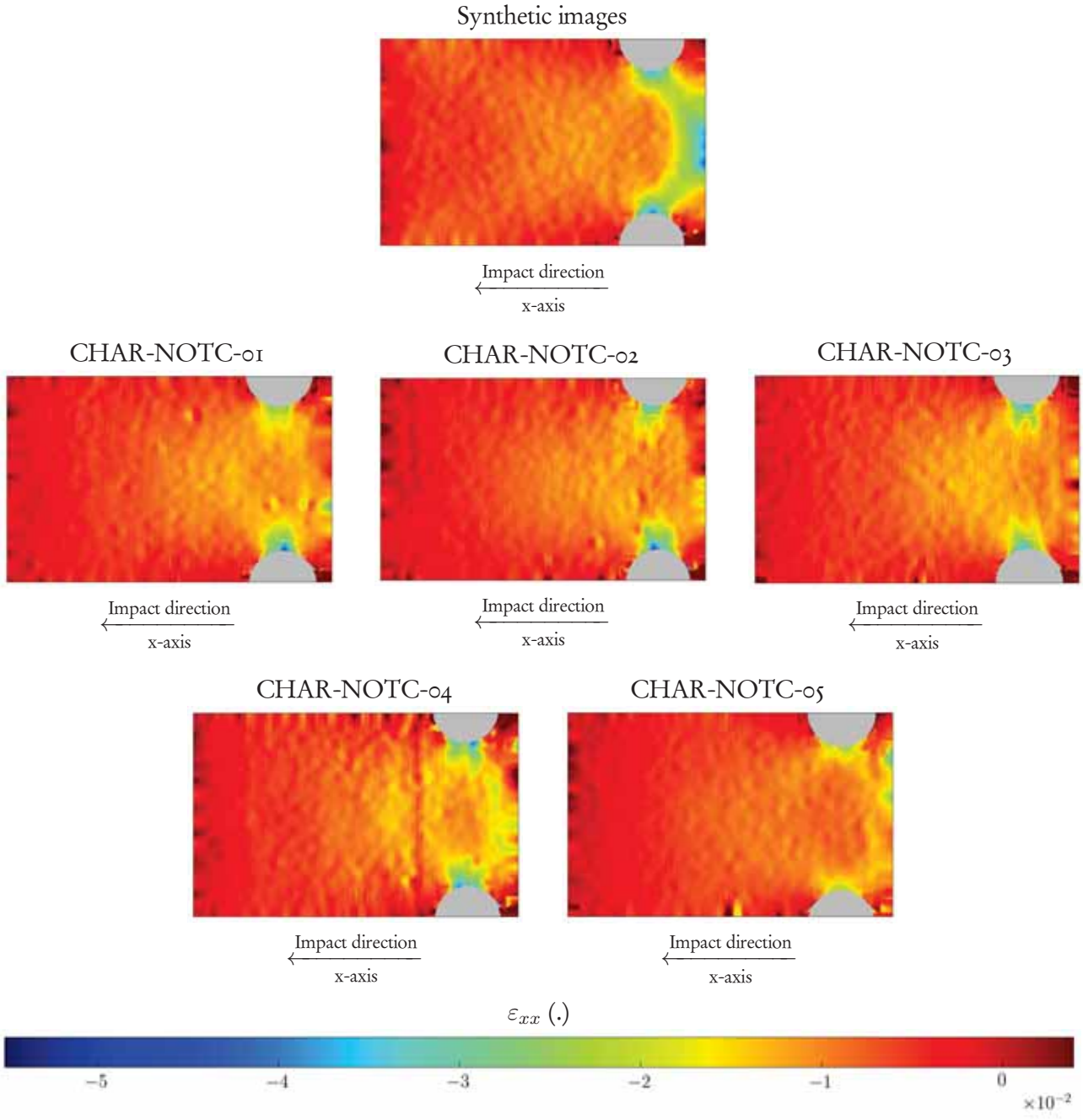

Figure 4.17: ε_{xx} at t = 14μs: experimental vs synthetic images

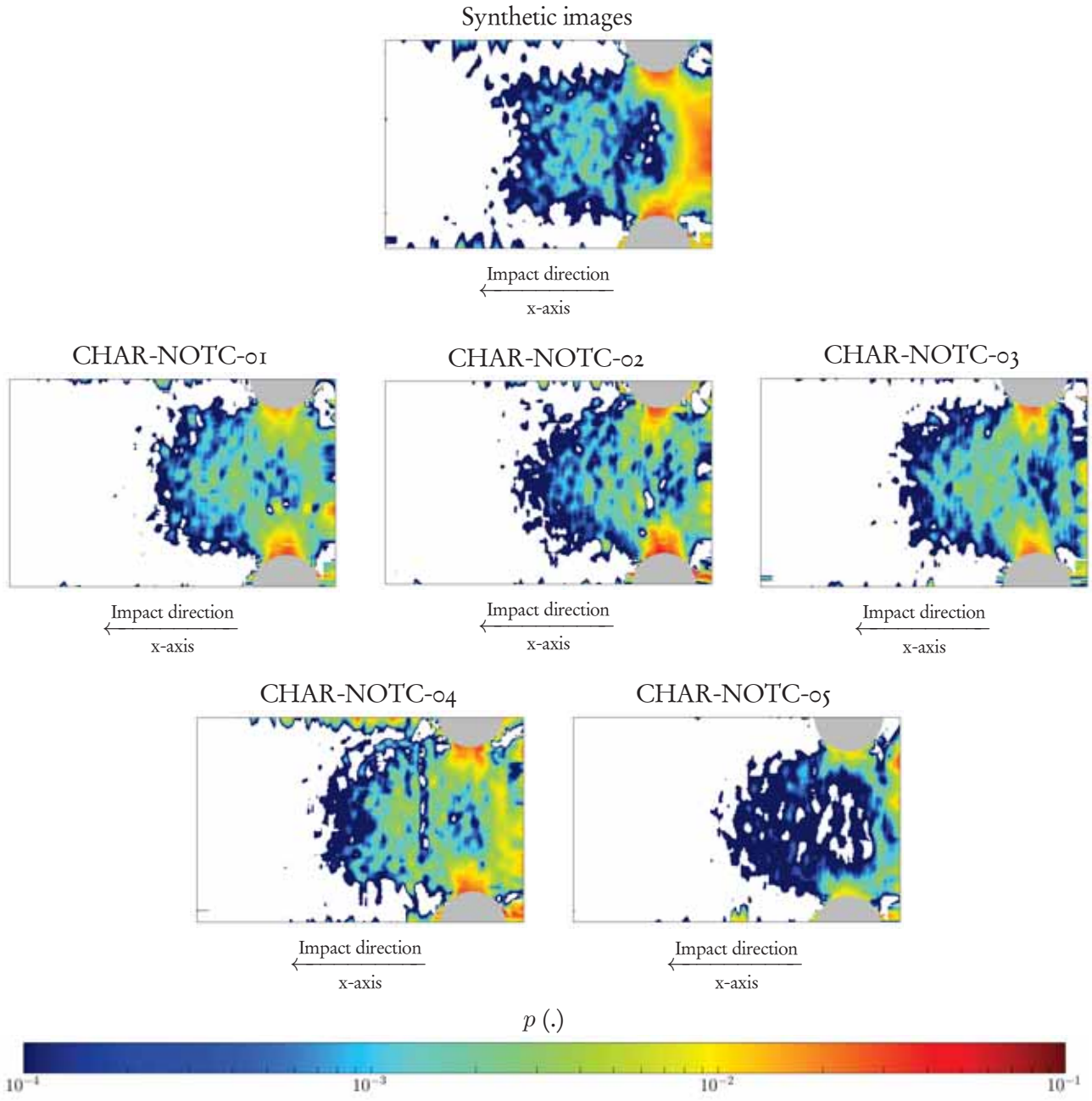

Figure 4.18: p at t $= 14\mu$s: experimental vs synthetic images

QUAL-FULL-01

Synthetic - x= 53.69mm

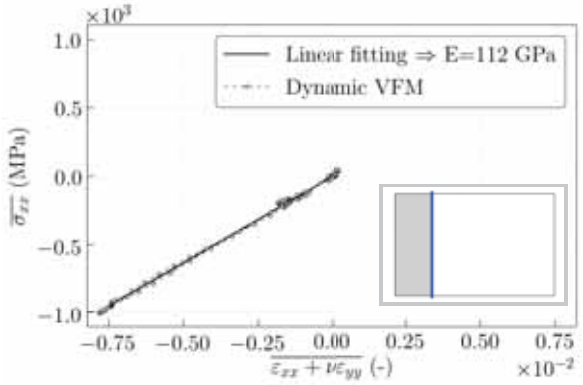

Experimental - x= 53.69mm

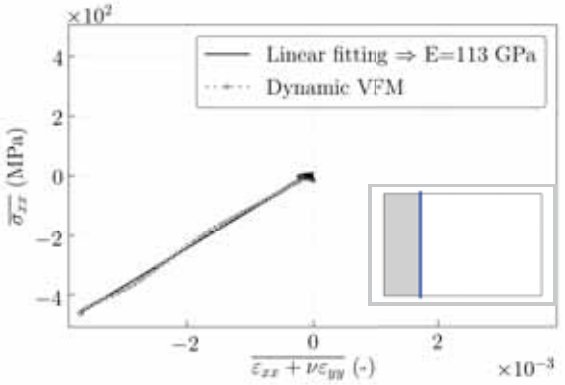

CHAR-HOLE-04

Synthetic - x= 50.05mm

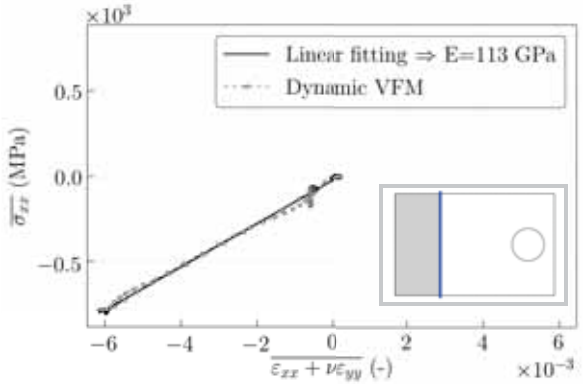

Experimental - x= 49.87mm

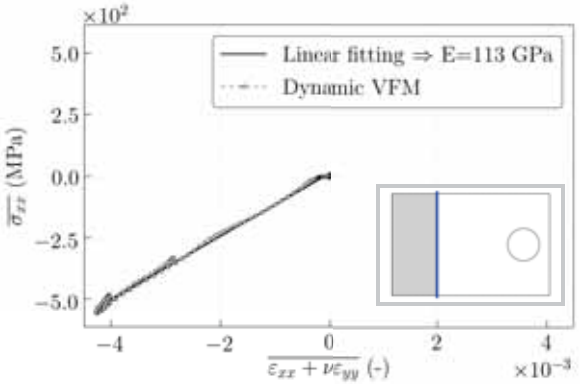

CHAR-NOTC-02

Synthetic - x= 53.69mm

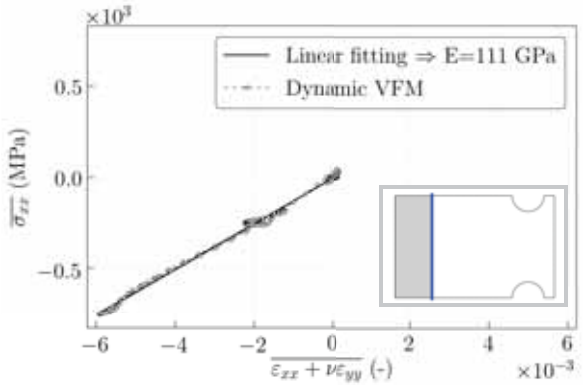

Experimental - x= 54.96mm

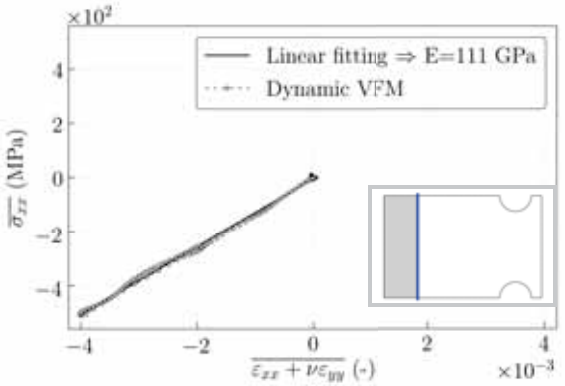

Figure 4.19: Stress/strain curves from dynamic VFM

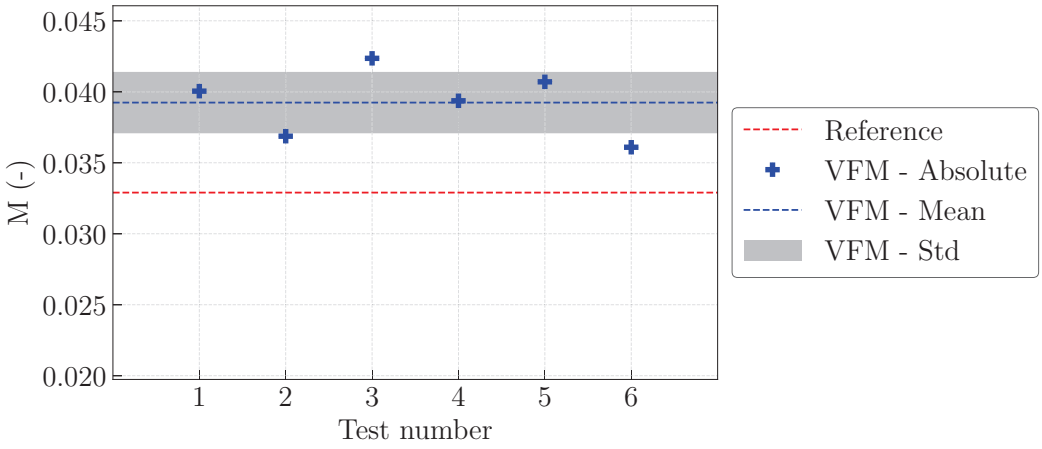

(a)

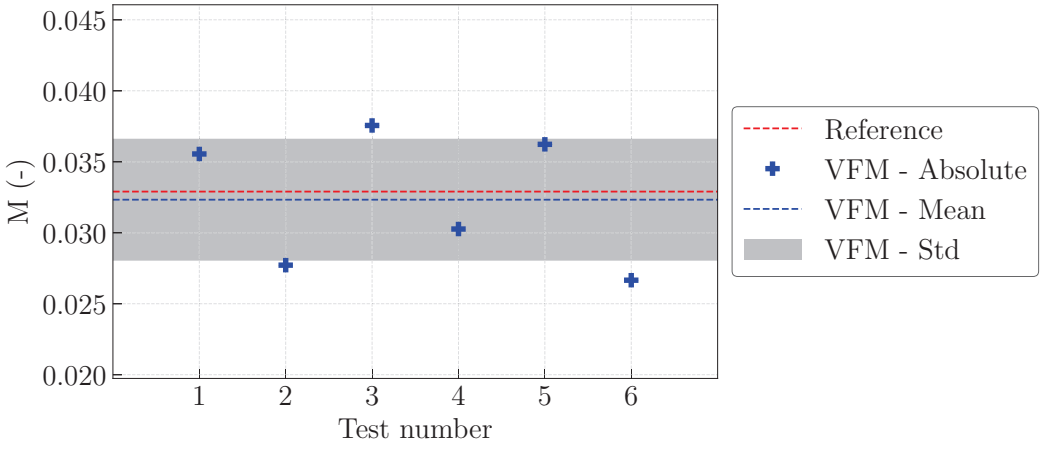

(b)

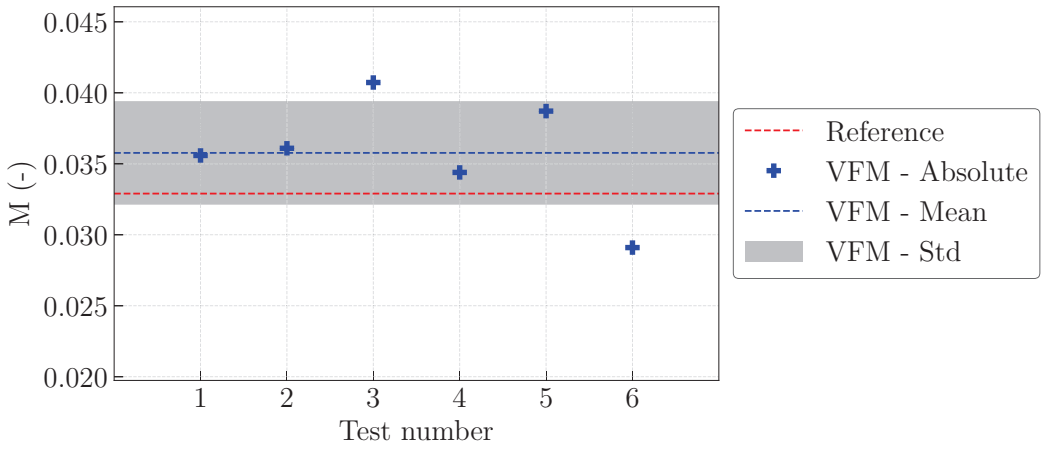

(c)

Figure 4.20: JC viscoplastic parameter identified values on synthetic images - quadratic virtual field - (a) Rectangular specimen - (b) Holed specimen - (c) Notched specimen

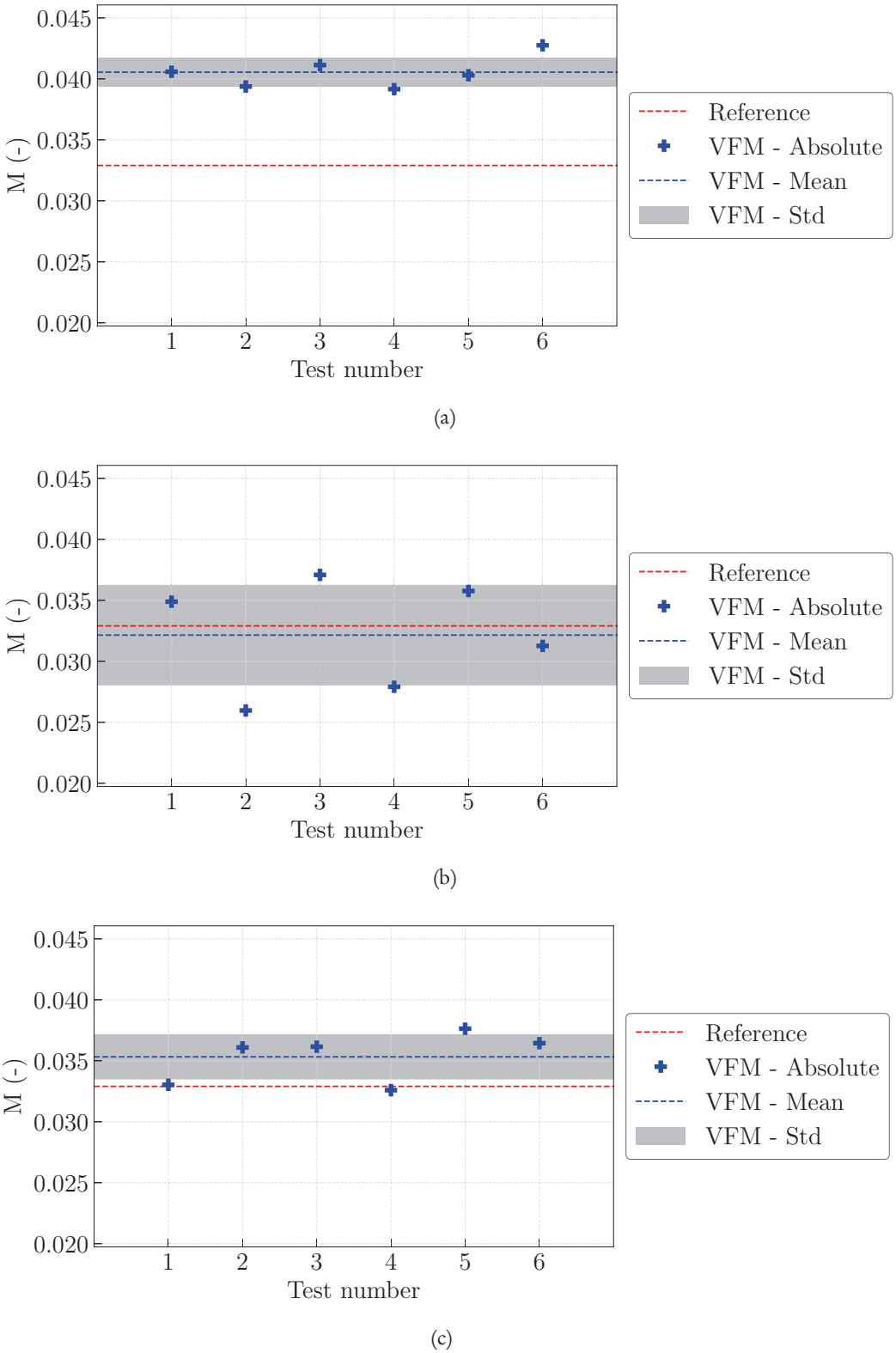

Figure 4.21: JC viscoplastic parameter identified values on synthetic images - linear virtual field - (a) Rectangular specimen - (b) Holed specimen - (c) Notched specimen

4.3.3 Viscoplastic spectra comparison

N.B.: In this section, results are shown for the notched specimen only. The results for all specimens are available in Appendix E.

Viscoplastic spectra of notched specimens (Figure 4.22) are consistent with the numerical predictions. For the lowest levels of plastic strain rate and strain, the viscoplastic spectra are similar. However, the highest levels of plastic strain may be different. This may be due to strain concentrations which are not generated in the same way because of slight misalignments or a reconstruction not accurate enough. However, this does not jeopardize the identification, but the spectrum on which M is identified is different. Finally, the combination of all IBII tests seems in good agreement with the predictions.

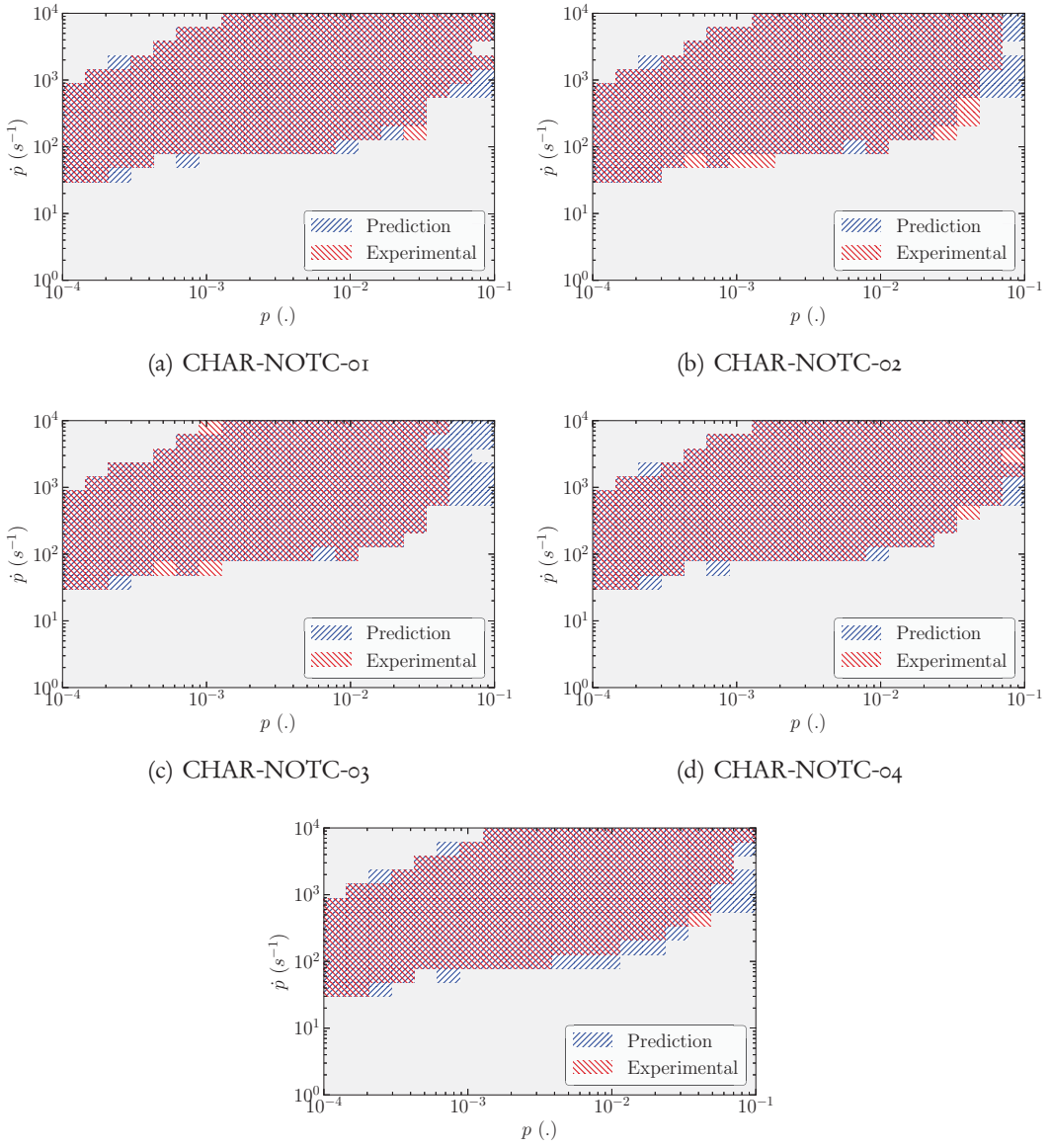

(a) CHAR-NOTC-01

(b) CHAR-NOTC-02

(c) CHAR-NOTC-03

(d) CHAR-NOTC-04

(e) CHAR-NOTC-05

Figure 4.22: Viscoplasticity histograms comparison: Synthetic vs experimental for notched specimens

This analysis highlights the necessity to repeat the tests to get an accurate identification. Both notched (Figure 4.22) and holed (Figure E.11) specimens enable the characterization of viscoplastic parameter over the ranges $[10^{-4}, 10^{-1}]$ for p and $[100, 10^{4}]$ s^{-1} for $\dot{p}$. However, no conclusions can be made on the rectangular specimens (Figure E.10), since there are not enough experimental values.

4.4 Summary

In this chapter, the IBII test methodology which have been numerically optimized was implemented experimentally to characterize the strain-rate sensitivity of titanium alloy Ti6Al4V. Using the Johnson-Cook model, the viscoplastic parameter M has been successfully identified owing to a set of eleven IBII tests, with three different geometries: rectangular specimens ($\times$ 2), holed specimens ($\times$ 4) and notched specimens ($\times$ 5). Even if the rectangular specimens were considered as"warm-ups", all of them led to consistent results.

The metrological performance was assessed owing to several tools, including the strain and acceleration fields computation resolution. This was done using static reference images further processed with grid method and SNR differentiators. Then, the dynamic VFM enables to validate the coherence of strain and acceleration fields measurements. Even if Young's modulus identification was not targeted, its value has been retrieved assuming Poisson's ratio value ν. Moreover, the identified values of M were in good accordance with the literature and are valid over very wide range of strain rates since the viscoplastic spectra span the ranges $[10^{-4}, 10^{-1}]$ for p and $[100, 10^{4}]$ s^{-1} for $\dot{p}$.

Another important aspect of this chapter is the critical comparison between experimental results and numerical predictions from the toolbox presented in Chapter 2. Indeed, sets of synthetic images have been generated and processed, with similar IBII test parameters. Following the same methodology, full-field maps, identification results and viscoplastic spectra have been compared to assess the consistency of the numerical predictions. A good coherence between synthetic and experimental results was observed, notably on the standard deviation for the identified values of M. This validates the use of six sets of images for uncertainties quantification.

To conclude, the IBII test methodology has been extended to viscoplasticity characterization. Using a single test, it was possible to identify viscoplasticity over a wide range of strain and strain-rates. This opens up the way for more complex identifications processes, *e.g.*, simultaneous determination of all JC constitutive parameters, but other problems like cost-function sensitivity might arise.

General conclusion

In order to increase passenger safety in air transport, structural crashworthiness is getting a growing attention. Indeed, aircraft structures might undergo loadings under extreme conditions, so that one needs to continuously improve the prediction of their mechanical behaviour. To do so, numerical simulations are more and more used but they require the knowledge of material behaviour from the early stages of loading until failure, over a wide range of strain and strain-rate. This work aims at extending the Image-Based Inertial Test (IBII) methodology to characterize material viscoplasticity with a limited number of tests. Indeed, the identification of viscoplastic behaviour at high rate often relies on statically determinate approaches, *i.e.*, methods which imply strong hypotheses on test conditions whereas they are difficult to be respected in practice (*e.g.*, constant strain-rate). This is all the more challenging that numerous tests are necessary when the material behaviour is characterized over a wide range of strain and strain rates. By contrast, the Virtual Fields Method (VFM) [90] enables the extraction of constitutive parameters without (or a few) hypotheses, using full-field measurements maps. Therefore, even heterogeneous mechanical fields can be processed, and wide viscoplastic spectra may be analysed. The dynamic configuration of the VFM enables identifications without load measurement, so that only strain and acceleration maps are necessary. To take full advantage of the method, the IBII test methodology has been recently proposed. It consists in a rectangular specimen hit by a projectile on its edge while the other one is free. However, the methodology has been up to now used to characterize rate-independent material behaviour only [7, 8, 112, 113].

The scientific contribution of this work is threefold:

- first, an FE-based numerical toolchain has been implemented to assess IBII test configurations and possibly optimize the related test parameters. This has already been done in the literature for IBII tests [112, 113] but through thickness effects were not taken into account up to now. Here, tridimensionnal FE simulations allowed the quantification of their impact on parameters identification and it was established that tests can indeed be performed using surface information only;

- secondly, different specimen geometries were designed to enable viscoplasticity characterization over a wide range of strain and strain rate. The literature only dealed with purely rectangular specimens. Here, notches and holes were used as strain concentrators to enhance large deformations at high rate and to produce heterogeneous mechanical fields. Yet, the possible identification of viscoplastic parameters needed to be demonstrated. Indeed, Ultra-High-Speed (UHS) cameras used to image these tests may have a high temporal resolution, but their spatial resolution is low. Therefore, a generator of synthetic images has been implemented to numerically assess the metrological performance. Finally, the experimental implementation of IBII tests with rectangular, notched and holed specimens was opened and uncertainties were quantified for a given VFM toolchain;

- thirdly, the experiments enabled the identification of JC viscoplastic parameter with a limited number of tests over a wide range of plastic strain and strain rate, *i.e.*, $[10^{-4}, 10^{-1}]$ and $[100, 10^{4}]$ s^{-1} respectively. The results are in accordance with the numerical predictions, from the full-field maps to the uncertainties predictions. Thus, the robustness of the numerical predictor has also been demonstrated in terms of generated mechanical fields as well as uncertainty predictions.

So, this work was seminal for rate-dependant behaviour characterization with IBII test methodology. Therefore, several improvement paths are still opened:

- more efforts can be done on specimen geometry definition. Even if new specimen geometries were introduced, the numerical toolchain can be used more intensively to optimize the IBII test specimen geometry. For instance, notches and holes distance from impacted edge was set in this work after few iterations with an handmade dichotomy. Yet, geometrical singularities play a key role in viscoplastic spectra which are characterized. However, their "machining" might jeopardize the identification since full-field measurements are corrupted in their vicinity (hence it would imply the reconstruction of a higher quantity of data). Therefore, a topological optimization of the inner geometry may be carried out to find the best trade-off between an improved viscoplastic spectra (which reduce the number of tests necessary for viscoplasticity characterization) and parameters identifiability;
- even if the synthetic images generator has been updated to take into account critical imaging parameters (fill factor), other phenomena have not been taken into account. This includes out-of-plane displacements (like in [130] for instance) and the related blurring which may hinder stress reconstruction, in particular near geometrical singularities. More generally, the whole metrological toolchain modelling may be improved, considering a irregular spatial distribution for camera noise for example;
- the metrological toolchain itself can also be improved. In particular, the grid method [65] has been implemented as a suitable solution for full-field maps extraction using cameras with a limited number of pixels. However, some of the method parameters have been selected more or less intuitively. Yet, new solutions have been recently proposed to improve its performance, such as the use of innovative patterns like rotated grids to reduce aliasing [134], or chequerboards [135] to reduce noise levels;
- as a first step of development, this work was focused on the identification of JC viscoplastic parameter only, *i.e.*, on a monovariate identification. This cancels all the arising issues which may come from multivariate problems such as the cost-function definition. Therefore, no strong efforts were made on the choice of the virtual field for instance, so that the identification may be challenging if one wanted to identify all parameters simultaneously. The available literature has recently proposed a methodology to deal with multivariate problems with VFM for elastoplastic behaviour characterization [136], but its possible use for rate-dependant behaviour has not been demonstrated. Furthermore, the main drawback of the method is the intensive use of the return mapping algorithm to compute virtual fields which are linked to stress value sensitivity w.r.t. material parameters. Up to now, these sensitivities are computed from discrete differences and the cost is expansive. Then, an improvement path would be to extract these sensitivities in one step.

These improvement paths may be required to consider more complex identifications, *i.e.*, ones which involve more physically-based models for instance (*e.g.*, the Zerilli-Amstrong flow rule [28]). Indeed, material parameters (*e.g.*, hardening and viscoplastic parameters) are often strongly coupled in those cases. Therefore, it is not possible to identify a parameter separately as done in this manuscript. To the author knowledge, only Notta *et al.* [104] used the VFM to identify a full non-linear behaviour (damage model with elastoplasticity) but it was with finite element data.

Appendix A

Complementary results for Return Mapping Algorithm validation

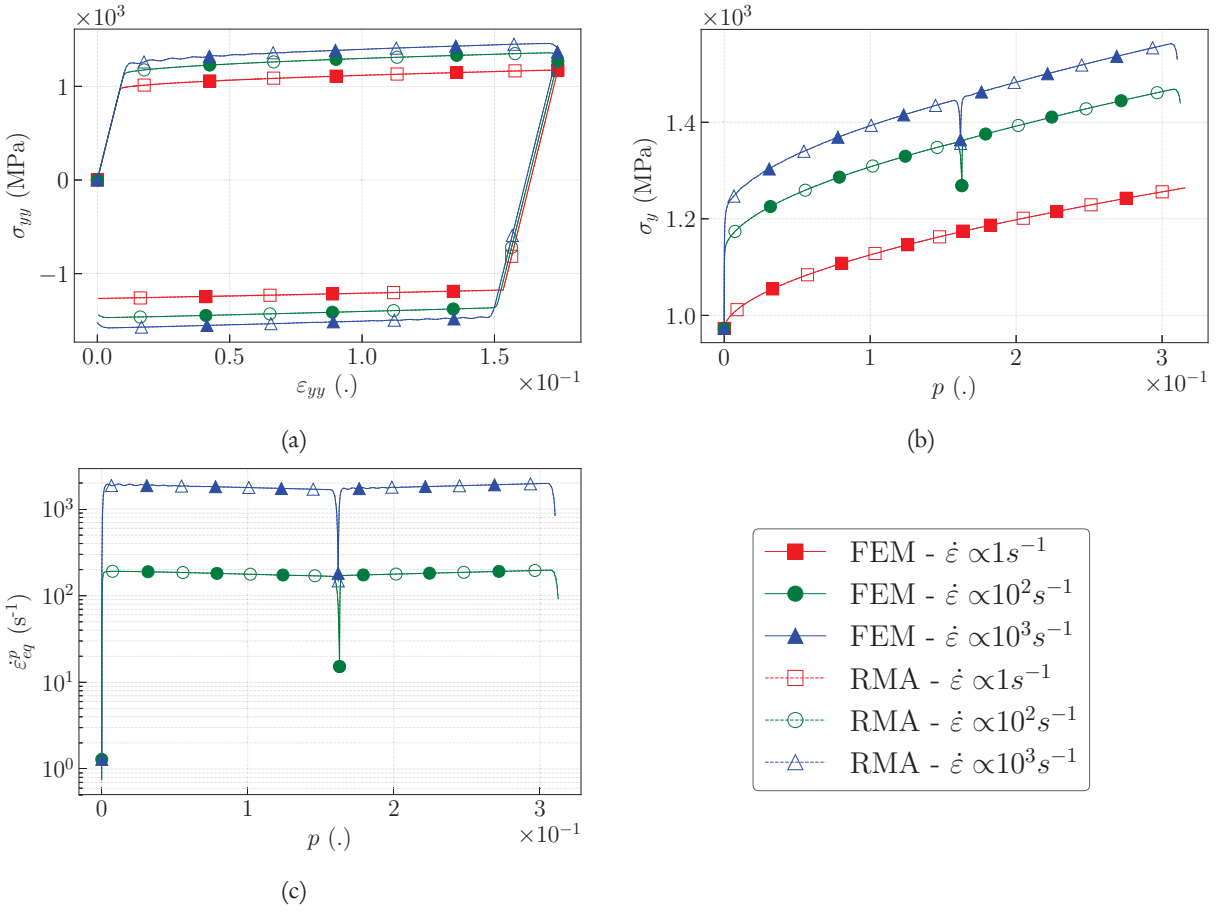

Figure A.1: Virtual tension/compression tests results - (a) σ_{yy} / ε_{yy} - (b) σ_y vs p - (c) $\dot{p}$ vs p

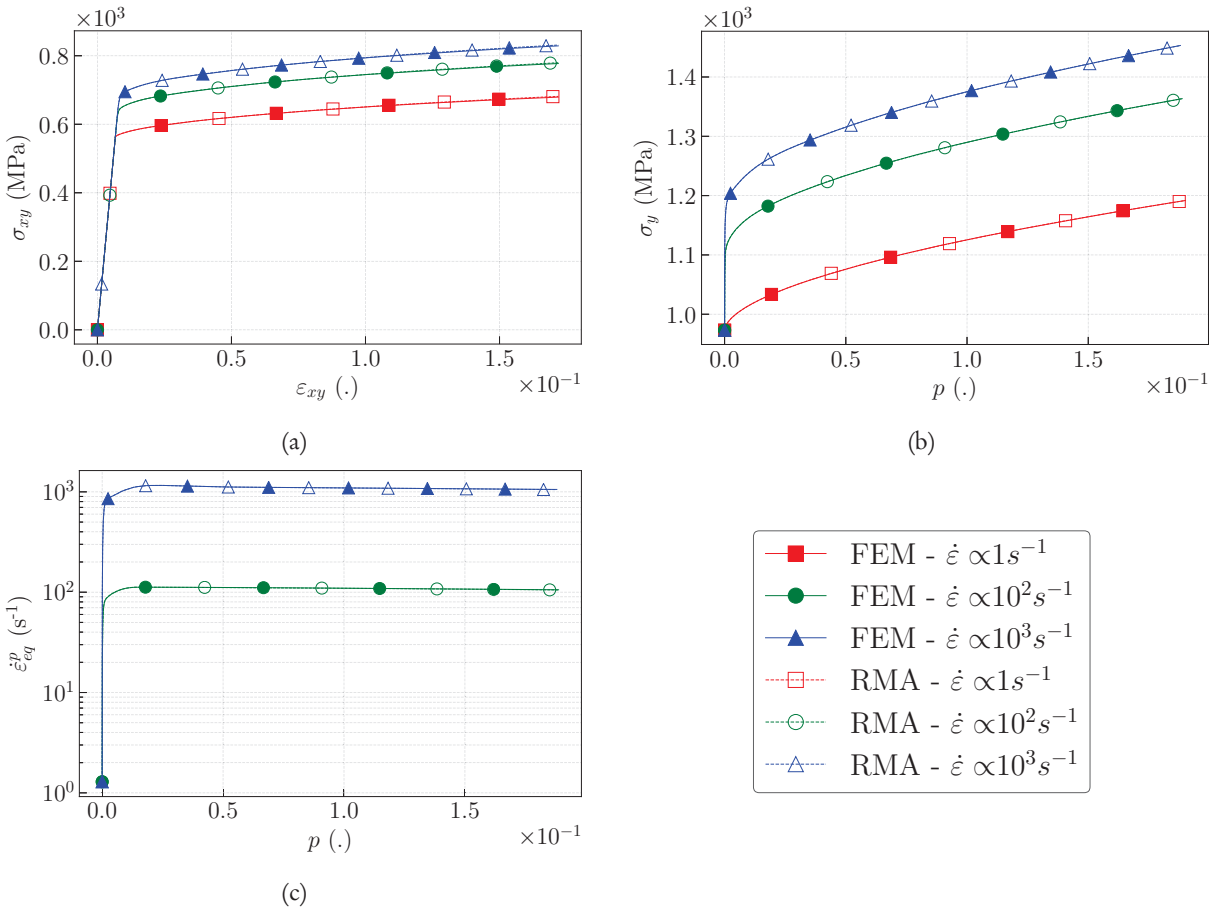

Figure A.2: Virtual shear tests results - (a) σ_{xy} / ε_{xy} - (b) σ_y vs p - (c) $\dot{p}$ vs p

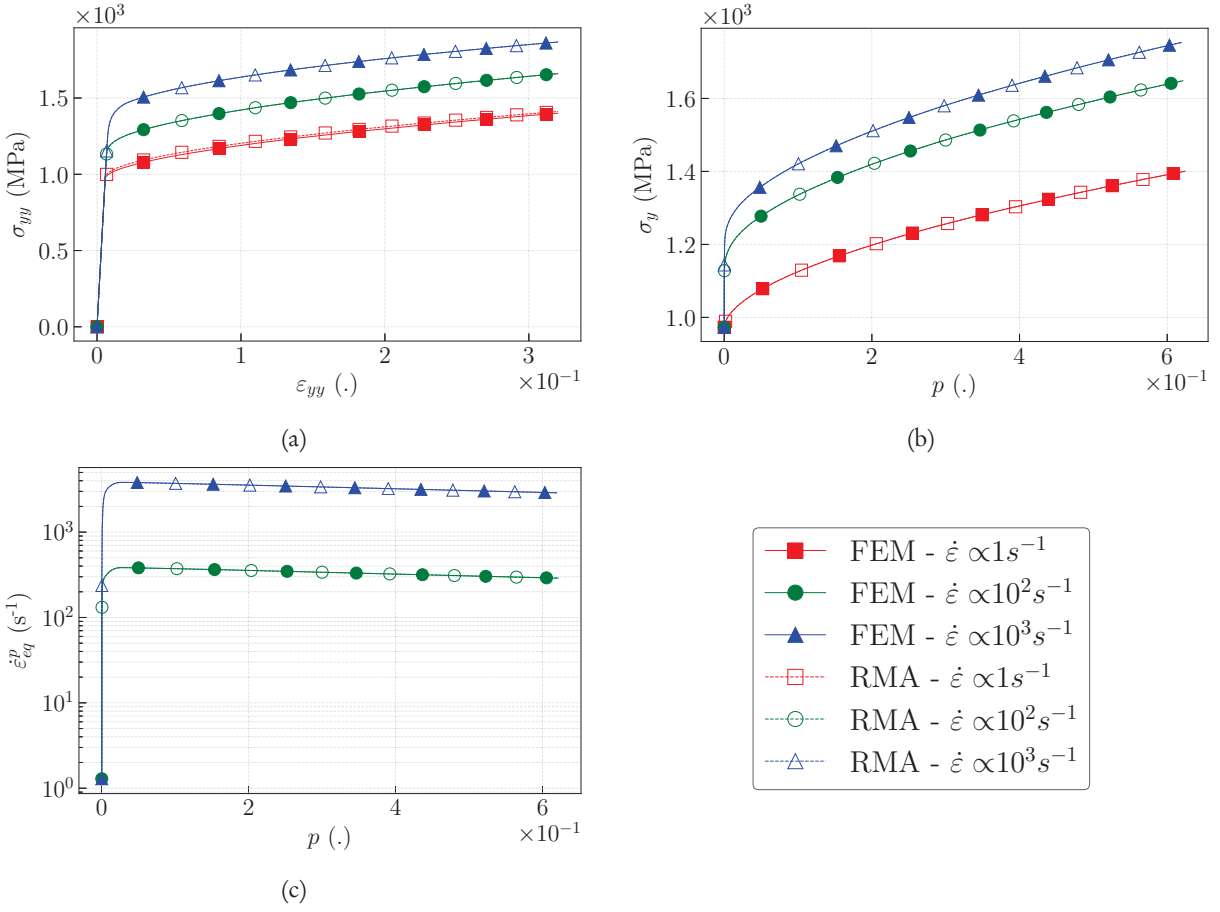

Figure A.3: Virtual biaxial tests results - (a) σ_{yy} / ε_{yy} - (b) σ_y vs p - (c) $\dot{p}$ vs p

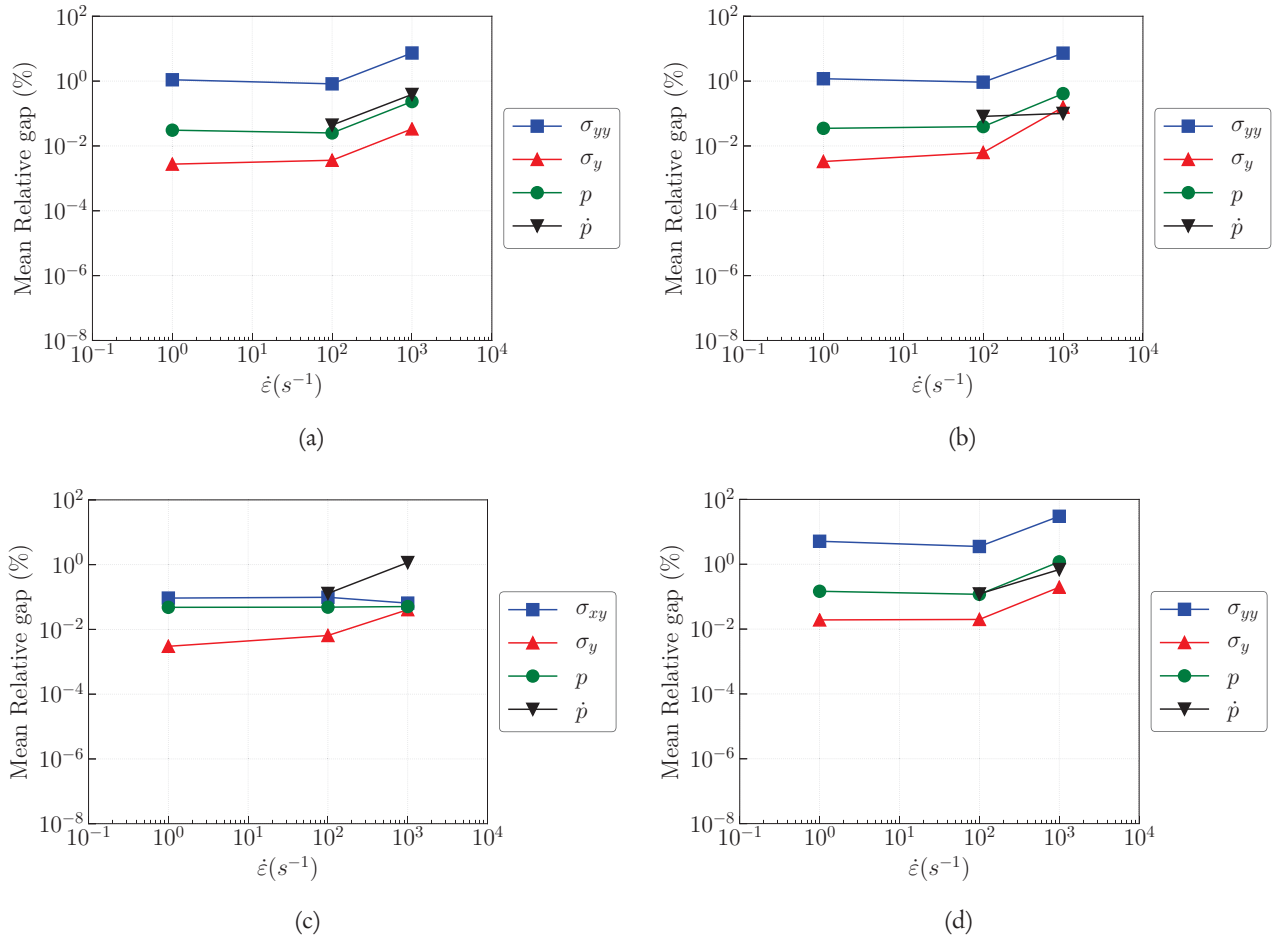

Figure A.4: RMA/FEA comparison: Mean relative gap (with subsampling) - (a) uniaxial tension - (b) uniaxial tension/compression - (c) shear - (d) biaxial tension

Appendix B

Cast3M script for IBII tests mesh generation

This appendix presents the Cast3M® script which have been developped to generate IBII virtual tests meshes introduced in [7] for FEA with Europlexus®. The script is built sequentially to get mesh "operators" which performs the different mesh transformations presented in Figure 2.9.

MAIN SOURCE CODE

```
************************************************************
*                     GLOBAL PROPERTIES                    *
************************************************************
epsil = 1.E-7;
epsilp = 0.1;
slipos =  1.1500E+01;
Nelem3D =  5.0000E-01;
Nelem2D =  5.0000E-01;
Nelemv =  1.2500E+00;

Ri =  2.4500E+01;
Li =  7.0000E+01;
Ni =  1.2500E+00;
Ls =  7.0000E+01;
Ds =  2.2500E+01;
Hs =  2.0000E+00;

Vini=   7.0000E+01;
Vwave=  5.0475E+03;
freq=  2.0000E-04;
dt=  1.0000E-03;
nstep=24.9;
************************************************************
************************************************************
file = 'H:\Calcul\Europlexus\Full_70_0.5\';
name1='impact_test_2D';
name2='impact_test_3D';
name3='vmesh';
ext1='.msh';
ext2='.dat';
************************************************************
*                      3D MESH BUILDING                    *
************************************************************
OPTI DIME 3 ELEM CUB8;

spec23D = BUILD2D Ls Ds Nelem3D epsil;
spec3D = SP2D23D spec23D Hs Nelem3D;

lstep = MINLINE spec23D 2;
lstep=Nelem3D;
Gap=nstep*Vini*(lstep/Vwave);

impa3D = IMP3D Gap Ri Li Ni Ds Hs Nelem3D epsil;
*list lstep;

* elements of the specimen related to the contact
xpos = FLOT (Nelem3D/2.);
sp3Dlel = GETELEM spec3D 1 xpos 1 epsilp;

* elements of the impactor related to the contact
xpos = ( FLOT ((-1)*Nelem3D/2.) ) + ( FLOT ((-1)*Gap) );
im3Drel = GETELEM impa3D 1 xpos 1 epsilp;


* elements for analysis
xpos = (FTRUN Nelem3D slipos)+(0.5*Nelem3D);
el3D = GETELEM spec3D 1 xpos 1 epsilp;

sli3Del = GETELEM spec3D 1 (Hs-(Nelem3D/2.)) 3 epsilp;
sli3Dno = GETNODE sli3Del Hs 3 epsilp;
************************************************************
*                       3D MESH EXPORT                     *
************************************************************

OPTI DIME 3 ELEM CUB8;
TRAC (spec3D ET impa3D) CACH;

OPTI SAUV FORM ( ET (ET file name2) ext1 );
SAUV spec3D impa3D sp3Dlel im3Drel sli3Del sli3Dno el3D;

FIN;
```

```
******************
*IMPACTOR BUILDING*
******************

DEBP IMP3D Gap*FLOTTANT Ri*FLOTTANT Li*FLOTTANT Ni*FLOTTANT
De*FLOTTANT He*FLOTTANT Nelem*FLOTTANT epsil*FLOTTANT;

*Constants
Ini = ((-1.)*Gap);
Depr = De+Nelem;
Hepr = He+Nelem;
delta = (4.)*( (2.)*(Ri**2) - ((Hepr-Depr)**2) );
yimp = 0.25*( (2.)*(Hepr-Depr) + (delta**(0.5)) );
zimp = 0.25*( (2.)*(Depr-Hepr) + (delta**(0.5)) );

*Points
Pext = ((-1)*(Gap+Li)) 0. 0.;

P0 = Ini 0. 0.;
P1 = Ini 0. Hepr ;
P2 = Ini 0. Ri;
P3 = Ini Depr Hepr;
P4 = Ini zimp yimp;
P5 = Ini Depr 0.;
P6 = Ini Ri 0.;

N1 = ENTI PROCHE (Depr/Nelem);
N2 = ENTI PROCHE (Hepr/Nelem);
*Lines
L1 = D N1 P1 P3;
L2 = C N1 P2 P0 P4;
L3 = D N2 P3 P5;
L4 = C N2 P4 P0 P6;

N3 = ENTI PROCHE (Ni/Nelem);
*right half part of the impactor
islic1 = L1 REGL N3 L2;
islic2 = L3 REGL N3 L4;
islic3 = L1 GENE L3;
impslic = ELIM epsil (islic1 ET islic2 ET islic3);

*2D slice of the impactor
impslic = (impslic ET (impslic SYME DROIT P5 P6));
impslic = ELIM epsil impslic;
impslic = (impslic ET (impslic SYME DROIT P1 P2));
impslic = ELIM epsil impslic;

*Extrusion: 3D impactor
impac = impslic VOLU (ENTI PROCHE (Li/Nelem)) TRAN Pext;

FINP impac;

**********************
*RAW SPECIMEN 2D -> 3D*
**********************

DEBP SP2D23D spec*MAILLAGE He*FLOTTANT Nelem*FLOTTANT;

*Points
Pt1 = 0. 0. He;
Pt2 = 0. 0. ((-1)*He);

N1 = ENTI PROCHE (He/Nelem);
*Extrusion
spec3D1 = spec VOLU N1 TRAN Pt1;
spec3D2 = spec VOLU N1 TRAN Pt2;

spec3D = spec3D1 ET spec3D2;

FINP spec3D;

************************
*RAW SPECIMEN TAILORING*
************************

DEBP 2DRAWSP Le*FLOTTANT De*FLOTTANT Nelem*FLOTTANT;

*Points
P1 = 0. De 0.;
P2 = 0. ((-1)*De) 0.;
P3 = Le De 0.;
P4 = Le ((-1)*De) 0.;

N1 = ENTI PROCHE ((2*De)/Nelem);
*Lines
L1 = D N1 P1 P2;
L2 = D N1 P3 P4;

*2D specimen extrusion
spec = L1 REGL DINI Nelem DFIN Nelem L2;

FINP spec;

********************************************************************************
********************************************************************************
********************************************************************************
********************************************************************************

```

```
****************
*MISCHELLANEOUS*
****************

DEBP LTRUN Nelem*FLOTTANT lis*LISTREEL;
val=((ENTIER PROCHE (lis/Nelem)))*Nelem;
FINP val ;

DEBP FTRUN Nelem*FLOTTANT lis*FLOTTANT;
val=((ENTIER PROCHE (lis/Nelem)))*Nelem;
FINP val ;

DEBP LENG P1*POINT P2*POINT;
x1 y1 z1 = COOR P1;
x2 y2 z2 = COOR P2;
val=( ((x1-x2)**2) + ((y1-y2)**2) + ((z1-z2)**2) )**(0.5);
FINP val ;

******************************
*BOUNDS FOR ELEMENT EXTRACTION*
******************************

DEBP BCOND Rt*LISTREEL Lt*LISTREEL Dt*LISTREEL
Nt*LISTREEL Nelem*FLOTTANT epsil*FLOTTANT;

Ntupd = LTRUN Nelem Nt;
nb=DIME Rt;

ymin = LTRUN Nelem (Dt-Ntupd);
ymax = LTRUN Nelem (Dt+Ntupd);
xmin = LTRUN Nelem (Lt-Ntupd);
xmax = LTRUN Nelem (Lt+Ntupd);

*Boundaries defining the working region
i=0;
REPETER LOOPLIM nb ;
i=i+1;

Rti=EXTR Rt i;
Lti=EXTR Lt i;
Dti=EXTR Dt i;

xmi=EXTR xmin i;
xma=EXTR xmax i;
ymi=EXTR ymin i;
yma=EXTR ymax i;

ymib = Dti-Rti;
ymab = Dti+Rti;
xmib = Lti-Rti;
xmab = Lti+Rti;

SI ( (ABS (ymi-ymib)) <EG epsil );
REMP ymin i (ymi - Nelem);
FINSI;
SI ( (ABS (yma-ymab)) <EG epsil );
REMP ymax i (yma + Nelem);
FINSI;
SI ( (ABS (xmi-xmib)) <EG epsil );
REMP xmin i (xmi - Nelem);
FINSI;
SI ( (ABS (xma-xmab)) <EG epsil );
REMP xmax i (xma + Nelem);
FINSI;
FIN LOOPLIM;

FINP xmin xmax ymin ymax;

****************
*HOLE PROPERTIES*
****************

DEBP POHOLE Lt*FLOTTANT Dt*FLOTTANT
xmin*FLOTTANT xmax*FLOTTANT ymin*FLOTTANT ymax*FLOTTANT
Nelem*FLOTTANT epsil*FLOTTANT;

*constants
x=Lt;
y=Dt;

xm = FTRUN Nelem (0.5*(xmin+xmax));
ym = FTRUN Nelem (0.5*(ymin+ymax));

rdiag = Rt/(2.**0.5);
xprd=Lt+rdiag;
yprd=Dt+rdiag;
xmrd=Lt-rdiag;
ymrd=Dt-rdiag;

xpr=Lt+Rt;
ypr=Dt+Rt;
xmr=Lt-Rt;
ymr=Dt-Rt;

*central point
P0 = x y 0.;

*internal points
P1 = xpr y 0.;
P2 = xprd yprd 0.;
P3 = x ypr 0.;
P4 = xmrd yprd 0.;
P5 = xmr y 0.;
P6 = xmrd ymrd 0.;
```

```
P7 = x ymr 0.;
P8 = xprd ymrd 0.;

*external points
P9 = xmax ym 0.;
P10 = xmax ymax 0.;
P11 = xm ymax 0.;
P12 = xmin ymax 0.;
P13 = xmin ym 0.;
P14 = xmin ymin 0.;
P15 = xm ymin 0.;
P16 = xmax ymin 0.;

L1 = LENG P2 P10;
L2 = LENG P4 P12;
L3 = LENG P6 P14;
L4 = LENG P8 P16;

FINP P0 P1 P2 P3 P4 P5 P6 P7 P8 P9 P10 P11
P12 P13 P14 P15 P16 L1 L2 L3 L4;

************************************************************************
************************************************************************
************************************************************************
************************************************************************

************************************
*TAILOR A CIRCULAR HOLE IN A SPECIMEN*
************************************

DEBP 2DSPHOL mesh*MAILLAGE Rt*LISTREEL Lt*LISTREEL Dt*LISTREEL
Nt*LISTREEL Comp*LISTREEL Nelem*FLOTTANT epsil*FLOTTANT;

nb=DIME Rt;

*Erase the elements related to the future hole
xmin xmax ymin ymax = BCOND Rt Lt Dt Nt Nelem epsil;
meshfin = ELELIM mesh 1 2 xmin xmax ymin ymax epsil;

i=0;
REPETER LOOPIND nb;
i=i+1;
Rti=EXTR Rt i;
Lti=EXTR Lt i;
Dti=EXTR Dt i;
Nti=EXTR Nt i;
Compi=EXTR Comp i;

xmi=EXTR xmin i;
xma=EXTR xmax i;
ymi=EXTR ymin i;
yma=EXTR ymax i;

*Build an hole and its neighbours elements
hol2mer = HOLE Rti Lti Dti xmi xma ymi yma Compi Nelem epsil;

*Mesh clearing
meshfin = ELIM epsil (meshfin ET hol2mer);
FIN LOOPIND;

FINP meshfin ;


*****************************
*TAILOR A NOTCH IN A SPECIMEN*
*****************************

DEBP 2DSPNOT mesh*MAILLAGE dir*LISTMOTS Rt*LISTREEL Lt*LISTREEL
Zt*FLOTTANT Nt*LISTREEL Comp*LISTREEL Nelem*FLOTTANT epsil*FLOTTANT;

nb=DIME Rt;
Dt=PROG (DIME Rt)*Zt;

i=0;
REPETER LOOPIND nb;
i=i+1;
diri=EXTR dir i;
SI (EGA diri 'sout');
REMP Dt i ((-1)*Zt);
FINSI;
FIN LOOPIND;

*Erase the elements related to the future notches
xmin xmax ymin ymax  = BCOND Rt Lt Dt Nt Nelem epsil;
meshfin = ELELIM mesh 1 2 xmin xmax ymin ymax epsil;

i=0;
*Notches drilling
REPETER LOOPIND nb;
i=i+1;
diri=EXTR dir i;
Rti=EXTR Rt i;
Lti=EXTR Lt i;
Nti=EXTR Nt i;
Dti=EXTR Dt i;
Compi=EXTR Comp i;
Ntupdi=EXTR Ntupd i;

xmi=EXTR xmin i;
xma=EXTR xmax i;
ymi=EXTR ymin i;
yma=EXTR ymax i;

*Notches building
```

```
not2mer = NOTCH diri Rti Lti Dti xmi xma ymi yma Compi Nelem epsil;
*Mesh merging and clearing
meshfin = ELIM epsil (meshfin ET not2mer);
FIN LOOPIND;

FINP meshfin;


************************************
*BUILD A C NOTCH (NORTH OR SOUTH ONE)*
************************************

DEBP NOTCH dir*MOT Rt*FLOTTANT Lt*FLOTTANT Dt*FLOTTANT
xmin*FLOTTANT xmax*FLOTTANT ymin*FLOTTANT ymax*FLOTTANT
Comp*FLOTTANT Nelem*FLOTTANT epsil*FLOTTANT;

*points generation
P0 P1 P2 P3 P4 P5 P6 P7 P8 P9 P10 P11
P12 P13 P14 P15 P16 L1 L2 L3 L4 = POHOLE Lt Dt
xmin xmax ymin ymax Nelem epsil;

tocomp = PROG L1 L2 L3 L4;
St= ENTI PROCHE ((MAXI tocomp)/Nelem);

*notch generation
SI (EGA dir 'nort');
dim=1;
Ct =          QHOLE St dim P0 P6 P14 P7 P15 Comp Nelem epsil  ;
Ct = Ct ET ( QHOLE St dim P0 P7 P15 P8 P16 Comp Nelem epsil );
dim=2;
Ct = Ct ET ( QHOLE St dim P0 P5 P13 P6 P14 Comp Nelem epsil );
Ct = Ct ET ( QHOLE St dim P0 P8 P16 P1 P9  Comp Nelem epsil );
FINSI;


SI (EGA dir 'sout');
dim=1;
Ct =          QHOLE St dim P0 P2 P10 P3 P11 Comp Nelem epsil  ;
Ct = Ct ET ( QHOLE St dim P0 P3 P11 P4 P12 Comp Nelem epsil );
dim=2;
Ct = Ct ET ( QHOLE St dim P0 P1 P9 P2 P10  Comp Nelem epsil );
Ct = Ct ET ( QHOLE St dim P0 P4 P12 P5 P13 Comp Nelem epsil );
FINSI;

Ct = ELIM epsil Ct;

FINP Ct ;

*******************************************
*BUILD A CENTERED CIRCULAR HOLE IN A REC HOLE*
*******************************************

DEBP HOLE Rt*FLOTTANT Lt*FLOTTANT Dt*FLOTTANT
xmin*FLOTTANT xmax*FLOTTANT ymin*FLOTTANT ymax*FLOTTANT
Comp*FLOTTANT Nelem*FLOTTANT epsil*FLOTTANT;

*points generation
P0 P1 P2 P3 P4 P5 P6 P7 P8 P9 P10 P11
P12 P13 P14 P15 P16 L1 L2 L3 L4 = POHOLE Lt Dt
xmin xmax ymin ymax Nelem epsil;

tocomp = PROG L1 L2 L3 L4;
St= ENTI PROCHE ((MAXI tocomp)/Nelem);

*1/8 holes generation
dim=1;
Ct = QHOLE St dim P0 P2 P10 P3 P11 Comp Nelem epsil;
Ct = Ct ET ( QHOLE St dim P0 P3 P11 P4 P12 Comp Nelem epsil );
Ct = Ct ET ( QHOLE St dim P0 P6 P14 P7 P15 Comp Nelem epsil );
Ct = Ct ET ( QHOLE St dim P0 P7 P15 P8 P16 Comp Nelem epsil );

dim=2;
Ct = Ct ET ( QHOLE St dim P0 P1 P9 P2 P10  Comp Nelem epsil );
Ct = Ct ET ( QHOLE St dim P0 P4 P12 P5 P13 Comp Nelem epsil );
Ct = Ct ET ( QHOLE St dim P0 P5 P13 P6 P14 Comp Nelem epsil );
Ct = Ct ET ( QHOLE St dim P0 P8 P16 P1 P9  Comp Nelem epsil );

Ct = ELIM epsil Ct;

FINP Ct;


***************************
*BUILD A 1/8 CIRCULAR HOLE*
***************************

DEBP QHOLE St*ENTIER dim*ENTIER
Pt0*POINT Pt1*POINT Pt2*POINT Pt3*POINT Pt4*POINT
Comp*FLOTTANT Nelem*FLOTTANT epsil*FLOTTANT;

c1 = COOR dim Pt2;
c2 = COOR dim Pt4;
length = ABS (c1-c2);
Mt = ENTI PROCHE (length/Nelem);

Lt1 = C Mt Pt1 Pt0 Pt3;
Lt2 = D Mt Pt2 Pt4;

Ht = Lt1 REGL St Lt2;

FINP Ht;

*****************************************
*CREATE A RECTANGULAR HOLE IN A 2D SPECIMEN*
```

```
****************************************

DEBP ELELIM mesh*MAILLAGE co1*ENTIER co2*ENTIER
xmin*LISTREEL xmax*LISTREEL ymin*LISTREEL ymax*LISTREEL
epsil*FLOTTANT;

*On input, we have the raw mesh.
*For each element, the criterion is calculated for its barycenter.
*If it is verified, the latter is added to the updated mesh.

i=0;
com=0;
REPETER REBUI (NBEL mesh);

i=i+1;
*get an element
test = mesh ELEM i;
*get its barycenter
pbary = BARY test;
xm = COOR co1 pbary;
ym = COOR co2 pbary;
nbsing=DIME xmax;
*criterion analysis
j=0;
crit=0;
REPETER CRITEST nbsing;
j=j+1;
xmi=EXTR xmin j;
xma=EXTR xmax j;
ymi=EXTR ymin j;
yma=EXTR ymax j;
ded = RECIN xm ym xmi xma ymi yma epsil;
SI (NON ded);
crit=crit+1;
FINSI;
FIN CRITEST;

*if the barycenter is inside the unwanted zone, the element
*is kept, excluded otherwise
SI (crit EGA nbsing);
SI (NON ded);
com=com+1;
SI (com EGA 1);
mail = test;
SINON;
mail = mail ET test;
FINSI;
FINSI;
FINSI;

FIN REBUI;

FINP mail;

************************************************************
*GET A GROUP OF NODES WITH RESPECTS TO A GEOMETRIC CRITERION*
************************************************************

DEBP GETNODE mesh*MAILLAGE coo*FLOTTANT
compo*ENTIER epsil*FLOTTANT;

i=0;
com=0;
*get the nodes of the mesh
meshp = CHAN POI1 mesh;
*On input, we have the raw mesh.
*The criterion is calculated for each point.
*If it is true, the latter is added to the selection
REPETER GET (NBNO mesh);
i=i+1;
*get a point
test = meshp POINT i;
*get its related coordinate
xm = COOR compo test;
*criterion analysis
keep = ( (ABS (xm-coo)) <EG epsil );
*if the point has the right coordinate, the latter
*is kept, excluded otherwise
SI (keep);
com=com+1;
SI (com EGA 1);
mail = test;
SINON;
mail = mail ET test;
FINSI;
FINSI;
FIN GET;

FINP mail;

****************************************************************
*GET A GROUP OF ELEMENTS WITH RESPECTS TO A GEOMETRIC CRITERION  *
* 1 - FIND AN ELEMENT WITH A GIVEN COORDINATE                    *
* 2 - FIND AN ELEMENT WHOSE COORDINATE IS SUPERIOR TO A GIVEN ONE*
* 3 - FIND AN ELEMENT WHOSE COORDINATE IS INFERIOR TO A GIVEN ONE*
****************************************************************

DEBP GETELEM mesh*MAILLAGE option*ENTIER coo*FLOTTANT
compo*ENTIER epsil*FLOTTANT;

i=0;
com=0;
*On input, we have the raw mesh.
*For each element, the criterion is calculated for its barycenter.
```

```
*If it is true, the latter is added to the selection
REPETER GET (NBEL mesh);
i=i+1;
*get an element
test = mesh ELEM i;
*get its barycenter
pbary = BARY test;
xm = COOR compo pbary;
*criterion analysis
SI (option EGA 1);
keep = ( (ABS (xm-coo)) <EG epsil );
FINSI;
SI (option EGA 2);
keep = ( (xm-coo) >EG ((-1)*epsil) );
FINSI;
SI (option EGA 3);
keep = ( (xm-coo) <EG epsil );
FINSI;
*if the barycenter has the right coordinate
*is kept, excluded otherwise
SI (keep);
com=com+1;
SI (com EGA 1);
mail = test;
SINON;
mail = mail ET test;
FINSI;
FINSI;
FIN GET;

FINP mail;

************************************************************
************************************************************

DEBP MINLINE mesh*MAILLAGE dim*ENTIER;

i=0;
nbelem=NBEL mesh;
areas = PROG nbelem * 0.;

REPETER GET nbelem;
i=i+1;
*get an element area
area = MESU (mesh ELEM i);
REMP areas 1 area;
FIN GET;
*maxmum value
value = (MAXI areas)**(1./dim);
FINP value;


***********************************************
*FIND IF A POINT IS INSIDE A COLINEAR RECTANGLE*
***********************************************

DEBP RECIN xm*FLOTTANT ym*FLOTTANT xmin*FLOTTANT
xmax*FLOTTANT ymin*FLOTTANT ymax*FLOTTANT eps*FLOTTANT ;


k1 = (xm-xmin)*(xmax-xmin);
k2 = (xmax-xmin)**(2);
k3 = (ym-ymax)*(ymin-ymax);
k4 = (ymax-ymin)**(2);


ded = ( k1 > ((-1)*eps) ) ET ( (k1-k2) < eps  )
ET ( k3 > ((-1)*eps) ) ET ( (k3-k4) < eps );

FINP ded;


DEBPROC BUILD2D Ls*FLOTTANT Ds*FLOTTANT Nelem*FLOTTANT
epsil*FLOTTANT;


spec2D = 2DRAWSP Ls Ds Nelem;

FINPROC spec2D;
```

Appendix C

Complementary results for IBII tests through-thickness analysis

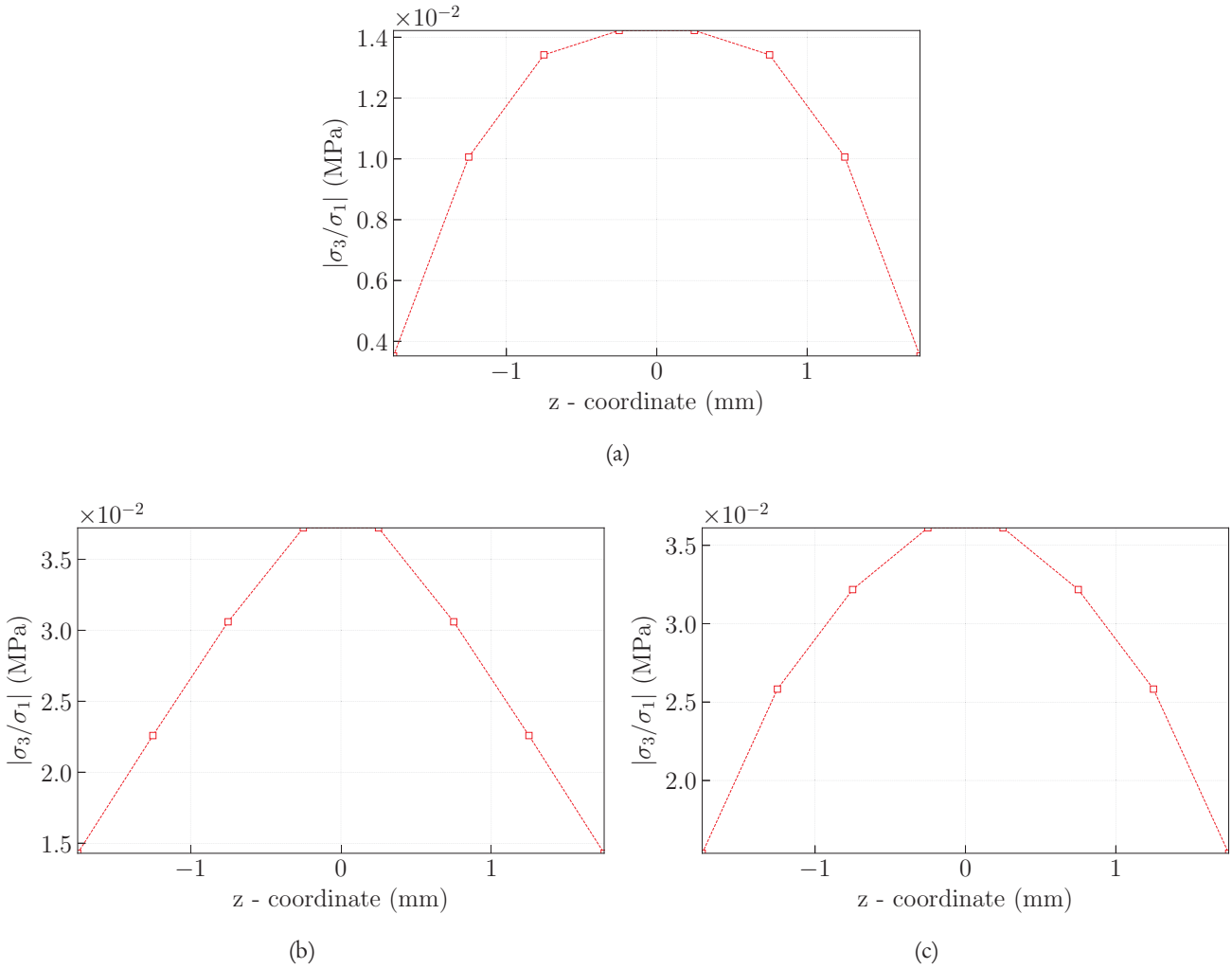

Figure C.1: Principal stress ratio mean time value, V_p= 70 m.s^{-1} - (a) Specimen 0 - (b) Specimen 1 - (c) Specimen 2

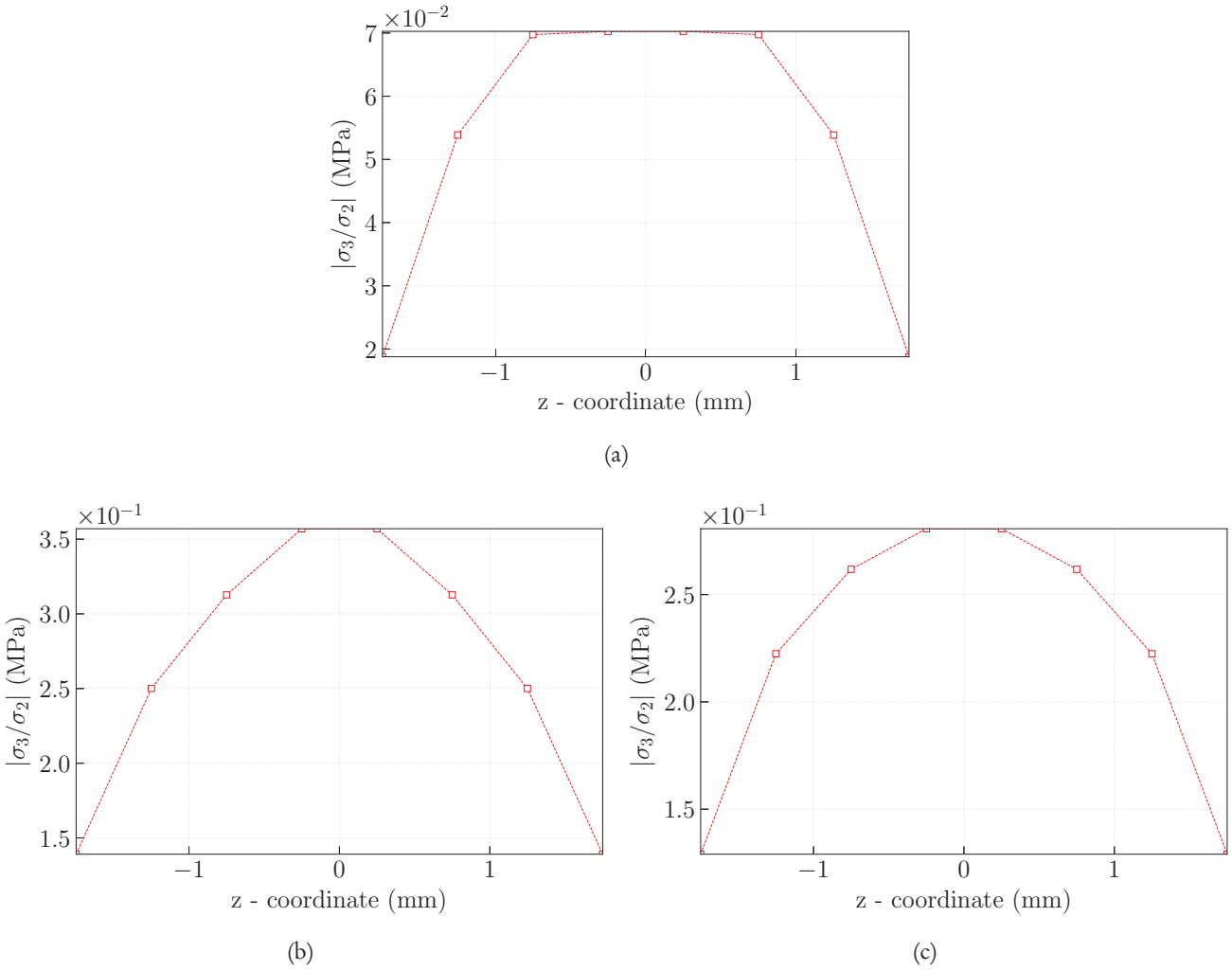

Figure C.2: Principal stress ratio mean time value, V_p= 70 m.s^{-1} - (a) Specimen 0 - (b) Specimen 1 - (c) Specimen 2

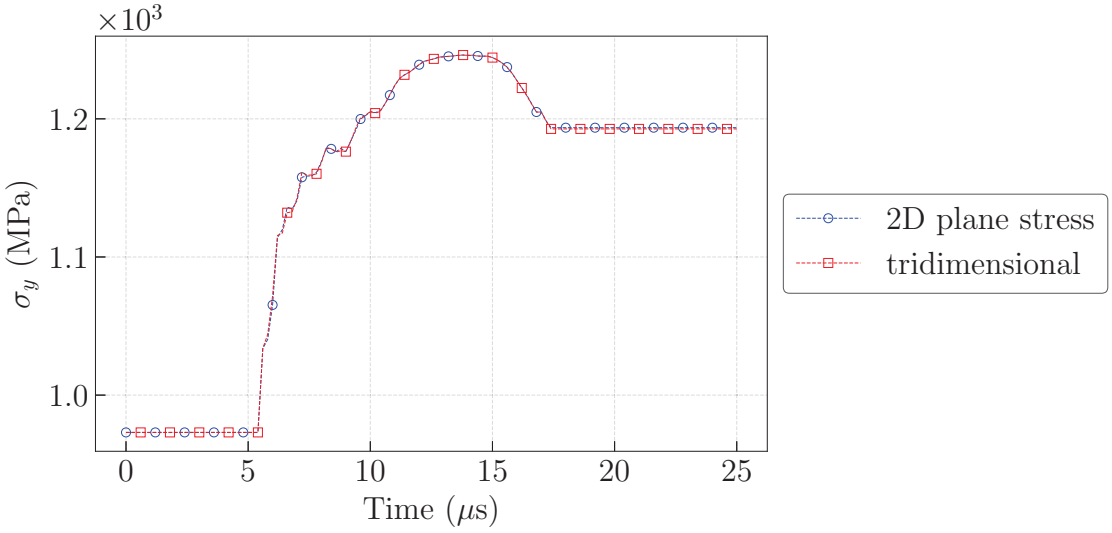

(a)

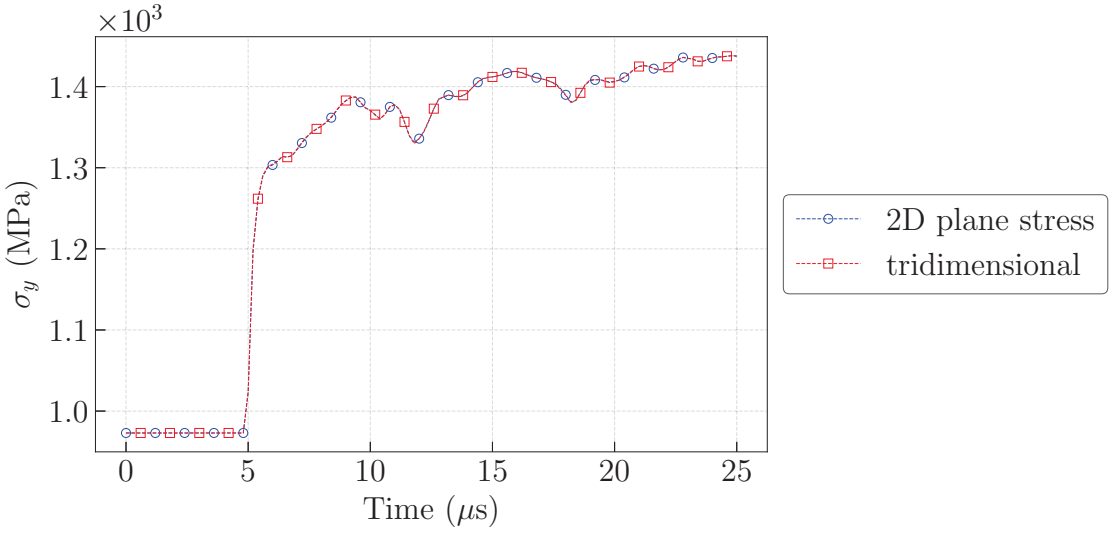

(b)

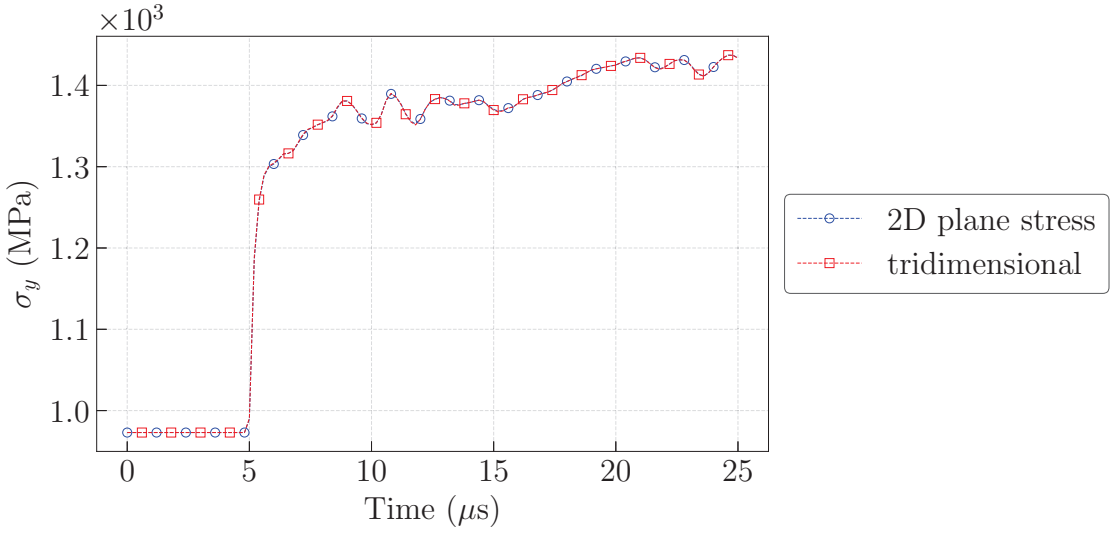

(c)

Figure C.3: σ_y reconstruction, V_p=70 m.s^{-1} at 5 Mfps - (a) Specimen 0 - (b) Specimen 1 - (c) Specimen 2

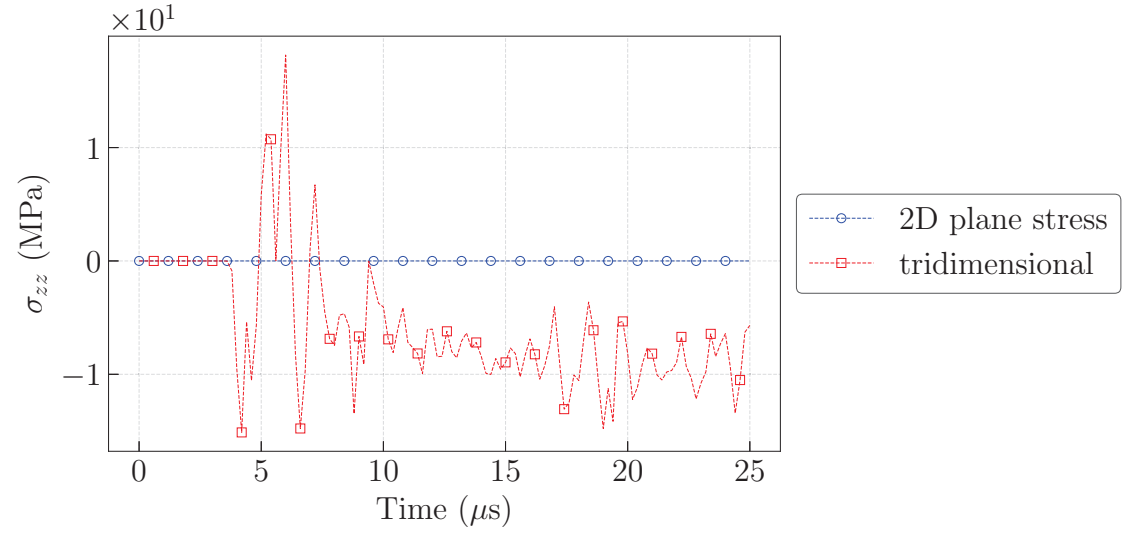

(a)

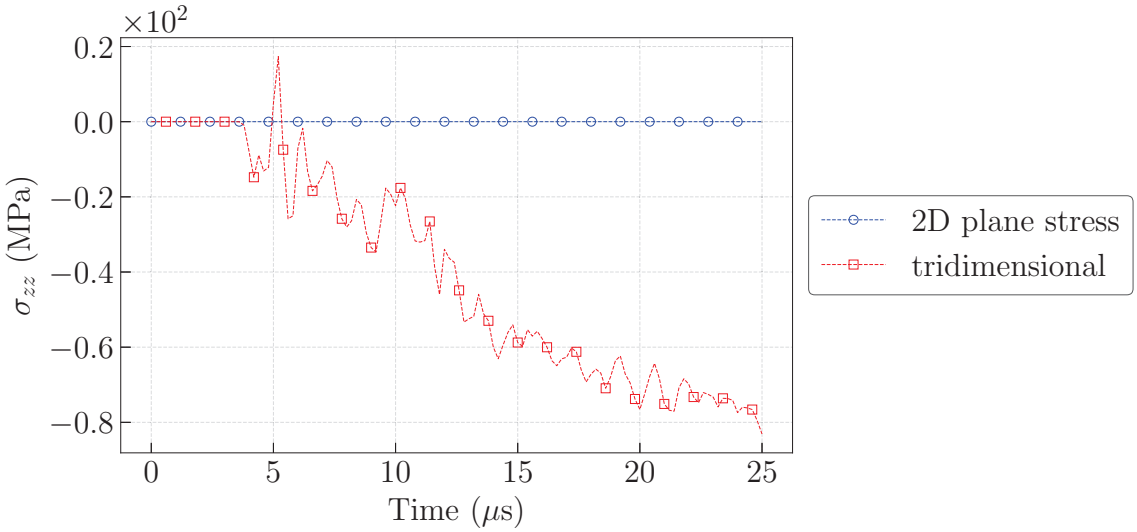

(b)

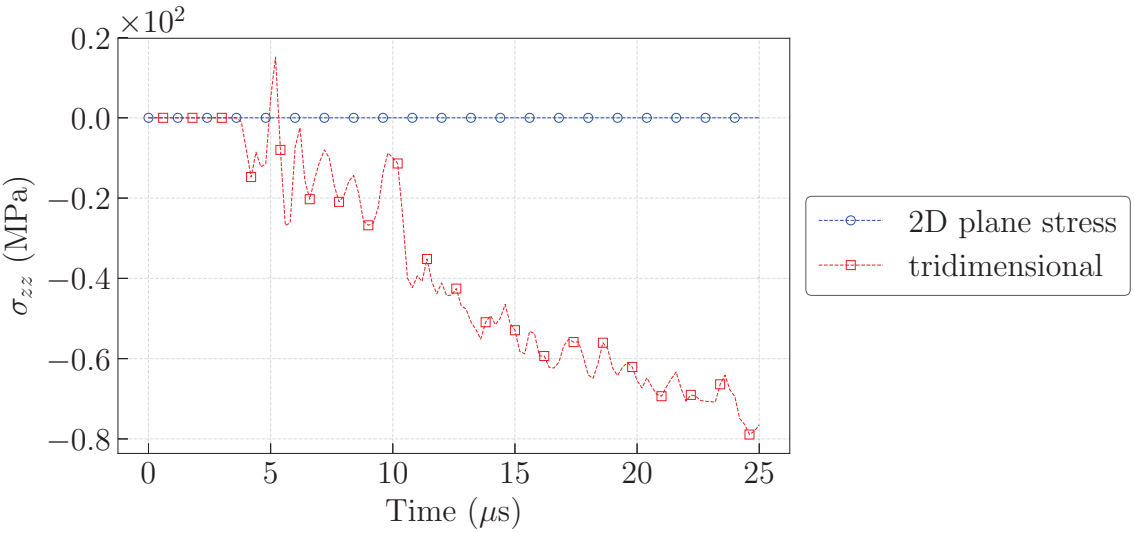

(c)

Figure C.4: σ_{zz} reconstruction, V_p=70 m.s^{-1} at 5 Mfps - (a) Specimen 0 - (b) Specimen 1 - (c) Specimen 2

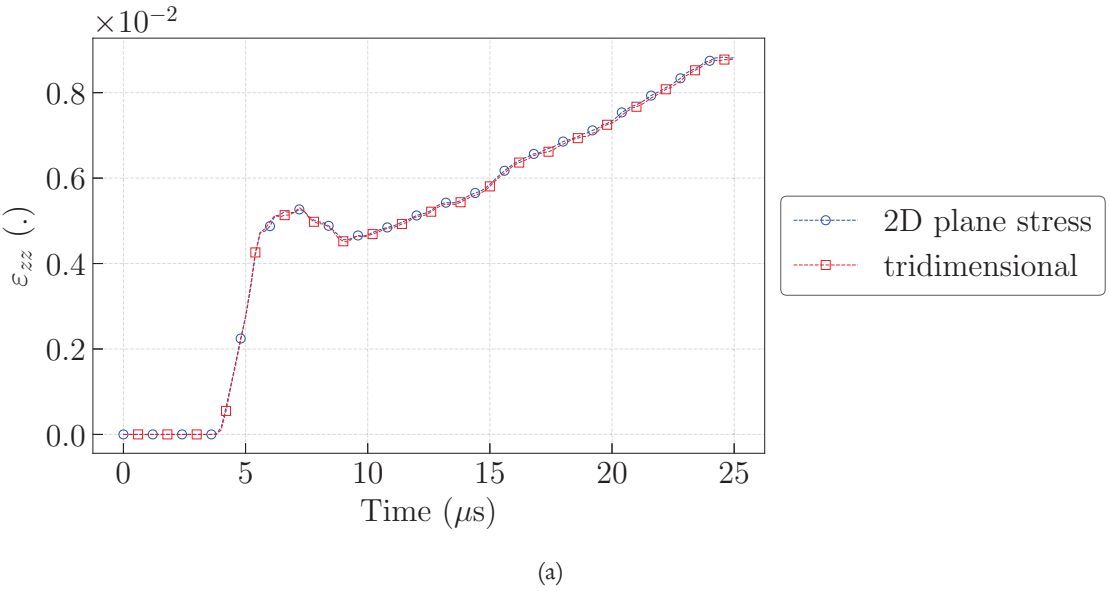

(a)

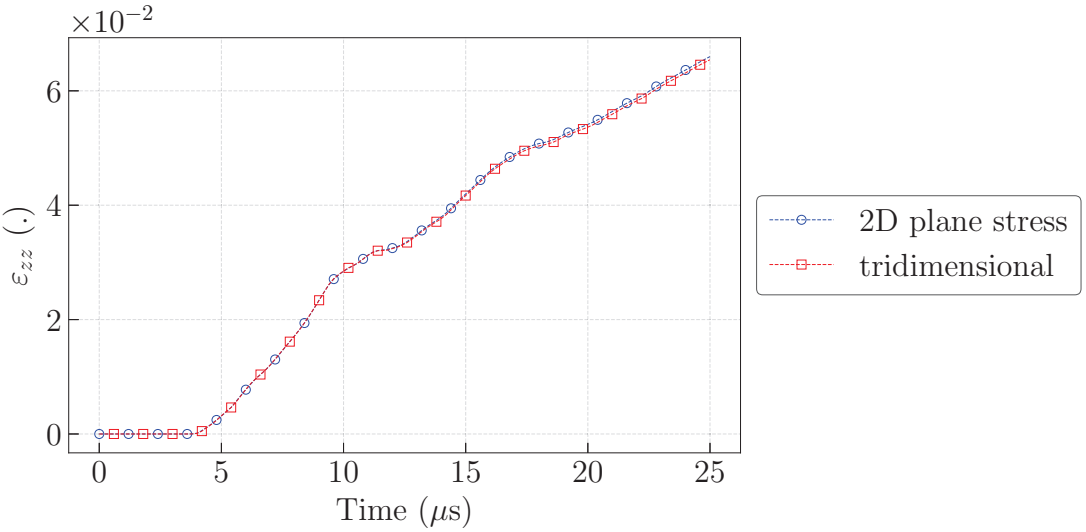

(b)

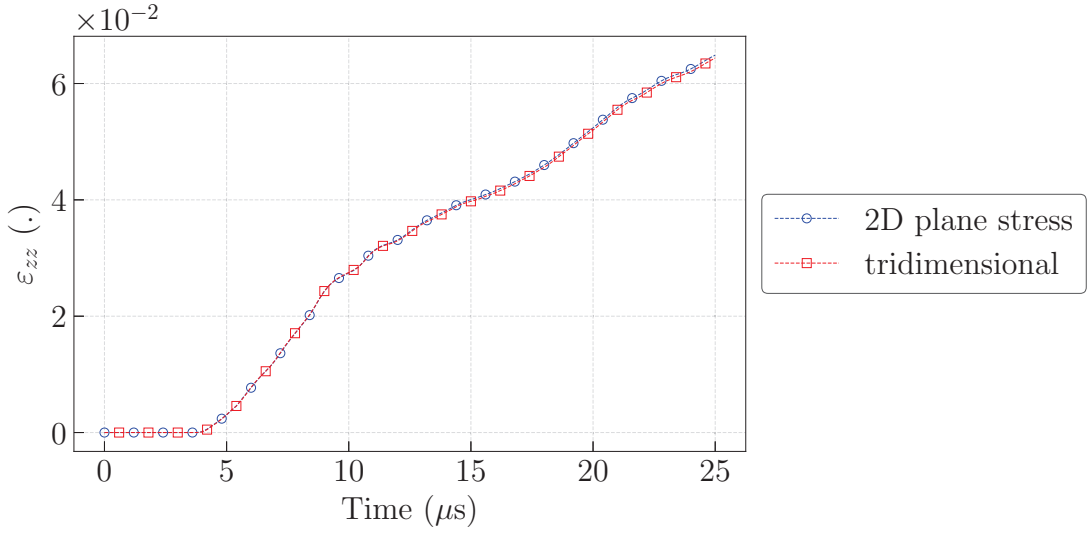

(c)

Figure C.5 : ε_{zz} reconstruction, V_p= 70 m.s^{-1} at 5 Mfps - (a) Specimen 0 - (b) Specimen 1 - (c) Specimen 2

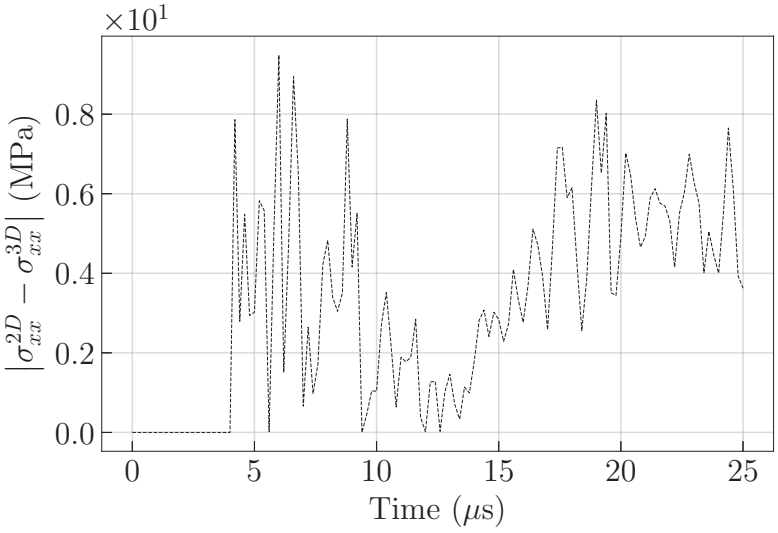

(a)

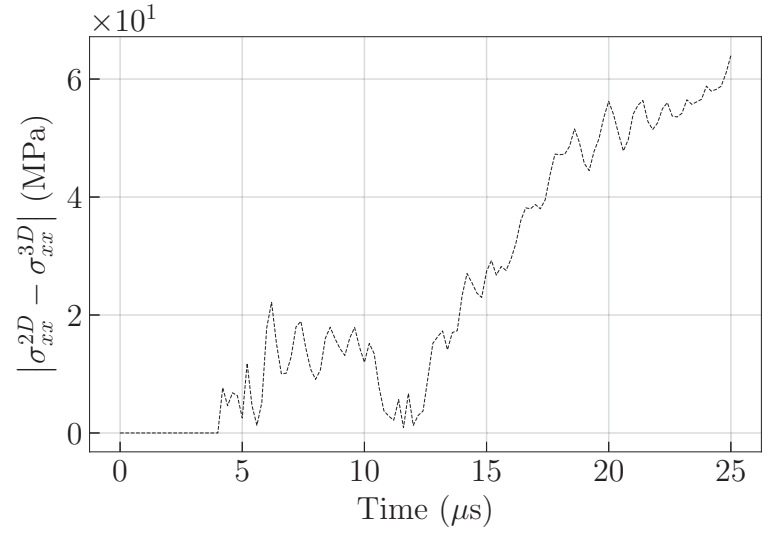

(b)

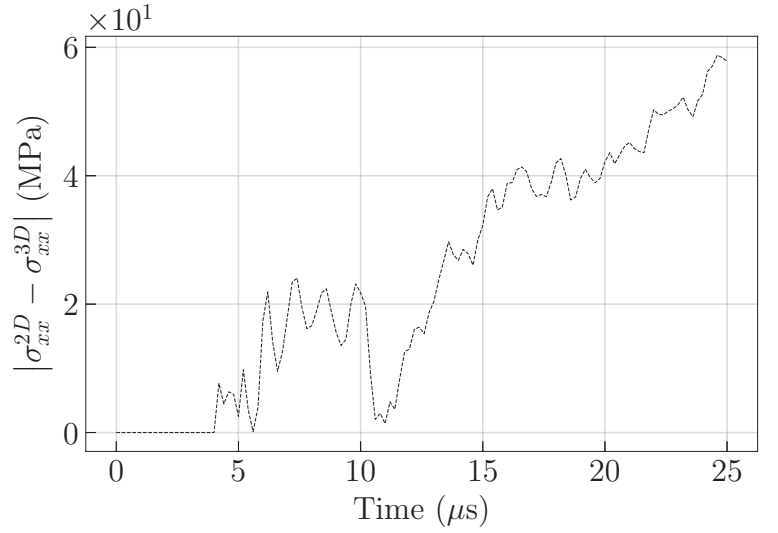

(c)

Figure C.6: σ_{xx} reconstruction error, V_p=70 m.s^{-1} at 5 Mfps - (a) Specimen 0 - (b) Specimen 1 - (c) Specimen 2

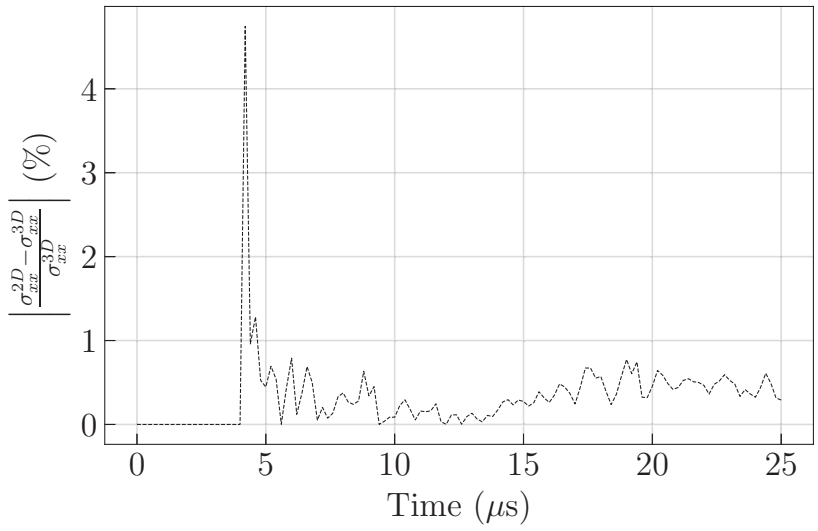

(a)

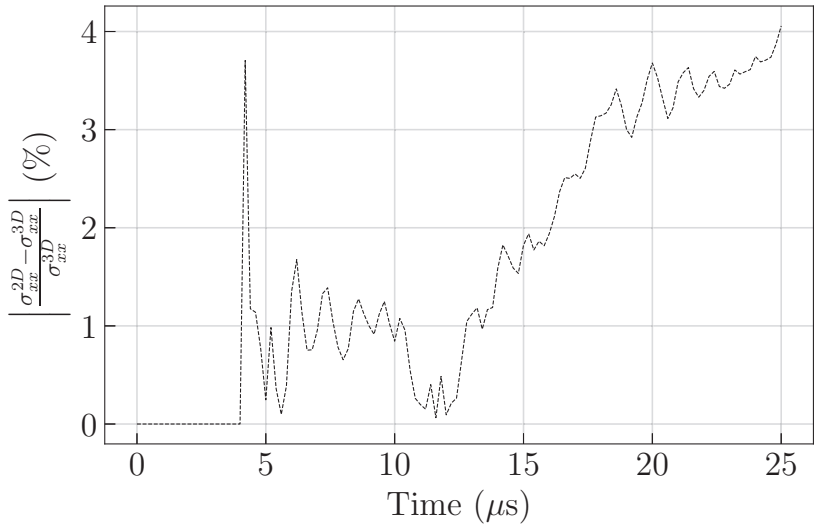

(b)

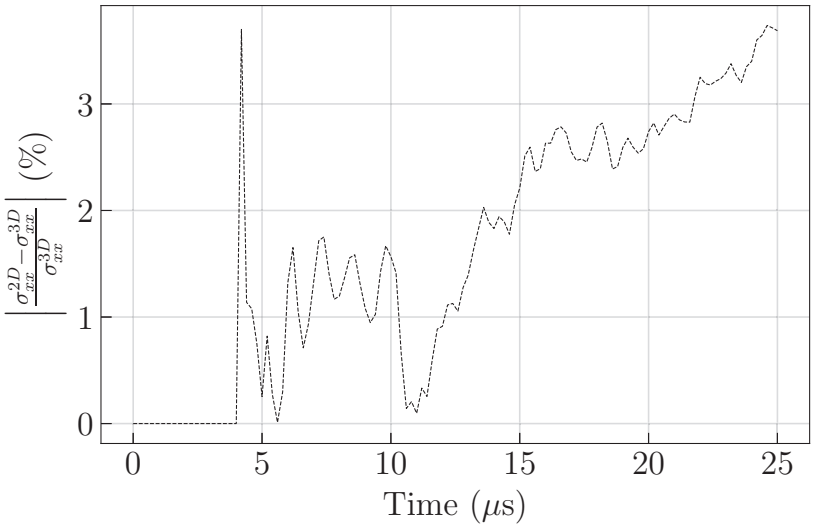

(c)

Figure C.7: σ_{xx} reconstruction error, V_p=70 m.s^{-1} at 5 Mfps - (a) Specimen 0 - (b) Specimen 1 - (c) Specimen 2

Appendix D

Complementary results for IBII test campaign metrological performance assessment

This appendix collects the IBII tests campaign full-field maps normalized histograms computed from the static references.

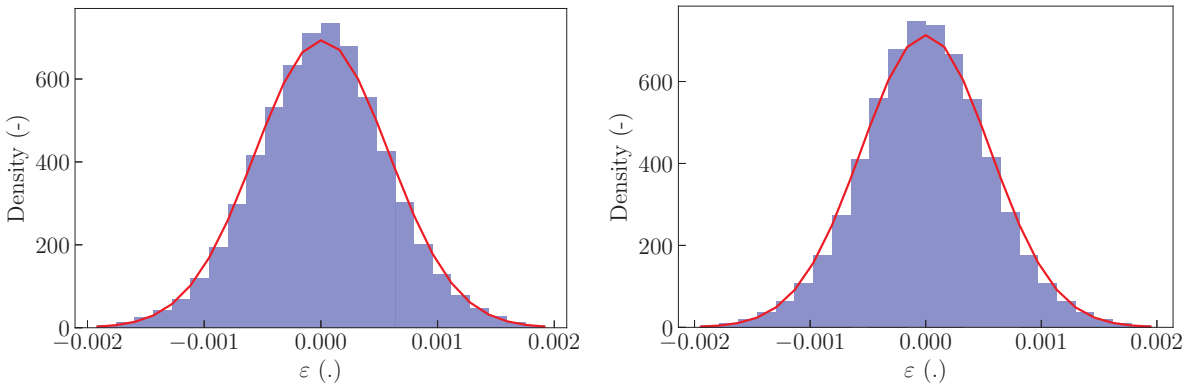

(a) QUAL-FULL-01 (b) QUAL-FULL-02

Figure D.1: Grid method histograms for rectangular specimens static reference - strains

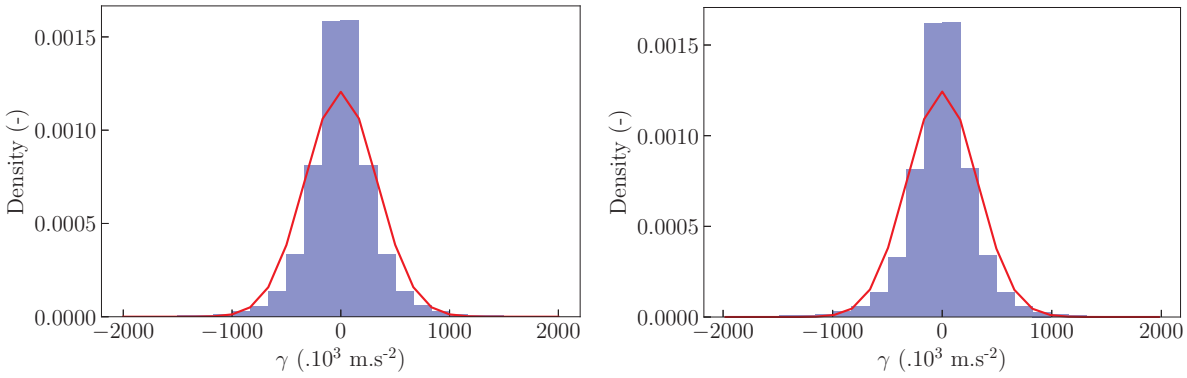

(a) QUAL-FULL-01 (b) QUAL-FULL-02

Figure D.2: Grid method histograms for rectangular specimens static reference - accelerations

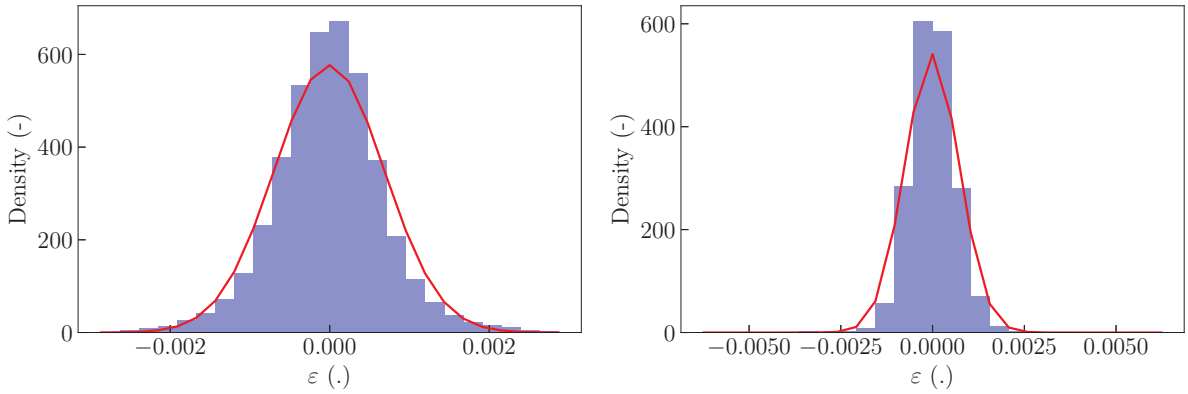

(a) CHAR-HOLE-01

(b) CHAR-HOLE-02

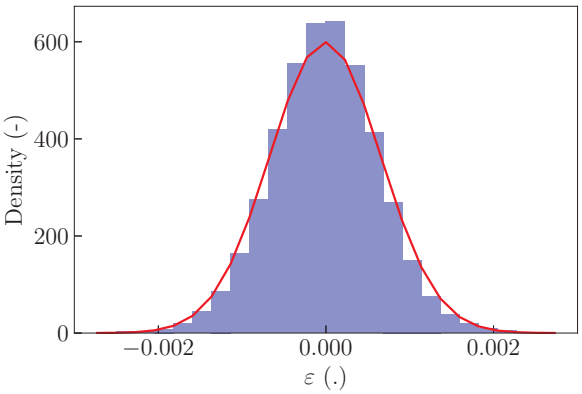

(c) CHAR-HOLE-03

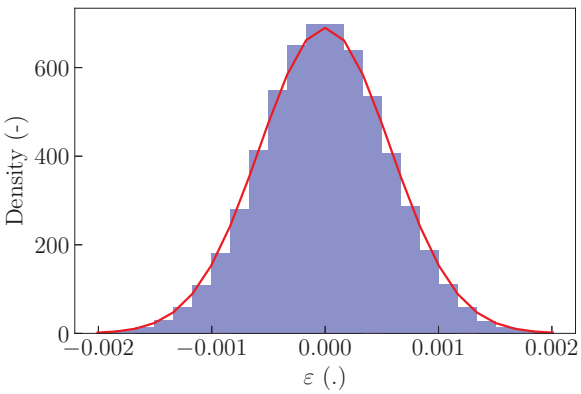

(d) CHAR-HOLE-04

Figure D.3: Grid method histograms for holed specimens static reference - strains

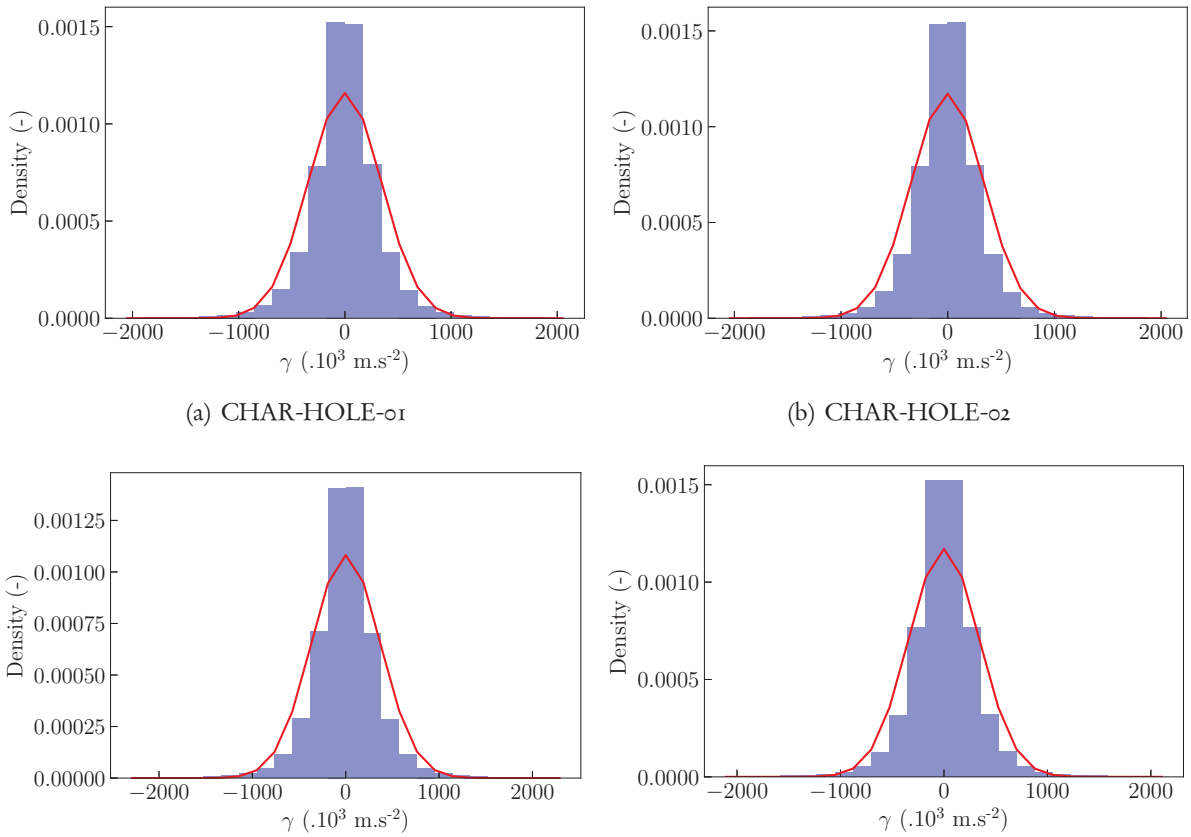

(a) CHAR-HOLE-01

(b) CHAR-HOLE-02

(c) CHAR-HOLE-03

(d) CHAR-HOLE-04

Figure D.4: Grid method histograms for holed specimens static reference - accelerations

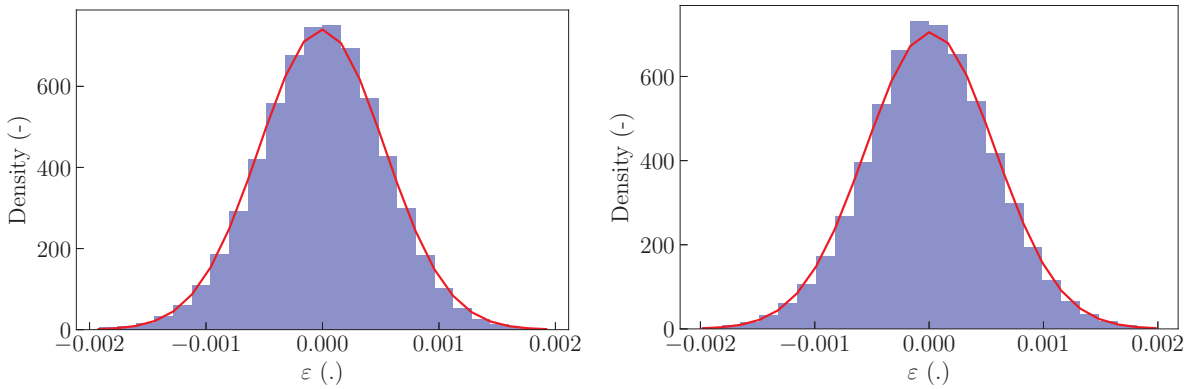

(a) CHAR-NOTC-01

(b) CHAR-NOTC-02

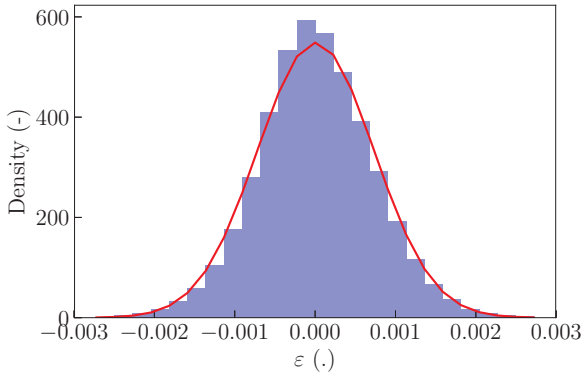

(c) CHAR-NOTC-03

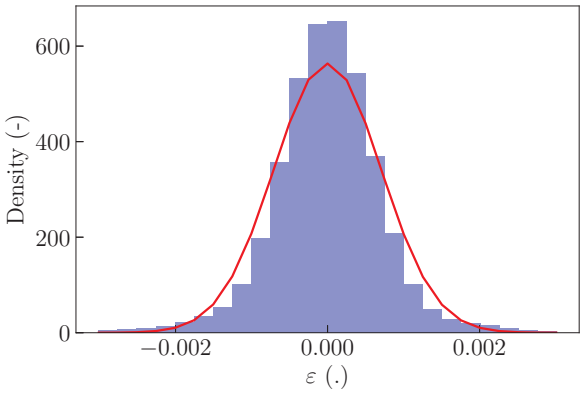

(d) CHAR-NOTC-04

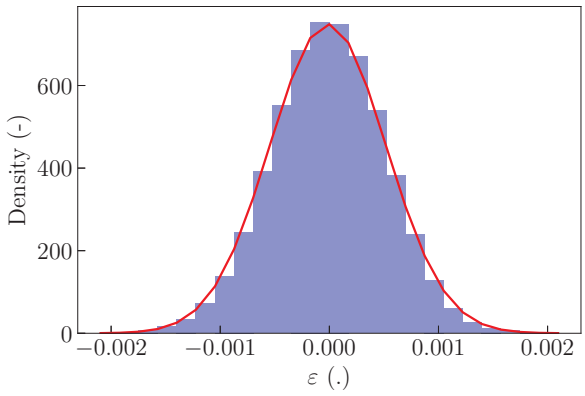

(e) CHAR-NOTC-05

Figure D.5: Grid method histograms for notched specimens static reference - strains

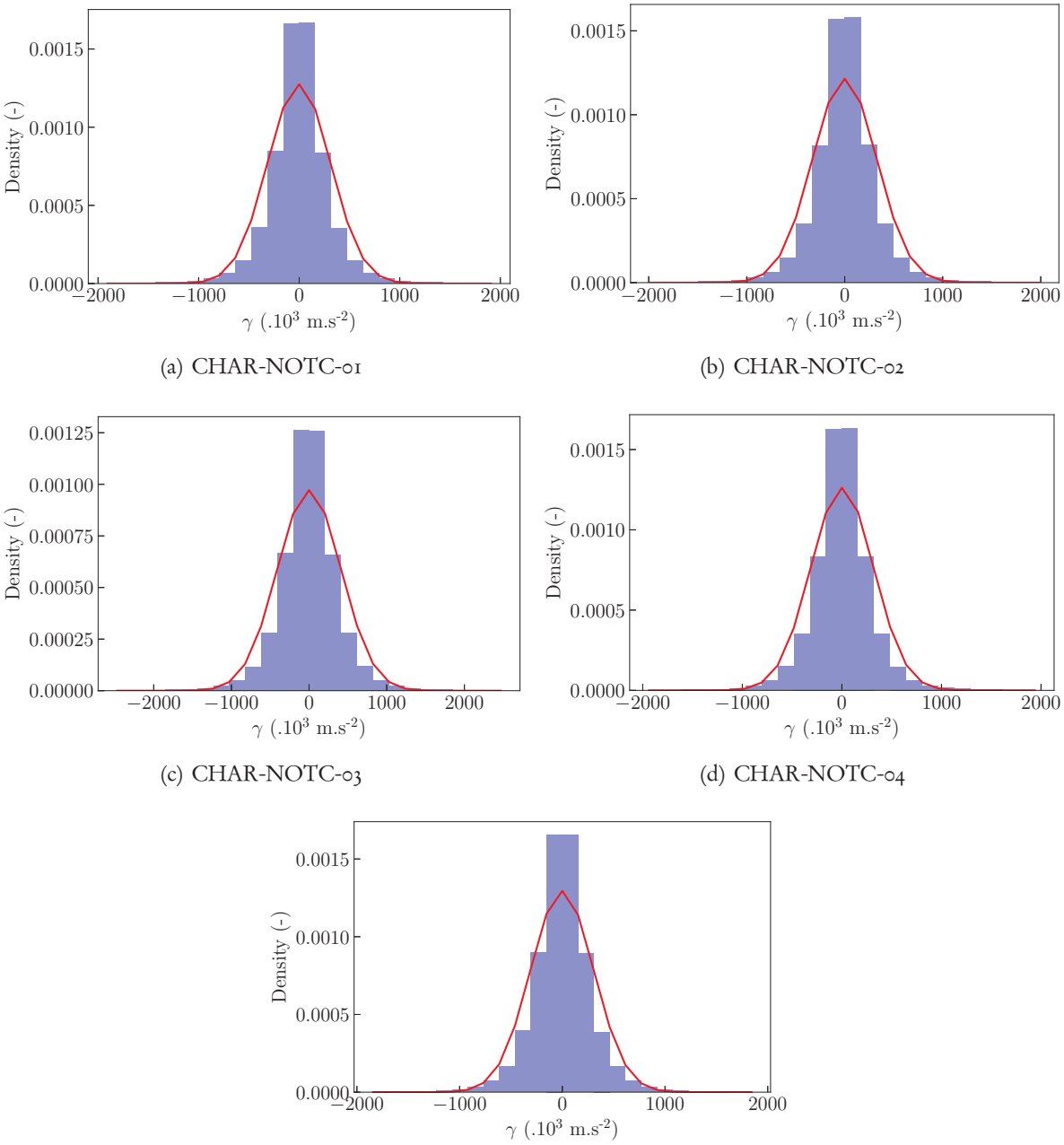

(a) CHAR-NOTC-01

(b) CHAR-NOTC-02

(c) CHAR-NOTC-03

(d) CHAR-NOTC-04

(e) CHAR-NOTC-05

Figure D.6: Grid method histograms for notched specimens static reference - accelerations

Appendix E

Complementary results for comparison between experimental results and numerical predictions

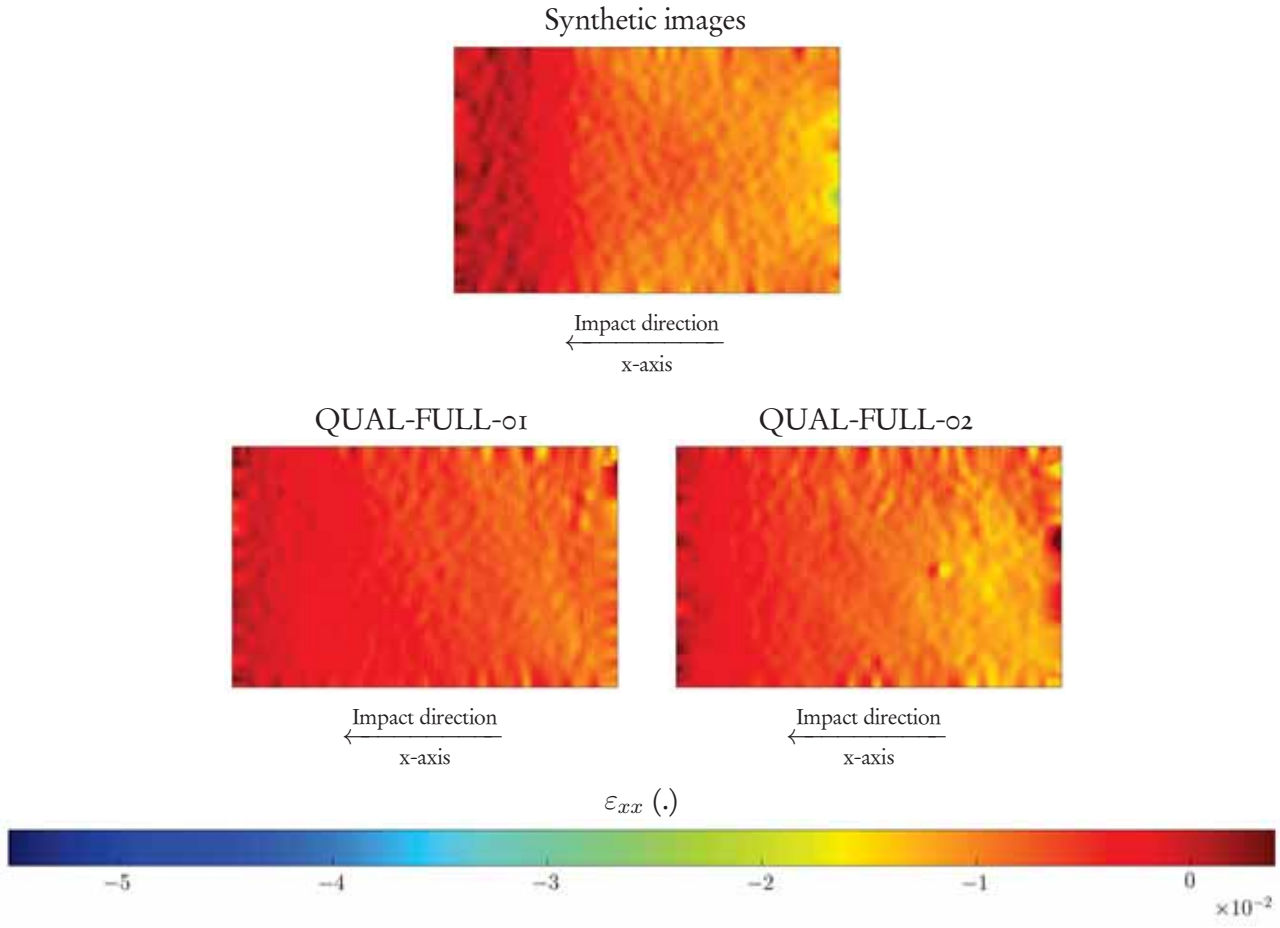

Figure E.1: ε_{xx} at t = 14μs: experimental vs synthetic images for rectangular specimens

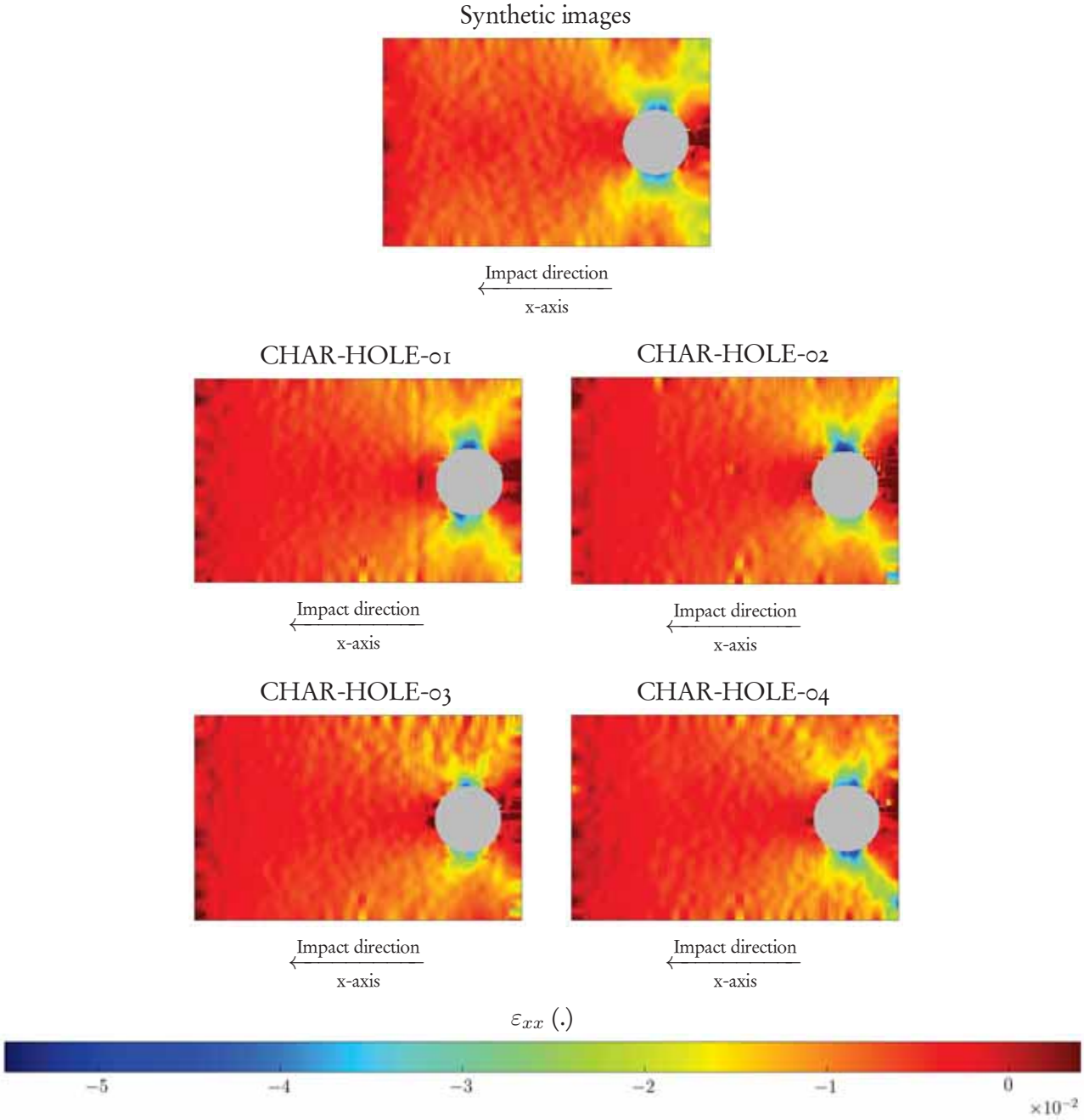

Figure E.2: ε_{xx} at t = 14μs: experimental vs synthetic images for holed specimens

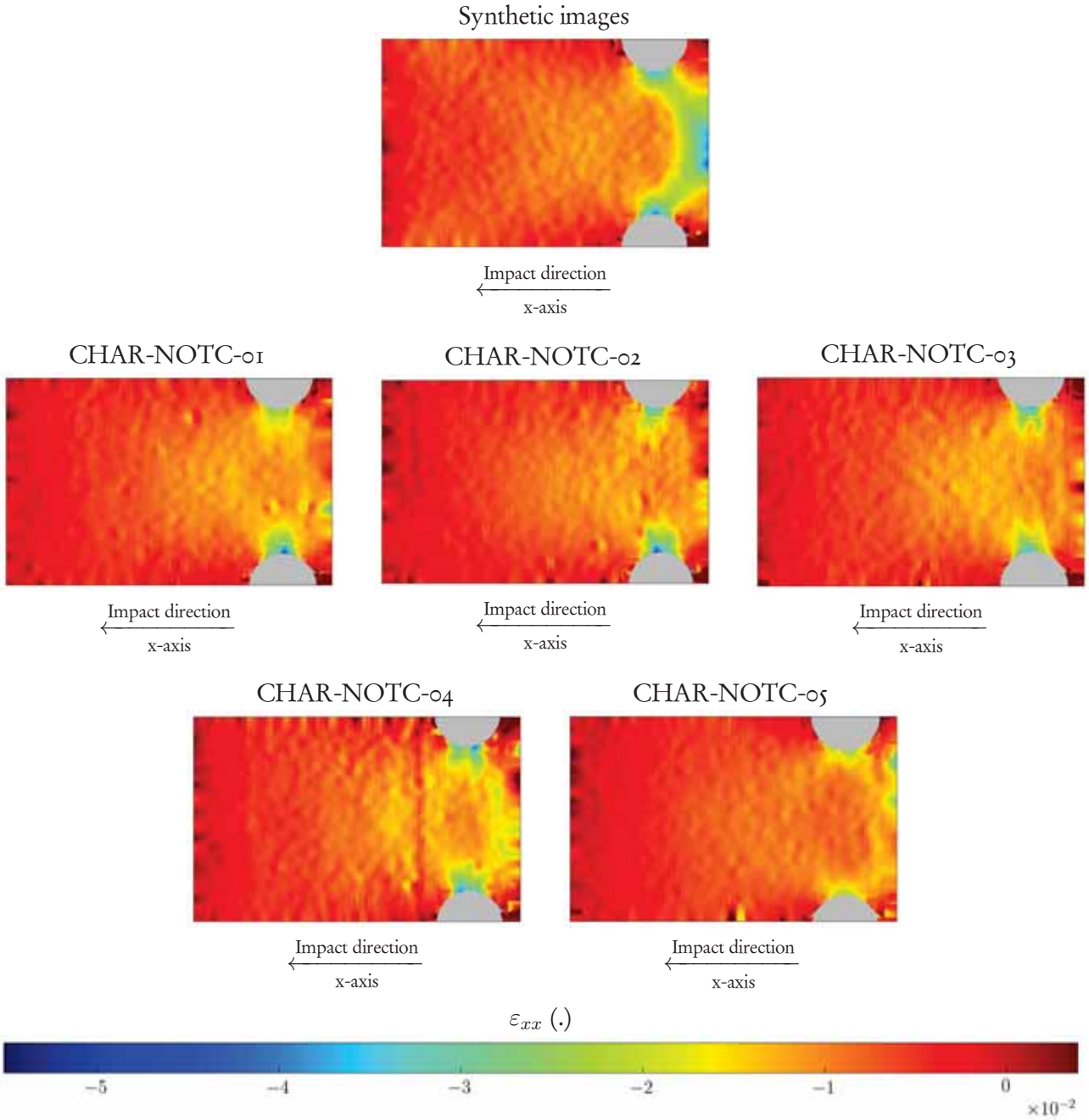

Figure E.3: ε_{xx} at t = 14μs: experimental vs synthetic images for notched specimens

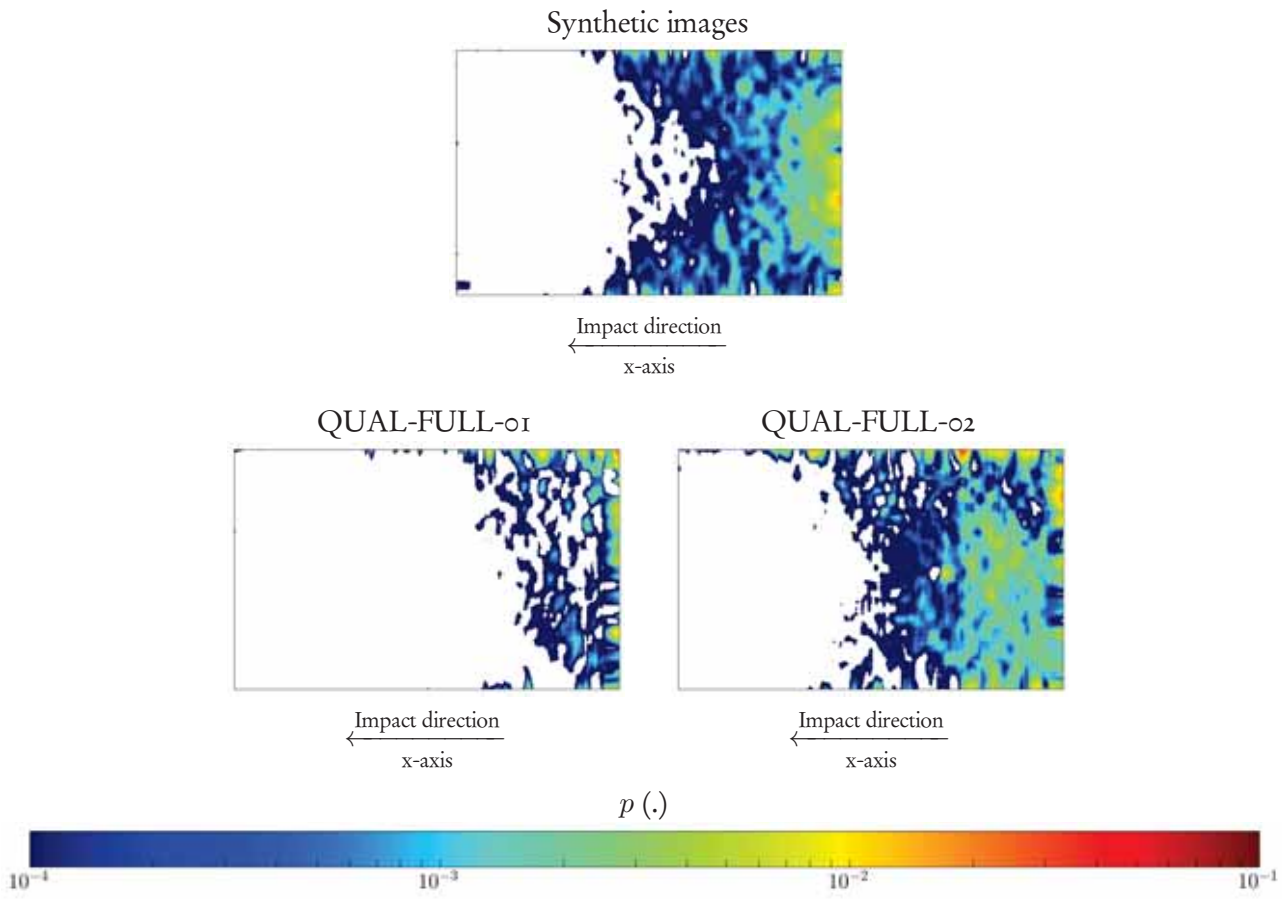

Figure E.4: p at t = 14μs: experimental vs synthetic images for rectangular specimens

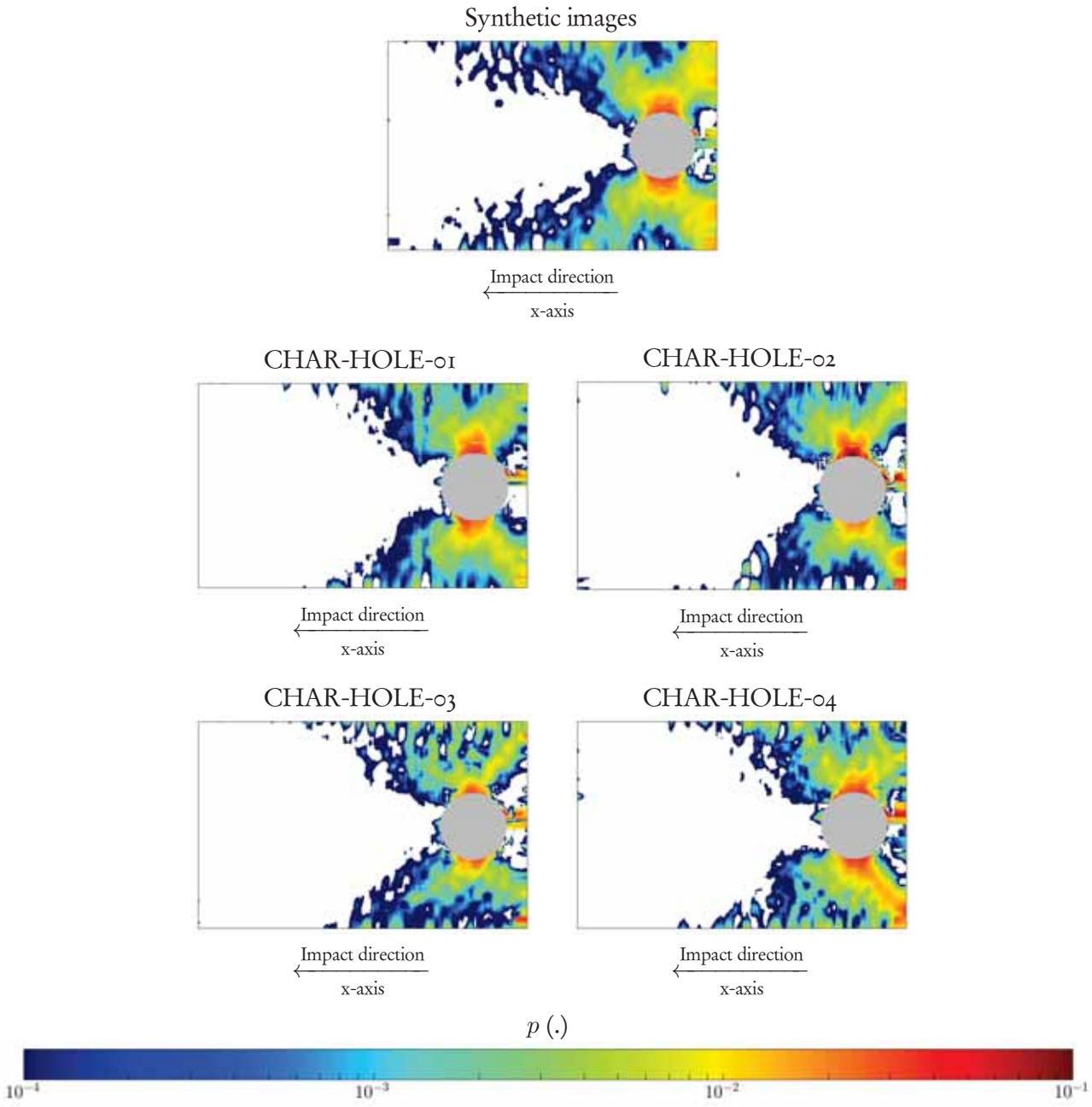

Figure E.5: p at t $= 14\mu$s: experimental vs synthetic images for holed specimens

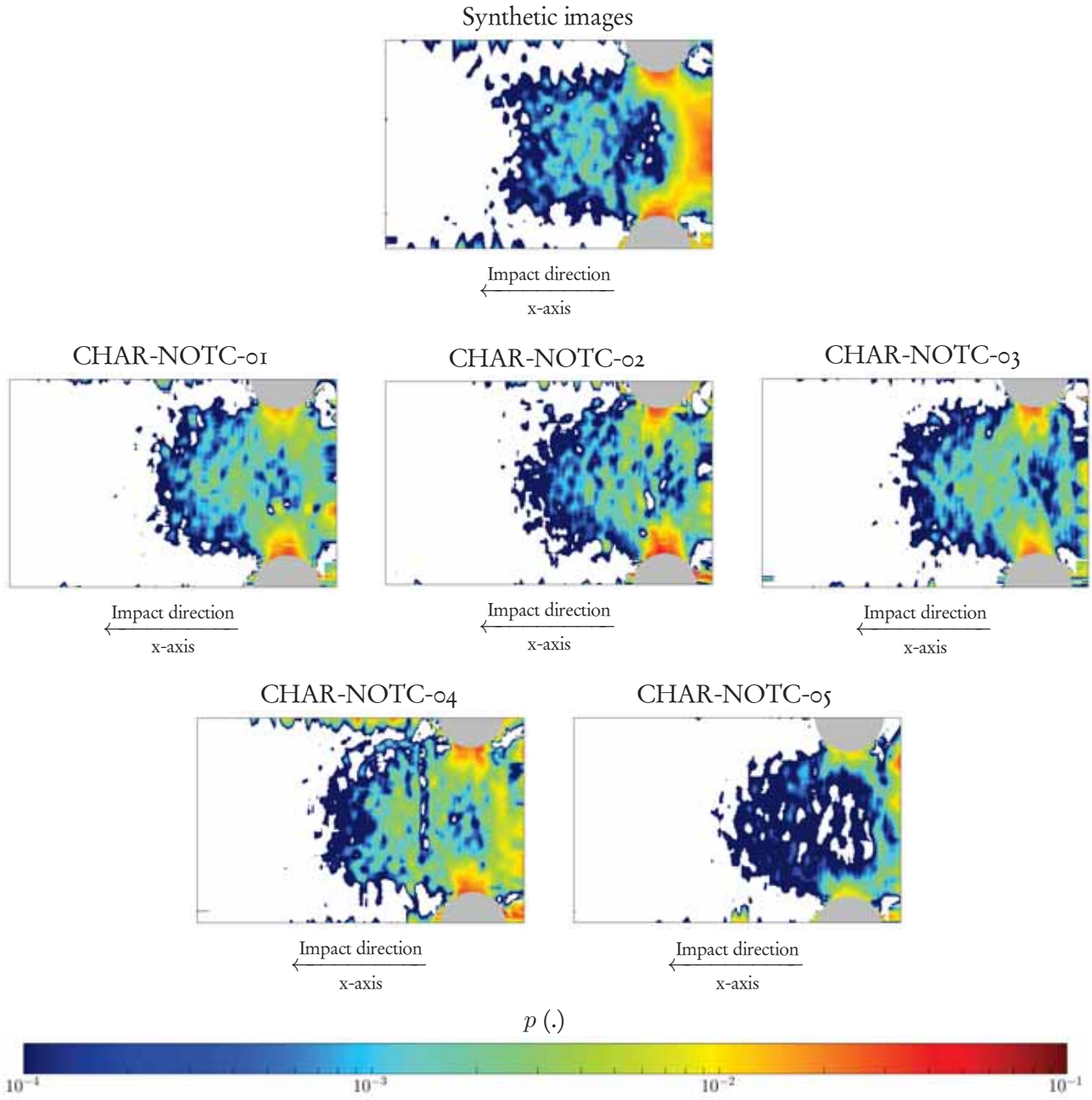

Figure E.6: p at t = 14μs, experimental vs synthetic images for notched specimens

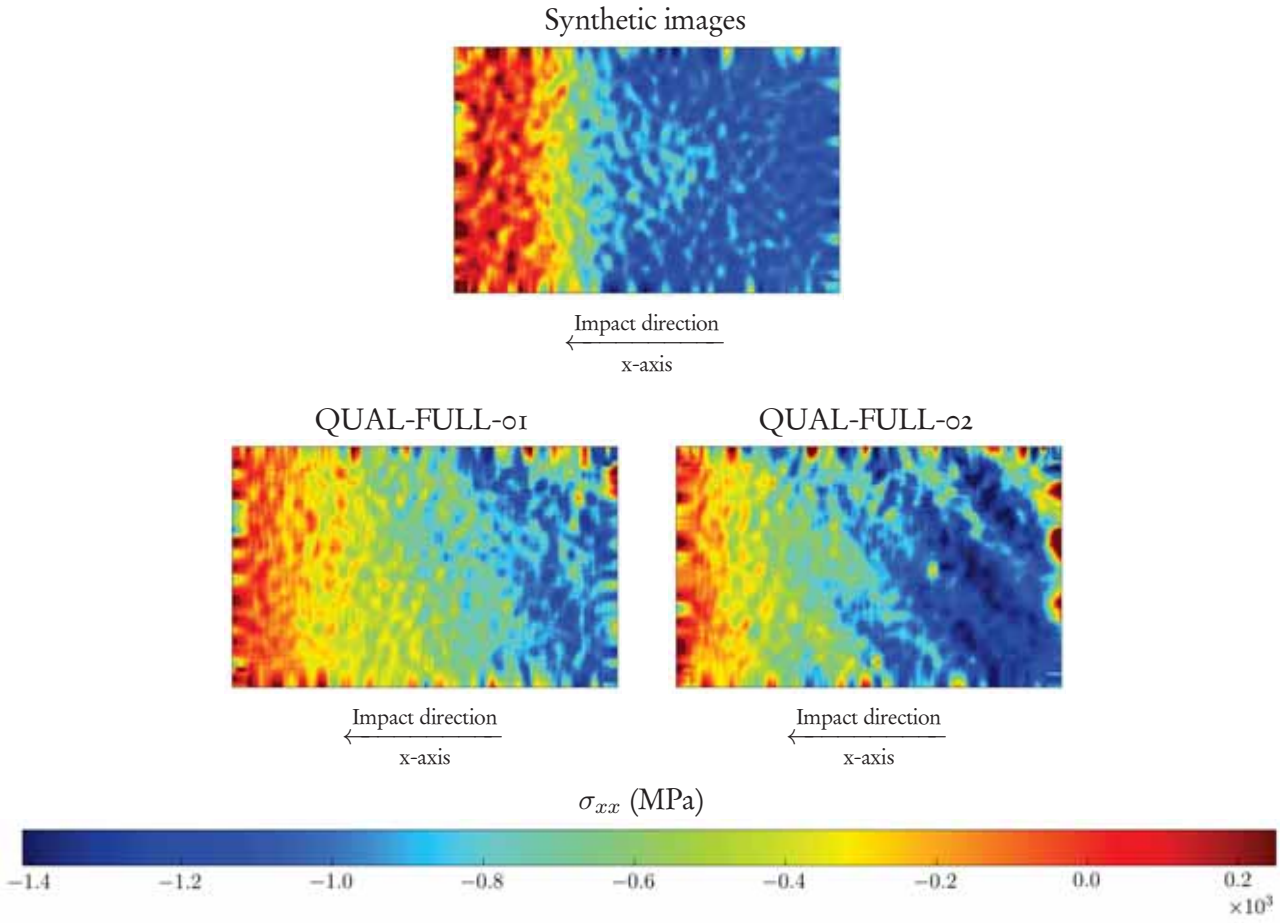

Figure E.7: σ_{xx} at t = 14μs, experimental vs synthetic images for rectangular specimens

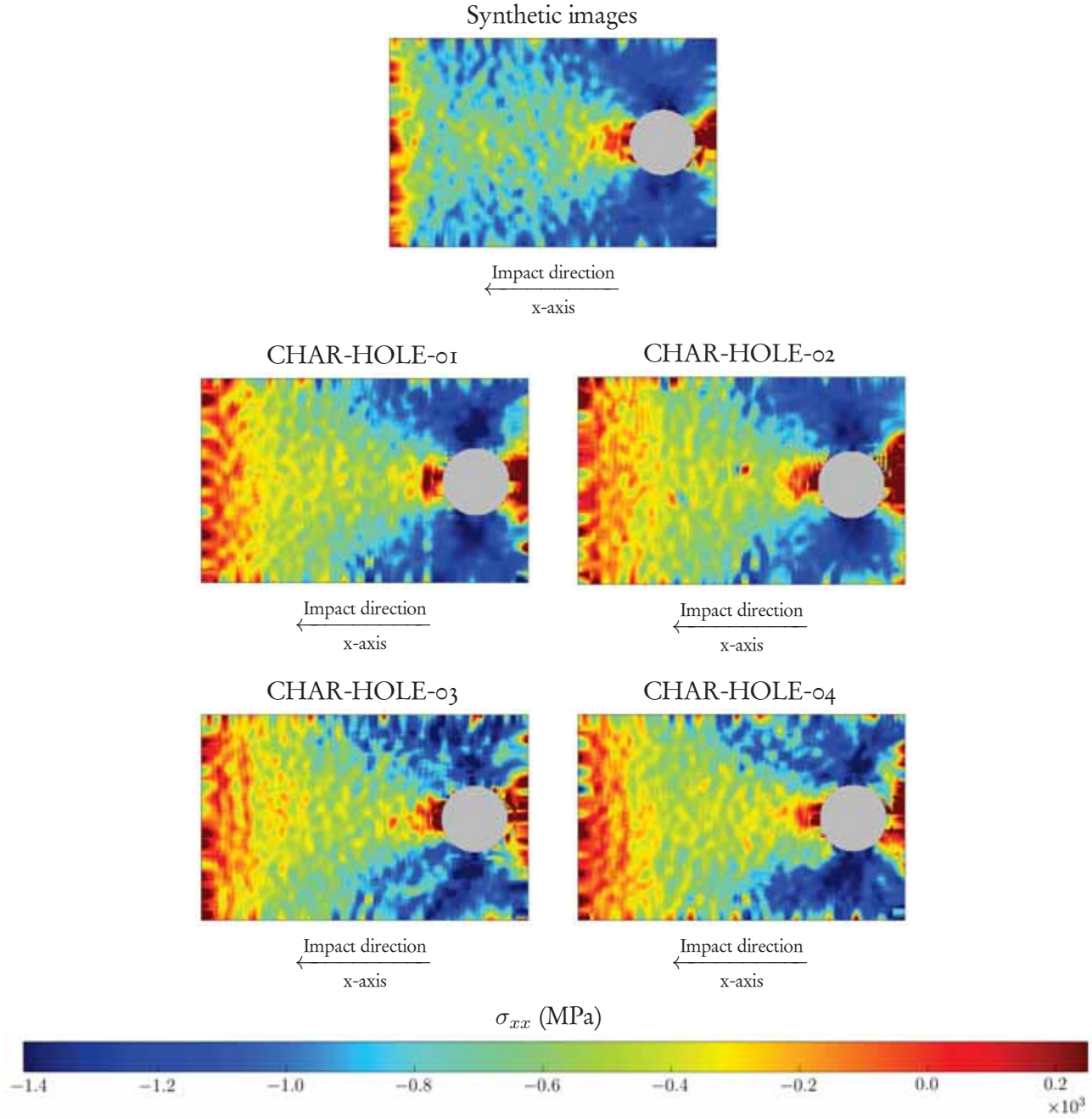

Figure E.8: σ_{xx} at t = 14μs, experimental vs synthetic images for holed specimens

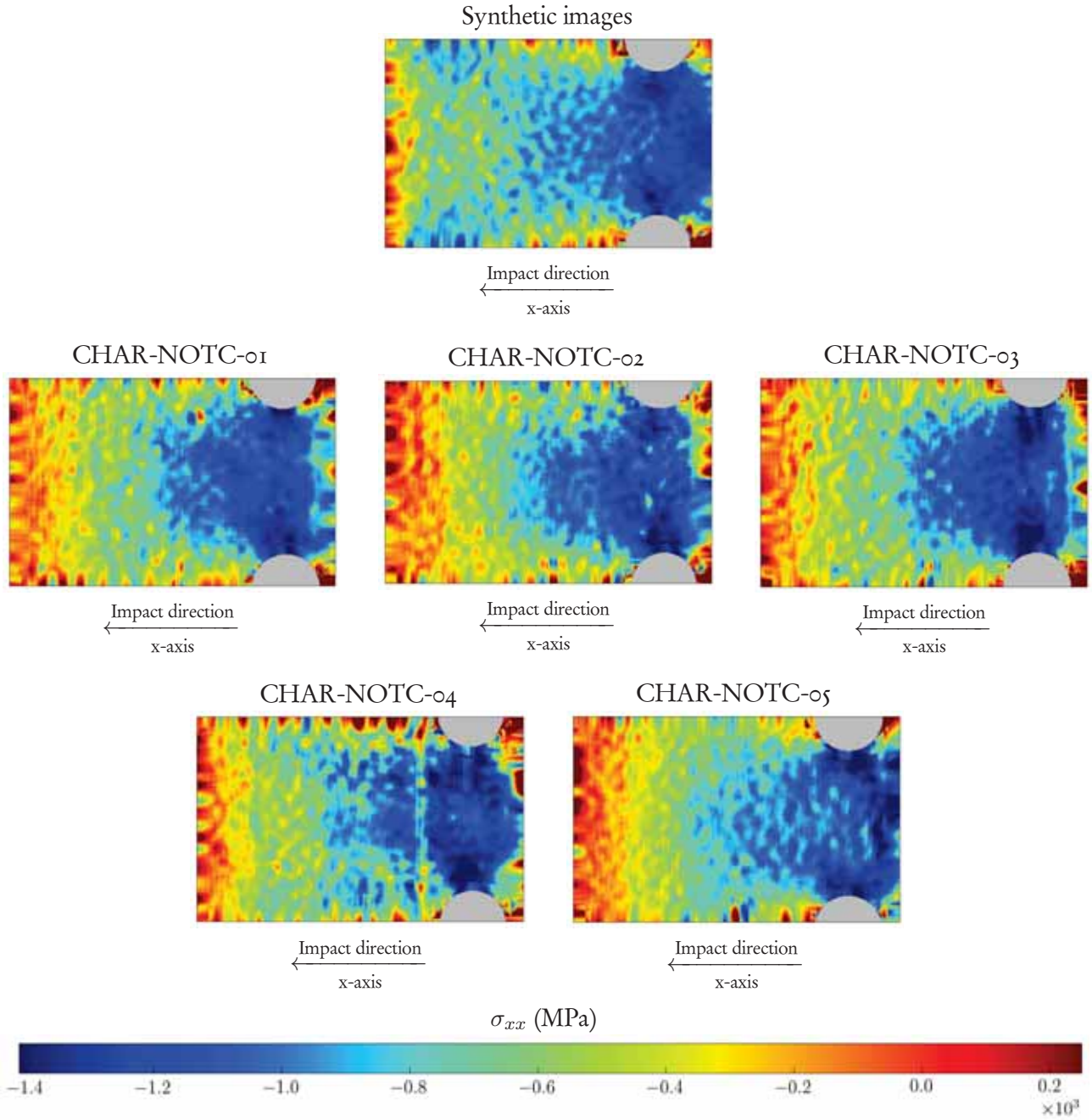

Figure E.9: σ_{xx} at t = 14μs, experimental vs synthetic images for notched specimens

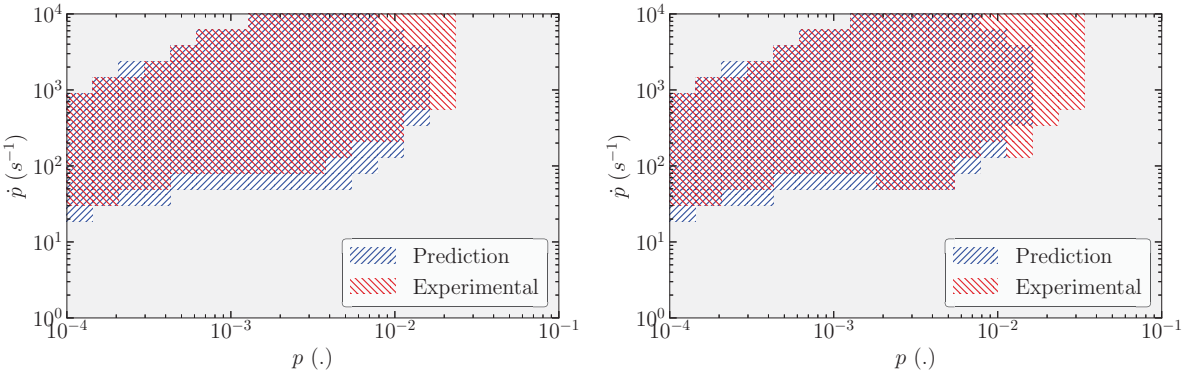

(a) QUAL-FULL-01 (b) QUAL-FULL-02

Figure E.10: Viscoplasticity histograms crossing: Synthetic vs experimental for rectangular specimens

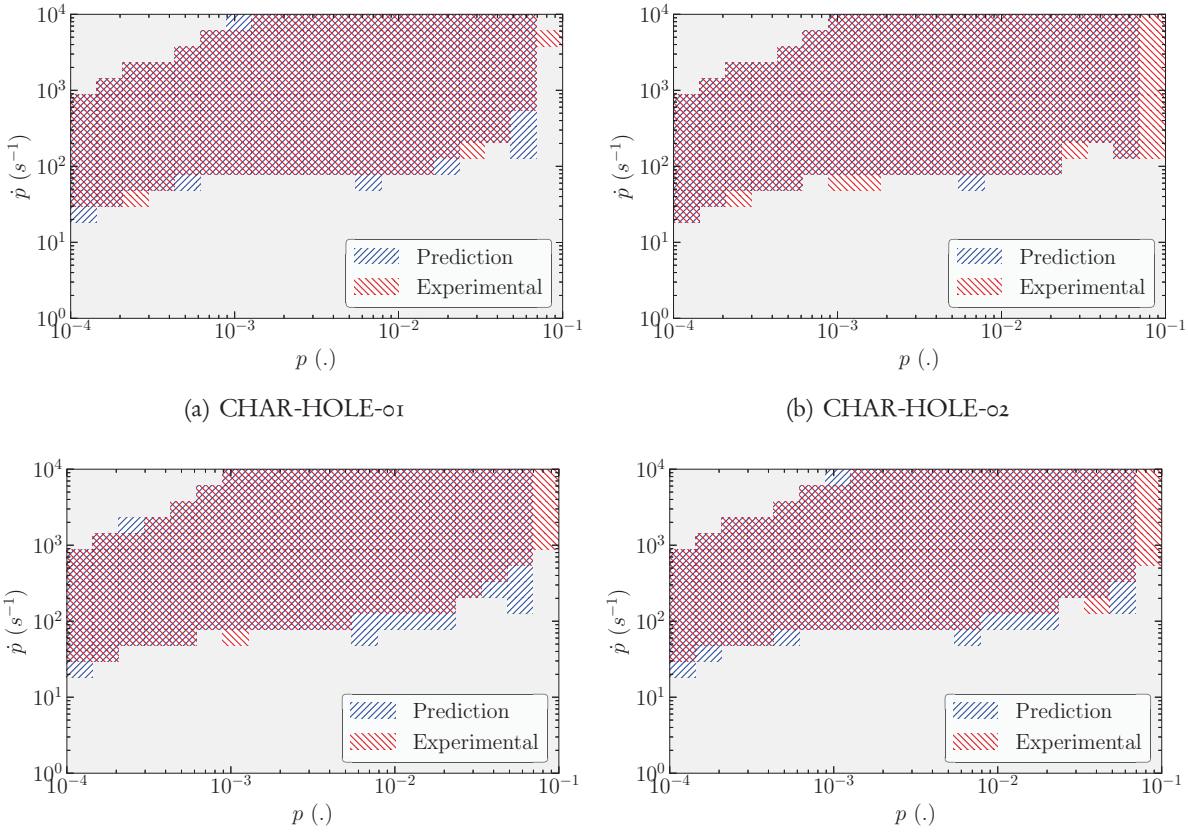

(a) CHAR-HOLE-01 (b) CHAR-HOLE-02

(c) CHAR-HOLE-03 (d) CHAR-HOLE-04

Figure E.11: Viscoplasticity histograms crossing: Synthetic vs experimental for holed specimens

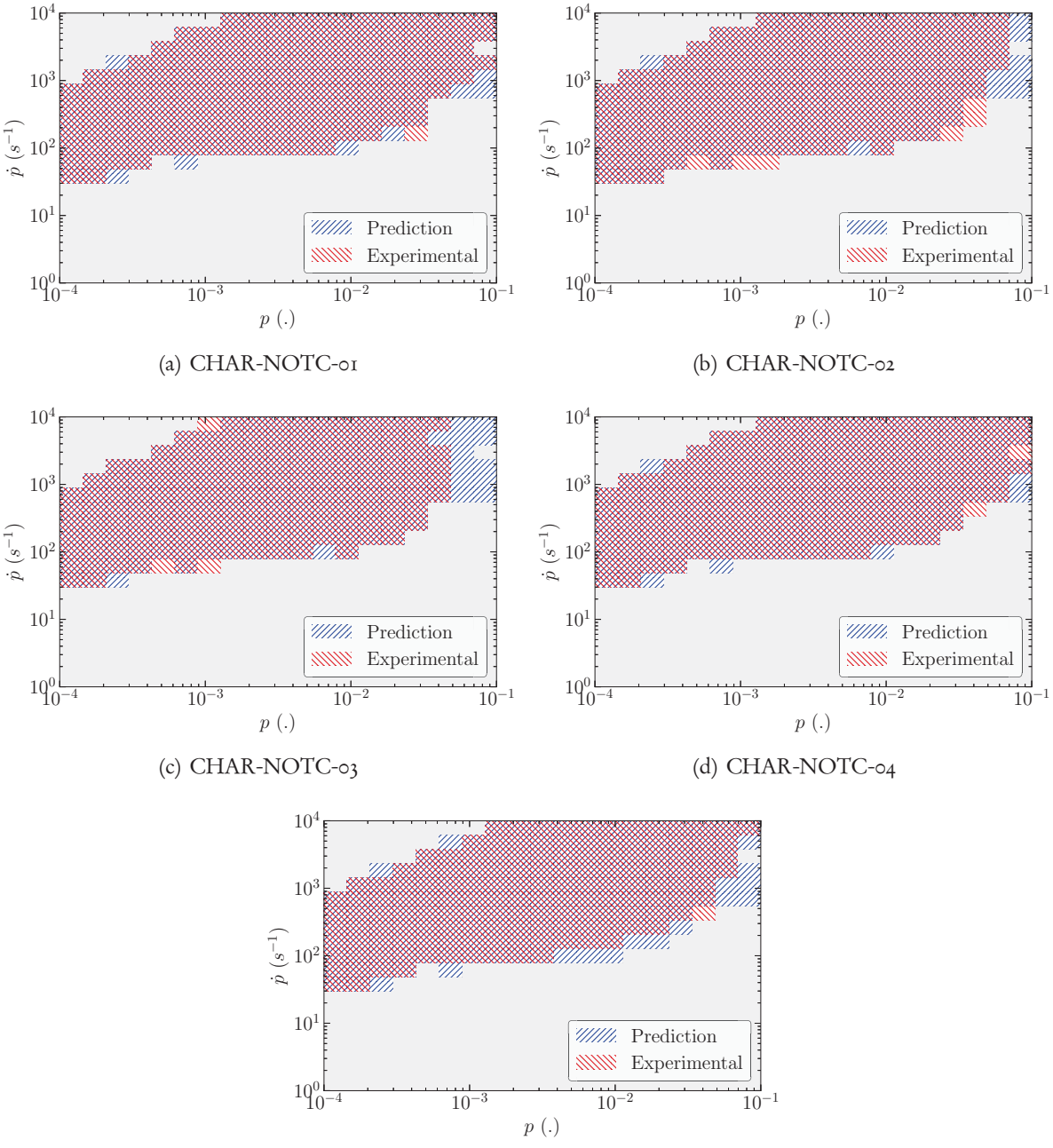

(a) CHAR-NOTC-01

(b) CHAR-NOTC-02

(c) CHAR-NOTC-03

(d) CHAR-NOTC-04

(e) CHAR-NOTC-05

Figure E.12: Viscoplasticity histograms crossing: Synthetic vs experimental for notched specimens

List of Figures

List of Tables

Bibliography

[1] National Transportation Safety Board. Loss of Thrust in Both Engines After Encountering a Flock of Birds and Subsequent Ditching on the Hudson River, US Airways Flight 1549, Airbus A320-214, N106US, Weehawken, New Jersey, January 15, 2009. Aircraft Accident Report NTSB/AAR-10/03. Technical report, National Transportation Safety Board, 2010.

[2] National Transportation Safety Board. Investigative Update, Southwest Airlines Flight 1380 Engine Failure. Technical report, National Transportation Safety Board, 2018.

[3] M.H. Siemann and B. Langrand. Coupled fluid-structure computational methods for aircraft ditching simulations: Comparison of ALE-FE and SPH-FE approaches. *Computers & Structures*, 188:95 – 108, 2017.

[4] ASTM E8 - 04, Standard Test Methods for Tension Testing of Metallic Materials. ASTM International, West Conshohocken, PA, 2004.

[5] E. Markiewicz, B. Langrand, and D. Notta-Cuvier. A review of characterisation and parameters identification of materials constitutive and damage models: From normalised direct approach to most advanced inverse problem resolution. *International Journal of Impact Engineering*, 110:371 – 381, 2017.

[6] D. Notta-Cuvier, B. Langrand, E. Markiewicz, F. Lauro, and G. Portemont. Identification of Johnson-Cook's Viscoplastic Model Parameters Using the Virtual Fields Method : Application to Titanium Alloy Ti6Al4V. *Strain*, 49:22–45, 2013.

[7] F. Pierron, H. Zhu, and C. Siviour. Beyond Hopkinson's bar. *Philosophical Transactions of the Royal Society of London A: Mathematical, Physical and Engineering Sciences*, 372, 2014.

[8] S. Dreuilhe. *Development of novel inertial tests for the identification of non-linear material model parameters at high strain rates.* PhD thesis, University of Southampton, 2017.

[9] B. Koohbor, A. Kidane, M. A. Sutton, X. Zhao, and S. Mallon. Analysis of dynamic bending test using Ultra High Speed DIC and the virtual fields method. *International Journal of Impact Engineering*, 110:299 – 310, 2017. Special Issue in honor of Seventy Fifth Birthday of Professor N. K. Gupta.

[10] B. Koohbor, A. Kidane, M. A. Sutton, X. Zhao, and S. Mallon. Corrigendum to "Analysis of dynamic bending test using Ultra High Speed DIC and the Virtual Fields Method" [Int. J. Impact Eng. 110 (2017) 299–310]. *International Journal of Impact Engineering*, 116:127 – 128, 2018.

[11] F. Pierron, M. A. Sutton, and V. Tiwari. Ultra High Speed DIC and virtual fields method analysis of a three point bending impact test on a aluminium bar. *Experimental Mechanics*, 51:537–563, 2010.

[12] J. Lemaitre. Coupled elasto-plasticity and damage constitutive equations. *Computer Methods in Applied Mechanics and Engineering*, 51(1-3):31–49, 1985.

[13] E.A. de Souza Neto, D. Peric, and D.R.J. Owen. *Computational Methods for Plasticity: Theory and Applications.* Wiley, 2008.

[14] J. Lemaitre and J.L. Chaboche. *Mechanics of Solid Materials.* Cambridge University Press, 1994.

[15] E. Voce. A practical strain-hardening function. *Metallurgia*, 51:219–226, 1955.

[16] P.J. Armstrong and C.O. Frederick. *A Mathematical Representation of the Multiaxial Bauschinger Effect.* RD/B/N 731. Central Electricity Generating Board & Berkeley Nuclear Laboratories, Research & Development Department, 1966.

[17] J-L. Chaboche. A review of some plasticity and viscoplasticity constitutive theories. *International Journal of Plasticity*, 24:1642–1693, 2008.

[18] B. Langrand, P. Geoffroy, J.-L. Petiniot, J. Fabis, E. Markiewicz, and P. Drazetic. Identification technique of constitutive model parameters for crashworthiness modelling. *Aerospace Science and Technology*, 4:215–227, 1999.

[19] G.R. Johnson and W.H. Cook. A constitutive model and data for metals subjected to large strains, high strain rates and high temperatures. *Proc. 7th International Symposium on Balistics*, pages 541–547, 1983.

[20] T. Borvik, M. Langseth, O.S. Hopperstad, and K.A. Malo. Ballistic penetration of steel plates. *International Journal of Impact Engineering*, 22:855–886, 1999.

[21] H.W. Meyer Jr and D.S. Kleponis. Modeling the high strain rate behavior of titanium undergoing ballistic impact and penetration. *International Journal of Impact Engineering*, 26:509–521, 2001.

[22] G. Haugou, E. Markiewicz, J. Fabis, and G. Gary. Contribution to the definition of a partial overlapping plastic strain rates domain for moderate loadings – application to tensile testing on metallic materials. *International Journal of Crashworthiness*, 9(2):187–194, Mar 2004.

[23] G. Haugou, E. Markiewicz, and J. Fabis. On the use of the non direct tensile loading on a classical split hopkinson bar apparatus dedicated to sheet metal specimen characterisation. *International Journal of Impact Engineering*, 32(5):778 – 798, 2006. International Symposium on the Crashworthiness of Light-weight Automotive Structures.

[24] J. Peirs, P. Verleysen, W. Van Paepegem, and J. Degrieck. Determining the stress-strain behaviour at large strains from high strain rate tensile and shear experiments. *International Journal of Impact Engineering*, 38:406–415, 2011.

[25] M.A. Iqbal, K. Senthil, P. Sharma, and N.K. Gupta. An investigation of the constitutive behavior of Armox 500T steel and armor piercing incendiary projectile material. *International Journal of Impact Engineering*, 96:146 – 164, 2016.

[26] G.R. Cowper and P.S. Symonds. *Strain-hardening and Strain-rate Effects in the Impact Loading of Cantilever Beams.* Technical report (Brown University. Division of Applied Mathematics). Division of Applied Mathematics, Brown University, 1957.

[27] Norman Jones. *Structural Impact.* Cambridge University Press, 1990.

[28] F.J. Zerilli and R. W. Armstrong. Dislocation mechanics based constitutive relations for material dynamics calculations. *Journal of Applied Physics*, 61(5):1816–1825, 1987.

[29] A. Rusinek and J.R Klepaczko. Shear testing of a sheet steel at wide range of strain rates and a constitutive relation with strain-rate and temperature dependence of the flow stress. *International Journal of Plasticity*, 17(1):87 – 115, 2001.

[30] J. C. Simo and T. J. R. Hughes. *Computational Inelasticity*. Springer, 1998.

[31] J. A. Nelder and R. Mead. A Simplex Method for Function Minimization. *The Computer Journal*, 7(4):308–313, 1965.

[32] A. Bolte and U.W. Thonemann. Optimizing simulated annealing schedules with genetic programming. *European Journal of Operational Research*, 92:402–416, 1996.

[33] R. Chelouah and P. Siarry. Tabu search applied to global optimization. *European Journal of Operational Research*, 123:256–270, 2000.

[34] R. Chelouah and P. Siarry. A hybrid method combining continuous tabu search and Nelder-Mead simplex algorithms for the global optimization of multiminima functions. *European Journal of Operational Research*, 161:636–654, 2005.

[35] B. Bennani and F. Lauro. Damage models and identification procedures for crashworthiness of automotive light materials. *Latin American Journal of Solids and Structures*, 3:75–87, 2006.

[36] R. Jones, M. Heller, D. Lombardo, S. Dunn, J. Paul, and D. Saunders. Thermoelastic assessment of damage growth in composites. *Composites Structures*, 12(4):291–314, 1989.

[37] J. Berthe and M. Ragonet. Passive infrared thermography measurement of transverse cracking evolution in cross-ply laminates. *Strain*, 54(6):e12293, 2018.

[38] G. Portemont, J. Berthe, A. Deudon, and F. X. Irisarri. Static and dynamic bearing failure of carbon/epoxy composite joints. *Composite Structures*, 204:131 – 141, 2018.

[39] D.W. Templeton. Computerization of carrier fringe data acquisition, reduction and display. *Experimental Techniques*, 11(11):26–30, 1987.

[40] J. Bulhak and Y. Surrel. Grating shearography. In *Interferometry'99: Techniques and Technologies*, pages 506–515, Pultusk (Poland), 1999.

[41] P.K. Rastogi. Speckle shearing photography: a tool for direct measurement of surface strains. *Applied optics*, 37:1292–1298, 1998.

[42] J.J. Wasowski and L.M. Wasowski. Computer based optical differentiation of fringe patterns. *Experimental Techniques*, 11(3):16–18, 1987.

[43] C. Badulescu, M. Grédiac, and J. D. Mathias. Investigation of the grid method for accurate in-plane strain measurement. *Measurement Science and Technology*, 20(9):095102, 2009.

[44] C. Badulescu, M. Grédiac, J. D. Mathias, and D. Roux. A Procedure for Accurate One-Dimensional Strain Measurement Using the Grid Method. *Experimental Mechanics*, 49(6):841–854, 2009.

[45] K. Patorski. *Handbook of the moiré fringe technique*. Elsevier, Amsterdam, 1993.

[46] D. Post, B. Han, and P. Ifju. *High sensitivity moiré: Experimental analysis for mechanics and materials*. Springer-Verlag, New York, 1994.

[47] M. Grédiac. The use of full-field measurement methods in composite material characterization: interest and limitations. *Composites: Part A*, 35:751–761, 2004.

[48] A. Asundi, M.T. Cheung, and C.S. Lee. Moiré interferometry for simultaneous measurements of u, v, w. *Experimental Mechanics*, 29:258–260, 1989.

[49] J.C. Dainty. *Laser speckle and related phenomenon*. Springer, Berlin, 1984.

[50] M.A. Sutton, W.J. Wolters, W.H. Perters, W.F. Ranson, and S.R. McNeill. Determination of displacements using an improved digital image correlation method. *Image and Vision Computing*, 1(3):133–139, 1983.

[51] T.C. Chu, W.F. Ranson, M.A. Sutton, and W.H. Petters. Application of digital image correlation techniques to experimental mechanics. *Experimental Mechanics*, 3:232–244, 1985.

[52] M.A. Sutton, S.R. McNeill, J. Helm, and Y.J. Chao. Advances in two-dimensional and three-dimensional computer vision. In *Photomecanics, topics applied physics*, pages 323–372, 2000.

[53] M.A. Sutton, J.-J. Orteu, and H. Schreier. *Image Correlation for Shape, Motion and Deformation Measurements: Basic Concepts, Theory and Applications*. Springer Publishing Company, Incorporated, 1st edition, 2009.

[54] M. Grédiac and F. Hild. *Full-Field Measurements and Identification in Solid Mechanics*. ISTE. Wiley, 2012.

[55] C.C. Tasan, J.P.M. Hoefnagels, and M.G.D. Geers. Microstructural banding effects clarified through micrographic digital image correlation. *Scripta Materialia*, 62(11):835 – 838, 2010.

[56] F. Hild, B. Raka, M. Baudequin, S. Roux, and F. Cantelaube. Multi-Scale Displacement Field Measurements of Compressed Mineral Wool Samples by Digital Image Correlation. *Applied optics*, IP 41:6815–6828, 2002.

[57] F. Hild and S. Roux. Comparison of local and global approaches to digital image correlation. *Experimental Mechanics*, 52(9):1503–1519, 2012.

[58] G. Besnard, F. Hild, and S. Roux. "Finite-Element" Displacement Fields Analysis from Digital Images: Application to Portevin–Le Châtelier Bands. *Experimental Mechanics*, 46(6):789–803, 2006.

[59] H. Leclerc, J. N. Périé, S. Roux, and F. Hild. Integrated Digital Image Correlation for the Identification of Mechanical Properties. In *Proceedings of the 4th International Conference on Computer Vision/Computer Graphics Collaboration Techniques*, MIRAGE '09, pages 161–171, Berlin, Heidelberg, 2009. Springer-Verlag.

[60] S. Roux, J. Réthoré, and F. Hild. Digital image correlation and fracture: an advanced technique for estimating stress intensity factors of 2D and 3D cracks. *Journal of Physics D: Applied Physics*, 42(21):214004, 2009.

[61] A. Ruybalid, J. P. M. Hoefnagels, O. Van der Sluis, and M. G. D. Geers. Comparison of the identification performance of conventional FEM updating and integrated DIC. *International Journal for Numerical Methods in Engineering*, 106:298–320, 2016.

[62] M. B. R. Bertin, F. Hild, and S. Roux. Optimization of a Cruciform Specimen Geometry for the Identification of Constitutive Parameters Based Upon Full-Field Measurements. *Strain*, 52(4):307–323, 2016.

[63] Y. Surrel. Moiré and grid methods: a signal processing approach. In *Interferometry'94: Photomechanics*, pages 213–220, 1999.

[64] Y. Surrel. La technique de la grille et ses applications. *Instrumentation mesure et métrologie*, 4(3-4):193–216, 2005.

[65] M. Grédiac, F. Sur, and B. Blaysat. The Grid Method for In-plane Displacement and Strain Measurement: A Review and Analysis. *Strain*, 52(3):205–243, 2016.

[66] D. Post. Developments in moiré interferometry. *Optical Engineering*, 21(3):458–467, 1982.

[67] V.J. Parks. Geometric moiré. *In: Handbook on Experimental Mechanics, Chap. 6*, pages 267–296, 1993.

[68] J.-L. Piro and M. Grédiac. Producing and transferring low-spatial-fequency grids for measuring displacement fields with Moiré and grid methods. *Experimental Techniques*, 28(4):23–26, 2004.

[69] M. Grédiac, B. Blaysat, and F. Sur. A Critical Comparison of Some Metrological Parameters Characterizing Local Digital Image Correlation and Grid Method. *Experimental Mechanics*, 57(6):871–903, 2017.

[70] M. A. Herráez, D. R. Burton, M. J. Lalor, and M. A. Gdeisat. Fast two-dimensional phase-unwrapping algorithm based on sorting by reliability following a noncontinuous path. *Appl. Opt.*, 41(35):7437–7444, Dec 2002.

[71] H. Abdul-Rahman, M. Gdeisat, D. Burton, and M. Lalor. Fast three-dimensional phase-unwrapping algorithm based on sorting by reliability following a non-continuous path. In *Proc. SPIE*, volume 5856, pages 32–40, 2005.

[72] R. Moulard, S. Avril, and F. Pierron. Identification of the through-thickness rigidities of a thick laminated composite tube. *Composites: Part A: Applied Science and Manufacturing*, 37(2):326–336, 2006.

[73] P. L. Reu and M. R. Nissen. The evolution of high and ultra-high speed imaging from qualitative to quantitative. https://www.osti.gov/servlets/purl/1242080, 2014.

[74] M. Rossi, R. Cheriguene, F. Pierron, and P. Forquin. Performance Assessment of Strain Measurement with an Ultra High Speed camera. In Tom Proulx, editor, *Optical Measurements, Modeling, and Metrology, Volume 5*, pages 299–306, New York, NY, 2011. Springer New York.

[75] S. Avril, M. Bonnet, AS. Bretelle, M. Grédiac, F. Hild, P. Ienny, F. Latourte, D. Lemosse, S. Pagano, E. Pagnacco, and F. Pierron. Overview of identification methods of mechanical parameters based on full-field measurements. *Experimental Mechanics*, 48:381–402, 2008.

[76] A. Ferhaoui and D. Nedjar. Correction paramétrique de modèles éléments finis à partir de résultats d'essais statiques et dynamiques. In *1st international conference on sustainable built environment infrastructures in developing countries*, volume 1, pages 49–56. SBEIDCO, 2009.

[77] M. Geradin and D. J. Rixen. *Mechanical Vibrations: Theory and Application to Structural Dynamics, 3rd edition*. Wiley, 2015.

[78] F. Latourte, A. Chrysochoos, S. Pagano, and B. Wattrisse. Elastoplastic behavior identification for heterogeneous loadings and materials. *Experimental Mechanics*, 48:435–449, 2008.

[79] S. Andrieux, A. Abda, and H.B Bui. Reciprocity principle and crack identification. *Inverse Problems*, 15(1):59, 1999.

[80] D. Claire, F. Hild, and S. Roux. A finite element formulation to identify damage fields: the equilibrium gap method. *International Journal for Numerical Methods in Engineering*, 61(2):189–208, 2004.

[81] M.H.H. Meuwissen, C.W.J. Oomens, F.P.T. Baaijens, R. Petterson, and J.D. Janssen. Determination of the elasto-plastic properties of aluminium using a mixed numerical–experimental method. *Journal of Materials Processing and Technology*, 75:204–211, 1998.

[82] J. Kajberg, K.G. Sundin, L.G. Melin, and P. Stahlea. High strain-rate tensile testing and viscoplastic parameter identification using microscopic high-speed photography. *International Journal of Plasticity*, 20(4-5):561–575, 2004.

[83] J. Kajberg and B. Wikman. Viscoplastic parameter estimation by high strain-rate experiments and inverse modelling - Speckle measurements and high-speed photography. *International Journal of Solids and Structures*, 44:145–164, 2007.

[84] P. Perzyna. The constitutive equations for rate-sensitive plastic materials. *Journal of Applied Mathematics*, 20:321–332, 1963.

[85] A.L. Gurson. Porous rigid-plastic materials containing rigid inclusions – Yield function, plastic potential and void nucleation. In D.M.R. Taplin, editor, *Int. Conf. on Fracture*, 1977.

[86] V. Tvergaard. Material failure by void coalescence in localized shear bands. *Int. J. of Solids and Structures*, 18:659–672, 1982.

[87] B. Langrand, E. Deletombe, E. Markiewicz, and P. Drazétic. Numerical approach for assessment of dynamic strength for riveted joints. *Aerospace Science and Technology*, 3(7):431–446, 1999.

[88] E. Markiewicz, P. Ducrocq, P. Drazétic, and G. Haugou. Behaviour law identification for the various zones of spot-weld under quasistatic loadings. *Int J of Materials and Product Technology*, 16:484–509, 2001.

[89] M. Grédiac. Principe des travaux virtuels et identifications. *C.R. Académie des Sciences, Série II, Paris*, 309:1–5, 1989.

[90] F. Pierron and M. Grédiac. *The Virtual Fields Method: Extracting Constitutive Mechanical Parameters from Full-field Deformation Measurements.* Springer New York, 2012.

[91] M. Grédiac, E. Toussaint, and F. Pierron. Special virtual fields for the direct determination of material parameters with the virtual fields method. 1 - Principle and definition. *International Journal of Solids and Structures*, 39:2691–2705, 2002.

[92] M. Grédiac, E. Toussaint, and F. Pierron. Special virtual fields for the direct determination of material parameters with the virtual fields method. 2 - Application to in-plane properties. *International Journal of Solids and Structures*, 39:2707–2730, 2002.

[93] M. Grédiac and A. Vautrin. A new method for determination of bending rigidities of thin anisotropic plates. *Journal of Applied Mechanics*, 57:964–968, 1990.

[94] M. Grédiac and F. Pierron. A T-shaped specimen for the direct characterization of orthotropic materials. *International Journal for Numerical Methods in Engineering*, 41:293–309, 1998.

[95] M. Grédiac, F. Pierron, and Y. Surrel. Novel procedure for complete in-plane composite characterization using a t-shaped specimen. *Experimental Mechanics*, 39:142–149, 1999.

[96] J.-H. Kim, F. Pierron, M.R. Wisnom, and K. Syed-Muhamad. Identification of the local stiffness reduction of a damaged composite plate using the virtual fields method. *Composites: Part A*, 38:2065–2075, 2007.

[97] H. Chalal, F. Meraghni, F. Pierron, and M. Grediac. Direct identification of the damage behaviour of composite materials using the virtual fields method. *Composites: Part A*, 35:841–848, 2004.

[98] M. Grédiac, F. Pierron, S. Avril, and E. Toussaint. The Virtual Fields Method for Extracting Constitutive Parameters From Full-Field Measurements: a Review. *Strain*, 42:233–253, 2006.

[99] S. Avril, F. Pierron, Y. Pannier, and R. Rotinat. Stress reconstruction and constitutive parameter identification in plane-stress elasto-plastic problems using surface measurements of deformation fields. *Experimental Mechanics*, 48:403–419, 2008.

[100] S. Blanchard, B. Langrand, J. Fabis, and E. Markiewicz. Identification of plastic behaviour parameters from strongly heterogeneous strain field. In *SEM-XIth International Congress & Exposition on Experimental and Applied Mechanics, Orlando, USA*, 2008.

[101] Y. Pannier, S. Avril, R. Rotinat, and F. Pierron. Identification of elasto-plastic constitutive parameters from statically undetermined tests using the virtual fields method. *Experimental Mechanics*, 46:735–755, 2006.

[102] V. T. Tran. *Identification du comportement des matériaux métalliques au-delà de leur limite d'élasticité par la méthode des champs virtuels*. PhD thesis, Thèse ENSAM Châlons en Champagne, 2008.

[103] F. Pierron, S. Avril, and V. T. Tran. Extension of the virtual fields method to elasto-plastic material identification with cyclic loads and kinematic hardening. *International Journal of Solids and Structures*, 47:2993–3010, 2010.

[104] D. Notta-Cuvier, B. Langrand, F. Lauro, and E. Markiewicz. An innovative procedure for characterising a coupled elastoplastic damage model of behaviour using the virtual fields method. *International Journal of Solids and Structures*, 69-70:415–427, 2015.

[105] G. Valeri, B. Koohbor, A. Kidane, and M.A. Sutton. Determining the tensile response of materials at high temperature using DIC and the Virtual Fields Method. *Optics and Lasers in Engineering*, 91:53–61, 2017.

[106] B. Hopkinson. A method of measuring the pressure produced in the detonation of high explosives of by the impact of bullets. *Philosophical Transactions of the Royal Society A*, 213:437–456, 1914.

[107] T. Nicholas. Tensile testing of materials at high rates of strain. *Experimental Mechanics*, 21(5):177–185, May 1981.

[108] R. Moulart, F. Pierron, S.R. Hallett, and M.R. Wisnom. Full-field strain measurement and identification of composites moduli at high strain rate with the virtual fields method. *Experimental Mechanics*, 51:509–536, 2011.

[109] F. Pierron and P. Forquin. Ultra-high-speed full-field deformation measurements on concrete spalling specimens and stiffness identification with the virtual fields method. *Strain*, 48:388–405, 2012.

[110] G. Le Louëdec, F. Pierron, M. A. Sutton, C. Siviour, and A. P. Reynolds. Identification of the Dynamic Properties of Al 5456 FSW Welds Using the Virtual Fields Method. *Journal of Dynamic Behavior of Materials*, 1(2):176–190, Jun 2015.

[111] S.-H. Yoon, M. Winters, and C.R. Siviour. High Strain-Rate Tensile Characterization of EPDM Rubber Using Non-equilibrium Loading and the Virtual Fields Method. *Experimental Mechanics*, 56:25–25, 2016.

[112] J. Van Blitterswyk, L. Fletcher, and F. Pierron. Image-Based Inertial Impact Test for Composite Interlaminar Tensile Properties. *Journal of Dynamic Behavior of Materials*, 4(4):543–572, Dec 2018.

[113] L. Fletcher and F. Pierron. An Image-Based Inertial Impact (IBII) Test for Tungsten Carbide Cermets. *Journal of Dynamic Behavior of Materials*, 4(4):481–504, Dec 2018.

[114] M. Rossi and F. Pierron. On the use of simulated experiments in designing tests for material characterization from full-field measurements. *International Journal of Solids and Structures*, 49(3–4):420 – 435, 2012.

[115] M. Rossi, P. Lava, F. Pierron, D. Debruyne, and M. Sasso. Effect of DIC Spatial Resolution, Noise and Interpolation Error on Identification Results with the VFM. *Strain*, 51:206–222, 2015.

[116] D. Notta-Cuvier. *Méthode des champs virtuels pour la caractérisation de comportement viscoplastiques et d'endommagement, à partir de mesures de champs mécaniques hétérogènes.* PhD thesis, Université de Valenciennes et du Hainaut-Cambrésis, 2011.

[117] B. Moras. Constitutive Equations of Strain rate sensitive metals for the automotive industry - PLEXIS-3C Implementation Report. Technical Report Techncal Note No. I.99.54, Joint Research Centre, March 1999.

[118] Europlexus Team. Europlexus: a computer program for the finite element simulation of fluid-structure systems under transient dynamic loading - User's manual, 2017.

[119] F. Sur and M. Grédiac. Influence of the analysis window on the metrological performance of the grid method. *Journal of Mathematical Imaging and Vision*, 56(3):472–498, 2016.

[120] A. Savitzky and M.J.E. Golay. Smoothing and Differentiation of Data by Simplified Least Squares Procedures. *Analytical chemistry*, 36:1627–1639, 07 1964.

[121] P. Holoborodko. (n.d) Smooth noise-robust differentiators. Retrieved from http://www.holoborodko.com/pavel/numerical-methods/noise-robust-smoothing-filter/, 2008.

[122] Cast3M®. (n.d) http://www-cast3m.cea.fr.

[123] T. Belytschko and M. O. Neal. Contact-impact by the pinball algorithm with penalty and Lagrangian methods. *International Journal for Numerical Methods in Engineering*, 31(3):547–572, 1991.

[124] T. Belytschko and I.S. Yeh. The splitting pinball method for contact-impact problems. *Computer Methods in Applied Mechanics and Engineering*, 105(3):375 – 393, 1993.

[125] B. Langrand, F. Casadei, V. Marcadon, G. Portemont, and S. Kruch. Experimental and finite element analysis of cellular materials under large compaction levels. *International Journal of Solids and Structures*, 128:pages 99 – 116, August 2017.

[126] M. Bornert, F. Brémand, P. Doumalin, J.-C. Dupré, M. Fazzini, M. Grédiac, F. Hild, S. Mistou, J. Molimard, J.-J. Orteu, L. Robert, Y. Surrel, P. Vacher, and B. Wattrisse. Assessment of Digital Image Correlation measurement errors: methodology and results. *Experimental Mechanics*, 49(3):353–370, Jun 2009.

[127] B. Lukic, D. Saletti, and P. Forquin. Use of simulated experiments for material characterization of brittle materials subjected to high strain rate dynamic tension. *Philosophical Transactions of the Royal Society of London A: Mathematical, Physical and Engineering Sciences*, 375(2085), 2016.

[128] J. J. Orteu, D. Garcia, L. Robert, and F. Bugarin. A speckle texture image generator. *Proc. SPIE*, 6341, 2006.

[129] Y. Tochigi, K. Hanzawa, Y. Kato, R. Kuroda, H. Mutoh, R. Hirose, H. Tominaga, K. Takubo, Y. Kondo, and S. Sugawa. A Global-Shutter CMOS Image Sensor With Readout Speed of 1-Tpixel/s Burst and 780-Mpixel/s Continuous. *IEEE Journal of Solid-State Circuits*, 48(1):329–338, Jan 2013.

[130] R. Balcaen, L. Wittevrongel, P. L. Reu, P. Lava, and D. Debruyne. Stereo-DIC Calibration and Speckle Image Generator Based on FE Formulations. *Experimental Mechanics*, 57(5):703–718, 2017.

[131] L. Fletcher and F. Pierron. The Image-Based Inertial Impact (IBII) Test Part 1: Design of a Purpose-Built Gas Gun. *Experimental Techniques*, Submitted.

[132] Y. Surrel. Grid printing part I. http://photodyn.org/wp-content/uploads/2016/03/Report_UniversityPrintCentre.pdf, 2018.

[133] Y. Surrel. Grid printing part II. http://photodyn.org/wp-content/uploads/2016/03/Report_UniversityPrintCentre_2.pdf, 2018.

[134] F. Sur, B. Blaysat, and M. Grédiac. Determining displacement and strain maps immune from aliasing effect with the grid method. *Optics and Lasers in Engineering*, 86:317 – 328, 2016.

[135] M. Grédiac, B. Blaysat, and F. Sur. Extracting displacement and strain fields from checkerboard images with the Localized Spectrum Analysis. *Experimental Mechanics*, 2018.

[136] A. Marek, F. M. Davis, and F. Pierron. Sensitivity-based virtual fields for the non-linear virtual fields method. *Computational Mechanics*, 60(3):409–431, Sep 2017.

Virtual Fields Method for the Dynamic Behaviour of Metallic Materials under Purely Inertial Loads

This thesis aims at developing an innovative methodology for viscoplastic material behaviour characterization of metallic materials under purely inertial loads. Indeed, their mechanical behaviour under extreme conditions (e.g., crash, impact or explosions) is often rate-dependant. Statically determinate approaches are mainly used to characterize their behaviour. However, they require numerous tests for which testing conditions are strongly constrained, such as the strain rate which has to remain constant in time and space for instance. By contrast, statically undeterminate approaches enable test processing with a few (or without) hypotheses on experimental conditions.
In this work, the Image-Based Inertial Impact test methodology has been extended to characterize the viscoplastic behaviour of metallic materials. Owing to the Virtual Fields Method, it enables the identification of constitutive material parameters with the sole knowledge of strain and acceleration fields (possibly heterogeneous in time and space). Therefore, constitutive models can be characterized over a wide range of plastic strain and strain rate, while the number of tests is limited. Tests design notably relies on the development of a synthetic images generator to determine the experimental setup (e.g., specimen geometry or testing conditions). Finally, experiments are carried out with optimized test configurations to identify Johnson-Cook parameters over a predicted range of plastic strain and strain rate for a titanium alloy widely used in aerospace industry. Identification uncertainties are also quantified and analysed in this work.

Keywords : VIRTUAL FIELDS METHOD ; IMPACT TEST ; VISCOPLASTICITY ; JOHNSON-COOK MODEL ; OPTIMIZATION

Méthode des Champs Virtuels pour la caractérisation du comportement dynamique de matériaux métalliques sous chargement purement inertiel

Les travaux de la thèse visent à mettre en place une méthodologie innovante de caractérisation du comportement viscoplastique des matériaux métalliques sous chargement purement inertiel. Sous chargements mécaniques extrêmes (e.g., crash, impact ou explosions), leur comportement mécanique présente en effet pour nombre d'entre eux une sensibilité à la vitesse de déformation. Des approches dites statiquement déterminées sont majoritairement utilisées pour caractériser leur comportement, mais elles requièrent de nombreux essais dont les conditions expérimentales sont souvent contraintes comme par exemple l'homogénéité de la vitesse de déformation qui doit être maintenue constante en temps par exemple. En revanche, des approches dites statiquement indéterminées permettent l'exploitation d'essais mécaniques avec peu d'hypothèses (voire sans) sur les conditions d'essai. Une méthodologie fondée sur un essai d'impact purement intertiel est mise en oeuvre ici pour identifier le comportement viscoplastique de ces matériaux.
Avec la Méthode des Champs Virtuels, la méthodologie permet l'identification des paramètres matériaux en exploitant uniquement la mesure des champs de déformation et d'accélération, potentiellement hétérogènes en temps et en espace. Ainsi, celui-ci peut être caractérisé sur une large gamme de déformations et de vitesses de déformation plastiques en procédant à un nombre limité d'expériences. La méthode repose sur le développement d'un simulateur d'images avancé permettant de définir au préalable l'ensemble du dispositif expérimental (géométrie de l'éprouvette et conditions expérimentales). Optimisées numériquement pour prescrire les paramètres d'essai critiques, les réalisations expérimentales menées sur un alliage de Titane utilisé dans l'industrie aéronautique ont permis d'identifier les paramètres d'un modèle de Johnson-Cook sur un spectre de déformations et de vitesses de déformation plastiques pré-déterminé. Les incertitudes de la mesure sont également intégrées et analysées dans ce travail.

Mots clés : METHODE DES CHAMPS VIRTUELS ; ESSAI D'IMPACT ; VISCOPLASTICITE ; MODELE DE JOHNSON-COOK ; OPTIMISATION

ONERA
THE FRENCH AEROSPACE LAB

ONERA - BP 80100 - 91123 PALAISEAU CEDEX - Tél. : +33 1 80 38 60 60 - Fax : +33 1 80 38 65 10

www.onera.fr